FINAL REPORT

Optically Driven Spin Based Quantum Dots for Quantum Computing

Principal Investigator: Duncan G. Steel
Department of Electrical Engineering and Computer Science
Department of Physics
Harrison M. Randall Laboratory of Physics
The University of Michigan
Ann Arbor, MI 48109
Phone: 734-764-4469
Email: dst@umich.edu

Co-Principal Investigator: L.J. Sham
Department of Physics
The University of California – San Diego
San Diego, CA
Email: lsham@ucsd.edu

ABSTRACT

This program conducted experimental and theoretical research aimed at developing an optically driven quantum dot quantum computer. In addition to the two co-principal investigators (Sham and Steel), the work was done in collaboration with Dan Gammon at the Naval Research Laboratory. D. Gammon had responsibility for designing, fabricating and basic spectroscopy of the material, LJ Sham is responsible for theoretical support and concept development, and DG Steel is responsible for experimental demonstration of key experimental demonstrations for quantum computing. For this program, qubit is the spin of the electron trapped in a self-assembled quantum dot in InAs. Optical manipulation using the trion state allows for fast (psec) rotations of the electron spin. The program achieved several milestones including demonstration of initialization, fast spin rotations and a phase gate, reduction of nuclear fluctuations extending the spin coherence time by 3 orders of magnitude, major advances in scalable gate proposals, and two proposals for measurement of measurement of true spin coherence time..

Report Documentation Page		*Form Approved* OMB No. 0704-0188

Public reporting burden for the collection of information is estimated to average 1 hour per response, including the time for reviewing instructions, searching existing data sources, gathering and maintaining the data needed, and completing and reviewing the collection of information. Send comments regarding this burden estimate or any other aspect of this collection of information, including suggestions for reducing this burden, to Washington Headquarters Services, Directorate for Information Operations and Reports, 1215 Jefferson Davis Highway, Suite 1204, Arlington VA 22202-4302. Respondents should be aware that notwithstanding any other provision of law, no person shall be subject to a penalty for failing to comply with a collection of information if it does not display a currently valid OMB control number.

1. REPORT DATE **2008**	2. REPORT TYPE	3. DATES COVERED **02-06-2004 to 31-12-2008**
4. TITLE AND SUBTITLE **Optically Driven Spin Based Quantum Dots for Quantum Computing**		5a. CONTRACT NUMBER **W911NF-04-1-0235**
		5b. GRANT NUMBER
		5c. PROGRAM ELEMENT NUMBER
6. AUTHOR(S)		5d. PROJECT NUMBER
		5e. TASK NUMBER
		5f. WORK UNIT NUMBER
7. PERFORMING ORGANIZATION NAME(S) AND ADDRESS(ES) **Department of Electrical Engineering and Computer Science,Department of Physics,Harrison M. Randall Laboratory of Physics, The University of Michigan,Ann Arbor,MI,48109**		8. PERFORMING ORGANIZATION REPORT NUMBER **; 46247-PH-QC.1**
9. SPONSORING/MONITORING AGENCY NAME(S) AND ADDRESS(ES) **U.S. Army Research Office, P.O. Box 12211, Research Triangle Park, NC, 27709-2211**		10. SPONSOR/MONITOR'S ACRONYM(S)
		11. SPONSOR/MONITOR'S REPORT NUMBER(S) **46247-PH-QC.1**
12. DISTRIBUTION/AVAILABILITY STATEMENT **Approved for public release; distribution unlimited**		
13. SUPPLEMENTARY NOTES		
14. ABSTRACT		
15. SUBJECT TERMS		

16. SECURITY CLASSIFICATION OF:			17. LIMITATION OF ABSTRACT	18. NUMBER OF PAGES	19a. NAME OF RESPONSIBLE PERSON
a. REPORT **unclassified**	b. ABSTRACT **unclassified**	c. THIS PAGE **unclassified**	**Same as Report (SAR)**	**108**	

Standard Form 298 (Rev. 8-98)
Prescribed by ANSI Std Z39-18

INTRODUCTION

This work focused on the study and development of single electron doped semiconductor quantum dots (QD) for application to the problem of optically driven quantum computing and future spin based quantum devices. The developments in this field are based on the recent advances in fabrication and nano-optical-probing and the new developments of our own group that have contributed with the first measurements and theory in coherent nonlinear optical manipulation of these systems. The primary advantage of the optical approach is that it allows for device speeds to be in the 100 GHz region, as discussed and demonstrated during this grant cycle, orders of magnitude faster than competing approaches for quantum architectures. Also, the absence of wires for electrical pulses reduces the architectural complexity as dimensions become smaller which would also lead to higher electrode densities.

Approach

Our approach to the study of these systems and device demonstration is based on the use of coherent nonlinear laser spectroscopy, coherent transient excitation and optical control, and the use of advanced materials. The qubit of interest is the electron spin confined to a semiconductor quantum dot. Materials are grown by MBE and further processing by lithography techniques by Dan Gammon and his group at NRL.

The dots are self-assembled quantum dots (SAQD) in Schottky diodes. A scalable architecture has been established by us (Lu J. Sham, UC-SD) based on individual qubits (electron spins) confined in adjacent quantum dots [Phys. Rev. Lett. **89**, 167402 (2002).] The qubit can experience an arbitrary rotation by excitation through a virtually excited trion state using a coherent Raman type excitation. Entanglement between spin in adjacent dots is accomplished by a modified optical RKKY (ORKKY) interaction yielding a Heisenberg Hamiltonian coupling between the two spins. High speed state initialization is achieved by spin cooling techniques [Phys. Rev. Lett. **98**, 047401 (2007)]

Figure 1. The general QD energy level diagram and polarization selection rules in a magnetic field in the x-direction (Voigt profile) for InAs SAQDs.
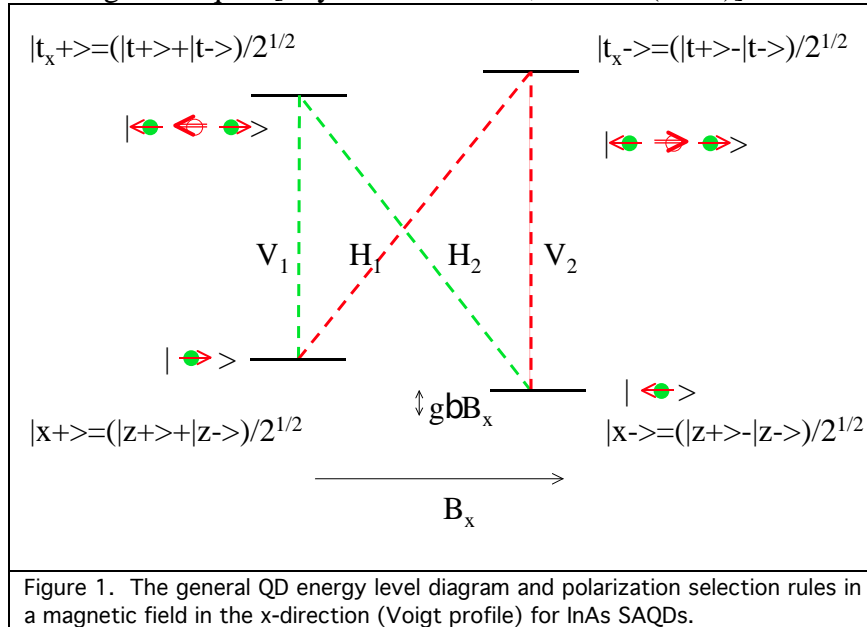
Figure 1 shows the basic idea of a SAQD spin qubit based on InAs on GaAs shown in the many-particle picture. By adding a single electron to the quantum dot, the ground state of this system becomes doubly degenerate and is known to exhibit long relaxation times. The long relaxation time is expected to lead to long coherence times. A scalable system is achieved by creating an array of such dots within a few 10's of nanometers of each other.
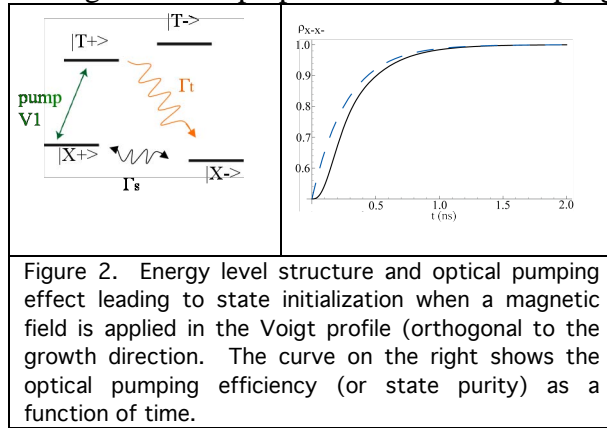
Brief Summary of Research Findings for the 3 year period:

All of the research findings presented in this report have been presented in the annual reports. We summarize the most exciting results below. NOTE: In areas where theory is complemented by experiments, the discussion is unified. Advanced theory is discussed separately.
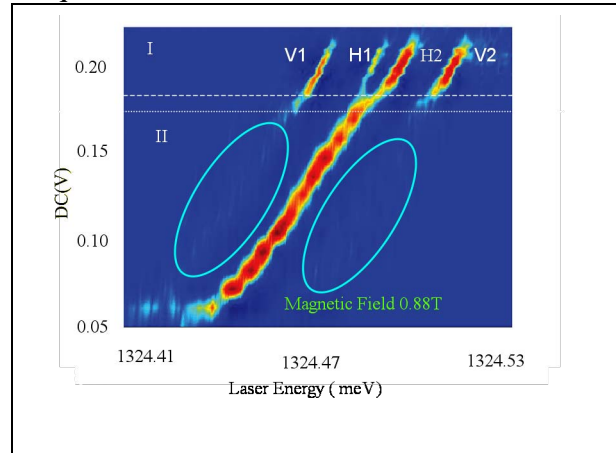
Fast Qubit Initialization and Spin Cooling

One of the DiVincenzo criteria requires that a proposed system for quantum computation not only have a set of qubits to be initialized to high fidelity, but also a continuous supply of fresh ancillary qubits in the shortest amount of time for quantum error correction. In this work, we demonstrate fast spin state initialization with near unity efficiency in a singly-charged quantum dot by optically cooling an electron spin.

In order to implement a fast spin state initialization, the dark transitions labeled H1 and H2 in Fig. 1 are forbidden and have to become bright, since the optical pumping rate depends on the spin flip Raman scattering process. This is shown in Fig. 2 along with the theory of the state initialization purity as a function of time. The forbidden transition becomes allowed by applying a magnetic field perpendicular to the sample growth direction [001].

Figure 2. Energy level structure and optical pumping effect leading to state initialization when a magnetic field is applied in the Voigt profile (orthogonal to the growth direction. The curve on the right shows the optical pumping efficiency (or state purity) as a function of time.

Figure 3 shows the VM absorption map as a function of the applied bias at a magnetic field of $0.88\ T$ along the [110] axis. The laser field is linearly polarized and 45° to the polarization axis of the quantum dot.

In bias region II, the optical pumping rate is larger than the spin relaxation rate. Fast spin cooling is demonstrated, where the absorption of the laser beam is strongly suppressed by optical pumping (in the regions identified by the blue circles). In region I, co-tunneling or tunneling exchange of the dot electron between the quantum dot and the electron in the Fermi sea which induces the dot electron spin relaxation, is comparable or larger than the optical pumping rate, so the depletion of the spin ground states is not achieved. Thus, the strong suppression of the absorption disappears in region I and a quartet transition pattern appears. The physics of the two bias regions is different because the g factor associated with transition H1 and H2 is bias dependent.
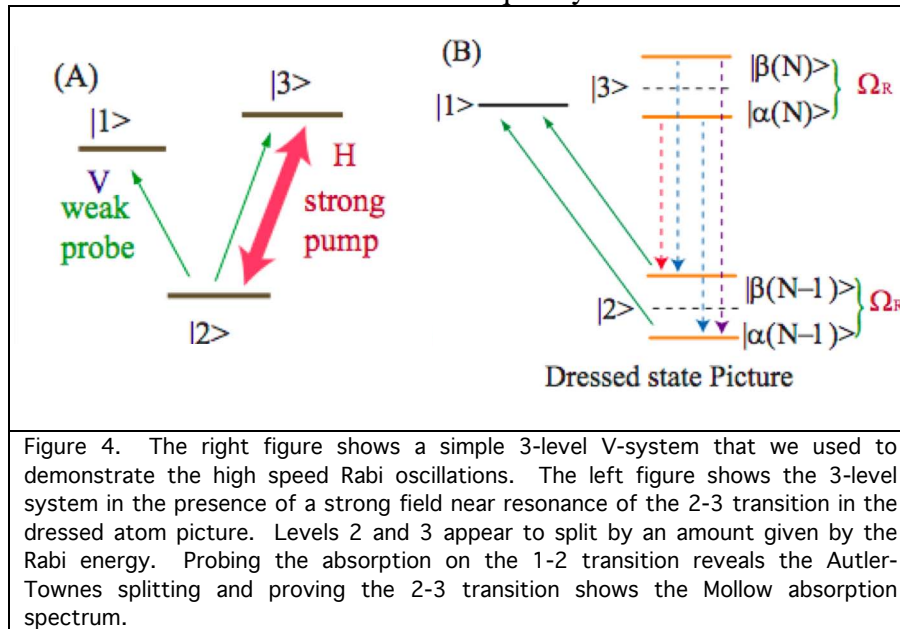
Figure 3. Demonstration of optical pumping. This shows the absorption as a function of bias voltage and laser energy. In region 1, because of co-tunneling, there is no effective optical pumping of the spin state. In region two, co-tunneling is suppressed and spin cooling occurs. On the V1 transition, the spin is transferred from the ground state of the V1 transition to the other spin state and depletion of the V1 ground state means no absorption is observed as indicated by the blue circle on the left. The same discussion applied when the laser is tuned to the V2 transition as shown by the blue circle on the right.

Rabi Splitting, AC Stark Effect and Dark State Formation

   Rabi Splitting: Critical to quantum computing is the qubit rotation accomplished by a Rabi oscillation. Using cw lasers of the type found in the telecom community, we demonstrated the ability to produce high speed Rabi oscillations in excess of 1.4 GHz. The power required for this demonstration was only ~15 nano-Watts corresponding to about 10^{-18} Joules per switching event or rotation (Rabi flop). The maximum rate is anticipated to be closer to 100 GHz.

   The measurements performed here report on the power spectrum since the rates are so high, rather than making the rotations apparent directly in the time domain. To do this, we used a well established technique used to measure the bandwidth of high speed detectors. We took two frequency stabilized lasers and mixed their output in the dot, producing a temporal modulation at the frequency difference. We then report the strength of oscillation as a function of detuning. A resonance is observed at the Rabi frequency.

Figure 4. The right figure shows a simple 3-level V-system that we used to demonstrate the high speed Rabi oscillations. The left figure shows the 3-level system in the presence of a strong field near resonance of the 2-3 transition in the dressed atom picture. Levels 2 and 3 appear to split by an amount given by the Rabi energy. Probing the absorption on the 1-2 transition reveals the Autler-Townes splitting and proving the 2-3 transition shows the Mollow absorption spectrum.

   To see the physics of this measurement and the measurement technique, we examine the energy level diagram of a simple 3 level system. For the first set of measurements, we configured the system for a 3-level V-system, shown in Fig. 4a. In the presence of a strong field driving the H-transition on resonance, the interaction between the field and atom lifts the degeneracy between the |2,n> state and the |3,n-1> state by an amount give by the Rabi frequency. n is the number of photons in the radiation mode. The result is a dress atom picture shown in Fig. 4b. In this picture, levels 2 and 3 appear to split by an amount given by $\hbar\Omega_R$.

   If the strong field is on resonance and we probe transition 2 to 3, we find a splitting in the absorption spectrum called the Autler Townes splitting. The splitting of the resonances is the Rabi frequency (data not shown). If the strong field is tuned off resonance, we easily observe the AC Stark effect (data not shown). If the strong field is on resonance and we probe the H-transition, we see the Mollow absorption spectrum as seen in Fig. 5. This is closely related to the Mollow 3-peak fluorescence spectrum. The solid line in the data represents the theory with no adjustable parameters except the oscillator strength. Not only is the agreement excellent, but the numbers agree well with independent determination of the numbers. Furthermore, the data shows we can drive the system up to the limit of the current setup which corresponded to a Rabi flopping rate of 1.4 GHz. The power spectrum shown here is more complicated than a typical power spectrum because there is both absorption and gain, even though there is no inversion in

the system. Hence, the structures around the Rabi frequencies show a dispersion like feature with gain for detunings below the Rabi resonance.
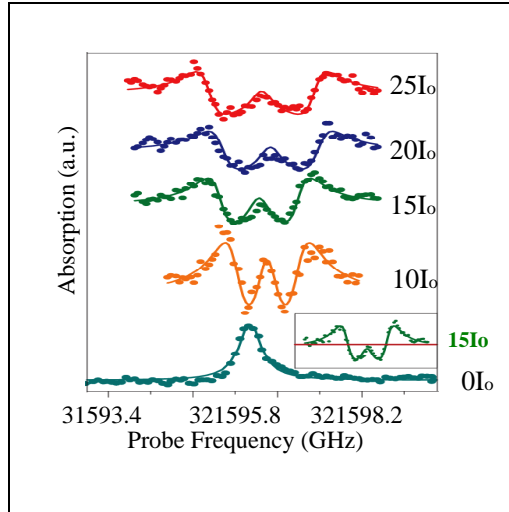

Figure 5. The Mollow absorption spectrum obtained by driving and probing the same transition in Fig. 4. The absorption goes negative as seen in the inset, which means there is gain in the system without inversion.

The results were published in *Science*, 2007. These results were extended to studies of the rotation (Rabi oscillation) also in charged dots, and show spin rotations above 200 MHz, limited only again by the current setup. A clear signature of the coherent nature of this oscillation will become more evident for rotation rates above GHz which is our current focus.

Dark State Formation: Coherent Trapping of an Arbitrary Spin State of a Single Electron in a Single SAQD

Using cw narrowband excitation, it is possible to excite just one of the trion states in Fig. 1. The resultant 3 level structure for our experiment is shown in Fig. 6 (left panel). This is the same 3 level system used to optically initialize the system using optical pumping and spin cooling discussed in the previous report. When only V2 was on, the electron was optically pumped from the X- state to the X+ state. However, when a probe field simultaneously illuminates the system and is resonant with the other transition (H1), the system evolves, in steady state, to a dark state. This state is a superposition state of the two ground states given, in the field interaction picture,

by $|Darkstate\rangle = \dfrac{\Omega_p|X_-\rangle + \Omega_d|X_+\rangle}{\sqrt{\Omega_p^2 + \Omega_d^2}}$
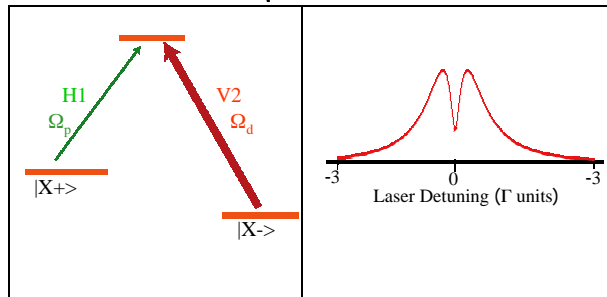

Figure 6. Left panel: 3 level structure for studying the dark state. Right panel: Theoretical line shape for absorption as a function of the detuning of the filed nearly resonant with H1 as a function of detuning from H1.

It is manifest as a dip in the probe absorption spectrum at when the probe is on the H1 resonance. The theoretical result is shown in the right panel of Fig. 6. The dip is evident even at low powers when the pump power is well below that needed to observe the onset of Autler splitting.

Figure 7 shows the experimental result for a number of different pump (V2) intensities (in units of the normalized Rabi frequency). The presence of the dark state dip is clear at intensities well below the onset of the Autler Townes splitting. The dark state shows not only arbitrary spin state preparation but also further proof of the spin coherence since the dark state can not form in the absence of this coherence. The observation of the dark state is a necessary step in demonstrating the ability to line up the laser frequencies with the spin coherence bandwidth needed for spin rotation.

R_x and R_y Rotations and a Fast Phase Gate

A major experimental effort focused on measurements of spin rotation working on single SAQDs in Schottky diode structure and biased to contain one extra electron. *Measurements demonstrated the single qubit rotations needed for universal gate operations. The fastest gate operations can be done with a clock rate of over 100 GHz based on using 2 psec pulses.*

A paper on this work is currently under review by PRL. Figure 8a shows the basic ideas in the context of the Bloch sphere of the electron spin. The system is first initialized as demonstrated above. Then, a two-photon resonant optical pulse rotates the Bloch vector around the x-axis (along the magnetic field), leading to R_x. Shown is the effect of a pi/2 pulse. Precession results in a
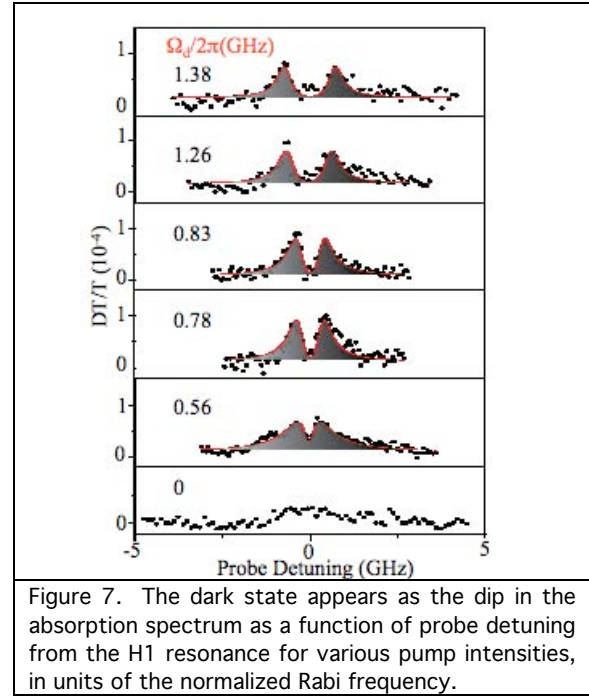

Figure 7. The dark state appears as the dip in the absorption spectrum as a function of probe detuning from the H1 resonance for various pump intensities, in units of the normalized Rabi frequency.

rotation around the z-axis (the optical axis), R_z. Rotation around R_y is then given by $R_{-y}(\theta) = R_z(-\pi/2)R_x(\theta)R_z(\pi/2)$. The inset (a) of data (the red curve is theory) shows the measurement with the arrows showing the different directions of the Bloch vector. Inset (b) shows the results as a function of magnetic field which controls the speed of the R_z rotation. Readout of the signal was made by a unique approach of following the absorption of light from the optical pumping beam. Optical pumping drove the absorption to near zero. Then, a rotation creating some probability amplitude of the system being driven to the other spin state resulting in absorption as the system was pumped back into the initial state of the operation.
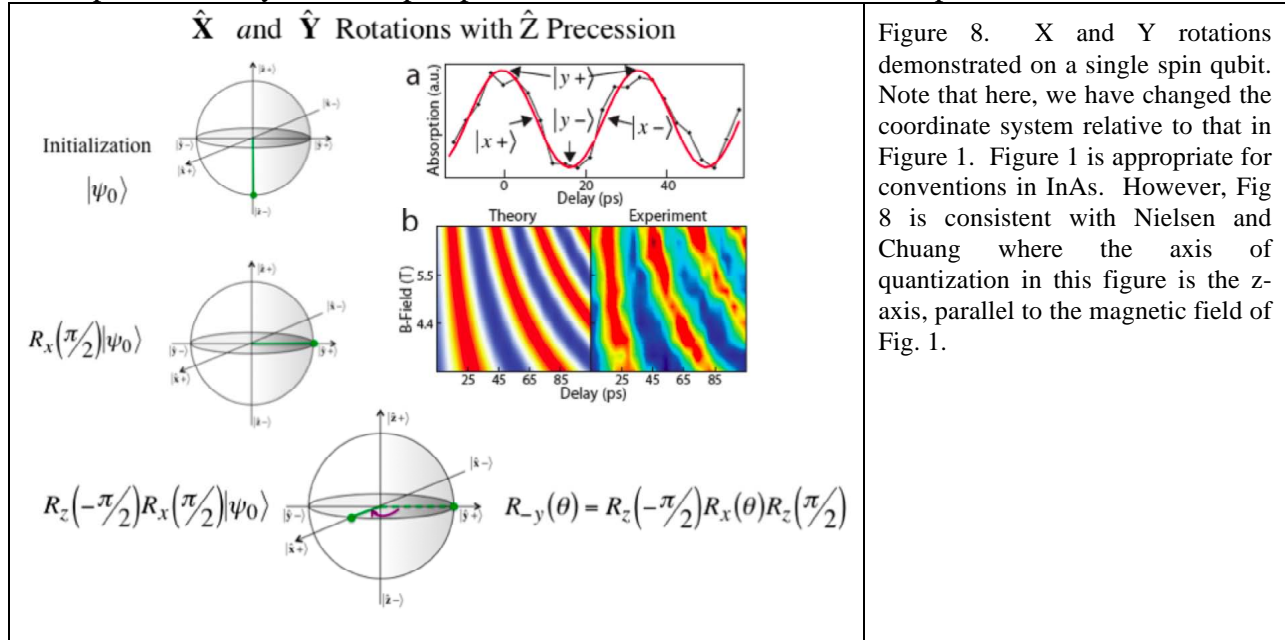

Figure 8. X and Y rotations demonstrated on a single spin qubit. Note that here, we have changed the coordinate system relative to that in Figure 1. Figure 1 is appropriate for conventions in InAs. However, Fig 8 is consistent with Nielsen and Chuang where the axis of quantization in this figure is the z-axis, parallel to the magnetic field of Fig. 1.

As part of this work, a phase gate was implemented by using another optical field, with a bandwidth narrow compared to the Zeeman splitting and performing a 2π rotation of a single spin state with a trion state. This leads to the Bloch sphere picture in Figure 9 along with the rotation matrix shown at the bottom of the figure. In these experiments, the qubit remains the spin, but we can exploit the specific coupling between a given spin state and the trion to perform a rotation of the corresponding optical Bloch vector. A 2π rotation of the optical Bloch vector leads to a change in the phase of that specific spin state. On resonance with the trion transition, the original probability amplitude is multiplied by -1. This is a so-called Z-gate. Off resonance with the trion and we can establish an arbitrary phase (a phase gate).

Figure 3. Experimental demonstration of a phase gate using 2pi rotations of one spin state with a trion state.
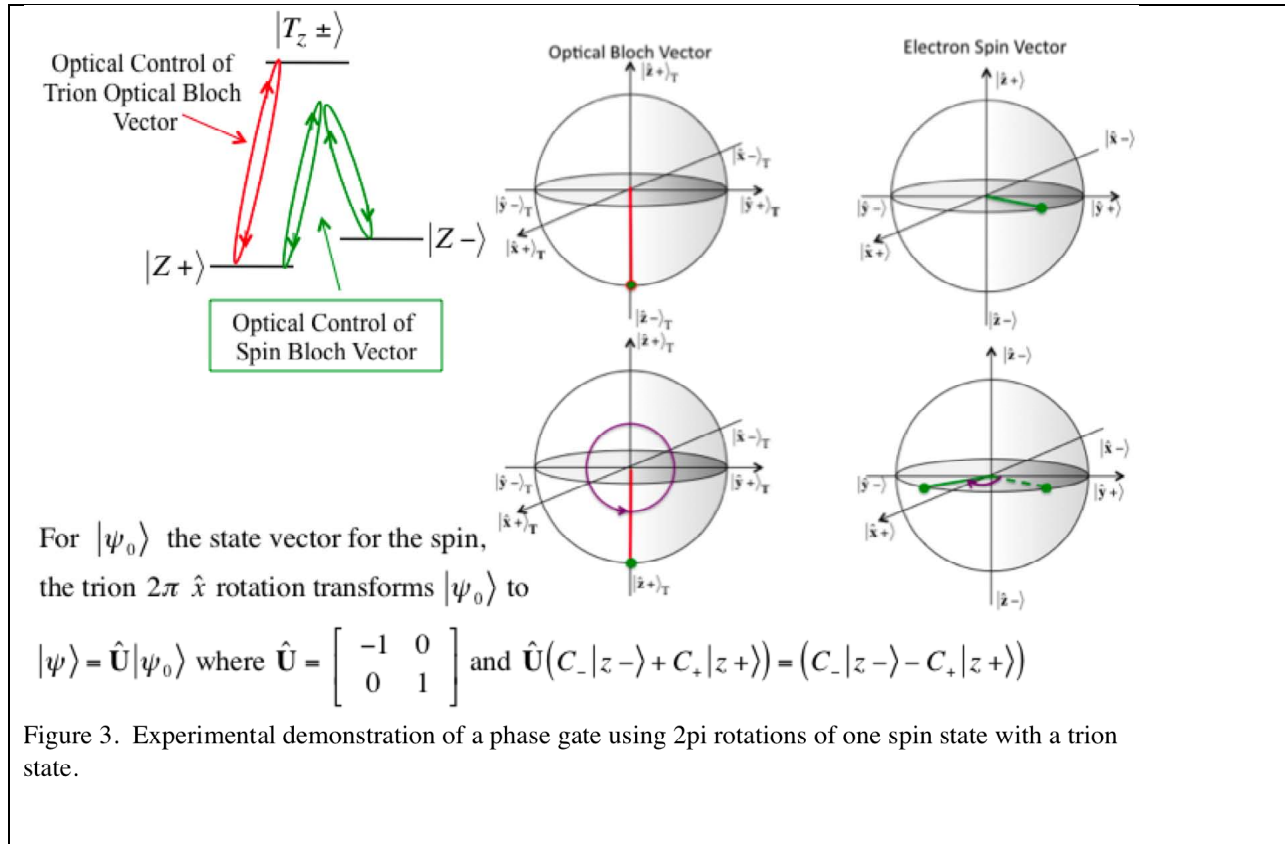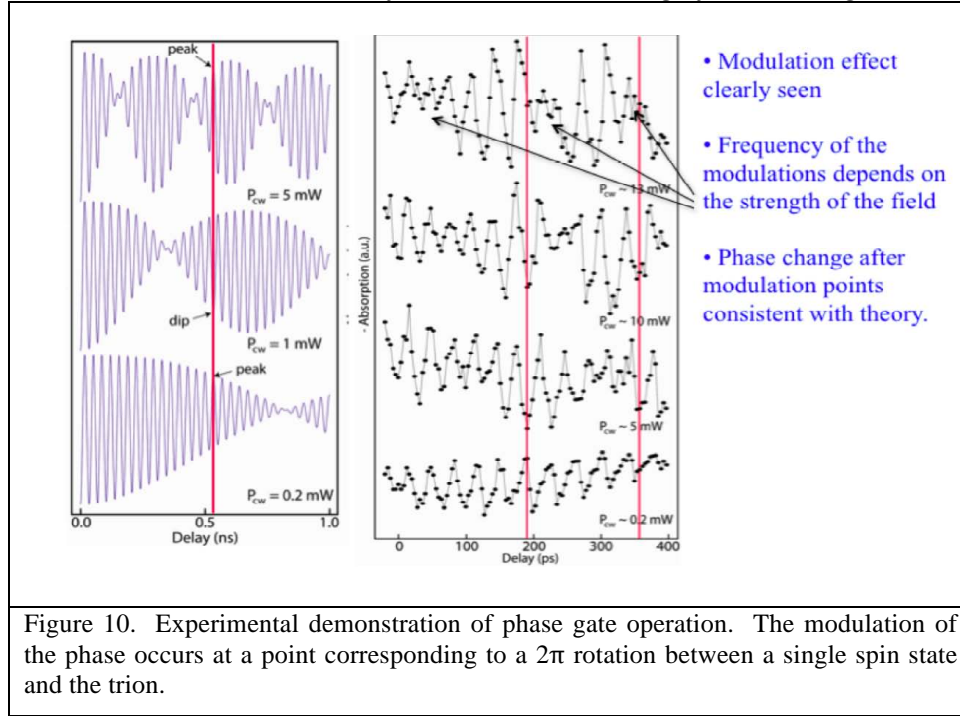
Figure 10 shows the theory and the data. In a two pulse experiment, the readout shows an oscillation corresponding to precession of the spin. However, as noted, there is a phase shift that occurs in the oscillation that corresponds to the change in the phase of the one spin state probability amplitude.

The Optically Driven Nuclear Spin Servo and an Increase in Electron Spin Coherence Time

Above, we detailed the identification and behavior of the coherently trapped spin leading to the optical dark state, a purely coherent phenomenon that can occur in a 3 level Λ system when long lived coherence occurs in the two nearly degenerate ground states. The location of the dark state is a precise measure of the Zeeman splitting and the depth of the transparency that forms in this dark state can be used to measure the electron spin coherence.

What we found is that by exciting the hole, the hole interacts with the nuclear spin through the anisotropic term and leads to a flipping of the nuclear spin. The flip of the nuclear spin changes the Overhauser field that shifts the trion resonance. The spin flip interaction is proportional to the probabilities of coupling to the hole both before and after the spin flip. Hence, it drives the nuclear configuration to maximize the hole excitation and stabilizes the nuclear fluctuation, i.e., reduces the fluctuations without causing a significant change in the nuclear polarization. Experimentally, this is observed as a deepening of the transparency hole in the dark state with a relatively small shift, *reflecting an increase in the electron spin coherence time due to reduced nuclear fluctuations but no significant changes in the nuclear polarization.*

Figure 10. Experimental demonstration of phase gate operation. The modulation of the phase occurs at a point corresponding to a 2π rotation between a single spin state and the trion.

The result is that we discovered that we were able to suppress nuclear fluctuations to a steady state value (rather than through use of rephrasing techniques such as an echo) that extends the spin coherence time to over three orders of magnitude, well beyond a microsecond. We believe the actual spin coherence time is longer. A paper describing this appeared in a June 2009 issue of *Nature*. The result and nuclear coupling model with feedback is shown in Fig. 11.

To avoid complications with measuring the spin decoherence rate by measuring the whole depth in real time while the second optical field simultaneously scans the transparency hole and also works to excite the hole to suppress nuclear fluctuations (black dots in Fig. 11, upper data set), we used a 3 beam experiment, so that two fixed frequency optical fields locked the nuclear spin and a 3rd field measured the hole depth (red dot). The red dot shows the dramatic (>3 orders of magnitude) improvement in the electron spin coherence time compared to that typically measured in the this system. The lower data set in Fig. 5 shows the coherent spin state trapping spectrum seen in the last report, using first two and then 3 optical fields. The red curve is a fit of the theory developed by our collaborators, Wang Yao and LJ Sham and the green curve shows the response predicted in the absence of this nuclear feedback.
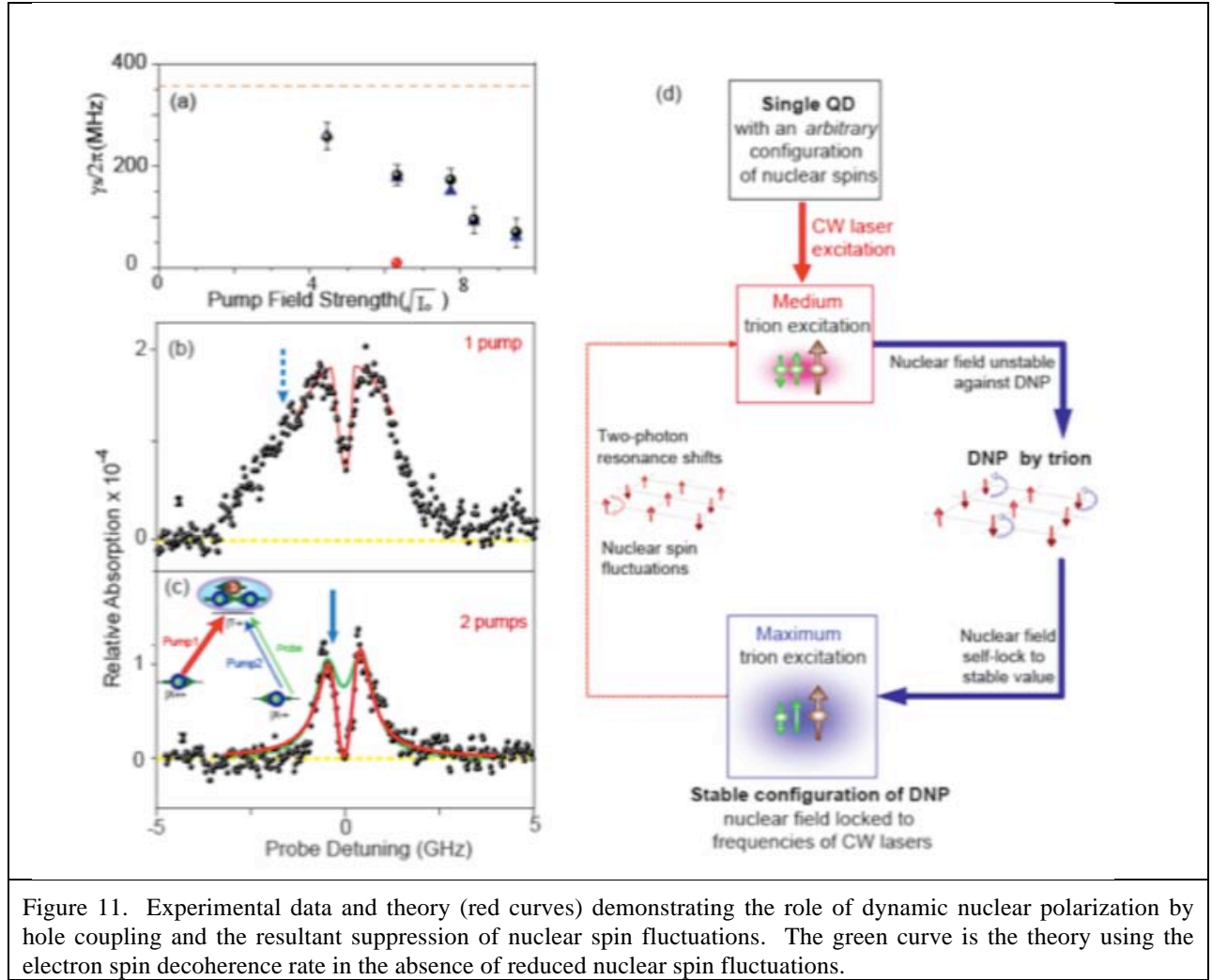
Figure 11. Experimental data and theory (red curves) demonstrating the role of dynamic nuclear polarization by hole coupling and the resultant suppression of nuclear spin fluctuations. The green curve is the theory using the electron spin decoherence rate in the absence of reduced nuclear spin fluctuations.

Proposal for Scalable Design

In addition to the theoretical support of experiments on fast initialization and single qubit rotations, we explored ways to implement entangling gates between two spins in two dots. We designed two architectures for the semiconductor dots system to ensure the scalability of the optical processing of quantum information.

We concentrated on utilizing the properties of the vertical dots fabricated by Gammon's group for the entangling operation by laser control. While the vertical dots in a column being limited in number are not sufficient for a generally scalable architecture, demonstration of entanglement in them is nonetheless a valuable step in experimental demonstration of optical control capability towards a scalable architecture involving horizontally arranged dots. Moreover, we have demonstrated in theory that a column of vertical dots may constitute a node in the quantum network of dots in nanocavities connected by wave guides for a scalable distributed quantum computer [Phys. Rev. Lett. **95**, 030504 (2005); J. Opt. B: Quantum Semiclass. Opt. **7,** S318 (2005).].

The process design and simulation based on the principle of optically induced exchange interaction between two dot spins (termed ORKKY) has been published [Phys. Rev. B 75,

125317 (2007)]. This would require two vertical dots to have tunneling p shell electron levels. The theory group and Steel's group collaborated in designing an entangling process that had fewer requirements on the dot fabrication. An alternative to ORKKY was to make use of the Coulomb interaction between the optical excitations of two spins (trions) in two vertical dots [Phys. Rev. B **78**, 235314 (2008)]. Fig. 12 shows the optical path used to entangle the |x+,x+> and |x-,x-> states of the two spins in the Voigt configuration through excitation and de-excitation of single and two trions. The interaction between the two trions residing in different dots makes the transition energy between the two trion state and a single trion state smaller than the transition energy between the single trion and the spin state. This enables the optical frequency selection of the transition processes in the path shown.

Figure 12. Optical path to entangle two dot spins via trions states T+ or T- from electron spin states x+ or x- from dot 1 or 2 by light of vertical (V) or horizontal (H) polarization.
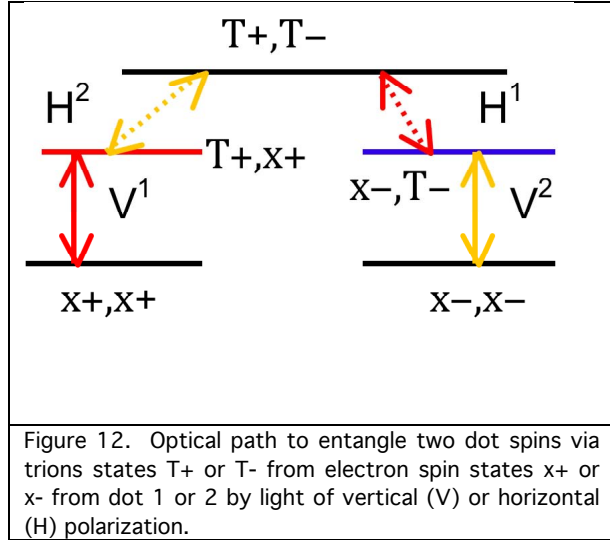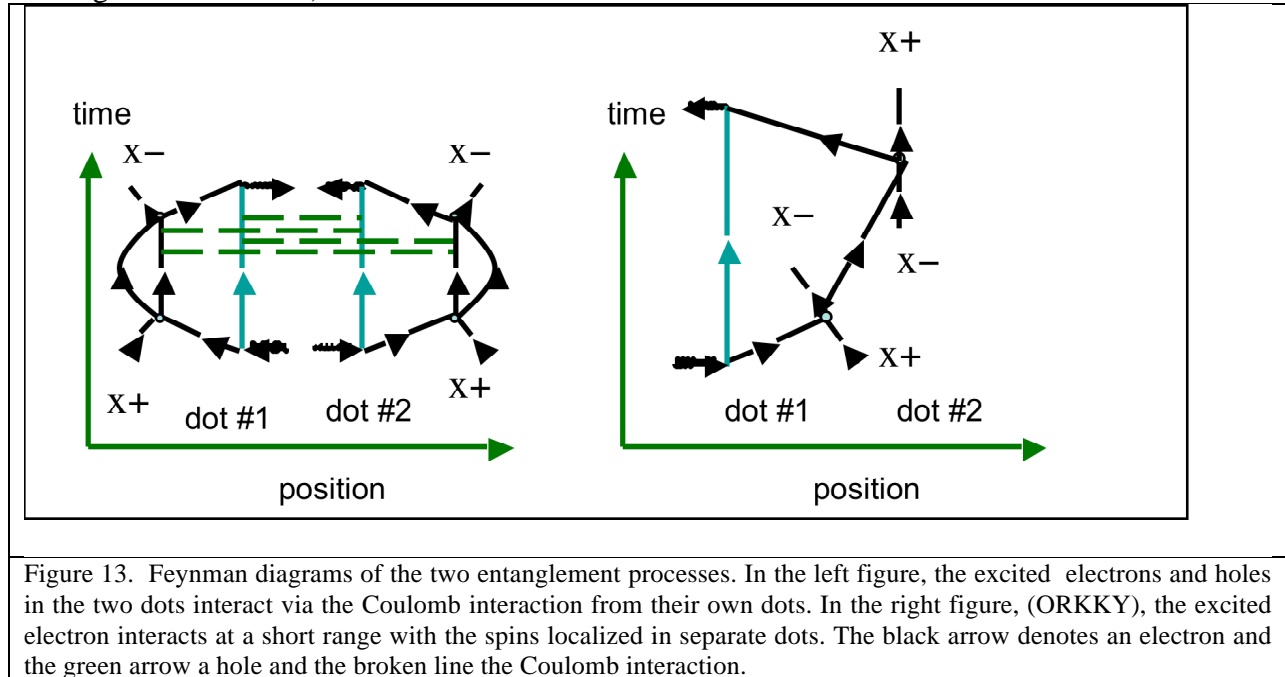
Fig. 13 contrasts the optical process using the two trion interaction with the one using ORKKY. The former lets the optically excited electrons and holes remain in their respective dots but requires four optical fields for control. The latter requires the two dots to permit tunneling of the excited electron between the two dots but uses only two optical fields. Thus, the former may use vertical dots already fabricated but makes more demands on the optical process.

The interaction method included a design of the optical control to minimize the unintended dynamics involving other possible excited states (eleven of them) to improve the concurrence (an entanglement measure) above 92%.

Figure 13. Feynman diagrams of the two entanglement processes. In the left figure, the excited electrons and holes in the two dots interact via the Coulomb interaction from their own dots. In the right figure, (ORKKY), the excited electron interacts at a short range with the spins localized in separate dots. The black arrow denotes an electron and the green arrow a hole and the broken line the Coulomb interaction.

The Improved Coulomb Logic Gate: Use of Adiabatic Passage

The salient features are:

- By utilizing the interaction between the optical interactions in separate dots, it is not necessary to design for tunneling of electrons between the dots. The concurrence of entanglement of the states can vary from 0.4 for a Coulomb interaction of 0.1 meV to over 0.85 for interaction above 1 meV.
- The use of adiabatic optical control minimizes noise effect and unintended dynamics while keeping the operational time in the nanosecond range. This theory is also in keeping with the next generation telecom lasers used for optical control in Steel's group.

The method was based on the Stimulated Raman adiabatic passage (STIRAP) but, unlike the population transfer for which STIRAP was designed, a quantum operation required more than one adiabatic paths so that the operation was independent of the initial state. The design principle was to optically dress (and thus connect) a pair of two-spin states, such as $|+,+\rangle$ and $|-,-\rangle$, or $|+,-\rangle$ and $|-,+\rangle$ in terms of the spin states along the in-plane magnetic field, to form a Bell state or to build a logic gate. The intermediate states required were the singly excited trion states, such as $|T+,+\rangle$ and $|-,T-\rangle$, and the bi-trion state, $|T+, T-\rangle$. We proposed to use two strong resonant laser beams to form the dressed states of these three excited states and then to use two weaker and detuned beams to connect them to the pair of two-spin states concerned. The adiabatic passage would involve five dressed states with three of them minimally involved in the net operation. The two states involved were weakly connected to the strong optical decay, even though they were not dark states as in the Λ system. The design principle of the laser pulses was sufficiently long to avoid unintended dynamics but short enough to avoid too much optical decoherence and significant spin decoherence.

Pulse design was first applied to the pair of states, $|+,+\rangle$ and $|-,-\rangle$ for a controlled phase gate, so as to help an experimental demonstration without the demand of single spin rotation of the initialized states. Simulation of the operation yielded results for the concurrence of the entangled state and the fidelity of the phase gate. Pulse design for the pair, $|+,-\rangle$ and $|-,+\rangle$, led to the simulation of a square-root swap gate which was entangling. The entanglement content and the quality of the final state were estimated by the concurrence and the purity (the trace of ρ^2) of the final state density matrix ρ. They were highly dependent on the Coulomb interaction between the trions. For an interaction of $100\ \mu eV$, the concurrence is about 0.8 and the purity 0.9 but for a weak interaction of $20\ \mu eV$, these quantities drop by 50%. In the simulations, the experimental decoherence time of the trion was used and the unintended dynamics was limited by optimizing the detuning and the pulse strength and duration. These calculated results may help in the choice of procedure in experimental implementation.

Quantum Theory of the Dot Spin Decoherence

At the magnetic fields of several teslas used in the experiments, the two eigenstates of the spin are very robust, so that the decay time of the higher energy spin state to the lower one is sufficiently long for meaningful quantum information processing. However, coherence of a state which is a measure of the supposition of these two spin states, deteriorates much faster with time into two classical states with appropriate probabilities, a process known as decoherence. In our research into the spin decoherence, experiments led to conditions, such as the working temperature below 5 K and small energy between the spin states, under which all mechanisms of

decoherence, such as the effects of lattice vibration and the spontaneous emission into the electromagnetic vacuum, could be eliminated, except the fundamental one: the interaction of the electron spin with the nuclear spins in the same dot.

We constructed a fundamental quantum theory of electron spin decoherence with mutually interacting nuclear spins [Phys. Rev. B **74**, 195301 (2006); Phys. Rev. B **75**, 125314 (2007)] without inserting the stochastic assumption by an explicit solution of the entangled state between the electron and the nuclear spins. The reversibility of the entire quantum system led to methods of regulating the nuclear ensemble by controlling the electron to remove the pure (not just inhomogeneous) decoherence of the electron [Phys. Rev. Lett. **98**, 077602 (2007)].

The all-quantum theory of decoherence followed the time evolution of the whole system from a prepared product state of the electron spin and the nuclear bath to entangled states of the electron spin up and down states in a magnetic field with nuclear parts. The decoherence of the superposition of the electron spin up and down states at any time could be obtained by the reduced density matrix of the electron spin, which corresponded in an experiment to the beginning of a process towards a measurement. The solution of the whole system was given in the approximation of keeping only the correlation of nuclear spin pairs as well as the inhomogeneous distribution of the hyperfine interaction of the electron with the nuclear spins. An important find of his calculation alone was that spin echo removed not just the inhomogeneous broadening but also a significant portion of the pure decoherence. While this was observed in past experiments, this was the first quantum theory that explained these inferences of pure decoherence recovery.

The approximation keeping only the pair correlation of the nuclear spins was justified in two ways. Theoretical estimates of the error in the illegitimate flip-flops of pairs of nuclear spin in the time of the inverse interaction energy of the nuclear spin-spin interaction is small. Thus, the flip-flops may be assumed to occur independent of one another. It follows that the nuclear spin pair correlation is well described by the rotational dynamics of the independent pseudo-spins, each consisting of a pair of flip-flop states. The effect magnetic field which governs the dynamics of each pseudo-spin is straightforwardly calculated from all the first principles interactions described above. The method yielded a simple picture of decoherence in terms of pseudo-spin rotations, which turns out to be an invaluable aid in designing measures of pulse sequence for the recovery from decoherence.

For a GaAs or InAs dot, we studied the time dependence of the electron spin decoherence for a range of the applied magnetic field (1--40~T) in a range of temperature 10~mK--1~K, low enough to avoid phonon induced decoherence but still high enough to randomize the nuclear spins. We find time dependence of exponential decay in powers of time, t^n, with cross-over behavior in different time regimes from one power of n to another (often 2 and 4) for both the single spin FID and ensemble spin echo profile. In both cases, the long-time behavior is a simple exponential decay (n=1). Because of the non-simple exponential decay, we define transverse electron spin relaxation $T_2^{(1/e)}$ as the time in which the electron spin coherence decreases by a factor of 1/e. The temporal behavior of single spin FID and that of the ensemble spin echo are different and are subjected to different predominant mechanisms. In an InAs dot, $T_2^{(1/e)}$ for the single spin FID shows a strong magnetic field dependence, and under one spin echo can be increased to over 1 μs below 10 T. The single spin FID is driven by the dipole-dipole and bulk excitation mediated nuclear spin-spin interaction and qubit spin mediated nuclear interaction at all fields while the spin echo signal involves little qubit mediated nuclear interaction. Details

including methods of composite optical pulses to recover spin coherence are in the long paper [New J. Phys. **9**, 226 (2007)].

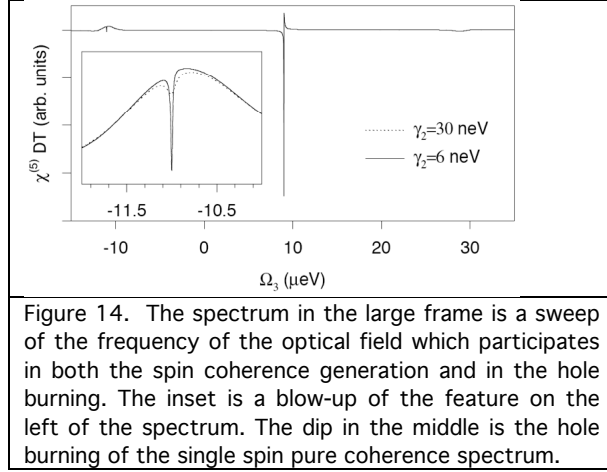## Hole Burning Proposal for Measurement of Spin Coherence

Figure 14. The spectrum in the large frame is a sweep of the frequency of the optical field which participates in both the spin coherence generation and in the hole burning. The inset is a blow-up of the feature on the left of the spectrum. The dip in the middle is the hole burning of the single spin pure coherence spectrum.

Sham's and Steel's groups collaborated in establishing a spectroscopic method for measuring the decoherence times [Phys. Rev. B **75**, 085322 (2007)]. It involved the spectrum in the fifth order nonlinear optical processes. Two orders of the optical field were needed to produce the electron spin coherence (a coherent Raman process) which produced an inhomogeneously broadened line. Two more orders were needed to produce by hole burning a sharp dip whose frequency corresponded to the Larmor frequency of the electron spin in a single dot and whose line width was the pure decoherence time. The fifth order was the probe field. A calculated hole burning spectrum is shown in Fig. 14.

A proposed weak measurement of spin decoherence

The problem with the quantum measurement of a single spin is the weak interaction between the single spin and the measurement instrument. For example, in optical measurements, a probe laser pulse produces in the process at most one photon. Thus, the current practice in our collaboration is to repeat the coherent pump and probe processes numerous times and collect the photons for averaging. Repeating the process has the drawback of averaging over a distribution of scenarios including the initial states. For example, such a measurement would produce the inhomogeneous decoherence time T_2^*. To obtain the intrinsic property of the spin state without inhomogeneous effects, we explored the quantum optics methods such as cycling transitions by exploring the auxiliary states of the spin in the same dot (Steel) and the auxiliary states of the optically excited trion in the measuring process in two coupled quantum dots (Gammon).

We pursued the idea of changing the current practice of repeated pump and probe to a single pump and repeated probes. The signals of change in transmission triggered by the photons were then collected and processed for their correlations which may reveal the properties of the spin state. The idea of finding correlations in these stochastic series of data was stimulated by Steel's group's experiment on noise spectra which yields T_2^*.

In a collaboration with Professors Renbao Liu and Alexander Korotkov, we chose to investigate the theory of measurement of a single spin using Faraday rotation. Because it involved linear optics, the experimental process was easier to simulate although the idea is equally applicable to the nonlinear change in transmission by coherent pump and probe method of Steel. While the Faraday rotation of a probe pulse due to a single spin is small (~ 10^{-5} radians), the coherent photon state simulating the probe pulse has a magnifying effect on the distinguishability of polarization rotation which might be measurable by the current technology.

The suggested measurement procedure is illustrated in Fig. 15. An electron spin state is initially normal to both a magnetic field and the optical axis. A periodic series of pulses are sent through the dot. The coherent photon state representing each pulse suffers a Faraday rotation of its polarization by the electron spin into, say, $|+\theta\rangle$ state for spin up and $|-\theta\rangle$ for spin down. A polarized beam splitter (PBS) lets the pulse $|+\theta\rangle$ pass but has only a small probability D in reflecting the $|-\theta\rangle$ pulse but mostly (with a probability of 1- D) $|\downarrow\rangle\langle\downarrow|$ lets it also transmitted. The measurement results may be summarized by a positive-operator valued measure (POVM) with a light pulse reflection operator caused by the down-spin, $: D|\downarrow\rangle\langle\downarrow|$, and the transmission one due to the up-spin and the light due to the down-spin which failed to be reflected, $|\uparrow\rangle\langle\uparrow| + (1-D)|\downarrow\rangle\langle\downarrow|$. Photon counts of successful measurements of spin in $|\downarrow\rangle$ state occur stochastically like shot noise. Analysis of the time series yield the second order correlation function, $g^{(2)}(t)$, for the probability of occurrence of two signals with a time interval t. Since the spin is in free induction decay between two signals, the correlation function measures the decoherence as a function of t but with inhomogeneous broadening. The third order correlation function, $g^{(3)}(t_1, t_2)$, which measures the probability of occurrence of three signals with the time intervals t_1 and t_2, is free from the inhomogeneous effect when $t_1 = t_2$. Under this condition, the time dependence yields the pure spin decoherence time T_2. Numerical simulation of the measurement process (Fig. 16) confirmed the above conclusions.

Figure 15. The arrangement for periodic Faraday rotation measurements, taken from Ref. [2].

Figure 16. Contour plot of the envelope of the third order correlation time from a Monte Carlo simulation of the measurement [2].
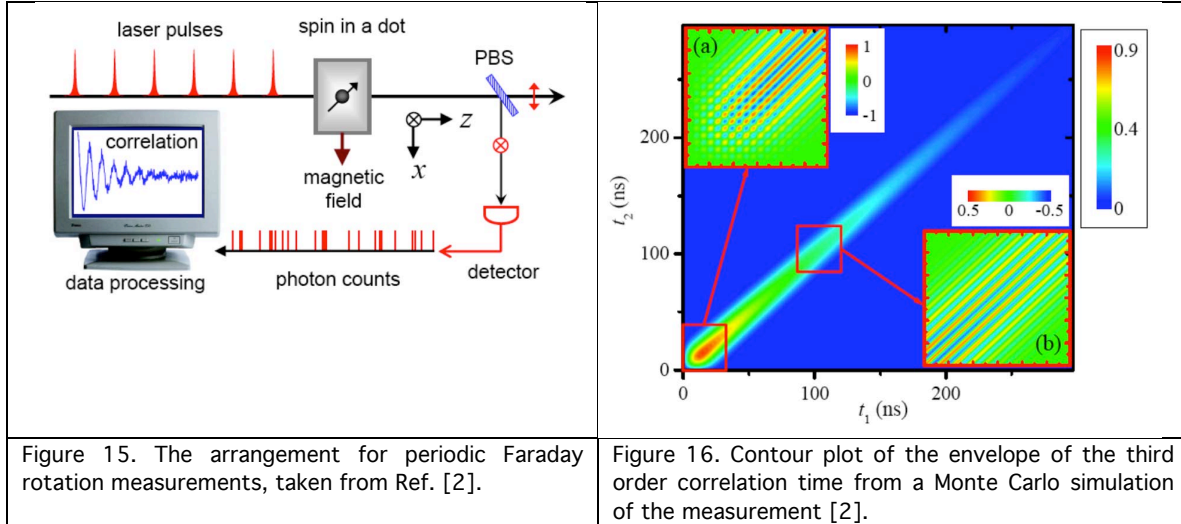
High Precision Qubit Rotation Essential in Scalability

Quantum Fourier Transform is basic to Shor's algorithm for factorization and to other related Hidden Group problems. Its implementation requires the ability to control rotation angle to the precision of $2\pi/2^n$, n being the number of qubits needed. The precision of this controlled operation presents then a limit to scaling the quantum computation to a required number of qubits. The situation is considerably eased by Don Coppersmith's approximation [arXiv:q-ph/0201067] in which rotations of angles smaller than $2\pi/2^m$ with cutoff m = $\log_2 (2n)$ may be neglected with a total phase error bound of $2\pi n/4^m$. Fowler & Hollenberg [PRA 70, 032329 (2004)] have improved the cutoff to scale more slowly with n, viz., m ~ $\log^4 (2n)$. For example, the Fowler-Hollenberg requirement for minimum rotation angle is $\pi/32$ vs Coppersmith's $\pi/1024$ for half a kilobit and an error about 0.3%.

Parin Dalal, [Ph. D. Thesis, Univ. of Calif. San Diego, (2009)], was key in developing an approach to overcome this important obstacle to scalable quantum computing – the limitation of precision operation for small angle rotation based on the quantum analog to a lookup table in classical computation. The important results were: (1) The table consisted of a set of spins accurately aligned in a number of angles around the clock, say 64. By swapping operations, the spin angle could be transferred to the quantum dot spin where information processing was carried out. To achieve fault-tolerant swap, quantum coherent feedback was used, and the error was in the control of unitary operations. (2) The theory was extended to design general unitary-fault tolerant, scalable computation processes. (3) A proposal was made for an experimental demonstration with our existing exciton platform. (4) A replacement of the time control of quantum operation by a spatial control but self-timed process was shown in theory to be capable of high precision quantum information processing.

A quantum look-up table is composed of a list of qubit spins, each pointing at a fixed direction in the zx plane. A subset of the angles are selected from all the multiples of the minimum angle, $2\pi/2^{m/2}$, so that all the multiples may be optimally constructed from the table. If each spin is in its ground state, we have a Hilbert space of spin states whose local bases are all different. We found two conceptual methods of initialization to arbitrary angles by dot spin alignment by a slanted magnetic field with nanomagnets [M. Pioro-Ladrière et al., Appl. Phys. Lett. **90**, 024105 (2007)] and by classical rotation of light polarization in a fiber as a geometrical phase [A. Tomita and R, Chiao, Phys. Rev. Lett. 57, 937 (1986)] which enables distant swapping of spins [W. Yao, R.-B. Liu, and L. J. Sham, Phys. Rev. Lett. **95**, 030504 (2005)].

Dalal constructed an algorithm using controlled swap operations for the look-up process. The resultant operation, $|\theta\rangle \rightarrow |\pm(\theta + \alpha + \beta)\rangle$, α and β being from the table, was an effective rotation without resorting to the usual rotational operator except at a large angle such as $\pi/2$ for the Hadamard transformation or spin flip. It was assumed that the spins in the table were lined up accurately to their angles with the precision higher than the minimum angle, such as $\pi/32$. For example, any angular state $|\theta\rangle$ may thus be rotated by any multiple of $\pi/32$ up to 2π, e.g., by breakdown $5\pi/32$ to $\theta + \pi/8 + \pi/32$, using the table entries $\pi/8$ and $\pi/32$. This algorithm contained fault tolerance by means of auxiliary qubits at different local bases, error corrections for every SWAP, diagnostic measurements of the auxiliary qubits at the end to test the quality of the output states, including ideas of quantum feedback of Lloyd [S. Lloyd, Phys. Rev. A **62**, 022108 (2000).] and the amplitude amplification of Brassard et al. [Gilles Brassard, Peter Høyer, Michele Mosca and Alain Tapp, arXiv quant-ph/0005055.]

In simulation of the look-up process, the error models used include the phase noise arising out of coupling of the control field to a thermal reservoir [M.O. Scully and M.S. Zubairy, "Quantum Optics (Cambridge 1997).], the back action of the indirect measurements of the field variables [M.A.Nielsen and I.L. Chuang, "Quantum computation and quantum information" (Cambridge 2000).], and the stochastic fluctuations of the angles of the spins. [K.M. Frahm, R. Fleckinger and D.L. Shepelyansky, Euro. Phys. J. D **29** 139 (2004).] The diagnostic test measurement can be over 98% successful in numerical simulations of the look-up process for quite large over and under rotation due to error and noise.

APPENDIX

SELECTED PREPRINTS AND REPRINTS

LETTERS

Optically controlled locking of the nuclear field via coherent dark-state spectroscopy

Xiaodong Xu[1]*, Wang Yao[4]*, Bo Sun[1]*, Duncan G. Steel[1], Allan S. Bracker[2], Daniel Gammon[2] & L. J. Sham[3]

A single electron or hole spin trapped inside a semiconductor quantum dot forms the foundation for many proposed quantum logic devices[1–6]. In group III–V materials, the resonance and coherence between two ground states of the single spin are inevitably affected by the lattice nuclear spins through the hyperfine interaction[7–9], while the dynamics of the single spin also influence the nuclear environment[10–15]. Recent efforts[12,16] have been made to protect the coherence of spins in quantum dots by suppressing the nuclear spin fluctuations. However, coherent control of a single spin in a single dot with simultaneous suppression of the nuclear fluctuations has yet to be achieved. Here we report the suppression of nuclear field fluctuations in a singly charged quantum dot to well below the thermal value, as shown by an enhancement of the single electron spin dephasing time T_2^*, which we measure using coherent dark-state spectroscopy. The suppression of nuclear fluctuations is found to result from a hole-spin assisted dynamic nuclear spin polarization feedback process, where the stable value of the nuclear field is determined only by the laser frequencies at fixed laser powers. This nuclear field locking is further demonstrated in a
three-laser measurement, indicating a possible enhancement of the electron spin T_2^* by a factor of several hundred. This is a simple and powerful method of enhancing the electron spin coherence time without use of 'spin echo'-type techniques[8,12]. We expect that our results will enable the reproducible preparation of the nuclear spin environment for repetitive control and measurement of a single spin with minimal statistical broadening.

We performed the experiment on a single negatively charged quantum dot embedded in a Schottky diode structure. Figure 1a shows the four-level energy diagram of the trion states under an external magnetic field perpendicular to the sample growth direction. In the pump–probe experiment, two narrow-linewidth continuous wave lasers selectively excite a three-level lambda subsystem, as shown in the dashed box of Fig. 1a (ref. 17; see Methods Summary). When the pump and probe lasers exactly match the two-photon Raman resonance (TPR) condition, a coherent superposition of the spin ground states are formed[18]. This is known as the dark state[19] and represents a coherent manipulation of the electron spin in the frequency domain (a brief comparison of ref. 18 with the
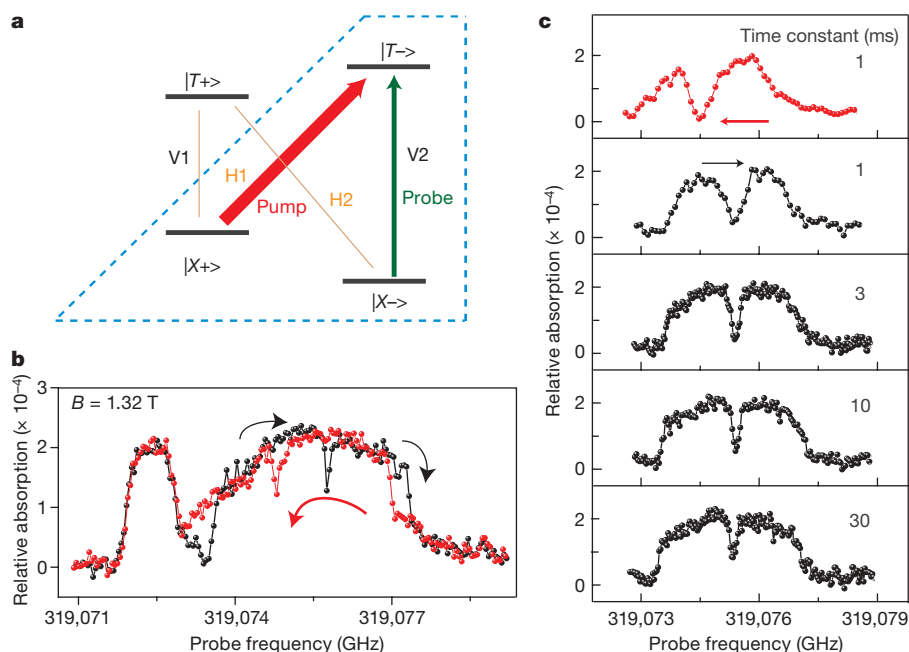

Figure 1 | Laser frequency sweep direction dependent probe absorption spectrum. a, The trion energy level diagram with a magnetic field applied in the Voigt geometry. The blue dashed box indicates the selected three-level Lambda system. A strong pump beam is near-resonant with transition H1 and a weak beam probes transition V2. **b**, The probe absorption spectrum at an external magnetic field of 1.32 T. The black (or red) curve represents the probe absorption spectrum of the forward (or backward) scan. **c**, The probe absorption spectrum as a function of the laser scan rate, indicated by the lock-in time constant. The top red curve is the backward scan with a 1-ms lock-in time constant.

[1]The H. M. Randall Laboratory of Physics, The University of Michigan, Ann Arbor, Michigan 48109, USA. [2]Naval Research Laboratory, Washington DC 20375, USA. [3]Department of Physics, University of California San Diego, La Jolla, California 92093, USA. [4]Department of Physics, The University of Hong Kong, Hong Kong, China.
*These authors contributed equally to this work.

current experiment can be found in the Supplementary Information). Because absorption of the probe laser by trion excitation increases abruptly with detuning from the TPR, the generated dark state is very sensitive to small changes in the nuclear field, which can affect the TPR and hence can be used as an *in situ* probe of the nuclear spin environment in a quantum dot[20].

Figure 1b shows the probe absorption spectrum at a magnetic field of 1.32 T. The black curve is the spectrum obtained by sweeping the probe laser from low frequency to high frequency (the forward scan). The red curve is the spectrum obtained by sweeping the probe laser from high frequency to low frequency (the backward scan). The narrow peak on the left and the broad peak on the right correspond to transitions H2 and V2, respectively. We focus on the optical response from transition V2.

Ideally, the overall lineshape of transition V2 should be Lorentzian-like with a dark-state dip, as shown in Fig. 4a. However, the spectrum clearly shows a broadened lineshape with a round top and sharp edges, which is far from Lorentzian. The width and the strength of the dip corresponding to the dark state are also narrower and shallower than expected. More remarkably, we observe hysteresis at the sharp edges of the V2 absorption peak between the forward and backward scans. Additionally, the spectral position of the dark state in each scan is shifted in the same direction as the scan, which indicates a change of TPR when the scan direction is switched. The external magnetic field is unchanged in the forward and backward scans, so these observations indicate that we optically create and probe the dynamic nuclear spin polarization (DNP) in this charged quantum dot system, where the nuclear spin configuration depends on the laser sweeping direction.

The dependence on laser scan rate is shown in Fig. 1c. The dark state becomes more pronounced, concomitant with a broader dip width as we increase the laser scan rate (that is, the probe laser frequency is held for a shorter interval at each value). Under faster scans, the observed lineshape is closer to the standard dark-state spectrum in a Lambda level scheme (compare Fig. 4a). As we show below, the anomalous spectral features and their scan-rate dependence reflect the dynamical control of the nuclear field by the laser frequency scans on a timescale comparable to the nuclear spin relaxation time, which is of the order of a second[12,14,16].

We performed a set of measurements by fixing the frequencies of both lasers and recording the optical response as a function of time; these measurements reveal that the DNP modifies the Zeeman splitting, via the nuclear field, to maximize the trion excitation. Figure 2a shows the probe absorption spectra with forward (black) and backward (red) scans. We begin by scanning the laser backward and stopping the laser just before the sharp rising edge of the trion peak, as shown by the green curve in Fig. 2b. We record the absorption signal as a function of time with the laser frequency fixed. As shown in Fig. 2c, the system remains in hysteresis state 1 for a while (shown by the signal level) and then abruptly switches into hysteresis state 2, where it remains. This signifies that the nuclear field switches to a stable value that maximizes the trion excitation. Finally, we scan the probe laser forward and find that the subsequent partial forward scan spectrum (the blue curve in Fig. 2d) overlaps considerably with its equivalent in the full forward scan.

We also examined the dynamics of the nuclear spin by monitoring the dark state. As shown in Fig. 2e, after a full forward scan to locate the dark-state position (black curve), we took a partial forward scan
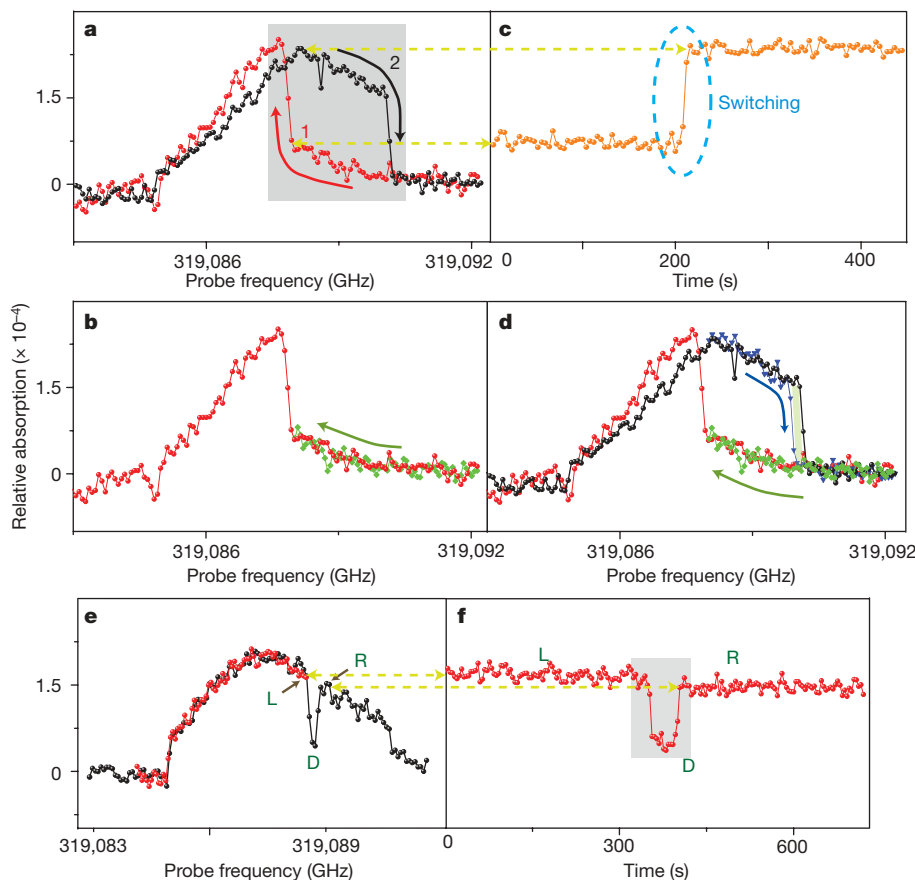

Figure 2 | Time-dependent probe absorption spectrum with fixed laser frequencies. Data are taken at a magnetic field of 2.64 T. **a**, The black (or red) curve represents a full forward (or backward) scan. **b**, The green curve is a partial backward scan. **c**, The probe absorption signal taken as a function of time immediately after stopping the laser just before the rising edge of the trion absorption. **d**, The blue curve is the partial forward scan taken after the switching of the hysteresis states. **e**, The black (or red) curve is the full forward (or partial forward) scan. L, D and R denote three system configurations. **f**, The absorption signal as a function of time, taken immediately after parking the laser just before the dark state is formed.

to prepare the initial nuclear spin configuration and stopped tuning the laser just before the formation of the dark state (red curve). Immediately, we measured the absorption signal as a function of time (Fig. 2f). The system starts in configuration L, indicated by the signal level, jumps into configuration D after some time, and then switches to configuration R, where it remains at high probe absorption. In experiments we noticed that the system can stay in the dark state D on a timescale from a few seconds to 3 min, indicating the meta-stable nature of the nuclear configuration at the TPR (see also the Supplementary Information). Figure 2f shows an example in which the system stays in the D configuration for ~40 s.

Power-dependent measurements of the dark state with a fast laser scan rate provide frequency domain information on the electron spin coherence time. Figure 3a shows the decreasing trend of the estimated spin decoherence rate $\gamma_s/2\pi$ with the increase of the square root of the pump intensities. The black dots represent $\gamma_s/2\pi$ inferred from the absorption minimum at the dark-state dip (normalized by the absorption maximum at the trion peak) and the blue triangles are values extracted from the best fit of the dark-state spectrum including the DNP dynamics. An example of the dark-state spectrum is given in Fig. 3b (identical to Supplementary Fig. S1 with pump Rabi of 0.9 GHz). Details of the data analysis leading to Fig. 3a can be found in the first section of Supplementary Information. For this time-ensemble-averaged measurement of a single spin, γ_s^{-1} corresponds to the inhomogeneous dephasing time T_2^* because of the measurement-to-measurement fluctuations of the nuclear field. For our dot, we estimate the spin inhomogeneous broadening due to a thermally distributed nuclear environment to be (360 ± 30) MHz (refs 7, 21). The dark-state spectrum clearly shows that the spin T_2^* has been enhanced well above the thermal value. As we show later, the enhancement of electron spin T_2^* is a natural result from the suppression of nuclear spin fluctuations by the positive DNP feedback

process and the data in Fig. 3a is a lower bound of this enhancement effect. This mechanism is in fact far more powerful in enhancing the spin T_2^* than the preliminary results from Fig. 3a and b suggest, as we will show using a different experimental set-up.

Both the rounded and broadened trion peak in the probe spectrum and the switching behaviours at fixed laser frequencies indicate that large trion excitation is favoured by the DNP process. When a trion is excited, its two constituent electron spins form an inert singlet, leaving its hole constituent to interact with the nuclear spins. This is a unique element for optical control of the nuclear spin environment while manipulating the electron spin, and it accounts for the experimental observations here.

The hyperfine interaction between the hole spin and nuclear spin is strongly anisotropic[22,23]. In particular, it has a non-collinear hyperfine coupling term $S_h^X I_k^Z$, where S_h^X is the heavy-hole pseudospin operator along the field direction (X) and I_k^Z is the nuclear spin operator along the growth direction (Z). This interaction can flip a nuclear spin without flipping the hole spin, costing only the nuclear Zeeman energy: $\hbar\omega_N \approx 0.01$ GHz T^{-1} (refs 24 and 25). This process stands out from the various DNP interactions because the small energy cost can be directly compensated by the homogeneous broadening of the trion state (~0.4 GHz), which is a lower-order process than the electron-nuclear flipflops assisted by phonons or photons.

From Fermi's Golden Rule, the nuclear spin flip rates are proportional to $\rho_{t,i}\rho_{t,f}$, where $\rho_{t,i}$ is the initial-state trion population and $\rho_{t,f}$ is the final-state trion population after a nuclear spin flip (see details in Supplementary Information). This is because $S_h^X I_k^Z$ has non-zero matrix elements only in the trion portion of the steady-state wave function. The up and down nuclear spin flip rates are different, because they change the electron Zeeman splitting—and hence the two-photon detuning δ from the TPR—in opposite ways, each of which lead to different final-state trion populations $\rho_{t,f}$. Clearly, the
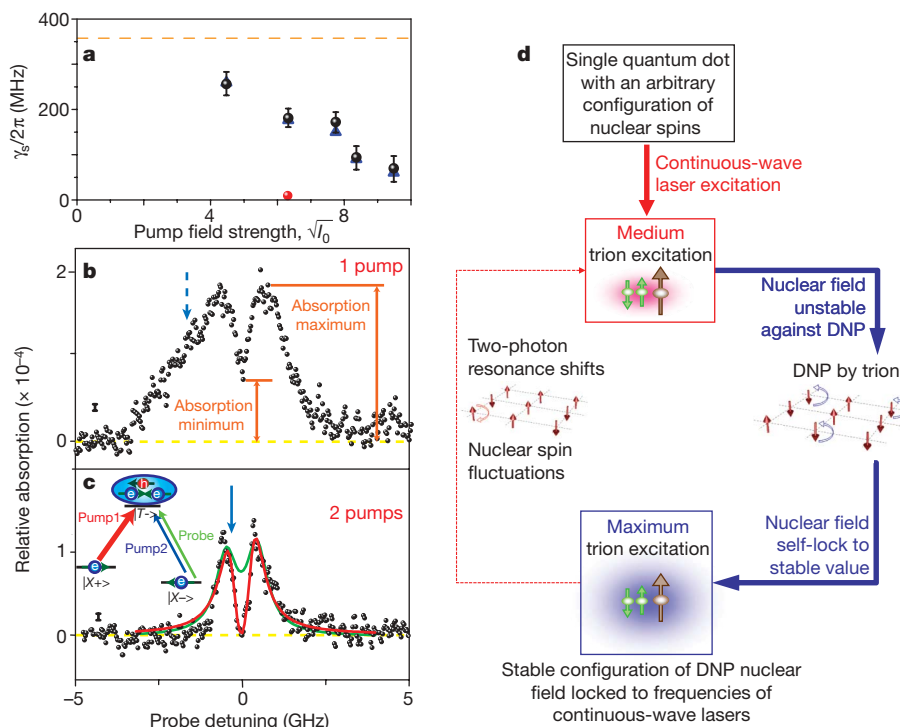

Figure 3 | The observation of the enhancement of electron spin T_2^*. a, The estimated $\gamma_s/2\pi$ from the two-beam dark-state spectrum with various pump field strengths, where $I_o = 2$ W cm^{-2}. Black dots and blue triangles are estimated from the dip-to-peak absorption ratio with error bars determined from the measurement noise (see black error bar symbol in **b**) and from the best fits of the spectrum by modelling the nuclear field dynamics (see Supplementary Information), respectively. The dashed horizontal line denotes the thermal value. The red dot is from fitting the three-beam spectrum in **c**. **b**, An example of the dark-state spectra obtained by fast forward scan in the two-beam set-up that yields the $\gamma_s/2\pi$ value in **a**. The yellow dashed line denotes the zero signal line. **c**, A three-beam measurement with the schematic set-up shown in the inset. The solid blue arrow indicates the spectral position of the second pump beam (also indicated in **b** as a reference with the dashed blue arrow). **d**, Schematic illustration of the self-locking DNP feedback process, which locks the nuclear field to a stable value that maximizes trion excitation.

one resulting in a larger $\rho_{t,f}$ always 'wins', that is, the DNP process tends to maximize trion excitation. The net DNP rate is proportional to $\rho_t(\partial\rho_t/\partial\delta)$, which goes to zero at the maxima of the trion excitation (also the position of strongest absorption), located at $\delta = \pm\Omega_{pump}/2$, where Ω_{pump} is the pump Rabi frequency (see Fig. 4b). The DNP process functions as a restoring force around the absorption maxima, such that when the laser is slightly detuned from the position of the strongest trion excitation, DNP acts to adjust the Zeeman splitting to maximize the trion excitation. We note that the net DNP rate is also zero at the TPR because it is a local minimum, which ties in with the meta-stable nature of the dark state observed in Fig. 2f.

We numerically simulate the self-locking process by including DNP into the optical Bloch equations (see Supplementary Information). Figure 4c simulates the result for fast scans, and
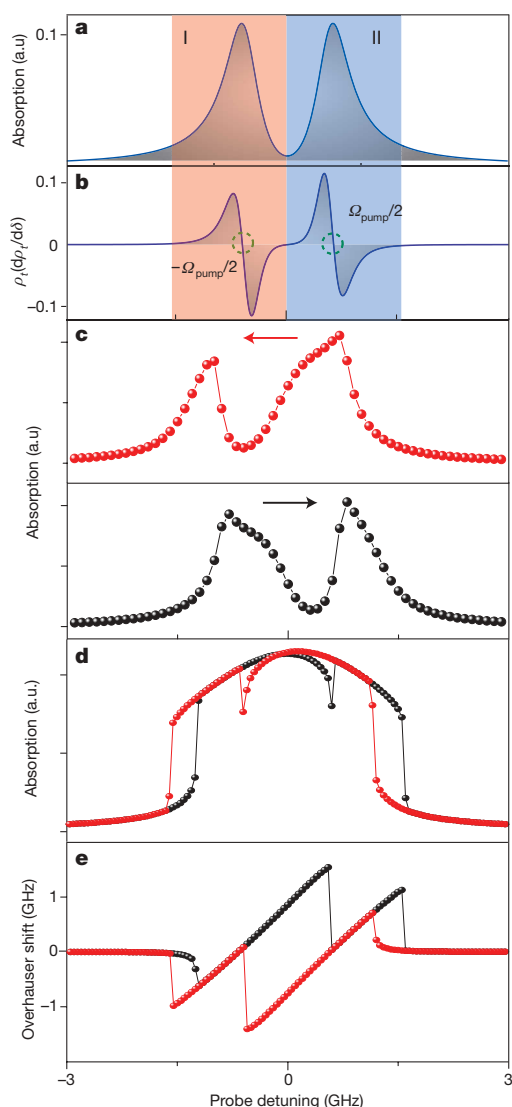
Figure 4 | Theoretical explanation of the nuclear field self-locking effect through the DNP feedback process. a, b, The calculated probe absorption spectrum (**a**) and $\rho_t(\partial\rho_t/\partial\delta)$ (**b**) by solving the three-level Lambda system with pump on resonance in the absence of DNP. **b** shows the DNP acting as a restoring force. The two stability regions corresponding to the absorption maxima are labelled I and II. **c, d,** Numerical simulation results including the self-locking DNP effects for fast (**c**) and slow (**d**) scan corresponding to a magnetic field of 1.32 T. The black (or red) curve represents the probe absorption spectrum of the forward (or backward) scan. **e,** The calculated nuclear field corresponding to the slow scan. The positive (or negative) nuclear field shifts the probe absorption spectrum to the blue (or red). a.u., arbitrary units.

Fig. 4d for slow scans, at magnetic field 1.32 T. The numerical simulations qualitatively reproduce the important features of the experimental observations. Figure 4e clearly shows that the resulting nuclear fields differ greatly depending on whether the probe frequency is scanned forward or backward, which explains the origins of the edge hysteresis and the spectral shift of the dark state. We note that the asymmetry between the forward and backward scans in Fig. 2a is due to the pump detuning (see Supplementary Fig. S3a).

The self-locking effect described in the theory also leads to the suppression of the nuclear spin fluctuations. Once the system has switched to a configuration of maximum trion excitation, the electron spin Zeeman energy and hence the nuclear field are determined and controlled only by the instantaneous laser frequencies, regardless of the initial nuclear spin configuration before the scan starts. In this regime, DNP can actively work to maximize the trion population, and any nuclear spin fluctuations that shift the Zeeman resonance are cancelled out through feedback via the DNP mechanism (Fig. 3d). The quantitative enhancement of T_2^* by this mechanism is determined by the slope of the DNP rate as a function of detuning at the locking points, that is, the two circled positions in Fig. 4b at $\pm\Omega_{pump}/2$. A larger slope means a stronger restoring force, and hence a better locking effect (see Supplementary Fig. S3b, which is qualitatively consistent with the trend shown in Fig. 3a). For spectra discussed in Fig. 3a and b, the locking position of the nuclear field follows the probe laser, which scans much faster than the DNP equilibration rate, so the suppression effect we obtained there is a lower bound of the capability of this nuclear field-locking technique.

Consequently, if the pump and probe beams are fixed spectrally to maximize the trion excitation, the nuclear field fluctuations should be suppressed further than when the probe continuously scans, as in Fig. 3b. Data taken using three beams (Fig. 3c) support this argument. The stronger pump 1 remains near-resonant with transition H1 and the weaker pump 2 is tuned to transition V2 and fixed at the spectral position that maximizes the trion absorption. The two pumps lock the nuclear field to a constant value and suppress nuclear fluctuations for the duration of the experiment. We use the weak probe beam to generate the dark-state spectrum with a fast scan rate, shown in Fig. 3c. The probe is weak and scans at a fast rate, so the effect of the probe beam on the nuclear field can be ignored.

The resulting spectrum in Fig. 3c shows a cleaner dark-state lineshape with a more pronounced dip than the two-beam dark-state spectrum in Fig. 3b with comparable pump intensity, which confirms that the nuclear field is locked by the two pumps. The dip strength represents the electron spin T_2^* and the measured absorption at the TPR approaches zero, so the data indicate a substantial enhancement of the T_2^* in this two-pump set-up. It is challenging to extract an accurate spin decoherence rate because the suppression of nuclear spin fluctuations is so strong that the signal approaches zero at the TPR. However, fitting the data with the standard two-beam optical Bloch equation, the red curve on top of the data (fitting parameters $\Omega_{pump}/2\pi = 0.9\,\text{GHz}$, $\gamma_t/2\pi = 0.4\,\text{GHz}$ and $\delta_{pump} = -30\,\text{MHz}$), yields a value for $\gamma_s/2\pi$ of the order of ~1 MHz with a 5 MHz upper bound error bar, limited by the mutual coherence bandwidth between the lasers. We can also estimate the T_2^* directly from the absorption minimum at the dark-state dip, although this will not be as accurate as the optical Bloch equation curve fitting because it does not exploit all the data points. This dip-to-peak ratio estimation gives a $\gamma_s/2\pi$ of 2 MHz, which agrees with the optical Bloch equation fit. The green curve on top of the data is a theoretical plot using the thermal value of T_2^*, which clearly shows the strong enhancement of the electron spin T_2^* by the DNP self-locking effect. The strongly suppressed γ_s indicates that the intrinsic T_2 could possibly be recovered by this nuclear field-locking technique. We expect that a time domain measurement may more accurately show the dramatic enhancement of T_2^* by the nuclear field-locking scheme described above. Further measurements and theory to explore this potential are in progress.

In conclusion, our results provide a simple but powerful method of suppressing the nuclear spin fluctuations. Once the nuclear spin environment is prepared by our nuclear field-locking method, it may be possible to perform coherent manipulations of a single electron spin for the entire duration of the intrinsic electron spin coherence time, unaffected by hyperfine-interaction-induced inhomogeneous spin dephasing.

METHODS SUMMARY

We give a brief review of the sample structure and experimental techniques, which are explained in detail in refs 26 and 27. The sample contains InAs self-assembled quantum dots grown by molecular beam epitaxy. The size of the dot is about 3 nm in height and 15 nm in base diameter[28]. The sample is embedded in a Schottky diode structure, so we set the DC voltage to charge only one electron into the dot. We use the DC Stark shift modulation absorption technique to achieve a high signal-to-noise ratio[29]. The modulation amplitude is large so that the data correspond directly to absorption. The sample is held in a continuous helium flow magneto cryostat. The magnetic field can be tuned up to 6.6 T. For the quantum dot of interest, the electron in-plane g factor is 0.49 and the hole in-plane g factor is 0.13. The experiment is performed at a temperature of ~5 K.

Two continuous-wave lasers are used in the experiment. As shown in Fig. 1a, a strong pump (red arrow) is horizontally polarized and fixed to be nearly resonant with transition H1 and the weak probe beam (green arrow) is vertically polarized. In the experiment, the estimated pump Rabi frequency ranges from ~0.63 to ~1.35 GHz, and the probe Rabi frequency is fixed at ~0.24 GHz. Since the polarization axis of the quantum dot is rotated about 20° away from the laboratory frame owing to the heavy and light hole mixing[30], the probe beam can pick up both V2 and H2 transitions in a single scan. For the slow scan data shown in the text, the probe laser frequency is held at each value for 4 s and each data point is the integrated signal over the last 1 s of this interval.

1. Berezovsky, J. *et al.* Picosecond coherent optical manipulation of a single electron spin in a quantum dot. *Science* **320**, 349–352 (2008).
2. Bracker, A. S. *et al.* Optical pumping of the electronic and nuclear spin of single charge-tunable quantum dots. *Phys. Rev. Lett.* **94**, 047402 (2005).
3. Gammon, D. & Steel, D. G. Optical studies of single quantum dots. *Phys. Today* **55**, 36–41 (2002).
4. Gerardot, B. D. *et al.* Optical pumping of a single hole spin in a quantum dot. *Nature* **451**, 441–444 (2008).
5. Kim, D. *et al.* and nondestructive measurement in a quantum dot molecule. *Phys. Rev. Lett.* **101**, 236804 (2008).
6. Kroutvar, M. *et al.* Optically programmable electron spin memory using semiconductor quantum dots. *Nature* **432**, 81–84 (2004).
7. Merkulov, I. A. Efros, A. L. & Rosen, M. Electron spin relaxation by nuclei in semiconductor quantum dots. *Phys. Rev. B* **65**, 205309 (2002).
8. Petta, J. R. *et al.* Coherent manipulation of coupled electron spins in semiconductor quantum dots. *Science* **309**, 2180–2184 (2005).
9. Baugh, J. Kitamura, Y. Ono, K. & Tarucha, S. Large nuclear Overhauser fields detected in vertically coupled double quantum dots. *Phys. Rev. Lett.* **99**, 096804 (2007).
10. Tartakovskii, A. I. *et al.* Nuclear spin switch in semiconductor quantum dots. *Phys. Rev. Lett.* **98**, 026806 (2007).
11. Eble, B. *et al.* Dynamic nuclear polarization of a single charge-tunable InAs/GaAs quantum dot. *Phys. Rev. B* **74**, 081306 (2006).
12. Greilich, A. *et al.* Nuclei-induced frequency focusing of electron spin coherence. *Science* **317**, 1896–1899 (2007).
13. Koppens, F. H. L. *et al.* Control and detection of singlet-triplet mixing in a random nuclear field. *Science* **309**, 1346–1350 (2005).
14. Maletinsky, P., Lai, C. W., Badolato, A. & Imamoglu, A. Nonlinear dynamics of quantum dot nuclear spins. *Phys. Rev. B* **75**, 035409 (2007).
15. Vink, I. T. *et al.* Locking electron spins into magnetic resonance by electron-nuclear feedback. Preprint at <http://arxiv.org/abs/0902.2659> (2009).
16. Reilly, D. J. *et al.* Suppressing spin qubit dephasing by nuclear state preparation. *Science* **321**, 817–821 (2008).
17. Xu, X. D. *et al.* Fast spin state initialization in a singly charged InAs-GaAs quantum dot by optical cooling. *Phys. Rev. Lett.* **99**, 097401 (2007).
18. Xu, X. *et al.* Coherent population trapping of an electron spin in a single negatively charged quantum dot. *Nature Phys.* **4**, 692–695 (2008).
19. Harris, S. E. Electromagnetically induced transparency. *Phys. Today* **50**, 36–42 (1997).
20. Stepanenko, D., Burkard, G., Giedke, G. & Imamoglu, A. Enhancement of electron spin coherence by optical preparation of nuclear spins. *Phys. Rev. Lett.* **96**, 136401–136404 (2006).
21. Braun, P. F. *et al.* Direct observation of the electron spin relaxation induced by nuclei in quantum dots. *Phys. Rev. Lett.* **94**, 116601 (2005).
22. Eble, B. *et al.* Hole–nuclear spin interaction in quantum dots. *Phys. Rev. Lett.* **102**, 146601–146604 (2009).
23. Fischer, J. Coish, W. A., Bulaev, D. V. & Loss, D. Spin decoherence of a heavy hole coupled to nuclear spins in a quantum dot. *Phys. Rev. B* **78**, 155329 (2008).
24. Kikkawa, J. M. & Awschalom, D. D. All-optical magnetic resonance in semiconductors. *Science* **287**, 473–476 (2000).
25. Gammon, D. *et al.* Nuclear spectroscopy in single quantum dots: nanoscopic raman scattering and nuclear magnetic resonance. *Science* **277**, 85–88 (1997).
26. Ware, M. E. *et al.* Polarized fine structure in the photoluminescence excitation spectrum of a negatively charged quantum dot. *Phys. Rev. Lett.* **95**, 177403 (2005).
27. Xu, X. *et al.* Coherent optical spectroscopy of a strongly driven quantum dot. *Science* **317**, 929–932 (2007).
28. Scheibner, M. *et al.* Optically mapping the electronic structure of coupled quantum dots. *Nature Phys.* **4**, 291–295 (2008).
29. Alen, B. *et al.* Stark-shift modulation absorption spectroscopy of single quantum dots. *Appl. Phys. Lett.* **83**, 2235–2237 (2003).
30. Koudinov, A. V. & Akimov, I. A. Kusrayev, Yu. G. & Henneberger, F. Optical and magnetic anisotropies of the hole states in Stranski-Krastanov quantum dots. *Phys. Rev. B* **70**, 241305 (2004).

Dynamics revealed by correlations of time-distributed weak measurements of a single spin

R.-B. Liu,[1, *] Shu-Hong Fung,[1] Hok-Kin Fung,[1] A. N. Korotkov,[2] and L. J. Sham[3]

[1]*Department of Physics, The Chinese University of Hong Kong, Shatin, N.T., Hong Kong, China*
[2]*Department of Electrical Engineering, University of California, Riverside, California 92521-0204*
[3]*Department of Physics, University of California San Diego, La Jolla, California 92093-0319*
(Dated: September 28, 2009)

We show that the correlations in stochastic outputs of time-distributed weak measurements can be used to study the dynamics of an individual quantum object, with a proof-of-principle setup based on small Faraday rotation caused by a single spin in a quantum dot. In particular, the third order correlation can reveal the "true" spin decoherence, which would otherwise be concealed by the inhomogeneous broadening effect in the second order correlations. The viability of such approaches lies in that (1) in weak measurement the state collapse which would disturb the system dynamics occurs at a very low probability, and (2) a shot of measurement projecting the quantum object to a known basis state serves as a starter or stopper of the evolution without pumping or coherent controlling the system as otherwise required in conventional spin echo.

The standard von Neumann quantum measurement may be generalized in two aspects. One is measurements distributed in time [1, 2], continuously or in a discrete sequence, as in the interesting Zeno [1] and anti-Zeno effects [3]. Time-distributed measurements intrinsically interfere with the evolution of the quantum object [2]. Another generalization is weak measurement in which the probability of distinguishing the state of a quantum object by a single shot of measurement is much smaller than one [4–8]. On the one hand, weak measurement has very low information yield rate; on the other hand, it only rarely disturbs the dynamics of a quantum object by state collapse. As a combination of the two generalizations, time-distributed weak measurements have been used to steer the quantum state evolution [9]. In this paper, we show that the statistical analysis of time-distributed weak measurements may be used to study the dynamics of a quantum object [8]. The outputs of time-distributed measurements bear the stochastic nature of quantum measurements, so the standard noise analysis in quantum optics [10] would be a natural method to be applied. Notwithstanding that, we should emphasize that the stochastic output of time-distributed weak measurement is not the noise in the system, but an intrinsic quantum mechanical phenomenon. Revealing quantum dynamics by correlations of time-distributed weak measurements is complementary to the fundamental dissipation-fluctuation theorem which relates correlations of thermal noises to the linear response of a system [11–14].

To demonstrate the basic idea, we consider the monitoring of coherent Lamor precession and decoherence of a single spin in a quantum dot, which is relevant to exploiting the spin coherence in quantum technologies such as quantum computing [15–18]. The difficulty of studying the spin decoherence lies in the fact that the "true" decoherence due to quantum entanglement with environments is often concealed by the rapid "phenomenological" dephasing caused by inhomogeneous broadening in ensemble measurements (e.g., in a typical GaAs quantum dot, the spin decoherence time is $\sim 10^{-6}$ sec, but the inhomogeneous broadening dephasing time is $\sim 10^{-9}$ sec [16–21]). To resolve the spin decoherence excluding the inhomogeneous broadening effect, spin echo [16, 19, 21–23] and mode-locking of spin frequency [18] have been invoked. In this paper, we will show that the spin dynamics can be revealed in correlations of the stochastic outputs of sequential weak probes. In particular, the third order correlation singles out the "true" spin decoherence. Unlike conventional spin echo, the present method involves no explicit pump or control of the spin but uses the state collapse as the starter or stopper of the spin precession.

We design a proof-of-principle setup (see Fig. 1) based on Faraday rotation, which has been used in experiments for spin measurements [18, 20, 21, 24, 25]. The probe consists of a sequence of linearly polarized laser pulses evenly spaced in delay time τ. After interaction with a single spin (in a quantum dot, e.g.), the light polarization is rotated by θ or $-\theta$ for the spin state parallel or anti-parallel to the light propagation direction (z-axis). The Faraday rotation angle θ by a single electron spin is usually very small ($\sim 10^{-6}$ rad in a quantum dot [24, 25]), so the two polarization states of the light corresponding to the two different spin states are almost identical. Thus a detection of the light polarization is a weak measurement of the spin. The light polarization is detected by filtering through a polarized beam splitter (PBS) which is
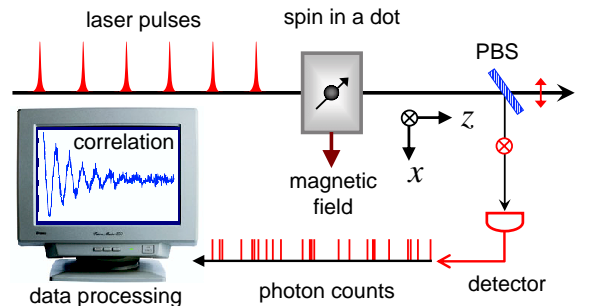

FIG. 1: (Color online) A proof-of-principle setup for weak measurement of a single spin in a quantum dot by Faraday rotation.

aligned to let the light with polarization rotated by θ fully pass through and the light with orthogonal polarization fully reflected. The light with Faraday rotation angle $-\theta$ is reflected with probability $\sin^2(2\theta)$. For a small θ, the average number of reflected photons is much less than one, so in most cases, a single-photon detector set at the reflection arm would be idle with no clicks and one cannot tell which state the spin could be in. The clicks of the detector form a stochastic sequence. The correlations in the sequence will be analyzed to study the spin dynamics, such as the precession under a transverse magnetic field and the decoherence. This proof-of-principle setup, being conceptually simple and adapted from existing experiments, is of course not the only possible implementation. For example, one can use continuous-wave probe instead of pulse sequences, interferometer measurement of the polarization instead of the PBS filtering, polarization-selective absorption instead of the Faraday rotation, and so on.

We shall derive from quantum optics description of the spin-light interaction a weak measurement theory in the formalism of positive operator value measure (POVM) [1, 26]. Consider a laser pulse in a coherent state $|\alpha, H\rangle \equiv e^{\alpha a_H^\dagger - \text{h.c.}}|0\rangle$ (where $a_{H/V}^\dagger$ creates a photon with linear polarization H or V) and a spin in an arbitrary superposition $C_+|+\rangle + C_-|-\rangle$ in the basis quantized along the z-axis, the initial spin-photon state is

$$|\psi\rangle = (C_+|+\rangle + C_-|-\rangle) \otimes |\alpha, H\rangle. \tag{1}$$

After interaction, the state becomes an entangled one as

$$|\psi'\rangle = C_+|+\rangle \otimes |\alpha, +\theta\rangle + C_-|-\rangle \otimes |\alpha, -\theta\rangle, \tag{2}$$

where $|\alpha, \pm\theta\rangle \equiv e^{\alpha a_{\pm\theta}^\dagger - \text{h.c.}}|0\rangle$ (with $a_{\pm\theta} \equiv a_H \cos\theta \pm a_V \sin\theta$) is a photon coherent state with polarization rotated by $\pm\theta$. How much the spin is measured is determined by the distinguishability between the two polarization states

$$\mathcal{D} \equiv 1 - |\langle\alpha, +\theta|\alpha, -\theta\rangle|^2 = 1 - \exp\left(-4|\alpha|^2 \sin^2\theta\right). \tag{3}$$

When the average number of photons $\bar{N} = |\alpha|^2 \gg 1$ and the Faraday rotation angle θ is not too small, the two coherent states are almost orthogonal and $\mathcal{D} \to 1$, thus a detection of the light polarization provides a von Neumann projective measurement of the spin. For a single spin in a quantum dot, the Faraday rotation angle θ is usually very small. For example, in a GaAs fluctuation quantum dot [24], $|\theta| \sim 10^{-5}$ rad for light tuned 1 meV below the optical resonance with a focus spot area $\sim 10\ \mu\text{m}^2$. The number of photons in a 10 picosecond pulse with power 10 mW is $\bar{N} \sim 0.5 \times 10^6$. In this case, $\mathcal{D} \cong 4\bar{N}\theta^2 \sim 2 \times 10^{-4} \ll 1$, the spin states are almost indistinguishable by the photon polarization states. After interaction with the spin, the laser pulse is subject to the PBS filtering which transforms the spin-photon state to be

$$|\psi''\rangle = C_+|+\rangle \otimes |\alpha\rangle_t \otimes |0\rangle_r + C_-|-\rangle \otimes |\alpha\cos(2\theta)\rangle_t \otimes |\alpha\sin(2\theta)\rangle_r, \tag{4}$$

where $|\beta\rangle_{t/r}$ denotes a coherent state of the transmitted/reflected mode with amplitude β. Separating the vacuum

state $|0\rangle_r$ from the reflected mode and keeping terms up to a relative error $O\left(\theta^2\right)$, we write the state as

$$|\psi''\rangle = \left(C_+|+\rangle + \sqrt{1 - \mathcal{D}}C_-|-\rangle\right) \otimes |\alpha\rangle_t \otimes |0\rangle_r + \sqrt{\mathcal{D}}C_-|-\rangle \otimes |\alpha\rangle_t \otimes |\alpha\sin(2\theta)\rangle_r', \tag{5}$$

where $|\alpha\sin(2\theta)\rangle_r'$ denotes the (normalized) state of the reflected mode but with the vacuum component dropped. With a probability $P_1 = \mathcal{D}|C_-|^2 \ll 1$, an ideal detector at the reflection arm will detect a photon-click and the spin state is known at $|-\rangle$, while in most cases (with probability $P_0 = 1 - P_1$), the detector will be idle and the spin state is unknown but keeps almost free evolution. In the POVM formalism [1, 26], the Kraus operators for the click and no-click are respectively

$$\hat{M}_1 = \sqrt{\mathcal{D}}|-\rangle\langle-|, \text{ and } \hat{M}_0 = \sqrt{1 - \mathcal{D}}|-\rangle\langle-| + |+\rangle\langle+|, \tag{6}$$

which determine the (non-normalized) post-measurement state $\hat{M}_{0/1}|\psi\rangle$ and the probability $P_{0/1} = \left\langle\psi\left|\hat{M}_{0/1}^\dagger\hat{M}_{0/1}\right|\psi\right\rangle$.

Between two subsequent shots of measurement, the spin precession under a transverse magnetic field (along x-direction) is described by

$$\hat{U} = \exp\left(-i\hat{\sigma}_x\omega\tau/2\right) \tag{7}$$

where $\hat{\sigma}_x$ is the Pauli matrix along the x-direction, and ω is the Lamor frequency. Coupled to the environment and subject to dynamically fluctuating local fields, the spin precession is always accompanied by decoherence. For simplicity, we consider an exponential coherence decay characterized by a decoherence time T_2. In the quantum trajectory picture [5, 10], the decoherence can be understood as a result of continuous measurement by the environment, for which the Kraus operators for the quantum jumps with and without phase flip are respectively [26]

$$\hat{E}_1 = \sqrt{\gamma/2}\hat{\sigma}_x, \text{ and } \hat{E}_0 = \sqrt{1 - \gamma/2}\hat{I}, \tag{8}$$

where $\gamma \equiv 1 - \exp(-\tau/T_2) \cong \tau/T_2$ is the coherence lost between two subsequent measurements. For a spin state described by a density operator $\hat{\rho}$, the decoherence within τ leads the state to $\hat{\mathscr{E}}[\hat{\rho}] \equiv \hat{E}_0\hat{\rho}\hat{E}_0^\dagger + \hat{E}_1\hat{\rho}\hat{E}_1^\dagger$.

To study the spin dynamics under sequential measurement, we generalize the POVM formalism for a sequence of n measurement. To incorporate the spin decoherence in the density operator evolution, we define the superoperators for the weak measurement and the free evolution as $\hat{\mathscr{M}}_{0/1}[\hat{\rho}] = \hat{M}_{0/1}\hat{\rho}\hat{M}_{0/1}^\dagger$, $\hat{\mathscr{U}}[\hat{\rho}] = \hat{U}\hat{\rho}\hat{U}^\dagger$, in addition to the decoherence superoperator $\hat{\mathscr{E}}$ defined above. For a sequence output $X \equiv [x_1 x_2 \cdots x_n]$ as a string of binary numbers, the superoperator,

$$\mathscr{M}_X = \mathscr{M}_{x_n}\hat{\mathscr{E}}\hat{\mathscr{U}}\mathscr{M}_{x_{n-1}} \cdots \mathscr{M}_{x_3}\hat{\mathscr{E}}\hat{\mathscr{U}}\mathscr{M}_{x_2}\hat{\mathscr{E}}\hat{\mathscr{U}}\mathscr{M}_{x_1}, \tag{9}$$

transforms an initial density operator $\hat{\rho}$ to $\mathscr{M}_X[\hat{\rho}]$ (not normalized) and determines the probability of the output $P_X = \text{Tr}\left(\mathscr{M}_X[\hat{\rho}]\right)$. With the POVM formalism, the spin state evolution under sequential measurement and hence the noise correlations discussed below can be readily evaluated.
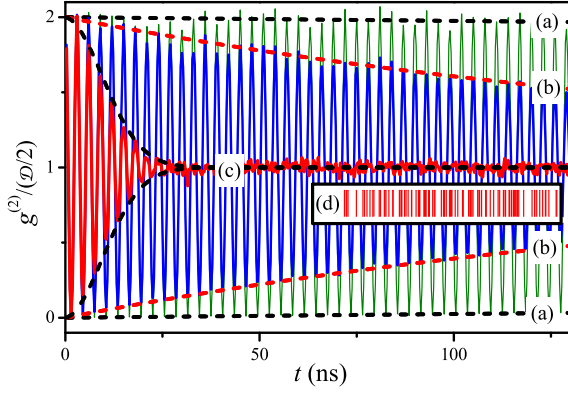
FIG. 2: (Color online) The Monte Carlo simulation (solid oscillating curves) and the analytical result (envelopes in dashed lines) of the 2nd order correlation function, calculated with distinguishability $\mathcal{D} = 3 \times 10^{-4}$, Lamor precession period $2\pi/\omega_0 = 3$ ns and the interval between two subsequent measurements $\tau = 0.3$ ns. In (a), no decoherence or inhomogeneous broadening is present ($T_2^{-1} = \sigma = 0$); In (b), $T_2 = 200$ ns but $\sigma = 0$; In (c), $T_2 = 200$ ns and $\sigma^{-1} = 10$ ns. (d) shows the stochastic output obtained in the Monte Carlo simulation. The Monte Carlo simulation is done with 10^{10} shots of measurement.

To illustrate how a real experiment would perform, we have carried out Monte Carlo simulations of the measurement with the following algorithm: (1) We start from a randomly chosen state of the spin $|\psi\rangle$; (2) The state after a free evolution is $\hat{U}|\psi\rangle$; (3) Then the decoherence effect is taken into account by applying randomly the Kraus operator $\hat{E}_0$ or $\hat{E}_1$ to the state (with normalization) with probability $1 - \gamma/2$ or $\gamma/2$, respectively; (4) The measurement is done by randomly applying the Kraus operator $\hat{M}_0$ or $\hat{M}_1$ to the state (with normalization) corresponding to the output 0 or 1 (no-click or click), with probability P_0 or P_1 given by the POVM formalism. Step (2)-(4) are repeated for many times. The output is a random sequence of clicks, as shown in Fig. 2 (d).

To study the correlation of the stochastic output, we first consider the interval distribution $K(n)$, defined as the probability of having two clicks separated by $n - 1$ no-clicks [10],

$$K(n) \equiv \mathrm{Tr}\left(\hat{\mathcal{M}}_{[1 0_{n-1} 1]}[\hat{\rho}]\right) \Big/ \mathrm{Tr}\left(\hat{\mathcal{M}}_1[\hat{\rho}]\right), \qquad (10)$$

where 0_{n-1} means a string of $n - 1$ zeros. By a straightforward calculation,

$$K(n) \approx \frac{\mathcal{D} + \mathcal{D}^2}{2} e^{-\frac{n\mathcal{D}}{2}} \left[1 + e^{-\frac{n\tau}{T_2}} \cos\left(n\omega\tau + \frac{\mathcal{D}}{2}\cot\frac{\omega\tau}{2}\right)\right], \qquad (11)$$

up to $O\left(\gamma\mathcal{D}^2\right)$ and $O\left(n\mathcal{D}^3\right)$, for $\gamma, \mathcal{D} \ll \omega\tau < \pi$. A successful measurement at the beginning of an interval projects the spin to the basis state $|-\rangle$ along the optical (z) axis. Then, the spin precesses under the external magnetic field about the x-axis. The interval is terminated by a second successful measurement among the periodic attempts after a time lapse of $n\tau$. The decay of the oscillation is due to the spin decoherence. The overall decay $e^{-n\mathcal{D}/2}$ is due to decreasing of the probability of unsuccessful measurement with increasing time. The
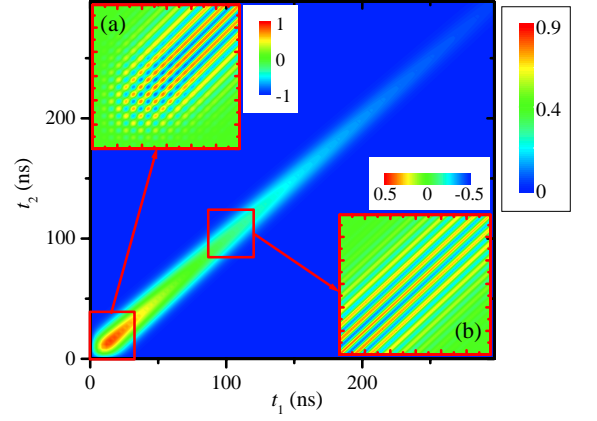

FIG. 3: (Color online) Contour plot of the envelope of the 3rd order correlation $G^{(3)}(t_1, t_2)$, with parameters the same as for Fig. 2 (c). The insets (a) and (b) show the oscillation details of $G(t_1, t_2)$ in the range 0 ns$\leq t_{1,2} \leq 30$ ns and 90 ns$\leq t_{1,2} \leq 120$ ns, respectively.

measurement also induces a little phaseshift to the oscillation. Obviously, the smaller the distinguishability $\mathcal{D}$, the less the spin dynamics is disturbed by the measurement.

In experiments, often the photon coincidence correlation instead of the interval distribution is measured. The second order correlation $g^{(2)}(n\tau)$ is the probability of having two clicks separated by $n - 1$ measurements [10], regardless of the results in between,

$$g^{(2)}(n\tau) = \sum_{x_1, x_2, \ldots, x_{n-1} \in \{0,1\}} \mathrm{Tr}\left(\hat{\mathcal{M}}_{1 x_1 x_2 \cdots x_{n-1} 1}[\hat{\rho}]\right) \Big/ \mathrm{Tr}\left(\hat{\mathcal{M}}_1[\hat{\rho}]\right)$$

$$= K(n) + \sum_{m=1}^{n-1} K(n-m)K(m)$$

$$+ \sum_{m=2}^{n-1}\sum_{l=1}^{m-1} K(n-m)K(m-l)K(l) + \cdots . \qquad (12)$$

By Fourier transformation and summation in the frequency domain,

$$g^{(2)}(n\tau) = \frac{\mathcal{D}}{2}\left[1 + e^{-n(\tau/T_2 + \mathcal{D}/4)}\cos(n\omega\tau) + O(\mathcal{D})\right]. \qquad (13)$$

The spin precession, the decoherence, and the measurement-induced decay are all seen in the second order correlation function [see Fig. 2]. Note that the overall decay of the interval distribution manifests itself as a measurement-induced dephasing of the oscillating signal in the correlation function. The Monte Carlo simulation shows that 10^{10} shots of measurement would yield a rather smooth profile of the spin dynamics, which requires a time span of about 3 seconds for the parameters used in Fig. 2.

In addition to the decoherence due to the dynamical fluctuation of the local field, there is also phenomenological dephasing due to static or slow fluctuations, i.e., inhomogeneous broadening which exists even for a single spin since the sequential measurement contains many shots which form an

ensemble. The inhomogeneous broadening is modeled by a Gaussian distribution of ω with mean value ω_0 and width σ. With the inhomogeneous broadening included, the ensemble-averaged correlation function becomes

$$\left\langle g^{(2)}(n\tau) \right\rangle = \frac{\mathcal{D}}{2} \left[1 + e^{-n(\tau/T_2 + \mathcal{D}/4) - n^2\tau^2\sigma^2/2} \cos(n\omega_0\tau) + O(\mathcal{D}) \right].$$
(14)

Since usually $\sigma \gg T_2^{-1}$, the decay of the 2nd order correlation is dominated by the inhomogeneous broadening effect [see Fig. 2 (c)].

To separate the spin decoherence from the inhomogeneous broadening, we resort to the 3rd order correlation $g^{(3)}(n_1\tau, n_2\tau)$, the probability of having three clicks separated by $n_1 - 1$ and $n_2 - 1$ measurements. The idea can be understood in a post-measurement selection picture: After the first click, the second click has the peak probability appearing at an integer multiple of the spin precession period, so the coincidence of the two earlier clicks serves as filtering of the spin frequency and the third click would have a peak probability appearing at $n_2\tau = n_1\tau$, similar to the spin echo. The 3rd order correlation in the absence of inhomogeneous broadening is $g^{(3)}(t_1, t_2) \propto g^{(2)}(t_1)g^{(2)}(t_2)$. The ensemble-average leads to (neglecting the measurement-induced decay)

$$\left\langle g^{(3)}(t_1, t_2) \right\rangle \propto 1 + \sum_{j=1,2} e^{-t_j/T_2 - \sigma^2 t_j^2/2} \cos(\omega_0 t_j)$$
$$+ \frac{1}{2} e^{-(t_1+t_2)/T_2} e^{-\sigma^2(t_1+t_2)^2/2} \cos(\omega_0(t_1 + t_2))$$
$$+ \frac{1}{2} e^{-(t_1+t_2)/T_2} e^{-\sigma^2(t_1-t_2)^2/2} \cos(\omega_0(t_1 - t_2)). \quad (15)$$

Fig. 3 plots $G^{(3)}(t_1, t_2) \equiv \left\langle g^{(3)}(t_1, t_2) \right\rangle - \left\langle g^{(2)}(t_1) \right\rangle \left\langle g^{(2)}(t_2) \right\rangle$ to exclude the trivial background. Along the direction $t_1 = -t_2$, the 3rd order correlation oscillates and decays rapidly (with timescale σ^{-1}). But the oscillation amplitude decays slowly (with timescale T_2) along the direction $t_1 = t_2$, as expected from the last term of Eq. (15).

In conclusion, we have given a statistical treatment of sequential weak measurements of a single spin. The characteristics of the weak measurement consist in the negligible perturbation of the spin state except for the projective state collapse when the measurement is successful in identifying the spin state. We show that the third order correlation reveals the spin decoherence from the inhomogeneous broadening. The theory presented here for sequential pulse measurement can be straightforwardly generalized to continuous weak measurement by letting the pulse separation $\tau \to 0$ while keeping the average power of the light unchanged (i.e., $\mathcal{D}/\tau = $ constant). In the proof-of-principle setup based on Faraday rotation, all optical elements have been assumed ideal for conceptual simplicity. An investigation of the defects, e.g., in the PBS and in the photon detector, shows that they do not change the essential results presented here but only reduce the visibility of the features. Details will be published elsewhere.

* Corresponding author; rbliu@phy.cuhk.edu.hk
[1] A. Peres, *Quantum Theory: Concepts and Methods* (Kluwer Academic, New York, 2002).
[2] C. M. Caves, Phys. Rev. D **33**, 1643 (1986).
[3] A. G. Kofman and G. Kurizki, Nature **405**, 546 (2000).
[4] H. J. Carmichael, *An open system approach to quantum optics*, Lecture Notes in Physics (Springer, Berlin, 1993).
[5] H. M. Wiseman and G. J. Milburn, Phys. Rev. Lett. **70**, 548 (1993).
[6] M. B. Mensky, Phys. Usp. **41**, 923 (1998).
[7] A. N. Korotkov, Phys. Rev. B **60**, 5737 (1999).
[8] A. N. Korotkov and D. V. Averin, Phys. Rev. B **64**, 165310 (2001).
[9] N. Katz, M. Ansmann, R. C. Bialczak, E. Lucero, R. Mcdermott, M. Neeley, M. Steffen, E. M. Weig, A. N. Cleland, J. M. Martinis, and A. N. Korotkov, Science **312**, 1498 (2006).
[10] M. O. Scully and M. S. Zubairy, *Quantum optics* (Cambridge, 1997).
[11] S. A. Crooker, D. G. Rickel, A. V. Balatsky, and D. L. Smith, Nature **431**, 49 (2004).
[12] M. Xiao, I. Martin, E. Yablonovitch, and H. W. Jiang, Nature **430**, 435 (2004).
[13] M. Oestreich, M. Romer, R. J. Haug, and D. Hagele, Phys. Rev. Lett. **95**, 216603 (2005).
[14] M. Braun and J. König, Phys. Rev. B **75**, 085310 (2007).
[15] F. H. L. Koppens, C. Buizert, K. J. Tielrooij, I. T. Vink, K. C. Nowack, T. Meunier, L. P. Kouwenhoven, and L. M. K. Vandersypen, Nature **442**, 766 (2006).
[16] J. R. Petta, A. C. Johnson, J. M. Taylor, E. A. Laird, A. Yacoby, M. D. Lukin, C. M. Marcus, M. P. Hanson, and A. C. Gossard, Science **309**, 2180 (2005).
[17] M. V. Gurudev Dutt, J. Cheng, B. Li, X. Xu, X. Li, P. R. Berman, D. G. Steel, A. S. Bracker, D. Gammon, S. E. Economou, et al., Phys. Rev. Lett. **94**, 227403 (2005).
[18] A. Greilich, D. R. Yakovlev, A. Shabaev, A. L. Efros, I. A. Yugova, R. Oulton, V. Stavarache, D. Reuter, A. Wieck, and M. Bayer, Science **313**, 341 (2006).
[19] F. H. L. Koppens, K. C. Nowack, and L. M. K. Vandersypen, Phys. Rev. Lett. **100**, 236802 (2008).
[20] M. H. Mikkelsen, J. Berezovsky, N. G. Stoltz, L. A. Coldren, and D. D. Awschalom, Nature Phys. **3**, 770 (2007).
[21] J. Berezovsky, M. H. Mikkelsen, N. G. Stoltz, L. A. Coldren, and D. D. Awschalom, Science **320**, 349 (2008).
[22] A. M. Tyryshkin, S. A. Lyon, A. V. Astashkin, and A. M. Raitsimring, Phys. Rev. B **68**, 193207 (2003).
[23] E. Abe, K. M. Itoh, J. Isoya, and S. Yamasaki, Phys. Rev. B **70**, 033204 (2004).
[24] J. Berezovsky, M. H. Mikkelsen, O. Gywat, N. G. Stoltz, L. A. Coldren, and D. D. Awschalom, Science **314**, 1916 (2006).
[25] M. Atatüre, J. Dreiser, A. Badolato, and A. Imamoglu, Nature Physics **3**, 101 (2007).
[26] M. A. Nielsen and I. L. Chuang, *Quantum computation and quantum information* (Cambridge University, Cambridge, 2000).

Precise Quantum Operation using Basis-Feedback for Digital Quantum Computation

P. Dalal[1], S. K. Saikin[2], and L. J. Sham[1]

[1]Department of Physics, University of California San Diego, La Jolla, California 92093, USA

[2]Department of Chemistry and Chemical Biology, Harvard University, Cambridge, MA 02138, USA

Scalable quantum computers are analog machines whose operating precisions must scale up with their size [1]. This relationship between the number of qubits and the analog precision required for useful quantum algorithms has been quantified and exploited in approximation algorithms [1–3]. Prior to this approach of improving operational precisions, researchers constructed a fault-tolerant quantum gate formalism [4–6] to measure and correct operational error. This formalism is effective for large angle ($\sim \pi/2$) operations, particularly for a subgroup called the Clifford group [6] which may be considered "digital." However, it is unhelpful for small angle rotations because the fault-tolerance threshold [3] is bounded by a 0.9999 operational Fidelity [7], a Fidelity already distinguishing quantum phases separated by 1/128th of a period. Thus, the scaling of quantum computers has reached an impasse: fault-tolerant quantum operations do not improve quantum information unless quantum operations are already precise enough to make them nearly superfluous by way of quantum approximation. Here we show an approach to create precise, general quantum operations, overcoming noisy interactions by quantum coherent feedback [8] and amplitude amplification [9,10]. Instead

of applying an accurate quantum field to generate the desired operation, coherent feedback from the classically-aligned bases of qubits (not from the general quantum states) directs the transformation of a particular quantum state by amplifying its desired components. Because quantum bases can be aligned with non-linear, classical precision (e.g. the angle of an optical polarizer), basis-directed feedback leads to a new scale of operational precision. As an example, we show how to implement the core quantum algorithms, Fourier transform and amplitude amplification, scalably. This method applies generally to any high-precision quantum operation needed and connects the fundamental quantum nature of phase evolution to classical geometry.

Because quantum operations are linear, quantum signal-to-noise ratios usually scale linearly, tracking the error of the control field. This is in stark contrast to the exponential signal-to-noise ratios found in the non-linear transistors used for classical, digital computation. Quantum fault-tolerance introduces non-linearity through indirect measurement attempting to collapse errant subspaces or redirect them. A fault-tolerant quantum gate works by encoding a quantum state into a redundant set of qubits, where the encoding ideally allows a measurement of any errors that take place during the gate's operation. The encoding is performed before the operation and subsequent partial measurements either herald a successful operation or identify (syndrome detection) additional, corrective fault-tolerant operations to perform. But, the domain of its improvement is practically limited by the structure of the measurement relative to the operation. Fault-tolerance traditionally follows from the assumption of statistical independence of error. Though this affords practical solutions for certain operations, including the Clifford group [11,12], this assumption fails

when the operational parameter is a phase [13]. For example, the simplest fault-tolerant implementation of a $\pi/128$ rotation more accurate than the identity requires 31 operations, while ordinary 7-qubit Steane codes require hundreds of thousands of qubits [2]. Other research to create high precision operation by direct rotation is limited to deterministic errors [14–17], uses ensemble statistics that are not scalable [18], requires multi-qubit encodings that either still require high-precision pulse timings [19] or combats decoherence rather than imprecision [20]. For many quantum systems, system-environment noise is too small to decohere the system beyond the 0.9999 threshold Fidelity alone. For example consider the following quantum computing system: qubits are represented as electrons in singly-doped, self-assembled quantum dots, energy states are split by a magnetic field, control is afforded by optically-induced Raman transitions, and environmental coupling is dominated by the quantum dot's nuclear spin-bath [21]. Decoherence during operation does not depreciate this system beyond 0.999999 Fidelity (since $0.1 - 1.0\ ns$ laser pulses can perform π-rotations [21], while transverse spin decoherence works on the order of $10\ \mu s$ at low temperature[22] and can be restored on much longer timescale by controlling system-bath dynamics [23]). Static operational errors are similarly innocuous as previous work [14–17] has shown such errors as inhomogeneous magnetic fields can be corrected when systematic. However, when the operational error is in dimensions external to the total qubit space, like the macroscopic, classical control of a laser, the interaction terms appears stochastic and the inherent imprecision [24] is linearly transferred into error.

On the other hand, the initialization and measurement of quantum systems, in which macroscopic, non-linear processes are available and essential, have seen drastic improvements in Fidelity [25]. Traditionally, researchers distinguish these precisions from quantum operational precision, as

3

classical versus quantum phenomenon. However, interactions like dipolar energy in a magnetic field connect the $O(3)$ topology in classical position space to the $SU(2)$ topology of the quantum two-state space. For example, because the orientation of a single two-level quantum system can be arbitrarily defined, it has been convenient to think of a system of qubits as also arbitrarily defined. Yet, because two arbitrarily-oriented qubits often exist in a common three-dimensional spatial basis there is an explicit parametrization for quantum fields whose symmetry group respects the global, spatial eigenbasis, and which interact with qubits in local, energy eigenbases. Every quantum, microscopic interaction can be represented in a classical, macroscopic basis, so a specific prescription for operations between locally-varying bases can directly convert classical information into precise quantum control. Exploiting this degree of freedom fundamentally connects the non-linear, classical nature of quantum bases with the linear, quantum nature of quantum states, increasing precisions for a pseudo-continuous set of operations in the full Hilbert space.

1 Quantum Coherent Feedback with Locally-Variant Bases

A system considered for quantum computing may have the bases of all of its qubits oriented in the same direction, i.e. the computational basis of this system is simply the global basis, denoted by, $\mathcal{Z}$, a tensor product of identical, local basis vectors. "Locally-variant" bases, denoted by $\mathcal{E}$, refer to basis vectors that vary from one qubit to another due to a varying of the axes of asymmetry creating their local energy splittings, for example the orientation of a magnetic field or crystal direction. Likewise, fields or virtual particles mediating interaction between qubits with different orientations in physical space must be parametrized by favoring the local basis states or not. We

term the former a *local-basis interaction* and the latter a *global-basis interaction*.

An example of a global-basis interaction between qubits is Heisenberg exchange, where a bases-invariant consideration of two spins, $\mathbf{S}_{(i)}$, in the global Hilbert space leads to the interaction, $J_{\mathcal{Z}}\mathbf{S}_{(1)}^{\mathcal{Z}} \cdot \mathbf{S}_{(2)}^{\mathcal{Z}}$. Hence the spin operators for the Heisenberg exchange interaction are specified in a global basis. On the other hand, local-basis interactions that mediate transitions between energy levels may track the orientation of the energy bases. For example, the anisotropic interaction couples two spins through the locally-variant basis of the interaction, $J_{\mathcal{E}}\mathbf{S}_{(1)}^{\mathcal{E}} \times \mathbf{S}_{(2)}^{\mathcal{E}}$, conditioning the quantum trajectory about the classical geometry of the bases. In general, some particles or fields mediating an interaction are local-basis interactions when the Cartesian axes of the interacting qubits are connected by a macroscopic rotation. For example, photonic exchange between two locally-variant qubits can effect a purely local-basis interaction with an optical fiber whose precise, classically imposed Berry phase twists the locally-variant bases into equivalence from the viewpoint of mediating photons [26]. The physics of these interactions are further explained in Supplementary Discussion A.

While an external control field may initiate and terminate interactions between qubits, quantum coherent feedback formalizes how one set of quantum bits can "sense" and coherently encode the operation to be performed on other qubits [8]. What follows is an alternate formulation where the locally-variant bases of a set of quantum bits can encode the desired quantum operation given their precise initializations, using only "digital" interactions from the Clifford group. Previous attempts to digitize quantum computing were too rigid to overcome the Gottesman-Knill theorem [27], which

states that with initialization and measurement in one computational basis, quantum operations limited to the Clifford group can provide no exponential speedup over classical computation. Here we show that, when there are two computational bases, even though all operations may be limited to Clifford operations in a given basis, these operations can implement Shor's factoring and Grover's search globally.

Consider without loss of generality the above quantum dot model with two different qubit swap operations represented by a completely global-basis interaction, $H^{\mathcal{Z}}$, and a completely local-basis interaction, $H^{\mathcal{E}}$,

$$H_I = \gamma_1\left(t\right)H^{\mathcal{Z}} + \gamma_2\left(t\right)H^{\mathcal{E}}, \tag{1}$$

where the precision of the interaction depends on the timing and strength of the control fields, $\gamma_i\left(t\right)$. If the magnetic field of the first qubit is oriented in the $+\hat{z}$ direction and the field of the second qubit is oriented at a polar angle α to the $+\hat{z}$ direction, we can rotate the quantum ground state of the first qubit by applying the two swap operations consecutively This process is illustrated in Figure 1(a) where the local energy and global spatial bases are denoted with the superscripts α and z. We can write this operation using a convenient short-hand where we characterize a spin state on the $Z - Y$ great circle of a local-basis Bloch sphere with its azimuthal angle, θ: $|\theta\rangle^z|0\rangle^\alpha \rightarrow |\theta - \alpha\rangle^z|\alpha\rangle^\alpha$. Note that the non-interacting Hamiltonian term creates local-basis precessions in each qubit which do not necessarily commute during the time of operational pulses. That the precessions have negligible effects on Fidelity in fast operations are shown in Supplementary Discussion B. The Area theorem [28] allows for the appropriate pulse-shaping to minimize the bandwidth of the control field. By exploiting the precision of initialization, the precision of basis alignment, the fault-

tolerance of Clifford operations, and by recognizing a difference between global-basis and local-basis interactions, a prescription for the precise rotation of an arbitrary qubit by a single angle is realized.

It is a small step to formulate a scalable, fault-tolerant quantum Fourier transform circuit as in Figure 1(b). The seven controlled rotations per qubit required for the transform [2] are implemented using the doubled swaps with a third qubit controlling each interaction. This type of three-qubit interaction can be easily be decomposed into fault-tolerant, two-qubit Clifford gates, but it is physically natural to operate directly since one qubit may control the interaction medium as resonant or non-resonant with the desired operation [29]. Then, each of seven control qubits initialized to their ground state, a binary product of seven angles states $\otimes_{i=1}^{7} |\pi/2^i\rangle^{\mathcal{Z}}$ in the spatial basis, may conditionally rotate any of the n qubits as directed by the approximate quantum Fourier transform [1,2]. We show in the next section that any scalable quantum algorithm (one admitting a polynomial approximation of the exponential phase) can be implemented as an extension of quantum amplitude amplification.

2   Amplitude Amplification with Locally-Variant Bases

One may create exponential parallelism in the use of base angles in much the same way Hadamard operations create parallelism in the use of quantum states. The seed operating step in this process, A_2, is an S-matrix scattering event between two angles, which we term a "quantum-walk on a Bloch sphere," given by the equation (2).

$$A_2 \ket{\theta_0} \ket{\theta_1} \equiv \exp\left(i \begin{bmatrix} 0 & 0 & 0 & i \\ 0 & 0 & -i & 0 \\ 0 & i & 0 & 0 \\ -i & 0 & 0 & 0 \end{bmatrix} \frac{\pi}{4} \right) \ket{\theta_0} \ket{\theta_1} \tag{2}$$

$$= \frac{1}{\sqrt{2}} \begin{bmatrix} \cos \frac{\theta_0 + \theta_1}{2} \\ \sin \frac{\theta_0 + \theta_1}{2} \\ \sin \frac{\theta_0 - \theta_1}{2} \\ \cos \frac{\theta_0 - \theta_1}{2} \end{bmatrix}. \tag{3}$$

This analogous to quantum-walks on lattices[30], where an exponential number of lattice steps may be taken in parallel in linear time. Supplementary Discussion C shows that this operation is easily made fault-tolerant and can be cascaded for application to an arbitrary number of qubits to traverse an exponential number of angle states with a linear number of operations. This traversal, parametrized by the angles θ_i, is illustrated on overlaid, disconnected Bloch spheres in Figure 2. The resultant wavefunction is restricted to an $SU\left(2^{m-1}\right)$ subspace of the total Hilbert space, $SU\left(2^m\right)$. Any state that lies outside this Hilbert subspace is errant, thereby suggesting a secondary system of fault-tolerance for a certain set of errors.

The qubit with initial state, $\ket{\theta_0}$, is considered the system qubit and the remaining the control qubits. Then any angle state, if it can be coherently amplified, may be entangled with the state of any other qubit, thereby supporting any scalable quantum algorithm. To amplify one disconnected Bloch sphere completely, we extend the quantum amplitude amplification algorithm in three ways:

use amplification to search for a quantum operation rather than a quantum state, initialize the amplification from a locally-variant zero quantum state instead of a global one, and implement the amplitude search "differentially" to increase the usable quantum information content and a produce immunity to a type of quantum error. This method is illustrated in Figure 3 where two control qubits, $m = 2$, are used to search for and perform an exact rotation operation, $R(\alpha + \beta)$, applied to the quantum state, $|\theta\rangle$. The details of how this quantum circuit coherently amplifies any given angle state is explained in Supplementary Notes A. The number of qubits may be extended arbitrarily as with the amplitude amplification algorithm. The term "differentially" is used in the sense of traditional circuit design, where the input is a symmetric difference between two analog signals. In the quantum analog, the input to the search is two qubits with the state $(|-\theta\rangle, |\theta\rangle)$ and output is two qubits $(|-(\theta + \alpha + \beta)\rangle, |\theta + \alpha + \beta\rangle)$. Certain common-mode, under-over rotation noise between the two differentials tracks may be eliminated as explained in Supplementary Notes A.

A simulation of this circuit with noise simultaneous applied to all operations is detailed in Supplementary Notes B. It is seen that the expected precision gains from traditional quantum fault tolerance of Clifford operations indeed apply to the small rotations performed by this circuit.

3 Conclusion

Our technique breaks with the traditional formalism of creating a universal set of gates to abstract physical technologies from quantum algorithm architectures. The simplicity afforded by universal

quantum gates unfortunately also creates unwieldy structures for fault-tolerance, which we have demonstrated are unnecessary for quantum computing. A non-universal quantum system, where quantum information may be encoded in both spatial and temporal degrees of freedom, may be superior to a universal quantum system with only pulse-encoded operations. Finally, our work shows that quantum Fourier transform can be written as a specific case of amplitude amplification with locally-variant bases, thereby suggesting a relation between the two major families of algorithms typified by factorization and by search. Our theory can be tested upon today's experimental computing platforms supporting two qubits or more with the availability of two distinct bases for each locality which are classically parametrized.

References

1. Coppersmith, D. An approximate Fourier transform useful in quantum factoring (2002). URL `http://www.citebase.org/abstract?id=oai:arXiv.org:quant-ph/0201067`.

2. Fowler, A. G. & Hollenberg, L. C. L. Scalability of Shor's algorithm with a limited set of rotation gates. *Phys. Rev. A* **70**, 032329 (2004).

3. Fowler, A. G., Devitt, S. J. & Hollenberg, L. C. L. Constructing steane code fault-tolerant gates. vol. 5650, 557–568 (SPIE, 2005). URL `http://link.aip.org/link/?PSI/5650/557/1`.

4. Shor, P. W. Fault-tolerant quantum computation. In *37th Symposium on Foundations of Computing, IEEE Computer Society Press*, 56–65 (IEEE Computer Society Press, 1996).

5. Knill, E. & Laflamme, R. Theory of quantum error-correcting codes. *Phys. Rev. A* **55**, 900–911 (1997).

6. Gottesman, D. Theory of fault-tolerant quantum computation. *Phys. Rev. A* **57**, 127–137 (1998).

7. Aliferis, P., Gottesman, D. & Preskill, J. Quantum accuracy threshold for concatenated distance-3 codes. *Quant.Inf.Comput.* **6**, 97 (2006). URL http://www.citebase.org/abstract?id=oai:arXiv.org:quant-ph/0504218.

8. Lloyd, S. Coherent quantum feedback. *Phys. Rev. A* **62**, 022108 (2000).

9. Grover, L. K. A fast quantum mechanical algorithm for database search. In *STOC '96: Proceedings of the twenty-eighth annual ACM symposium on Theory of computing*, 212–219 (ACM, New York, NY, USA, 1996).

10. Brassard, G., Hoyer, P., Mosca, M. & Tapp, A. Quantum amplitude amplification and estimation. *Quantum Computation and Quantum Information: A Millennium Volume, AMS Contemporary Mathematics Series* **305** (2002). URL http://www.citebase.org/abstract?id=oai:arXiv.org:quant-ph/0005055.

11. Calderbank, A. R. & Shor, P. W. Good quantum error-correcting codes exist. *Phys. Rev. A* **54**, 1098–1105 (1996).

12. Steane, A. M. Error correcting codes in quantum theory. *Phys. Rev. Lett.* **77**, 793–797 (1996).

13. Carruthers, P. & Nieto, M. M. Phase and angle variables in quantum mechanics. *Rev. Mod. Phys.* **40**, 411–440 (1968).

14. Morton, J. J. L. *et al.* High fidelity single qubit operations using pulsed electron paramagnetic resonance. *Physical Review Letters* **95**, 200501 (2005). URL http://link.aps.org/abstract/PRL/v95/e200501.

15. Li, J.-S. & Khaneja, N. Control of inhomogeneous quantum ensembles. *Physical Review A (Atomic, Molecular, and Optical Physics)* **73**, 030302 (2006). URL http://link.aps.org/abstract/PRA/v73/e030302.

16. Reichardt, B. W. & Grover, L. K. Quantum error correction of systematic errors using a quantum search framework. *Physical Review A (Atomic, Molecular, and Optical Physics)* **72**, 042326 (2005). URL http://link.aps.org/abstract/PRA/v72/e042326.

17. Hill, C. D. Robust controlled-not gates from almost any interaction. *Physical Review Letters* **98**, 180501 (2007). URL http://link.aps.org/abstract/PRL/v98/e180501.

18. Vandersypen, L. M. K., Yannoni, C. S. & Chuang, I. L. *Liquid state NMR Quantum Computing*, vol. 9 of *Encyclopedia of Nuclear Magnetic Resonance* (John Wiley & Sons, Ltd, 2002). URL http://www.citebase.org/abstract?id=oai:arXiv.org:quant-ph/0012108.

19. DiVincenzo, D. P., Bacon, D., Kempe, J., Burkard, G. & Whaley, K. B. Universal quantum computation with the exchange interaction. *Nature* **408**, 339–342 (2000). URL http://dx.doi.org/10.1038/35042541.

20. Bacon, D., Kempe, J., Lidar, D. A. & Whaley, K. B. Universal fault-tolerant quantum computation on decoherence-free subspaces. *Phys. Rev. Lett.* **85**, 1758–1761 (2000).

21. Emary, C. & Sham, L. J. Optically controlled single-qubit rotations in self-assembled inas quantum dots. *Journal of Physics: Condensed Matter* **19**, 056203 (10pp) (2007). URL http://stacks.iop.org/0953-8984/19/056203.

22. Yao, W., Liu, R.-B. & Sham, L. J. Theory of electron spin decoherence by interacting nuclear spins in a quantum dot. *Physical Review B (Condensed Matter and Materials Physics)* **74**, 195301 (2006). URL http://link.aps.org/abstract/PRB/v74/e195301.

23. Yao, W., Liu, R.-B. & Sham, L. J. Restoring coherence lost to a slow interacting mesoscopic spin bath. *Physical Review Letters* **98**, 077602 (2007). URL http://link.aps.org/abstract/PRL/v98/e077602.

24. Dutta, P. & Horn, P. M. Low-frequency fluctuations in solids: $1/f$ noise. *Rev. Mod. Phys.* **53**, 497–516 (1981).

25. Atature, M. *et al.* Quantum-Dot Spin-State Preparation with Near-Unity Fidelity. *Science* **312**, 551–553 (2006). URL http://www.sciencemag.org/cgi/content/abstract/312/5773/551. http://www.sciencemag.org/cgi/reprint/312/5773/551.pdf.

26. Tomita, A. & Chiao, R. Y. Observation of Berry's topological phase by use of an optical fiber. *Phys. Rev. Lett.* **57**, 937–940 (1986).

27. Gottesman, D. The heisenberg representation of quantum computers. Proceedings of the XXII International Colloquium on Group Theoretical Methods in Physics (International Press, Cabrdige, MA, 1999).

28. Eberly, J. Area theorem rederived. *Opt. Express* **2**, 173–176 (1998). URL http://www.opticsexpress.org/abstract.cfm?URI=oe-2-5-173.

29. Wang, B. & Duan, L.-M. Implementation scheme of controlled swap gates for quantum fingerprinting and photonic quantum computation. *Physical Review A (Atomic, Molecular, and Optical Physics)* **75**, 050304 (2007). URL http://link.aps.org/abstract/PRA/v75/e050304.

30. Aharonov, Y., Davidovich, L. & Zagury, N. Quantum random walks. *Phys. Rev. A* **48**, 1687–1690 (1993).

Competing Interests The authors declare that they have no competing financial interests.

Correspondence Correspondence and requests for materials should be addressed to L.J.S. (email: lsham@ucsd.edu).

Figure Legends

Figure 1: Precision rotation through feedback of locally-variant basis to produce cross-section of quantum Fourier transform

a. To add a classical angle, α, to a quantum angle, θ, one can twice swap two quantum dots whose energy splitting asymmetries (e.g. magnetization axes) may be at very precise relative angles, illustrated by dotted lines on the Bloch spheres and vectors for two unentangled qubits. The first swap respects a common spatial basis, for example the optical z-axis, while the second swap respects the local energy bases of each respective quantum dot. The control qubit, in the α-aligned basis, is assumed to be precisely initialized to its local ground state, as denoted by its initial Bloch vector. The system qubit is oriented at some arbitrary, unknown angle, θ. We have defined this "double-swap operation" with diamonds in place of direct product symbols. The text "+" and "-" in the diamonds are only a diagrammatic tool, if we were to reverse the operation, do an local swap followed by a global-basis swap, the "+" and "-" would flip positions in the application of α. **b.** This panel depicts the cross-section of operations performed on each qubit in a quantum Fourier transform using only Clifford operations and locally-variant bases. The four top qubits depict four of the seven required control qubits for approximate quantum Fourier transform and are oriented at the binary fractions of: $\pi/4$, $\pi/8$, $\pi/16$, and $\pi/32$, to encode the operation required. The bottom dots represent the controlled operations from other neighboring qubits not pictured in this cross-section conditioning the swap operations described in Figure 1(a).

Figure 2: Quantum walk on Bloch Spheres

An exponential number of rotation operations are performed in the full Hilbert space of three qubits using three operations but can be scaled arbitrarily. The output of the quantum circuit is a traversal of four rotations on four topologically disconnected Bloch spheres that have been drawn overlaid to illustrate the quantum walk from the original angle θ to $|\theta - \alpha - \beta\rangle$, $|\theta - \alpha + \beta\rangle$, $|\theta + \alpha - \beta\rangle$, and $|\theta + \alpha + \beta\rangle$ in parallel.

Figure 3: Differential Amplitude Amplification of an Operation

This circuit adds the angle $\alpha + \beta$ to the differential qubit $(|-\theta\rangle, |\theta\rangle)$ input to the system by using only Clifford operations and produces the differential output $(|-(\theta + \alpha + \beta)\rangle, |\theta + \alpha + \beta\rangle)$. Four control qubits are initialized to $|0\rangle$ within their local basis. Operations that are represented in the global basis, $\mathcal{Z}$, are shaded darkly (brown), while operations that use the local energy basis, $\mathcal{E}$, are shaded lightly (green). The control qubits may be measured to be zero with probability greater than 0.9999 (see Supplementary Figure 4(c)). The details of the circuit are discussed in Supplementary Notes A.

Global/z
swap

Local/E
swap

$|\theta\rangle^z$ $\quad\quad$ $|\theta-\alpha\rangle^z$

$|0\rangle^\alpha$ $\quad\quad$ $|\alpha\rangle^\alpha$
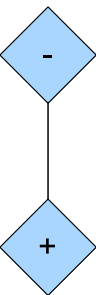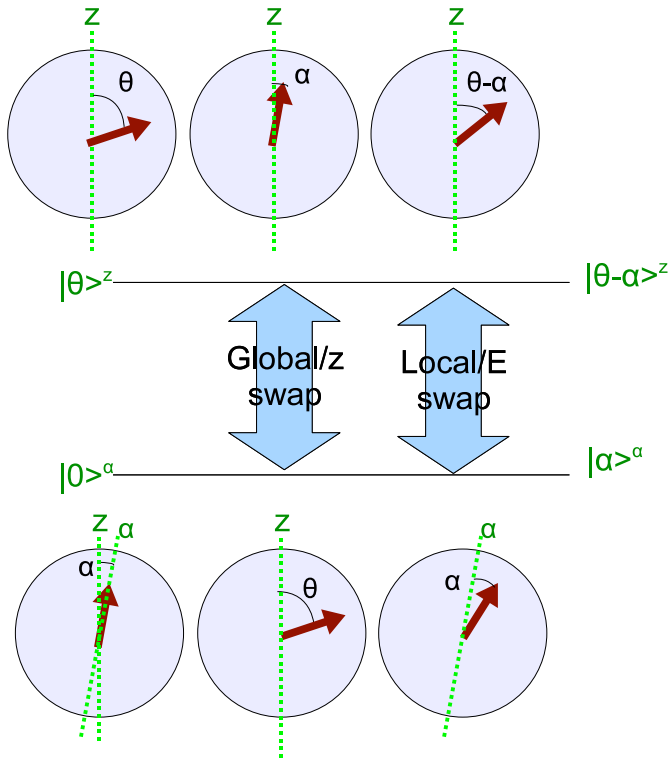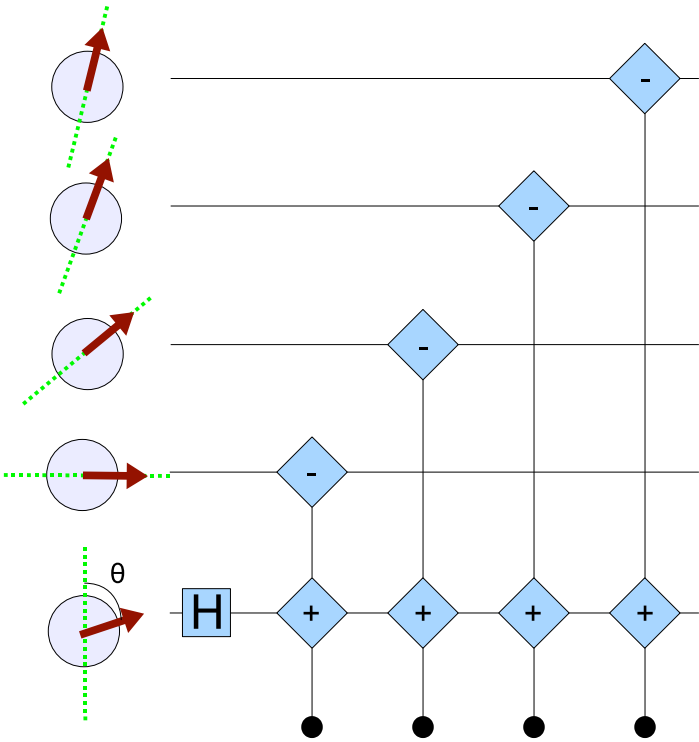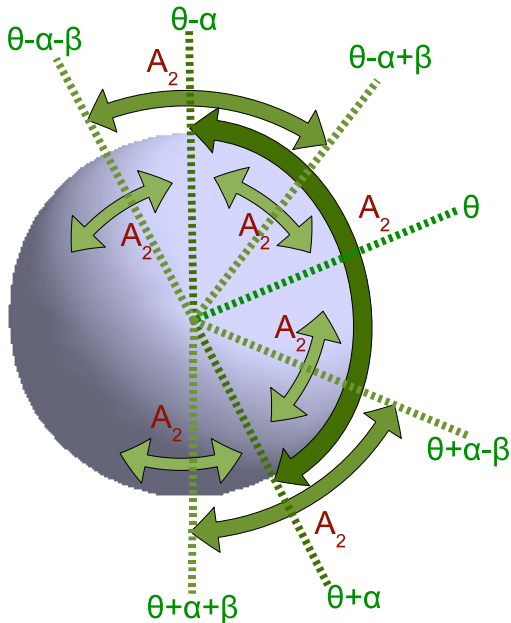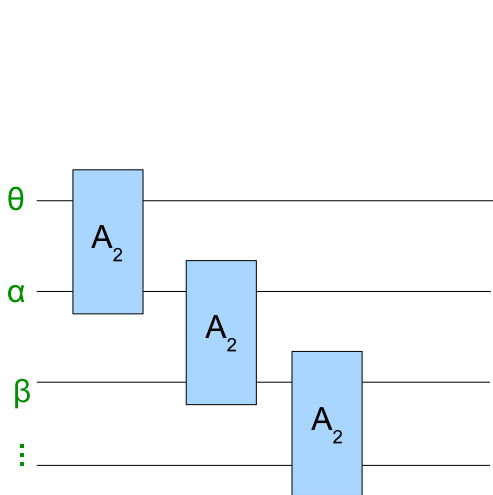
Legend:
- Operations in global basis
- Operations in local basis
- *ground state in local basis

Input labels (left to right, top to bottom): $-\theta$, $0_\alpha*$, $0_\beta*$, θ, 0, 0

Angle annotations: $-\theta$, α, β, θ

Output labels: $-(\theta+\alpha+\beta)$, $\theta+\alpha+\beta$

Stage labels (bottom): Seed Table — Quantum Walk — Angle Selection — Reverse Walk — Reflection about θ — Quantum Walk — Projective correction
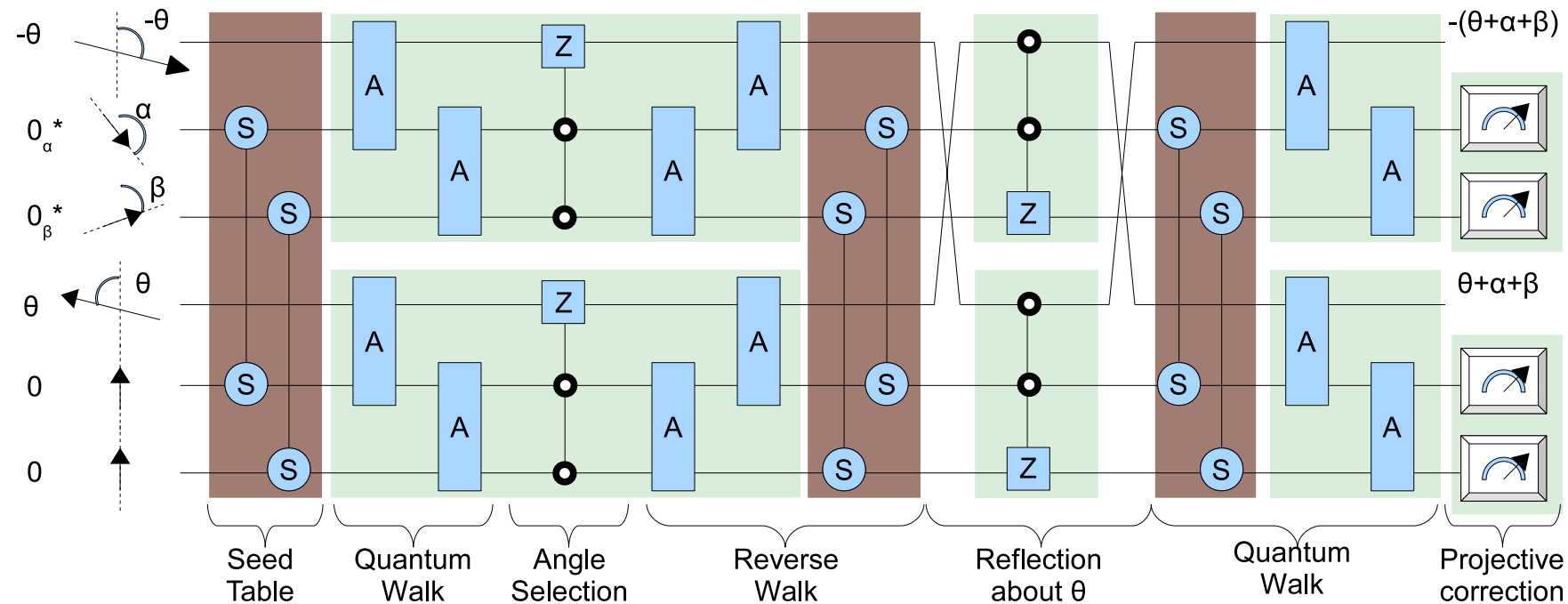
Supplementary Information

P. Dalal[1], S. K. Saikin[2], and L. J. Sham[1]

[1]Department of Physics, University of California San Diego, La Jolla, California 92093, USA
[2]Department of Chemistry and Chemical Biology, Harvard University, Cambridge, MA 02138, USA

Contents

Supplementary Figures and Legends

(a) Engineering a local-basis interaction

(b) Energy level transition structure for a single self-assembled QD trapping an electron and a control field

Supplementary Figure 1 – Example of local-basis interaction

a. The design of a local-basis interaction which produces a quantum swap operation. The electrons localized in two quantum dots (QDs) form a two-qubit system. The differing, but co-planar, magnetic polarizations of two nano-magnets define the local bases, *#1 (solid lines)* and *#2 (dotted lines)*, of the operation. To perform the operation, locally-polarized laser beams excite locally-oriented quantum cavities that contain the quantum dots. The subsequent quantum evolution of the system creates a procession of the lasers' number states with the spin-state of the quantum dots. The two cavities can be coupled by optical fiber, as shown, to macroscopically twist the two local-bases into polarization equivalence. For example, this operation will be stationary, aside from a non-local phase, when the two qubits are both "spin-up" (or any identical quantum state) in their local basis. Additionally, an exchange interaction between the two electrons (see for example [1]) allow these same qubits to interact conventionally, i,e. global-basis interaction. **b.** Transitions relevant to the local-basis interaction for each local quantum dot-field system are sketched. In a local magnetic field the electron spin states and the trion spin states are split by the Zeeman energy ω_e and ω_h respectively. The trion sub-levels are separated from the single electron sub-levels by the exciton energy ω_T. The allowed optical transitions for the two orthogonal polarizations, **H** and **V**, in each local basis are shown by arrows. The cavities modes are designed to resonate only with the $|-\rangle \leftrightarrow |T-\rangle$ transition. The qubit is encoded in the spin states of an electron, $|+\rangle$ and $|-\rangle$, while the negative trion states, $|T+\rangle$ and $|T-\rangle$, are utilized as mediating axillary states.
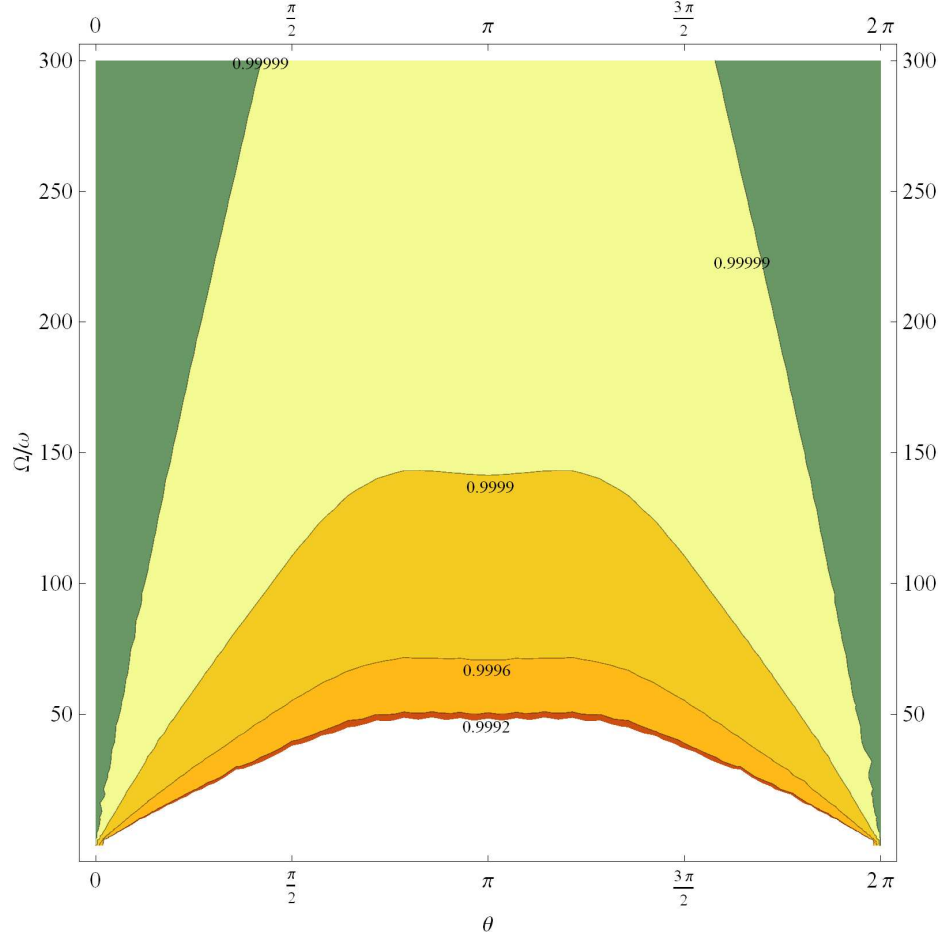
(a) Contour plot of Fidelity for swap in $\mathcal{Z}$ basis with local Larmor precession
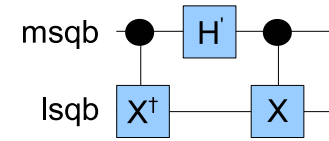
(b) Clifford Decomposition of $A_2^{\mathcal{Z}}$

Supplementary Figure 2 – Properties of Clifford operation in local basis

a. The decreased Fidelity of a swap operation between qubits of locally-variant basis is plotted. The horizontal axis sets the angle between the local bases, while the vertical axis sets the ratio of Larmor precession period to the operational pulse time. As shown, at pulse speeds 150 times faster than the Larmor precession, the Fidelity is kept above 0.9999. Moreover, for the small angles used in precision rotation, a ratio of 50 is more than sufficient.
b. This figure shows that the fundamental quantum operation in the quantum walk on a Bloch sphere, $A_2^{\mathcal{Z}} = (P_0 \otimes I + P_1 \otimes X)^\dagger (H' \otimes I) (P_0 \otimes I + P_1 \otimes X)$, is a Clifford operation. In the diagram $msqb$ and $lsqb$ refers to the most and least significant qubit respectively. P_1 and P_0 are projectors onto the logical zero and logical one subspaces respectively. The operation H' is the alternate Hadamard transform, $H' = 1/\sqrt{2} (|0\rangle \langle 0| - |1\rangle \langle 0| + |0\rangle \langle 1| + |1\rangle \langle 1|)$, and the operation X is the π-gate, $X = |1\rangle \langle 0| - |0\rangle \langle 1|$. All decomposed operations have been represented in the $\mathcal{Z}$-basis.

3
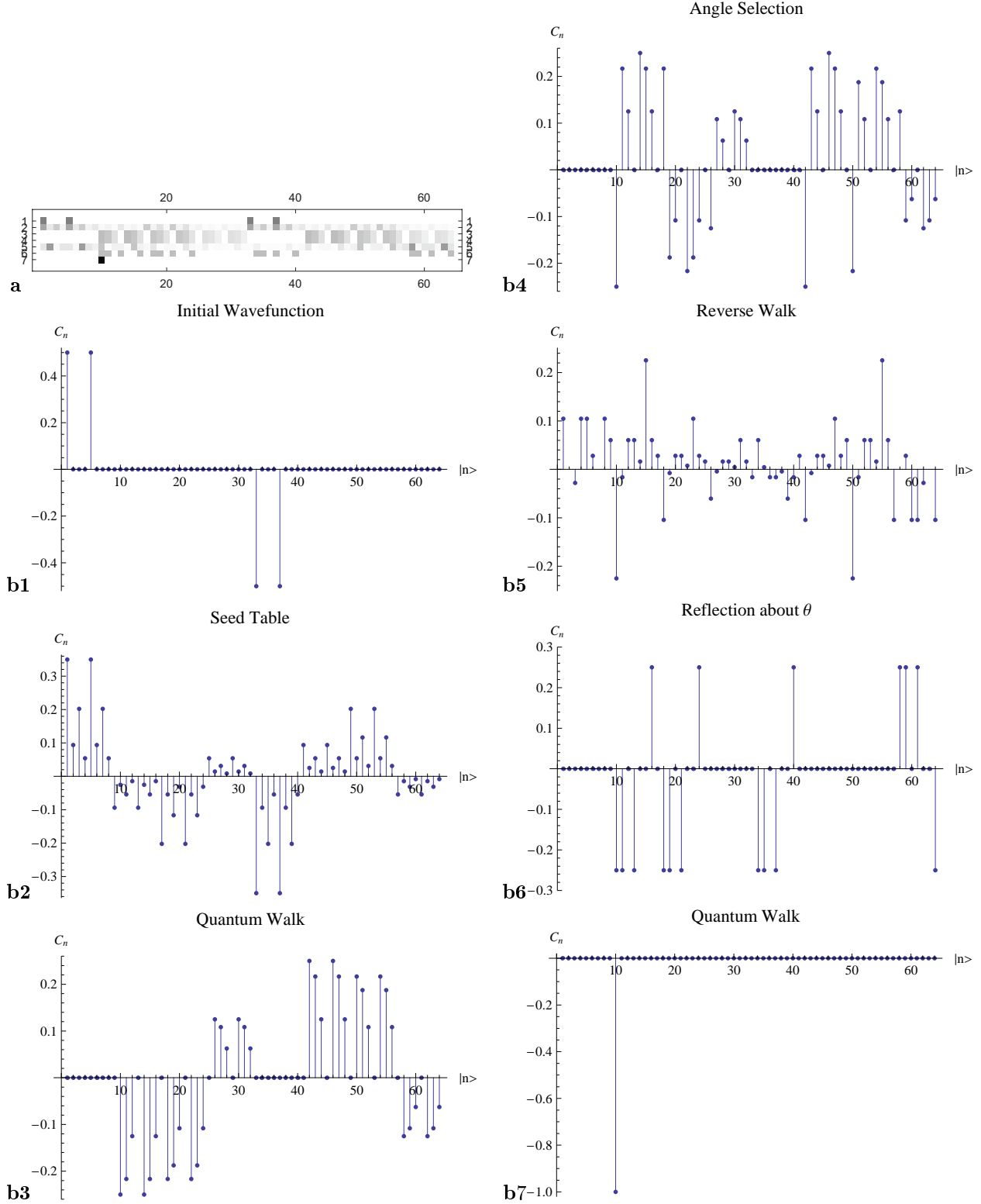
Supplementary Figure 3 − Simulation of circuit in for $\theta = \frac{\pi}{2}$

To help understand the quantum circuit in Figure 3 of the main text, the amplitudes of each eigenvector in the local basis are plotted after each labeled step. For simplicity we chose $\theta = \pi/2$, $\alpha = \pi/3$, and $\beta = \pi/6$, though similar dynamics occur for any angle. The composite circuit applies a $\pi/2$ rotation. **a.** A plot of amplitude intensity (phase is ignored) for each of 64 eigenvectors of the total system before and after each of six major steps. The actual amplitudes (phase is ignored) are plotted in **b1-b7**. The initial amplitude is $|\pi/2, 0, 0, -\pi/2, 0, 0\rangle$ and the final amplitude is $|\pi, 0, 0, -\pi, 0, 0\rangle = -|1, 0, 0, 1, 0, 0\rangle$
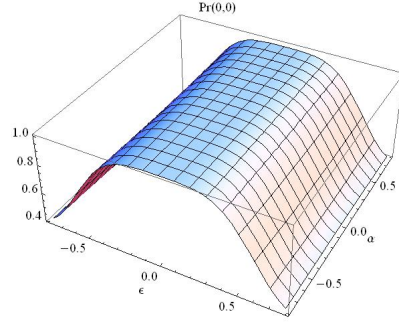
(a) Probability of measuring control bits correctly (error in *Swap*)
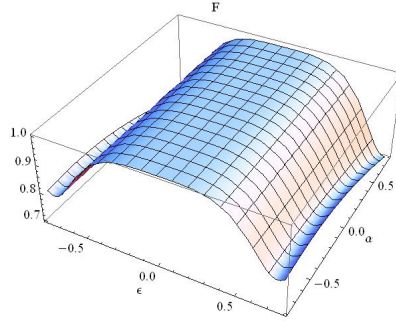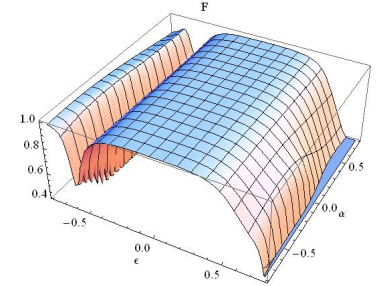
(b) Fidelity of circuit (error in *Swap*)
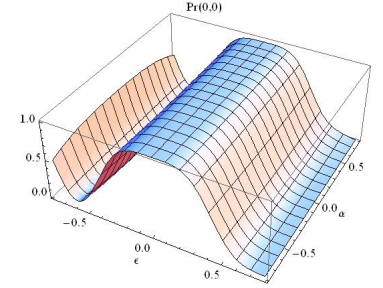
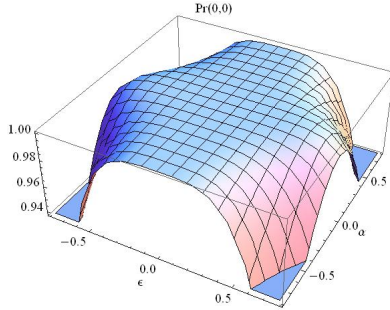(c) Probability of measuring control bits correctly (error in all operations)
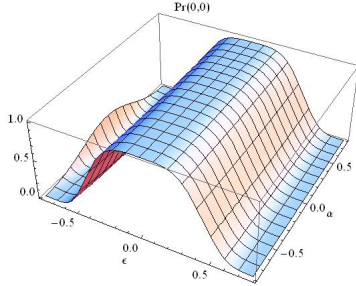
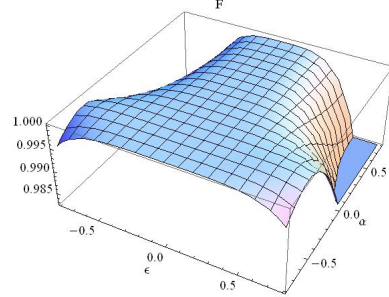(d) Probability of measuring control bits correctly (error in A_2)
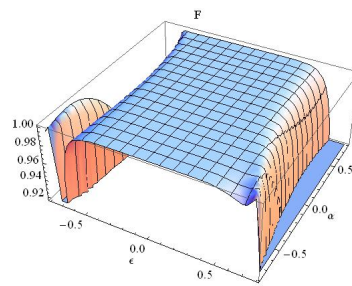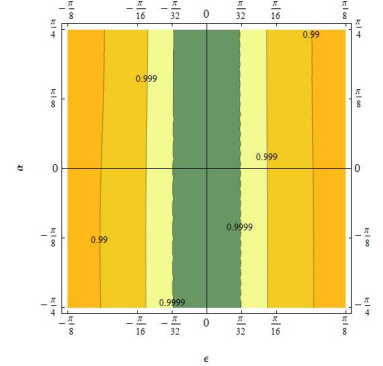
(e) Fidelity of circuit (error in A_2)

(f) Fidelity of circuit (error in all operations)

(g) Probability of measuring control bits correctly (error in *Angle Selection* and *Reflection about θ*)
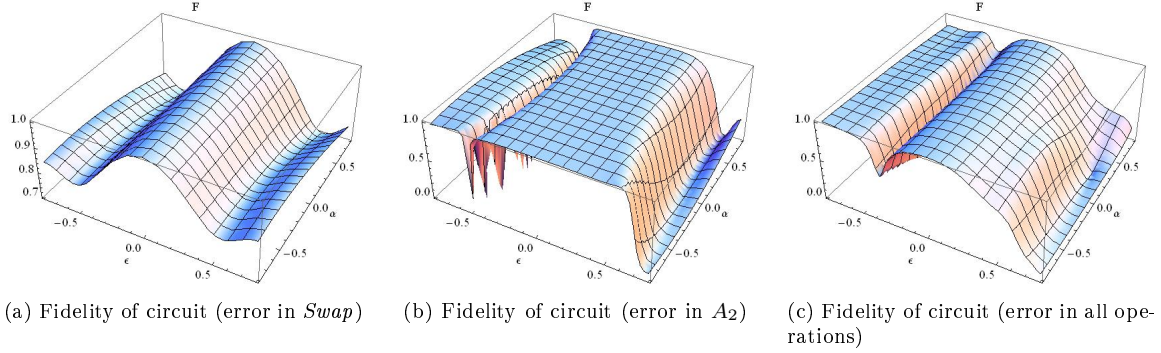
(h) Fidelity of circuit (error in *Angle Selection* and *Reflection about θ*)

(i) Fidelity of circuit (error in all operations)

Supplementary Figure 4 – Simulating Unitary Error

A pair of plots are given for four different classes of error when the control qubits are swept as $\alpha = [-\pi/4, \pi/4]$ and $\beta = \alpha/2$. The vertical axes in one set of plots is given by the probability that one will successfully measure a zero in the control qubits, $Pr(0,0)$ at the end of the quantum circuit. The vertical axes in the other plots the Fidelity that the circuit performed the correction rotation, F, given that the above successful measurement occurs. The horizontal axes specify the domain of α and a unitary error (under-over-rotation angle), ϵ. The initial differential state is set arbitrarily to $|\pi/8\rangle |-\pi/8\rangle$. All operations here are Clifford and are assumed to be equipped with traditional Quantum Fault Tolerance as explained in Supplementary Notes B. The accuracy of the total circuit is plotted when unitary error is present in all the operations of swap (**a**, **b**), A_2 (**d**, **e**), *Angle Selection and Reflection about θ* (**g**, **h**), and finally in aggregate (**c**, **f**). Asymmetries arise due to the non-locality of the A_2 operation (**d**, **e**) versus the locality of the desired rotation. This non-commutation gives rise to a preferred direction of angular error. The final contour plot (**i**) shows that unitary error of $\pm\pi/32$ in all operations will still produce a Fidelity of 0.9999.

(a) Fidelity of circuit (error in *Swap*) (b) Fidelity of circuit (error in A_2) (c) Fidelity of circuit (error in all operations)

Supplementary Figure 5 – Fidelity without applying quantum fault tolerance to operations

In these figures no traditional fault tolerance is applied to any of the Clifford operation composing the circuit. The vertical axes plot the Fidelity that the circuit performed the correction rotation, F, given that successful measurement of the control qubits occurs. The horizontal axes specify the domain of α and a unitary error (under-over-rotation angle), ϵ. The initial differential state is set arbitrarily to $|\pi/8\rangle|-\pi/8\rangle$. The Fidelity of the total circuit is plotted when unitary error is present in all the operations of swap (**a**), A_2 (**b**), and finally in aggregate for all operations (**c**). The unitary error in the swap circuit dominates the other errors when left unchecked (without traditional quantum fault tolerance).

Supplementary Discussion A :
Designing a local-basis interaction

Consider two qubits encoded in the spins of electrons localized in two self-assembled QDs. Spins in each dot can be controlled by external optical pulses [2] and information between between the dots is transferred through a photon wave packet [3, 4]. Below we recapitulate the results of [4] emphasizing the operational basis.

The local energy basis in each dot is determined by the direction of a local magnetic field, for example, from a nanomagnet. The corresponding qubit states are $|+\rangle^{\mathcal{E}}$ and $|-\rangle^{\mathcal{E}}$. Additionally negative trion states, $|T+\rangle^{\mathcal{E}}$ and $|T-\rangle^{\mathcal{E}}$, formed by an electron singlet and a heavy hole, can be coupled to the qubit states by optical excitations to engineer the operation. This coupling is accomplished using specific optical polarizations [5]. We assume the QDs to be in the Voigt geometry (the local magnetic field is orthogonal to the optical axis). The energy level and excitation selection diagram of a single dot and control field are given in Supplementary Figure 1(b). The directions of two orthogonal polarizations **H** and **V**, in general, are determined by the orientation of the local magnetic field.

The two dots connected by an optical fiber are considered in a planar geometry, see Supplementary Figure 1(a). The local bases are defined by the common optical axis (Z-axis) and the local polarizations, **H** and **V**, given the local, macroscopic anisotropies of the microcavities and the nanomagnets. Embedding each dot in into a 2D microcavity enhances the coupling between the dots and the fiber and sets additional constraints on the polarization of photons transmitted through the fiber. The microcavities support **V**- and **Z**-polarized photons only. However, due to large heavy-light hole splitting in the QDs only**V**-polarized photons may be strongly coupled to the heavy hole trions.

The quantum swap operation may be presented as follows. In a single dot, an external **H**-polarized optical pulse excites the $|+\rangle \leftrightarrow |T-\rangle$ and the $|-\rangle \leftrightarrow |T+\rangle$ transitions. However, only the $|T-\rangle$ state is strongly coupled to the **V**-polarized photon in a cavity. Prior work [4] shows that an optical pulse of the excitation frequency, of a rather general shape, will swap the qubit state and a cavity photon as

$$(\alpha|+\rangle + \beta|-\rangle)\,|0_{\mathbf{V}}\rangle \longrightarrow |-\rangle\,(\alpha|1_{\mathbf{V}}\rangle + \beta|0_{\mathbf{V}}\rangle)\,. \tag{1}$$

This operation is designed to swap a qubit state, defined in a local basis, with a photon number state. And, a similar gate may be applied to swap a photon number state with the local qubit state of another dot. In particular, a half-area pulse results in a qubit-photon Bell state. The cavity-fiber coupling is designed to be of a linear form (does not change any photon polarization). However, the optical fiber macroscopically rotates the polarization of transient photons from one local basis to another. In general, a photon propagating through a twisted fiber obtains a Berry phase [6, 7]. Because the rotation angle is proportional to the macroscopic integrated helicity-fiber direction product, the fiber connection can be designed to rotate the photon polarization precisely from one local basis to another. Any imprecision in polarization that results from the fiber will be a static, systematic error. This can be corrected completely using traditional techniques, e.g. [8]. Thus, the conclusions of [4] about robustness and high Fidelity of the gate are applicable to the local basis swap operation in the local basis.

Local interactions can be significant when considering noise in quantum operations. A quantum operation using coherent feedback upon a qubit is defined by both an operating field plus the state of at least one other qubit, the control qubit [9]. However, when coding the quantum operation against noise, there is a distinction between feedback from their quantum bases rather than their wavefunctions. Because the ground-state of a qubit is local and macroscopically precise it can encode an operation more precisely than a quantum dynamical variable. In this respect the ground state of a quantum system plus states generated from fault-tolerant Clifford operation may be used for better source coding of algorithmic information. The main text of the paper shows that precise local-basis interactions (Clifford quantum field plus feedback from qubits in ground state of locally-variant bases) combined with precise global-interactions (Clifford quantum field plus feedback from variant qubits within a common basis) lead an operational set that covers the core quantum algorithms.

Supplementary Discussion B :
Operations between qubits with non-commutative precession

We calculate the Fidelity of a swap operation between qubits with locally-variant bases but which evolve under a common control field. In particular, we calculate the operation when each qubit is initialized to its local ground state. Because the Larmor precession of one of the two-level systems does not commute with the other, only a subset of quantum operational dynamics between the two level systems will have high Fidelity. Intuitively, if the desired operations are fast enough then the precession should have little effect. The following simulation answers the two questions : (1) how fast does the operation need to be with respect to the rate of Larmor precession and (2) how does that speed depend on the azimuthal angle between the two local bases. For the quantum swap operation, we calculate greater than 0.9999 Fidelity for pulse speeds 150 times faster than the Larmor precession for any angle.

If we begin with two qubits each within their own local two-level basis, we must start with a generalized Hamiltonian

$$H = \mu \mathbf{S}^1 \cdot \mathbf{B}^1 + \mu \mathbf{S}^2 \cdot \mathbf{B}^2 + \frac{i\Omega}{2} \left(|\uparrow, \downarrow\rangle \langle \downarrow, \uparrow|^{\mathcal{Z}} + |\downarrow, \uparrow\rangle \langle \uparrow, \downarrow|^{\mathcal{Z}} \right),$$ (2)

where the control field (to swap the two qubits) references a common $\hat{z}$ spatial direction. In this common basis, $\mathcal{Z}$ (not the local bases), the generator of the above swap interaction appears without any local angle and is given by

$$G = \begin{bmatrix} 0 & 0 & 0 & 0 \\ 0 & 0 & -i & 0 \\ 0 & i & 0 & 0 \\ 0 & 0 & 0 & 0 \end{bmatrix}.$$ (3)

Without loss of generality, we orient the first qubit to have magnetic field oriented in the $+\hat{z}$ direction, the second qubit's field is oriented at an angle θ to that direction, to produce the Hamiltonian

$$H = \mu S_z^1 B + \mu S_z^2 B \cos\theta + \mu S_y^2 B \sin\theta + \frac{\Omega}{2} G.$$ (4)

Going into the co-rotating frame $\psi' = e^{-iS_\theta^2 \omega t} e^{-iS_z^1 \omega t} \psi$, we examine the effect of the local basis on the swap operation

$$\partial_t \psi' = i\frac{\Omega}{2} \left(e^{-i\omega S_z^1 t} e^{-i\omega S_\theta^2 t} [G] e^{i\omega S_\theta^2 t} e^{i\omega S_z^1 t} \right) \psi'.$$ (5)

The equations of motion are then given by $\partial_t \psi' = i\frac{\Omega}{2} Q G Q^\dagger \psi'$. We numerically solve this differential equation and plot the Fidelity, $F = \left| \left\langle e^{-iG\pi/2} \left| e^{-iQGQ^\dagger \pi/2} \right\rangle \right|$, in Supplementary Figure 2(a). If the pulse speed is 300 times faster than the Larmor precession frequency (as in trion-trion operations) the rotation angle is irrelevant. If the rotation angle is very small, then operational speed need not be much faster than the Larmor precession.

Supplementary Discussion C :
Fault-Tolerance of scattering amplitudes

The operation, $A_2^{\mathcal{Z}}$, is based on the $\pi/4$ rotation of the Pauli-Y operator in both the local and non-local basis. By their definition, the Clifford operators include the Hadamard and controlled-not gates. We show the operation $A_2^{\mathcal{Z}}$ is decomposed into these operators in Supplementary Figure 2(b) and hence it is a Clifford operation that can be

easily made fault-tolerant. For example, the seven-qubit Calderbank-Shor-Steane (CSS) code [10, 11, 12] can fault-tolerantly implement any Clifford gate tranversally. Given a particular noise structure and/or scaling requirements more economized codes like [13] are available as well.

When performed pairwise on a consecutive set of m qubits, the scattering operation, A_2, generates all $M = 2^m$ permutations of adding and subtracting the angles $\{\theta_i | i \in (1 \ldots m-1)\}$ to the first angle θ_0. Or more formally, if we represent the Hilbert space vectors with the binary label $j = j_{m-1} \ldots j_1 j_0$ as commonly represented in the Quantum Fourier Transform, we can write the operation as

$$A_m^{\mathcal{Z}} \prod_{i=0}^{m-1} |\theta_i\rangle^{\mathcal{Z}} \quad = \quad \sum_{j_1, j_2, \ldots, j_{m-1}=0}^{1} \cos \frac{\xi_j + \theta_0}{2} |f(j)\rangle^{\mathcal{Z}} + \sin \frac{\xi_j + \theta_0}{2} |g(j)\rangle^{\mathcal{Z}} \qquad (6)$$

where $\xi_j = (-1)^{j_n} \theta_m + \ldots + (-1)^{j_1} \theta_1$ and the functions f and g map integers to two particular Grey Codes. When done fault-tolerantly, the amplitudes for every pair of eigenstates($|f(j)\rangle, |g(j)\rangle$) can be parametrized by a point on a Bloch sphere. Therefore, the resulting wavefunction is an exponential traversal of rotations on $M/2$ topologically disconnected Bloch spheres.

Supplementary Notes A :
Differential amplitude amplification of an operation

To explain the mechanics of the Differential Amplitude Amplification circuit as shown in Figure 3 of the main text, we make use of the example case : $\theta = \pi/2$, $\alpha = \pi/3$, and $\beta = \pi/6$. In this example, the initial unknown, differential qubit occupies the state $\left|\frac{\pi}{2}\right\rangle \left|-\frac{\pi}{2}\right\rangle$, and the control bits are initialized to their local ground states, $\left|\frac{\pi}{3}\right\rangle$ and $\left|\frac{\pi}{6}\right\rangle$. The goal of the circuit is to rotate the initial system state, $|\theta\rangle$, using the control qubits to amplify the operation, $R\left(\frac{\pi}{3} + \frac{\pi}{6}\right) \left|\frac{\pi}{2}\right\rangle \left|-\frac{\pi}{2}\right\rangle$, so producing the end state $|\pi\rangle |-\pi\rangle$. The circuit's progression towards this goal is shown in Supplementary Figure 3 using the absolute amplitudes for each of the 64 eigenvectors in the $\mathcal{Z}$-basis comprising the six-qubit quantum system. The first step is to generate a differential set of angles labeled "Seeding the table". In one differential track all the qubits share a common local and global basis, while in the other each of the control qubits have a different orientation angle. As in Figure 1(a) of the main text, if θ equals zero, a swap in the global $\mathcal{Z}$ basis produces the differential signal for $|\alpha\rangle_E$. Hence, swapping each differential pair of control qubits creates a differential set of angles in the local bases of the control qubits. For the example case, this transforms the amplitudes of the initial state in Supplementary Figure 3(b1) to the amplitudes given in Supplementary Figure 3(b2). Next, the scattering operation, A_{m+1} is applied in the local energy bases, $\mathcal{E}$, to all the qubits in each differential track (the initial unknown wavefunction and its neighboring control qubits), as shown in Supplementary Figure 3(b3) for the example. In this fashion, we generate a repository of 2^m angles with the ground state of m locally-variant qubits. Next, the "angle selection" step derives from the oracle-call prescription used in the Grover algorithm [14], but in this case the sub-circuit flips the phase of the classically-known, desired operation. Although one angle, $\theta + \alpha + \beta$, is selected in this example by a controlled-controlled-Z operation as in Supplementary Figure 3(b4), to produce high operational complexity a coherent superposition of selections could create a coherent superposition of rotation operations. As necessary in amplitude amplification, the selection process is followed by the Hermitian conjugate of the quantum walk and seeding operations [15]. This is labeled a "reverse walk" since it inverts the initial superposition step, shown for the example in Supplementary Figure 3(b5). All of the above operations take place in the energy basis, and only the seeding operations and their Hermitian conjugates need take place in the global basis. In the next step, the differential nature of the algorithm is exploited to replace the traditional Grover call. The operation identified as angle selection in Figure 3 of the main text is a means to reflect about an unknown differential state. This is done by relabeling the differential signal qubits to reverse their polarity, flipping the phase of the appropriate eigenvectors in each track, followed by the restoration of signal polarity. This is shown diagrammatically with a reordering of the qubit lines so that all operations stay exactly parallel in the tracks. This construction allows a reflection of the wave-function about the dynamic angle $|\theta\rangle \langle \theta|$ (instead of a reflection about the static $|0\rangle \langle 0|$ as in the Grover search algorithm), shown for the example in Supplementary Figure 3(b6). Although in this example a controlled-controlled-Z operation amplifies the currently desired angle, in general the Grey code used in the quantum-walk on a Bloch sphere and the specific desired angle determine the functionally correct sub-circuit to use. As with the traditional amplification algorithm, one repeats all the previous steps until they have fully amplified the desired operation. In this case, since there are only two oracle-identified answers in each track from a possible eight eigenvectors, it takes only one set of reflections to completely shift all the amplitude of the wavefunction to $\cos(\theta + \alpha + \beta)/2 |000\rangle + \sin(\theta + \alpha + \beta)/2 |001\rangle$ in the top track and $\cos(\theta + \alpha + \beta)/2 |000\rangle - \sin(\theta + \alpha + \beta)/2 |001\rangle$ in the bottom track. So one final "quantum walk"

fully amplifies the desired rotation angle, shown for the example in Supplementary Figure 3(b7). Note that any stray phase-flips created by fermionic loops in the quantum-walk operation get reversed in the reverse-quantum-walk and so that the phases used to control reflections in Amplitude Amplification are preserved and physically correct for fermionic qubits. Because all operations between the two tracks take place concurrently, the same operating field may be used for each track simultaneously. This allows for a natural rejection of certain common mode noise in the operational fields applied in the local basis. For example if the initial state of the differential qubit is given by

$$|\psi_i\rangle |-\psi_i\rangle = \left(\cos\left(\frac{\theta}{2}\right)|1\rangle + e^{i\phi}\sin\left(\frac{\theta}{2}\right)|0\rangle\right)\left(\cos\left(\frac{\theta}{2}\right)|1\rangle - e^{-i\phi}\sin\left(\frac{\theta}{2}\right)|0\rangle\right),$$

having arbitrary initial differential phase error, ϕ, common mode errors will accumulate differentially in the angle selection and reflection steps to make ϕ stochastic. However, if we compute the entropy of the ensuing density matrix, there is still a full qubit of information. Cross coupling two differential tracks provides enough information about a single qubit that it forms a decoherence-free subspace against a certain differential common mode error.

As with traditional amplitude-amplification algorithm, the number of reflections required grows linearly with the number of control bits. However in the case of quantum Fourier transform, all seven controlled rotations needed to reach the critical bound of $\pi/128$ may be done in one instantiation of the above algorithm with ten reflections, without the need for an oracle that is more complex. In general, one can create a repository of precise base angles in an extended Hilbert space and use them for quantum operations by amplifying the desired angles.

Supplementary Notes B :
Simulating unitary error

We calculate the improvement in arbitrary quantum rotation using differential amplitude amplification by applying simultaneous, unitary error to all qubit operations. We assume a quantum system where decoherence, phase error, and static inhomogeneity are negligible. Instead, we assume the interactions between the qubits and the control fields defy the assumptions of quantum fault tolerance when parity checks between small rotations are applied, due to a sizable standard deviation of the mean error. In other words, the interaction imprecision is too large and the number of qubits too small to approximate their mean error as zero when seeking a Fidelity greater than 0.9999. Because unitary error perpendicular to the interaction geodesic (phase-error) is shown to be negligible [16], only unitary error parallel to the interaction geodesic (under-over rotation) need be considered.

We simulate the effect of under and over rotation of control pulses of intended Area, A, by an errant amount, ϵ, by applying each operation, having generator, G, as $\exp\left[iG\left(A+\epsilon\right)\right]$. Clifford operations equipped with quantum fault tolerance can be applied using the improved operation, $\exp\left[iG\left(A+\epsilon^2\right)\right]$, instead. This is an upper-bounding approximation as $\sin^2\left(\epsilon\right) \leq \epsilon^2$. In Supplementary Figures 4(b,e,h), we plot the Fidelity for the circuit, when under and over rotation error is applied to each type of operation and then finally in simultaneous aggregate. These plots assume an application of quantum fault-tolerance to the Clifford operations that compose the circuit and that the control qubits were measured to be zero. The probability of this occurring is given by the adjacent plots in Supplementary Figures 4(a,d,g).

For reference a plot of the circuit's Fidelity when the constituent operations are applied without quantum fault tolerance is given in Supplementary Figure 5. The Supplementary Figures 5(a) and 5(b) show that the Fidelity of the circuit without quantum fault tolerance is much lower than a direct rotation. In this case, the total Fidelity drops to 0.9 even with minimal error applied to all operations as shown in 5(c).

Static shifts in the area of the control pulse produce deviations from the correct Bloch sphere after measurements are made of the control qubits. Measurement is not necessary, but serves two purposes. First, all the control qubits should be zero at the end of the operation, and if they are measured otherwise, it heralds an errant operation. Second, measuring zeros collapses residual error and prevents it from propagating further. Upon adding significant unitary error, ϵ, we see that probability of successful measurement of the control qubits (measuring zero) is still very high and should not deter scalability as shown in Figure 4(i). However, it is seen that simultaneous error impacts the probability of correct measurement due to the A_2 operation and impacts the Fidelity due to the swap operation, and they so limit the total error. The precision of the rotation circuit drops precipitously at approximately $\epsilon = \pm 0.5$ due to the normal limits of traditional quantum fault tolerance upon Clifford operations.

References

[1] Piermarocchi, C., Chen, P., Sham, L. J. & Steel, D. G. Optical RKKY interaction between charged semiconductor quantum dots. *Phys. Rev. Lett.* **89**, 167402 (2002).

[2] Emary, C. & Sham, L. J. Optically controlled single-qubit rotations in self-assembled inas quantum dots. *Journal of Physics : Condensed Matter* **19**, 056203 (10pp) (2007). URL http://stacks.iop.org/0953-8984/19/056203.

[3] Cirac, J. I., Zoller, P., Kimble, H. J. & Mabuchi, H. Quantum state transfer and entanglement distribution among distant nodes in a quantum network. *Phys. Rev. Lett.* **78**, 3221–3224 (1997).

[4] Yao, W., Liu, R.-B. & Sham, L. J. Theory of control of the spin-photon interface for quantum networks. *Physical Review Letters* **95**, 030504 (2005). URL http://link.aps.org/abstract/PRL/v95/e030504.

[5] Xu, X. *et al.* Fast spin state initialization in a singly charged InAs-GaAs quantum dot by optical cooling. *Physical Review Letters* **99**, 097401 (2007). URL http://link.aps.org/abstract/PRL/v99/e097401.

[6] Chiao, R. Y. & Wu, Y.-S. Manifestations of berry's topological phase for the photon. *Phys. Rev. Lett.* **57**, 933–936 (1986).

[7] Tomita, A. & Chiao, R. Y. Observation of Berry's topological phase by use of an optical fiber. *Phys. Rev. Lett.* **57**, 937–940 (1986).

[8] Hill, C. D. Robust controlled-not gates from almost any interaction. *Physical Review Letters* **98**, 180501 (2007). URL http://link.aps.org/abstract/PRL/v98/e180501.

[9] Lloyd, S. Coherent quantum feedback. *Phys. Rev. A* **62**, 022108 (2000).

[10] Calderbank, A. R. & Shor, P. W. Good quantum error-correcting codes exist. *Phys. Rev. A* **54**, 1098–1105 (1996).

[11] Steane, A. Multiple particle interference and quantum error correction. *PROC.ROY.SOC.LOND.A* **452**, 2551 (1996). URL http://www.citebase.org/abstract?id=oai:arXiv.org:quant-ph/9601029.

[12] Steane, A. M. Error correcting codes in quantum theory. *Phys. Rev. Lett.* **77**, 793–797 (1996).

[13] Salas, P. J. & Sanz, A. L. Effect of ancilla's structure on quantum error correction using the seven-qubit calderbank-shor-steane code. *Phys. Rev. A* **69**, 052322 (2004).

[14] Grover, L. K. A fast quantum mechanical algorithm for database search. In *STOC '96 : Proceedings of the twenty-eighth annual ACM symposium on Theory of computing*, 212–219 (ACM, New York, NY, USA, 1996).

[15] Brassard, G., Hoyer, P., Mosca, M. & Tapp, A. Quantum amplitude amplification and estimation. *Quantum Computation and Quantum Information : A Millennium Volume, AMS Contemporary Mathematics Series* **305** (2002). URL http://www.citebase.org/abstract?id=oai:arXiv.org:quant-ph/0005055.

[16] Morton, J. J. L. *et al.* Measuring errors in single-qubit rotations by pulsed electron paramagnetic resonance. *Physical Review A (Atomic, Molecular, and Optical Physics)* **71**, 012332 (2005). URL http://link.aps.org/abstract/PRA/v71/e012332.

Coherent population trapping of an electron spin in a single negatively charged quantum dot

XIAODONG XU[1], BO SUN[1], PAUL R. BERMAN[1], DUNCAN G. STEEL[1]*, ALLAN S. BRACKER[2],
DAN GAMMON[2] AND L. J. SHAM[3]

[1] The H. M. Randall Laboratory of Physics, The University of Michigan, Ann Arbor, Michigan 48109, USA
[2] The Naval Research Laboratory, Washington DC 20375, USA
[3] Department of Physics, The University of California-San Diego, La Jolla, California 92093, USA
*e-mail: dst@umich.edu

Coherent population trapping (CPT) refers to the steady-state trapping of population in a coherent superposition of two ground states that are coupled by coherent optical fields to an intermediate state in a three-level atomic system[1]. Recently, CPT has been observed in an ensemble of donor-bound spins in GaAs (ref. 2) and in single nitrogen-vacancy centres in diamond[3] by using a fluorescence technique. Here, we report the demonstration of CPT of an electron spin in a single quantum dot. The observation demonstrates both the CPT of an electron spin and the successful generation of Raman coherence between the two spin ground states of the electron[4–6]. This technique can be used to initialize, at about a gigahertz rate, an electron spin state in an arbitrary superposition by varying the ratio of the Rabi frequencies between the driving and probe fields. The results show the potential importance of charged quantum dots for a solid-state approach to the implementation of electromagnetically induced transparency[7,8], slow light[9], quantum information storage[10] and quantum repeaters[11,12].

A critical condition for realizing coherent population trapping (CPT) is to have a pair of stable ground states with a relatively long coherence time compared with the excited-state decay time. An electron spin trapped inside a single quantum dot is a system that meets this requirement and constitutes an excellent opportunity for the realization of CPT. The demonstration of CPT shows the existence of the dark state which is important for various physical phenomena, for example, CPT is the central physics of electromagnetically induced transparency[8], and the fast change of refractive index can lead to the effect of slow light[9], assuming an ensemble of identical charged quantum dots is available.

The electron spin inside a quantum dot has been proposed as a qubit for quantum computing owing to its long coherence time compared with fast optical operations[13]. An important step towards optically driven quantum computation in the quantum dot system is to generate electron spin coherence. The usual method of creating electron spin coherence in quantum dots is to use pulsed lasers[4–6]. Here, the demonstration of CPT by measurement of the absorption spectrum is evidence of the creation of electron spin coherence at a single quantum dot level by continuous-wave lasers.

Another critical element for quantum information science is the initial quantum state preparation[14]. Electron spin state initialization has recently been realized in a single quantum dot by optical spin cooling techniques with a high fidelity[15,16]. However, the limitation is that only two possible initial qubit states can be prepared, either spin up or spin down. CPT is a process that generates an arbitrary coherent superposition of electron spin ground states, the probability amplitudes of which can be controlled by varying the ratio of Rabi frequencies between the driving and probe optical fields. Therefore, we can prepare an arbitrary initial qubit state by using the CPT technique. In this scheme, the initialization rate is limited by the excited-state decay rate, which is of the order of $10^9\,\mathrm{s}^{-1}$ (ref. 15).

The sample under study contains self-assembled InAs quantum dots embedded in a Schottky diode structure, which gives us the ability to control the charging state of the quantum dot[15,17] (see the Supplementary Information). In the experiment, we set the voltage such that only one electron is trapped inside the quantum dot. At zero magnetic field, the energy level structure for the lowest-lying states of the negatively charged quantum dot can be modelled as shown in the upper left inset of Fig. 1. The electron spin ground states (trion states) are labelled as $|\pm(1/2)\rangle$ ($|\pm(3/2)\rangle$), where $|\pm(1/2)\rangle$ ($|\pm(3/2)\rangle$) denotes the electron (hole) spin states along the growth axis[15]. The only dipole-allowed transition is from the spin ground state $|(1/2)\rangle$ ($|-(1/2)\rangle$) to the trion state $|(3/2)\rangle$ ($|-(3/2)\rangle$) with σ^+ (σ^-) polarized light excitation. As the spin-flip Raman transitions are dipole forbidden, the trion system at zero magnetic field can be considered as a double two-level structure, not possible for the realization of CPT.

To create a three-level lambda system, we apply a magnetic field in the Voigt geometry (**X** axis), perpendicular to the sample growth direction (**Z** axis). As the electron and hole in-plane g factors are non-zero, which are 0.49 and 0.13 for this particular quantum dot, the applied field mixes the spin ground states as well as the trion states. The energy level diagram and the associated selection rules of the trion system are shown in the upper right inset of Fig. 1. The new electron spin eigenstates $|X\pm\rangle$ can be excited to either of the trion states $|T\pm\rangle$ with linearly polarized light[15]. Hence, the
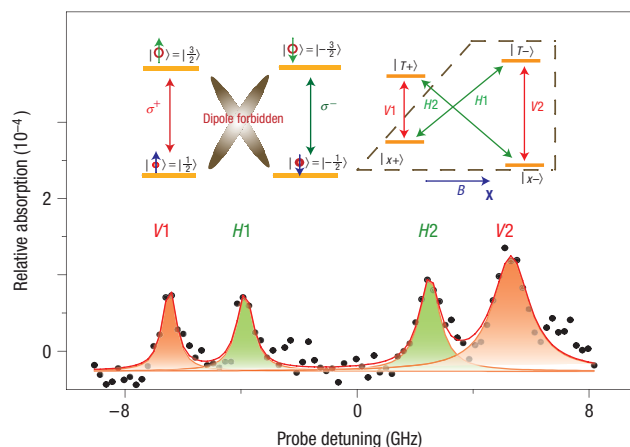
Figure 1 The trion model and its characterization. Inset: Trion energy level diagrams (upper left) without and (upper right) with magnetic field applied in the Voigt geometry. V (H) means the transition is vertically (horizontally) polarized. At zero magnetic field, the spin-flip Raman transitions are dipole forbidden. By applying a magnetic field in the Voigt geometry, the dark transitions become bright. A three-level lambda system is formed by these levels enclosed in the dashed line. The main figure shows the single-beam absorption spectrum of the trion state at a magnetic field of 1.32 T with 45° linearly polarized light excitation. A quartet transition pattern is observed as the gate voltage is set in the non-optical pumping region.

forbidden Raman transitions at zero magnetic field are turned on when the magnetic field is applied along the **X** axis. As shown in the upper right inset of Fig. 1, we choose $|X\pm\rangle$ and $|T-\rangle$ to form a three-level lambda system. As the transitions from one trion state to the spin ground states are orthogonally polarized, the spontaneously generated coherence that was observed in GaAs interface-fluctuation quantum dots[4] is absent here.

We first characterized the quantum dot with a single-beam voltage-modulation absorption experiment[15,18]. We set the gate voltage at the edge of the trion charge plateau, where the optical pumping of the electron spin effect is suppressed[15,16]. Figure 1 shows the quartet transition pattern of the trion state using 45° linearly polarized light excitation at a magnetic field of 1.32 T. The observation of the four transition lines confirms that all four trion transitions are turned on and have similar transition strengths[15]. The four transitions are labelled as $V1$, $H1$, $H2$ and $V2$.

We then set the gate voltage to where the co-tunnelling-induced spin-flip process is suppressed[19]. Figure 2a shows a single-beam absorption spectrum by scanning the laser across transition $H1$ at a magnetic field of 2.64 T. We observed an almost flat line for the probe absorption spectrum, reflecting the absence of the absorption due to optical pumping[15]. The optical-pumping-induced saturation of the absorption shows that the spin relaxation rate is much slower than the trion relaxation rate. Hence, the spin ground states can be considered as metastable states compared with the short-lived trion states.

To understand the experimental conditions for the measurements, we consider the interaction scheme shown in Fig. 3. A strong optical field (the driving field) is tuned on resonance with transition $V2$ and a weak optical field (the probe) is scanned across transition $H1$. When the probe laser is resonant with transition $H1$, the two-photon Raman resonance condition is reached. As seen in Fig. 2b, a clear dip in the probe absorption spectrum is observed for $\Omega_d/2\pi = 0.56$ GHz. This observation demonstrates
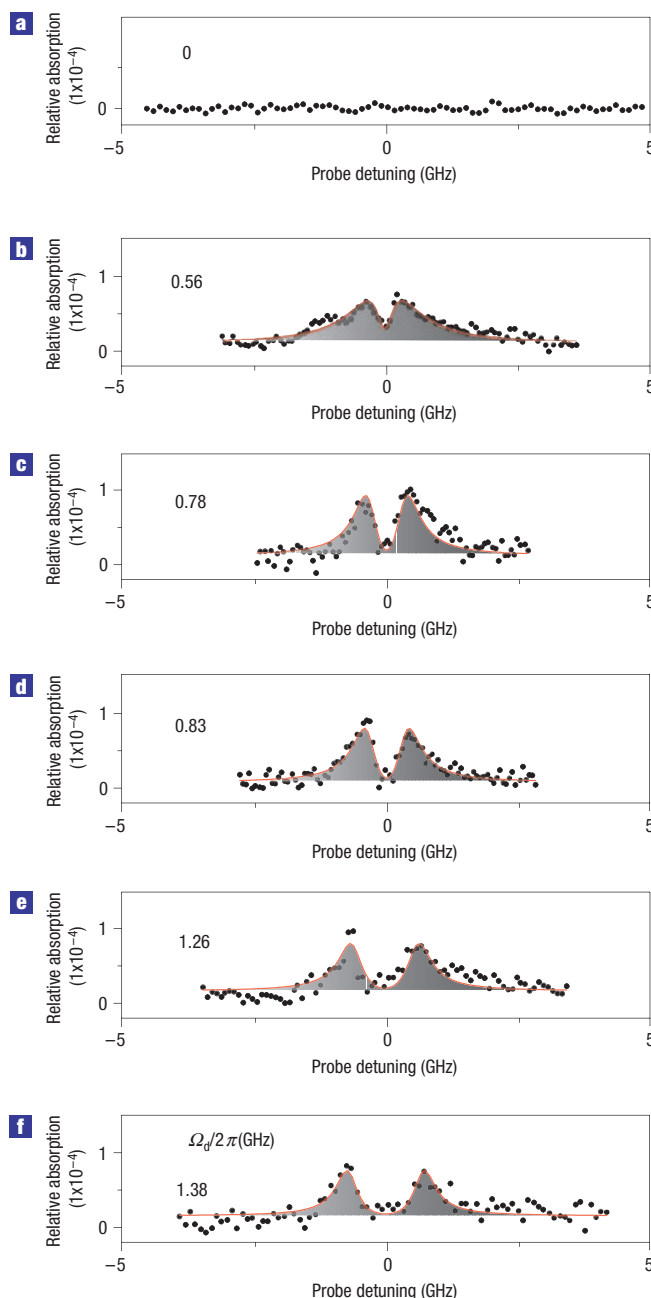

Figure 2 The experimental evidence of the CPT of an electron spin. The gate voltage is set in the optical pumping region and the applied magnetic field is 2.64 T. **a**, The probe absorption spectrum across transition $H1$ in the absence of the driving field. **b–f**, Probe absorption spectra with various driving-field Rabi frequencies. The driving field is set to be resonant with the transition from $|X-\rangle$ to $|T-\rangle$. The red solid lines are the theoretical fits by solving the optical Bloch equations. A pronounced dip is observed in the probe absorption due to generation of the dark state.

both the generation of the CPT of an electron spin and the Raman coherence between the spin ground states. For this particular set of data, the applied magnetic field is 2.64 T, corresponding to an electron Zeeman splitting of 75.4 µeV (18.2 GHz).

The system is described by the optical Bloch equations for the three-level lambda system shown in Fig. 3, where Γ_{ij} (γ_{ij}) is
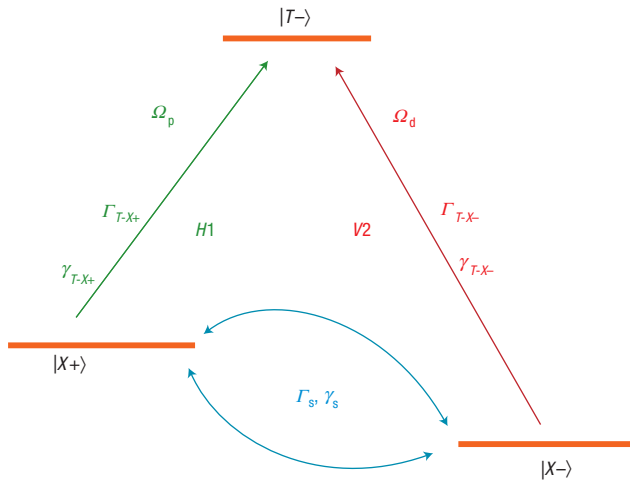
Figure 3 The interaction scheme of the generation of CPT. A three-level lambda system formed by spin ground states $|X\pm\rangle$ of an electron and an intermediate trion state $|T-\rangle$.

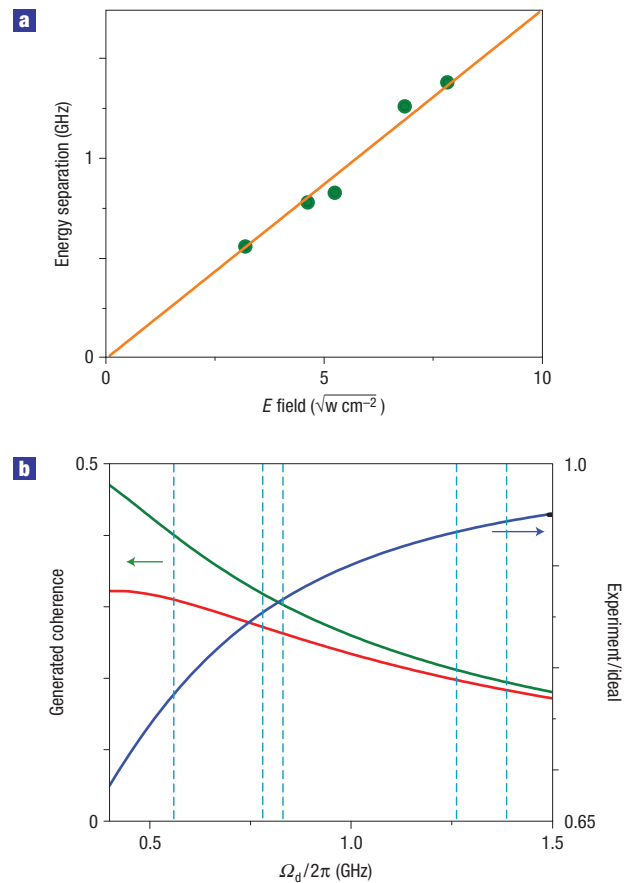**Figure 4 The analysis of the CPT effect. a**, The energy separation of the Autler–Townes doublets as a function of driving-field strength. **b**, Theoretical curves of the creation of the electron spin coherence in a single charged quantum dot. Red line: experimentally generated electron spin Raman coherence (ρ_{X+X-}) inferred from the optical Bloch equations calculation by using the experimental parameters. The calculation is done under the experimental condition that the driving and probe fields are resonant with transition $V2$ and $H1$, respectively. Green line: the calculated maximum electron spin Raman coherence in the absence of the electron spin dephasing. Blue line: the ratio of the calculated coherence with and without electron spin dephasing.

the trion population decay (dipole dephasing) rate, Γ_s (γ_s) is the electron spin relaxation (decoherence) rate, $\Omega_i = (\mu_i \times E_i/\hbar)$ is the Rabi frequency, μ_i is the transition dipole moment and E_i is the optical field strength. For simplicity, we assume $\Gamma_s, \gamma_s \ll \Gamma_{ij}, \gamma_{ij}, \Omega_i$.

The analytical result of the probe absorption spectrum is generally complicated. However, a relatively simple form can be obtained when the driving and probe beams are both on resonance. After simplification, the absorption of the probe beam can be written as

$$\alpha = \alpha_o \frac{\left(\gamma_s - \Gamma_s + \lambda^2 \Gamma_s\right)}{(1+\lambda^2)^2} \frac{\gamma_{T-X+}}{\Omega_d^2},$$

where $\lambda = (\Omega_p/\Omega_d)$ and α_o is a constant. To understand the physics of the dip, we can take $\lambda = 1$, the absorption expression is simplified to $\alpha = (\alpha_o \gamma_{T-X+}/4)(\gamma_s/\Omega_d^2)$. Therefore, the height of the dip is linearly proportional to the spin decoherence rate. If $\gamma_s = 0$ ($\gamma_s \ll \Omega_d$), the probe absorption vanishes (almost vanishes), that is, the transition becomes transparent to the incident light owing to the destructive interference of the coupled transitions driven by the coherent optical fields.

The observation of CPT can also be understood from the point of view of optical pumping. When the driving and probe lasers are on the two-photon Raman resonance, a coherent dark state is created that is decoupled from the applied optical fields and can be represented as $|D\rangle = (\Omega_d|X+\rangle - \Omega_p|X-\rangle)/(\sqrt{\Omega_d^2 + \Omega_p^2})$. Part of the population is excited from the electron spin ground state to the trion state and relaxes spontaneously into the dark state. As the dark state is not 'seen' by the optical fields, the total population is eventually trapped there within a few radiative cycles of the trion state. In CPT, the coherence between the spin ground states is created by the coherent optical fields. Therefore, the whole process is an optical pumping process, the rate of which is ultimately limited by the excited-state decay rate, with the transfer of the mutual coherence between the optical fields to the electron spin coherence.

An arbitrary initial state for the quantum computation can be prepared by varying the ratio of the Rabi frequencies between the driving and probe fields. Ultimately, if we set Ω_d to zero, the initialized spin state will be $|X-\rangle$. This is the fast spin-state

preparation effect as discussed in ref. 15. The difference is that when Ω_d is zero, there is no coherence involved in the state initialization, and the preparation efficiency is determined by the electron spin relaxation rate. In the initialization of the coherent superposition state, we generate an electron spin coherence by the optical fields, and the state preparation efficiency is limited by the electron spin decoherence rate.

The linewidth of the dip in the probe absorption spectrum is ultimately limited by the electron spin decoherence rate. In the experiment, the smallest Ω_d we applied is 0.56 GHz, which is about half of the trion transition linewidth, but still much larger than γ_s. Hence, the linewidth of the dip is broadened by the laser power. When Ω_d is strong, it will dress the spin ground state $|X-\rangle$ and the trion state $|T-\rangle$. In the case where Ω_d is larger than the trion transition linewidth, the absorption spectrum of the probe beam will split into two peaks when scanning across transition $H1$, which are known as Autler–Townes doublets[20], and has been demonstrated in a neutral quantum dot[21,22]. The spectral features of the probe absorption spectrum in our experiment are a

combination of the Autler–Townes splitting and the CPT quantum interference effect[7], where the spectral positions of the side bands can be determined by the Autler–Townes splitting and the central feature in the absorption spectrum is due to the CPT effect, not a simple summation of the tails of the Autler–Townes Lorentzian line shapes.

The probe absorption spectra with various driving field and fixed probe Rabi frequencies are shown in Fig. 2b–f. The energy separation of the two peaks is increased by increasing the driving field intensity. As Ω_d becomes larger than the trion transition linewidth, two Autler–Townes peaks with Lorentzian line shapes appear in the probe absorption spectrum, as shown in Fig. 2e,f. Figure 4a shows the energy separation of the Autler–Townes splitting peaks as a function of the driving field strength. A linear regression fits the data and extends to zero in the absence of the driving field, which indicates that the splitting is dominated by Ω_d. The red solid lines on top of the data shown in Fig. 2b–f are the theoretical fits obtained by solving the optical Bloch equations to all orders in the driving field and to first order in the probe. Assuming that γ_s is a few orders of magnitude larger than Γ_s (as we show below), we find $\gamma_{T-X+}/2\pi$, and $\gamma_s/2\pi$ equal to (0.54 ± 0.1) GHz and (40 ± 12) MHz, respectively. The value of 40 MHz corresponds to the electron spin decoherence time T_2^* $(1/\gamma_s)$ of 4 ns. Although we measure an electron spin trapped inside a single quantum dot, the electron spin T_2^* extracted from the data is not the intrinsic electron spin decoherence time owing to the hyperfine interaction between the electron spin and the neighbouring nuclei ensemble[23–27]. The intrinsic T_2 can be measured by spin echo[28] or mode locking of spin coherence techniques[5].

The generation of the dark state is accompanied by the excitation of the electron spin coherence, which corresponds to the density matrix element ρ_{X+X-}. We inserted the parameters extracted from the fits into the optical Bloch equations and obtained values for the coherence between the spin ground states, which are represented by the red line in Fig. 4b. The green line in Fig. 4b represents the theoretical values for the coherence in the absence of spin decoherence, given by $\Omega_d \Omega_p / (\Omega_d^2 + \Omega_p^2)$. The blue line represents the ratio of the experimentally generated coherence to the ideal case. The light blue dashed vertical lines indicate the applied Ω_d in the experiment. At the maximally applied Rabi frequency 1.38 GHz, we infer that 94% of the optimal coherence is generated in our system.

Our results open the way to the demonstration of numerous quantum phenomena in spin-based semiconductor quantum dot systems. A direct step is to demonstrate electron spin ground-state Rabi splitting by introducing a third continuous-wave laser, which is an analogy of electron spin Rabi oscillations in the time domain.

References

1. Gray, H. R., Whitley, R. M. & Stroud, C. R. Jr. Coherent trapping of atomic populations. *Opt. Lett.* **3**, 218–220 (1978).
2. Fu, K.-M. C., Santori, C., Stanley, C., Holland, M. C. & Yamamoto, Y. Coherent population trapping of electron spins in a high-purity n-type GaAs semiconductor. *Phys. Rev. Lett.* **95**, 187405 (2005).
3. Santori, C. *et al.* Coherent population trapping of single spins in diamond under optical excitation. *Phys. Rev. Lett.* **97**, 247401 (2006).
4. Dutt, M.V. G. *et al.* Stimulated and spontaneous optical generation of electron spin coherence in charged GaAs quantum dots. *Phys. Rev. Lett.* **94**, 227403 (2005).
5. Greilich, A. *et al.* Mode locking of electron spin coherences in singly charged quantum dots. *Science* **313**, 341–345 (2006).
6. Mikkelsen, M. H., Berezovsky, J., Stoltz, G. N., Coldren, L. A. & Awschalom, D. D. Optically detected coherent spin dynamics of a single electron in a quantum dot. *Nature Phys.* **3**, 770–773 (2007).
7. Boller, K. J., Imamoglu, A. & Harris, S. E. Observation of electromagnetically induced transparency. *Phys. Rev. Lett.* **66**, 2593–2596 (1991).
8. Harris, S. E. Electromagnetically induced transparency. *Phys. Today* **50** (7), 36–42 (1997).
9. Hau, L. V., Harris, S. E., Dutton, Z. & Behroozi, C. H. Light speed reduction to 17 metres per second in an ultracold atomic gas. *Nature* **397**, 594–598 (1999).
10. Liu, C., Dutton, Z., Behroozi, C. H. & Hau, L. V. Observation of coherent optical information storage in an atomic medium using halted light pulses. *Nature* **409**, 490–493 (2001).
11. Briegel, H. J., Duer, W., Cirac, J. I. & Zoller, P. Quantum repeaters: The role of imperfect local operations in quantum communication. *Phys. Rev. Lett.* **81**, 5932–5935 (1998).
12. Duan, L. M., Lukin, M. D., Cirac, J. I. & Zoller, P. Long-distance quantum communication with atomic ensembles and linear optics. *Nature* **414**, 413–418 (2001).
13. Loss, D. & DiVincenzo, D. P. Quantum computation with quantum dots. *Phys. Rev. A* **57**, 120–126 (1998).
14. DiVincenzo, D. P. The physical implementation of quantum computation. *Fortschr. Phys.* **48**, 771–783 (2000).
15. Xu, X. *et al.* Fast spin state initialization in a singly charged InAs–GaAs quantum dot by optical cooling. *Phys. Rev. Lett.* **99**, 097401 (2007).
16. Atature, M. *et al.* Quantum-dot spin-state preparation with near-unity fidelity. *Science* **312**, 551–553 (2006).
17. Ware, M. E. *et al.* Polarized fine structure in the photoluminescence excitation spectrum of a negatively charged quantum dot. *Phys. Rev. Lett.* **95**, 177403 (2005).
18. Alen, B. *et al.* Stark-shift modulation absorption spectroscopy of single quantum dots. *Appl. Phys. Lett.* **83**, 2235–2237 (2003).
19. Smith, J. M. *et al.* Voltage control of the spin dynamics of an exciton in a semiconductor quantum dot. *Phys. Rev. Lett.* **94**, 197402 (2005).
20. Autler, S. H. & Townes, C. H. Stark effect in rapidly varying fields. *Phys. Rev.* **100**, 703–722 (1955).
21. Kamada, H., Gotoh, H., Temmyo, J., Takagahara, T. & Ando, H. Exciton Rabi oscillation in a single quantum dot. *Phys. Rev. Lett.* **87**, 246401 (2001).
22. Xu, X. *et al.* Coherent optical spectroscopy of a strongly driven quantum dot. *Science* **317**, 929–932 (2007).
23. Khaetskii, A. V., Loss, D. & Glazman, L. Electron spin decoherence in quantum dots due to interaction with nuclei. *Phys. Rev. Lett.* **88**, 186802 (2002).
24. Coish, W. A. & Loss, D. Hyperfine interaction in a quantum dot: Non-Markovian electron spin dynamics. *Phys. Rev. B* **70**, 195340 (2004).
25. Johnson, A. C. *et al.* Triplet–singlet spin relaxation via nuclei in a double quantum dot. *Nature* **435**, 925–928 (2005).
26. Bracker, A. S. *et al.* Optical pumping of the electronic and nuclear spin of single charge-tunable quantum dots. *Phys. Rev. Lett.* **94**, 047402 (2005).
27. Wang, Y., Liu, R. B. & Sham, L. J. Restoring coherence lost to a slow interacting mesoscopic spin bath. *Phys. Rev. Lett.* **98**, 077602 (2007).
28. Petta, J. R. *et al.* Coherent manipulation of coupled electron spins in semiconductor quantum dots. *Science* **309**, 2180–2184 (2005).

Supplementary Information accompanies this paper on www.nature.com/naturephysics.

Author information

Reprints and permission information is available online at http://npg.nature.com/reprintsandpermissions. Correspondence and requests for materials should be addressed to D.G.S.

Adiabatic optical entanglement between electron spins in separate quantum dots

S. K. Saikin,[1,2,][*] C. Emary,[3] D. G. Steel,[4] and L. J. Sham[1]

[1]*Department of Physics, University of California–San Diego, La Jolla, California 92093, USA*
[2]*Department of Physics, Kazan State University, Kazan 420008, Russian Federation*
[3]*Institut für Theoretische Physik, TU Berlin, Hardenbergstr. 36, Berlin D-10623, Germany*
[4]*Department of Physics, The University of Michigan, Ann Arbor, Michigan 48109-1040, USA*

We present an adiabatic approach to the design of entangling quantum operations with two electron spins localized in separate InAs/GaAs quantum dots via the Coulomb interaction between optically excited localized states. Slowly varying optical pulses minimize the pulse noise and the relaxation of the excited states. An analytical "dressed-state" solution gives a clear physical picture of the entangling process and a numerical solution is used to investigate the error dynamics. For two vertically stacked quantum dots we show that, for a broad range of dot parameters, a two-spin state with concurrence $C > 0.85$ can be obtained by four optical pulses with durations $\sim 0.1 - 1$ ns.

PACS number(s): 78.67.Hc, 03.67.Bg, 42.50.Ex

Adiabatic passage uses the slow variation of a system's Hamiltonian to select a particular quantum path while avoiding unintended dynamics. Controlled adiabatic evolution of the ground state has been proposed as a model for quantum computation.[1] Stimulated Raman adiabatic passage (STIRAP) (Ref. [2]) can be used to transfer populations or coherences between quantum states through a "dark state" which efficiently suppresses relaxation. Arbitrary single-qubit operations can be produced, for example, by STIRAP in a tripod system[3] or adiabatically controlled Raman excitation in a Λ system.[4] In this work we study how adiabatic control can be used in design of optically induced two-qubit quantum operations.

In systems with a permanent interaction between qubits, it is known that adiabatic passage through degenerate dressed states can also be used to construct two-qubit entangling gates.[5] However, for scalable solid-state quantum computation, it is important to keep the qubits isolated from each other except during gating. Electron spins in semiconductor quantum dots (QDs) are promising candidates for just such qubits.[6] They have long coherence time,[7] can be manipulated by electric gates[8] or optically,[9,10] and the coupling between the qubits can be induced externally.

Significant experimental and theoretical effort has been invested in optical manipulation of electrons in single and coupled semiconductor QDs. Schottky diode structures with embedded self-assembled QDs have been designed to control the number of electrons in the dots by adjusting the external bias voltage.[11] The particular optical transitions between the charged and the excitonic states can be addressed in these dots by frequency and polarization selection.[12] Efficient spin-initialization schemes have been demonstrated recently using optical pumping in the Faraday[13] (magnetic field parallel to the optical axis) and the Voigt[12] (magnetic field orthogonal to the optical axis) configurations. The Faraday[14] and the Kerr[15] rotations from single spins confined in QDs have been observed, which should allow spin-readout and single-spin rotation operations. For two-qubit quantum operations the energy level structure and the interdot coupling in vertically aligned QD pairs have been studied.[16,17]

Several designs of two-qubit gates have been recently proposed utilizing, for example, tunneling between excited states of QDs,[18] Förster-type interaction[19] long-range coupling through a photon bus,[20] and electrostatic coupling between the excited states.[21,22] These schemes are yet to be demonstrated experimentally however. The major difficulties are as follows:

(i) The proposals utilize properties of the QDs or device structures which do not exist yet. For instance, two-qubit gates in Ref. [20] utilize QDs in cavities coupled to a common waveguide. Although such a design could potentially allow large spatial separation of the qubits, there are no reliable device structures yet.

(ii) The interdot coupling via, for example, electron tunneling between the excited orbitals or a Förster-type interaction requires precise alignment of the energy levels and cannot be controlled experimentally at the present stage of technology.

(iii) Demonstration of a two-qubit operation is complicated because of the gate structure. Although mathematically all the two-qubit entangling gates are equivalent, their physical realization, demonstration, and implementation into a particular quantum algorithm require different amount of resources. It is particularly important when the operational noise is a main limiting factor. For instance, demonstration of conditional phase operation additionally involves a number of single-qubit gates that themselves are very noisy and require a substantial experimental effort.

In this study we present a general approach to the design of two-qubit entangling operations with uncoupled electron spins in semiconductor QDs utilizing the Coulomb interaction of transient optically excited states localized in the dots. We show that adiabatic pulses combined with the counterintuitive pulse ordering of STIRAP allows the construction of nonlocal two-spin unitary transformations, while efficiently suppressing population transfer out of the qubit subspace. Compared to other two-qubit gates with spins in semiconductor QDs our proposal

(i) utilizes the conventional Schottky barrier device structures within which QDs are routinely grown;

(ii) is based on the Coulomb interaction between the excited electronic states in different dots, and therefore does

not require precise control for the energy level structure; and

(iii) provides flexibility in the gate design. In addition to the controlled-phase gates one can construct operations resulting in a coherent oscillation of two-spin state population, which is a more accessible signature of entanglement.

As illustration we describe an operation for two spins in separate self-assembled InAs/GaAs QDs. While for clarity the entangling process is described in the path language, it, in fact, represents a quantum operation made up of a product of $\sqrt{i\text{SWAP}}$ and controlled-phase gates. Combined with single-qubit rotations[4] and optical initialization,[12,23] we obtain a set of gates for universal quantum computation. We employ the Voigt configuration to obtain the flexibility required to select the desired quantum paths through polarization and frequency selection. The evolution of the system is then guided through a particular subset of quantum paths by a sequence of adiabatic pulses. In our dressed-state picture the scheme can be viewed as an adiabatic passage of an arbitrary initial two-spin state through two long-lived states. The interference between the two paths results in an effective rotation in the spin subspace. The method proposed here can be adapted to construct controlled-phase and controlled-NOT gates.

In two self-assembled InAs/GaAs QDs, the direct electron or hole tunneling between the dots may be suppressed by selecting the dot heights and the interdot distance.[16,18] Then, because the electrons and holes are confined differently, the intrinsic Coulomb coupling between particles in different dots modifies the optical transition energies.[16,17] We employ this phenomenon to perform two-qubit operations. This is similar to the dipole blockade.[24] However, we do not rely on an external electric field. This substantially simplifies the experimental setup and makes the operation less sensitive to external noise than the proposal of Ref. 21 in which in-plane gates were used. The particular path used for the entangling operation is shown in Fig. 1(a). In the ideal case of strong Coulomb interaction, starting with the polarized state $|+,+\rangle$ one obtains the maximally entangled state $\frac{1}{2}(|+,+\rangle+i|-,-\rangle)$ after an effective $\pi/2$ two-spin rotation. A longer excitation pulse results in coherent oscillations between $|+,+\rangle$ and $|-,-\rangle$ populations—an experimentally observable signature of the entanglement between the spins. Schematics of the pulse sequence and of the evolution of the appropriate dressed states are shown in Figs. 1(b) and 1(c). The long optical pulses used here may be generated by modulating cw lasers, which would provide sufficiently narrow frequency spectra of the pulses. Coherent optical coupling of the five-state system shown in Fig. 1(a) does not yield a dark state unlike in the familiar Λ system. However, the two states we use are long lived under two-photon resonance,[25] and we can further reduce trion relaxation by detuning the optical pulses and by adjusting their amplitudes.

For a single QD in the Voigt configuration with two single-electron spin states,

$$|\pm\rangle = \frac{1}{\sqrt{2}}(e_\downarrow^\dagger \mp e_\uparrow^\dagger)|0\rangle, \qquad (1)$$

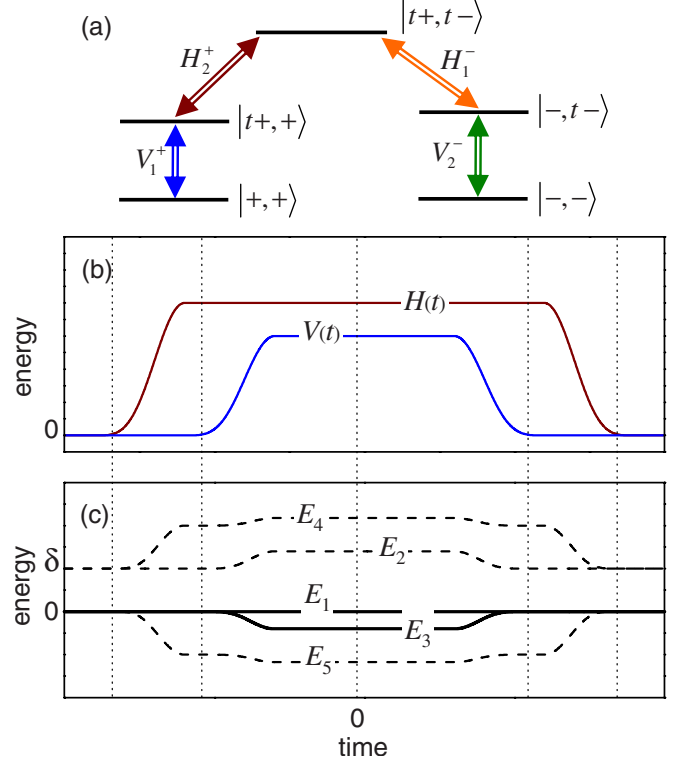we consider only two lowest-energy negative-trion states,

FIG. 1. (Color online) (a) Optical scheme to control the entanglement between spins in two InAs/GaAs QDs in the Voigt configuration. Two-dot states are denoted by kets such as $|t+,+\rangle$, with $|\pm\rangle$ for the spin states and $|t\pm\rangle$ for the trion states. Arrows indicate the linear polarizations $V_j^\pm$ and $H_j^\pm$ for the transitions $|\pm\rangle\leftrightarrow|t\pm\rangle$ and $|\pm\rangle\leftrightarrow|t\mp\rangle$ of dot $j=1,2$. (b) Timing of pulses for either dot. $V(t)$ and $H(t)$ are envelope functions, for which we use the same shape, rectangular with fronts shaped as $\sin^4(\pi t/T_f)$, for all pulses, and the same amplitudes for both V pulses and for both H pulses. (c) Adiabatic time evolution of the dressed-state energies. Solid lines show the essential energies which drive the operation.

$$|t\pm\rangle = \frac{1}{\sqrt{2}}e_\downarrow^\dagger e_\uparrow^\dagger (h_\downarrow^\dagger \mp h_\uparrow^\dagger)|0\rangle, \qquad (2)$$

where the operators $e_{\uparrow,\downarrow}^\dagger$ and $h_{\uparrow,\downarrow}^\dagger$ create, respectively, an electron and a heavy hole with spin along or against the growth direction, which we also take as the optical axis. Because of the large confinement splitting, the heavy hole is only weakly mixed with the light hole, and this can be easily compensated for by adjusting polarizations of the optical fields.[4] With these restrictions, the system of two dots has 16 states. The four lowest-energy spin states form the qubit sector. They are separated by a gap from eight single-trion states, which are similarly distant from four bitrion states. The interdot Coulomb interaction of electrons and holes gives rise to a binding energy of the bitrion,

$$\Delta = E_{1221}^{eeee} + E_{1221}^{hhhh} - E_{1221}^{ehhe} - E_{2112}^{ehhe}, \qquad (3)$$

where E_{jkkj}^{abba} is a two-particle Coulomb integral, e or h denotes electron or hole, and $j=1,2$ labels the dots, and we assume that the interdot electron-hole exchange is negligible due to the large distance. In zero magnetic field, let the tran-

sition energy from the qubit sector to the single-trion sector be ω_{tj}. The single-trion-to-bitrion transition energy is shifted by the binding energy Δ, thus enabling the two types of transition to be independently addressed. Four optical fields can thus couple the states $|+,-\rangle$ and $|-,+\rangle$ or states $|+,+\rangle$ and $|-,-\rangle$. In the following we use the latter pair because an efficient initialization of the state $|+,+\rangle$ is possible.[12]

First, we develop an analytical model describing the two-qubit gate. It assumes strong Coulomb interaction between the trions and does not account for relaxation from the excited states. These assumptions are relaxed later using numerical simulations of the system's dynamics.

The essential process of the quantum operation can be described by a Hamiltonian

$$
H = \begin{pmatrix}
0 & V_1^*(t) & 0 & 0 & 0 \\
V_1(t) & \delta & H_1^*(t) & 0 & 0 \\
0 & H_1(t) & 0 & H_2(t) & 0 \\
0 & 0 & H_2^*(t) & \delta & V_2(t) \\
0 & 0 & 0 & V_2^*(t) & 0
\end{pmatrix} \quad (4)
$$

acting on the five-level system [Fig. 1(a)] written in the rotating wave approximation and an interaction picture. The stationary basis states of the Hamiltonian are $|+,+\rangle$, $|t+,+\rangle$, $|t+,t-\rangle$, $|-,t-\rangle$, and $|-,-\rangle$. The optical fields are detuned by δ from the single-trion transitions to avoid populating the intermediate states, while the two-photon processes are resonant with the bitrion transition. For the sake of simplicity we use the same shape for both H pulses and both V pulses. We therefore omit the indices of the pulse envelopes in Eq. (4) in the following discussion. The two H-polarized pulses create the interaction between two dots by optically coupling the bitrion state to two single-trion states in the dots. Then, the shorter V polarized pulses couple the qubit sector to the renormalized excited states and rotate the spins in a way similar to the single-qubit operation.[4] The operation can be described in terms of dressed states $\mathbf{C}_{1-5}$. In the adiabatic approximation for positive δ their energies are

$$ E_1 = 0, $$

$$ E_{2,3} = \frac{1}{2}(\delta \pm \sqrt{\delta^2 + 4V(t)^2}), $$

$$ E_{4,5} = \frac{1}{2}(\delta \pm \sqrt{\delta^2 + 4V(t)^2 + 8H(t)^2}), \quad (5) $$

which are sketched in Fig. 1(c). Adiabatic pulses do not excite transitions to the split-off levels $E_{2,4}$, and thus states $\mathbf{C}_2, \mathbf{C}_4$ may be ignored. The H pulse is applied first and lifts the degeneracy of $E_{1,3}$ and E_5 levels, but state $\mathbf{C}_5$ remains orthogonal to the spin subspace and thus the initial spin state is not transferred to it. The transformation of a spin state is controlled only by the evolution of the states $\mathbf{C}_1$ and $\mathbf{C}_3$, which can be written as

$$ \mathbf{C}_1 = -\frac{1}{\sqrt{2}}[\cos\theta, 0, -\sin\theta, 0, \cos\theta], $$

$$ \mathbf{C}_3 = -\frac{1}{\sqrt{2}}[\cos\varphi_1, -\sin\varphi_1, 0, \sin\varphi_1, -\cos\varphi_1], \quad (6) $$

in terms of time-varying angles defined by

$$ \tan\theta = \frac{V(t)}{\sqrt{2}H(t)}, \quad \tan 2\varphi_1 = \frac{2V(t)}{\delta}. \quad (7) $$

When the optical fields are switched off, $\mathbf{C}_1$ and $\mathbf{C}_3$ reduce to $\frac{1}{\sqrt{2}}[1,0,0,0,\pm 1]$ which belong to the spin sector, $\mathbf{C}_{2,4}$ to single-trion states, and $\mathbf{C}_5$ to $|t+,t-\rangle$. The evolution of the spin states $|+,+\rangle$ and $|-,-\rangle$ is controlled by the unitary transformation $e^{-i\phi_1(1-\sigma_x)}$, where $\sigma_x = |+,+\rangle\langle-,-|+|-,-\rangle\langle+,+|$ and

$$ \phi_1 = \frac{1}{2}\int E_3(\tau)d\tau, \quad (8) $$

where $\hbar=1$ is assumed. An excitation with $\phi_1 = \pi/4$ would create a maximally entangled state from either $|+,+\rangle$ or $|-,-\rangle$. The operation is designed to minimize the effects of relaxation from excited states and pulse imperfections. The states $\mathbf{C}_1$ and $\mathbf{C}_3$ overlap within the qubit sector only. Therefore, the initial state always returns back to the qubit sector at the end of the operation. If a part of the population is transferred to $\mathbf{C}_5$, for example, by applying optical pulses simultaneously, the bitrion state will be left populated. However, this can be minimized by detuning of the two-photon excitation processes from the bitrion transitions. Also the populations of the excited state components of $\mathbf{C}_1$ and $\mathbf{C}_3$ are controlled by the small parameters $(V/\delta)^2$ and $(V/H)^2$. Below we show that it is possible to maintain the total population of the excited states below 10% for pulse durations of the order of 1 ns. This makes the lifetime of $\mathbf{C}_1$ and $\mathbf{C}_3$ about ten times longer than that of bare trions. For an arbitrary initial state, in addition to two-spin rotation described above, the $|+,-\rangle$ state acquires a phase $e^{-i\phi_2}$, where

$$ \phi_2 = \frac{1}{2}\int [\delta - \sqrt{\delta^2 + 8V(\tau)^2}]d\tau, \quad (9) $$

driven by the V fields coupling to the single trions $|t+,-\rangle$ and $|+,t-\rangle$. The optically induced transformation of an arbitrary two-spin state in the approximation of a strong Coulomb coupling and a large splitting between the Zeeman sublevels is

$$
U_{\text{id}} = \begin{pmatrix}
e^{-i\phi_1}\cos\phi_1 & 0 & 0 & ie^{-i\phi_1}\sin\phi_1 \\
0 & e^{-i\phi_2} & 0 & 0 \\
0 & 0 & 1 & 0 \\
ie^{-i\phi_1}\sin\phi_1 & 0 & 0 & e^{-i\phi_1}\cos\phi_1
\end{pmatrix}, \quad (10)
$$

where the phases $\phi_{1,2}$ are defined by Eqs. (8) and (9), respectively.

Detuning the optical fields is required to avoid unintended dynamics such as population transfer from $|+,-\rangle$ to the single-trion states $|t+,-\rangle$ or $|+,t-\rangle$. As an aid to the design of this process, we gather in Fig. 2 all the transition energies for
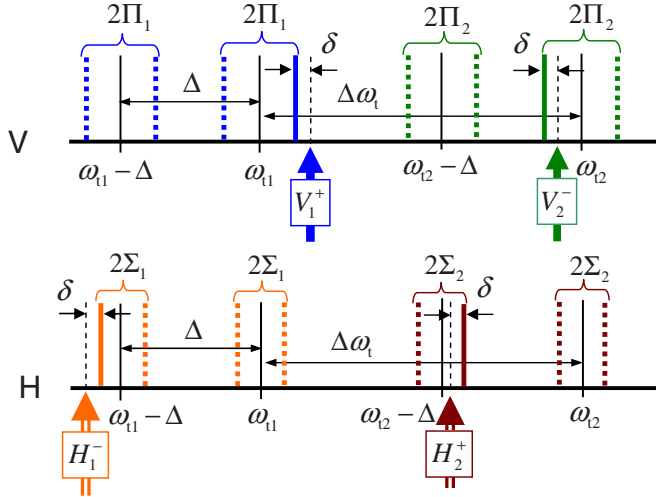
FIG. 2. (Color online) Energies of allowed optical transitions versus the optical frequencies (measured in energy units) for V polarization (upper figure) and H polarization (lower figure). The thin solid lines mark the transition energies in zero magnetic field. ω_{tj} is the transition energy between a spin state and a trion state in dot j. Their difference between the dots is shown as $\Delta\omega_t = \omega_{t2} - \omega_{t1}$. Δ is the bitrion binding energy, thus making the transition energy between the single and bitrion $\omega_{tj} - \Delta$. In a magnetic field, the electron and hole Zeeman splittings ω_j^e and ω_j^h in dot j cause the transition energy splitting $2\Pi_j = \omega_j^e + \omega_j^h$ in the V polarization and $2\Sigma_j = \omega_j^e - \omega_j^h$ in the H polarization. The Zeeman split transitions used in the quantum operation and off-resonant transitions are denoted by the thick solid lines and thick dashed lines, respectively. The vertical arrows show the central frequencies of the optical pulses and their detuning δ from the corresponding transitions.

both polarizations. The input parameters are the energy levels from the dot fabrication, Δ from dot placement, the Zeeman splittings, and the central frequencies of the optical pulses parametrized by single detuning δ for simplicity. Correction operation constrains these parameters as

$$\Delta\omega_t \gg \Delta \gg \Pi_i, \Sigma_i \gg \delta, \tag{11}$$

which is physically reasonable. If the bitrion binding energy Δ and the Zeeman splittings Π_i and Σ_i are comparable to the detuning δ, off-resonant processes have the undesired effect that the pulse sequence which excites the desired quantum path also excites an path involving the single trion states $|+,t-\rangle$ and $|t+,-\rangle$, albeit off resonantly. This reduces the two-spin rotation angle. This secondary process can be investigated with a five-level model similar to that of the resonant path. All other off-resonant excitations just give rise to phases in second-order perturbation. Including these effects [Eq. (10)] can thus be generalized as

$$U = \begin{pmatrix} e^{-i\phi_{11}}\cos\alpha & 0 & 0 & ie^{-i\phi_{14}}\sin\alpha \\ 0 & e^{-i\phi_{22}} & 0 & 0 \\ 0 & 0 & e^{-i\phi_{33}} & 0 \\ ie^{-i\phi_{41}}\sin\alpha & 0 & 0 & e^{-i\phi_{44}}\cos\alpha \end{pmatrix}, \tag{12}$$

where the phases ϕ_{ij} and α are defined in the Appendix. Equation (12) is not a standard quantum gate. Its usefulness

for quantum information processing has been discussed in Ref. 18. In general, the gate can be factorized as a product of control phase gates and a SWAP gate. Starting with an initially spin-polarized $|+,+\rangle$ or $|-,-\rangle$ state, one can generate a maximally entangled state with $\alpha = \pi/4$. Moreover, a longer excitation pulse should result in coherent two-spin oscillations.

To examine the effects of trion relaxation and off-resonant pumping, we numerically integrate the equation of motion for the 16-level density matrix including all transitions of Fig. 2. In particular, we consider two vertically stacked InAs QDs. We model the trion relaxation with a Lindblad form[23] and assume that all transitions are independent with the total relaxation rate $\Gamma = 1.2$ μeV.[13] The recombination rate of electrons and holes in different dots, as well as their spin decoherence rate,[7] is negligible on the operation time scale. We take the interdot difference of the two single-trion energies to be $\Delta\omega_t = 10$ meV, and the electron and hole g factors to be $g_e = -0.48$ and $g_h = -0.31$ (Ref. 12) for both dots. There appears to be no experimental data on the bitrion binding energy in the literature. Gerardot *et al.*[16] obtained 4.56 meV for binding energy of two excitons located in dots with a vertical separation of 4.5 nm. Scheibner *et al.*[17] measured -0.3 meV for the shift of a negative-trion transition when a second dot is occupied by a hole with respect to a bare transition (interdot distance is 6 nm). These give us two disparate values for the biexciton binding energy. From a simple analytical model[11] we estimate $\Delta = 0.8$ meV for dots with vertical separation 8 nm. To characterize the entanglement of the output qubit state we use the concurrence C.[26]

The most crucial parameter of the operation is the bitrion binding energy Δ. Figure 3 shows the concurrence of the output state as a function of Δ for several different excitations. The laser fields are weak enough to avoid unintentional dynamics outside the 16-level system (not studied here). We find that a state with a concurrence $C > 0.85$ can be generated if $\Delta \geq 0.3$ meV for a broad range of excitation parameters. The lower boundary for Δ is determined by the symmetry of the excitation scheme. One can see in Fig. 2 that if Δ is comparable to the Zeeman splitting the fields V_2^- and H_2^+ will excite transitions from the Coulomb-split doublets, in addition to the intended transitions. This effect is avoided if we design a gate to swap $|+,-\rangle$ and $|-,+\rangle$ states. In the latter case the concurrence of the gate remains $C > 0.85$ for $\Delta \geq 0.1$ meV and smoothly decays to zero at $\Delta \approx 10$ μeV.

The time required to entangle two spins is on the order of fractions of a nanosecond for the whole range of Δ. It is much shorter than the free-qubit decoherence time (~ 1 μs) at low temperatures determined by the interaction with a nuclear spin bath.[7] The main factors limiting the precision of an operation in this case are excitation of unintended transitions and relaxation from the optically excited states utilized in the scheme. Our approach allows precise control for unintended excitations. Within the 16-level model, if we assume an infinite relaxation time for the single-trion and bitrion states, the population of the excited states, after the optical fields are turned off, is less than 10^{-5}. Variations in pulse shapes or field intensities do not affect this value. In this sense our adiabatic excitation scheme is more robust compared to fast resonant operations utilizing
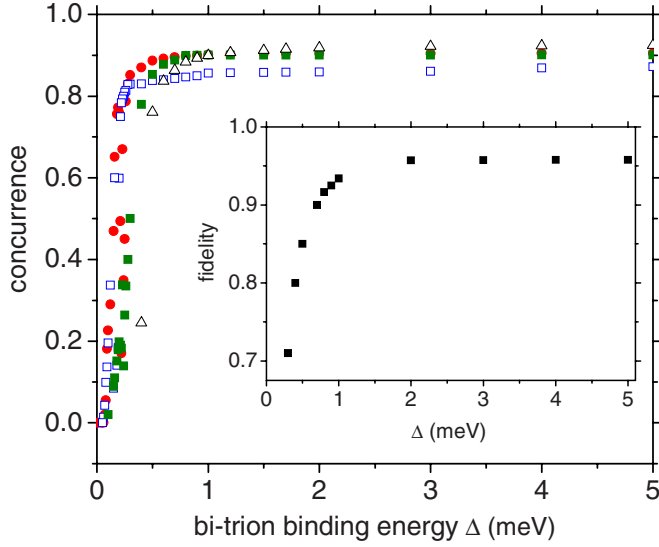
FIG. 3. (Color online) Concurrence of the output two-spin state for different bitrion binding energies. Excitation parameters: filled circles $-\delta=-0.1$ meV, $V_0=20$ meV, and $H_0=44$ meV; open squares $-\delta=-0.13$ meV, $V_0=20$ meV, $H_0=44$ meV; filled squares $-\delta=-0.1$ meV, $V_0=10$ meV, and $H_0=44$ meV; open triangles $-\delta=0.12$ meV, $V_0=15$ meV, and $H_0=65$ meV. V_0 and H_0 denote amplitudes of the V- and H-polarized fields. Inset: fidelity of the analytical model compared to numerical simulations as a function of Δ.

pulse shaping. Although the effect of relaxation from the excited states in our scheme is strongly suppressed by detuning of optical fields, it is still noticeable and limits the concurrence of a maximally entangled state. To further reduce the relaxation effects one has to increase detunings of optical fields and use QDs with greater separation between the energy levels (stronger Zeeman splitting and larger Δ).

To characterize the precision of the designed operation we define a fidelity of the gate[18,27]

$$F = \overline{\langle\psi_0|(U')^\dagger\rho_f U'|\psi_0\rangle} \qquad (13)$$

as it is described by our adiabatic analytical solution [Eq. (12)] compared to numerical simulation of quantum dynamics of the 16-level system that includes nonadiabaticity effects and relaxation. The bar over Eq. (13) is for average over all initial states of two qubits and ρ_f is a two-qubit density matrix obtained in the numerical simulations. This is the most objective method to analyze the theoretical model short of having experimental data for comparison. The inset of Fig. 3 show that the analytical model provides a good description of the operation in the same range of Δ.

An example of an entangling two-qubit evolution is given in Fig. 4 for two dots with the Coulomb coupling $\Delta=0.3$ meV. The optical pulses, centered at $t=0$, have been optimized to obtain a final state with a maximal entanglement from $|+,+\rangle$. The output concurrence $C\approx0.87$ is limited by relaxation from the single-trion and bitrion states. However, because only a small part of population is transferred to the excited states the entangling operation is weakly sensitive to the trion relaxation rate, doubling it results in less
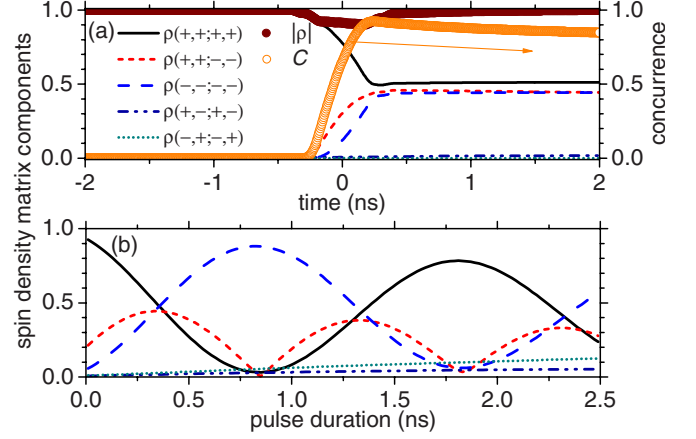

FIG. 4. (Color online) Evolution of a spin state controlled by four optical fields. The Coulomb coupling is $\Delta=0.3$ meV, the detuning is $\delta=-0.1$ meV, the magnetic field is $B=8$ T, and the field amplitudes are $V_0=20$ μeV and $H_0=44$ μeV. Durations of the H and V pulses interrelated as $T_H=T_V+2T_f, T_f=250$ ps is the front duration. (a) Optical pulses are centered at $t=0, T_V=340$ ps. The components not shown in the figure are below 10^{-3} at the end of the excitation. (b) Spin density matrix as a function of T_V.

than 10% variation in the concurrence. Longer excitation pulses result in Rabi oscillations of the pseudospin [Fig. 4(b)], which is consistent with the analytical model. The decay time of the Rabi oscillations is on the order of 10 ns. The conventional three-dimensional (3D) tomography plot [Fig. 5] shows the two-spin density matrix after the en-
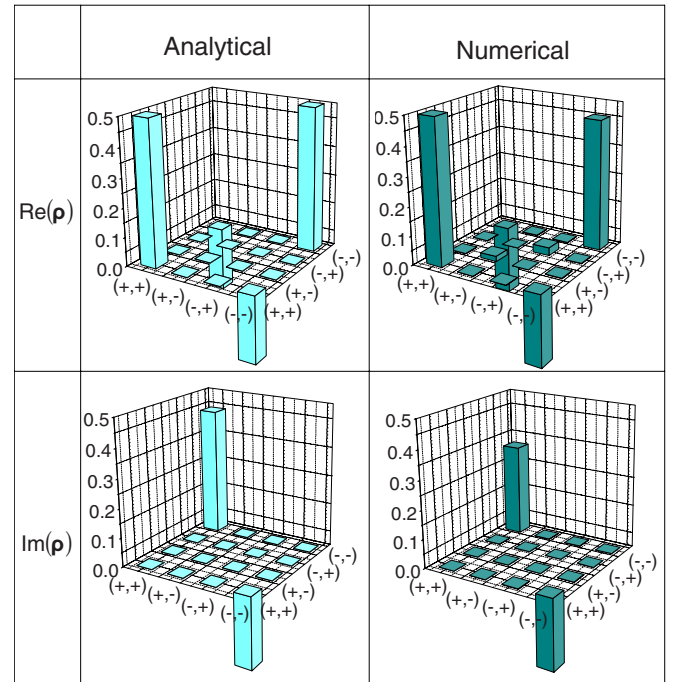

FIG. 5. (Color online) Density matrix of the output two-qubit state prepared from $|+,+\rangle$ using an optimized entangling gate. The analytical solution, obtained using Eq. (12), is compared with the numerical simulations. Parameters of the dots and the optical fields are the same as in Fig. 4.

tangling gate is applied compared with the ideal one obtained from Eq. (12).

Measuring the entanglement of the output state in an experiment requires a full-state tomography,[28] which could be rather difficult and a discussion of which is outside the scope of this work. However partial indication is provided by the oscillations between states $|+,+\rangle$ and $|-,-\rangle$ under longer excitation [Fig. 4(b)]. This effect can be probed by exciting resonantly the population of a given spin state and then measuring absorption or fluorescence. With two optical fields, one can selectively excite a transition from a single two-spin state to a bitrion state. For instance, optical fields V_1^+ and H_2^+ applied to the systems excite resonantly two-photon transition between $|+,+\rangle$ and $|t+,t-\rangle$ states only [see Fig. 1(a)]. All other transitions are off resonant. Therefore, fluorescence should be proportional to the population of $|+,+\rangle$. To confirm that the fields excite a two-photon transition one could measure two-photon cross correlations.[16]

In conclusion, we have developed an adiabatic approach for the optically controlled entangling quantum operations with two electron spins in semiconductor self-assembled quantum dots. The scheme, utilizing the Coulomb interaction between trions, is insensitive to material parameters, pulse imperfections, and trion relaxation. We show that using four optical fields a highly entangled two-spin state with the concurrence $C > 0.85$ can be prepared on the time scale of the order of 1 ns.

APPENDIX

The phases in the transformation matrix [Eq. (12)] are defined as follows:

$$\alpha = \phi_1 + \psi^-,$$

$$\phi_{11} = \phi_1 + \psi^+ + \int h_1(\tau) d\tau,$$

$$\phi_{22} = \phi_2 + \int h_2(\tau) d\tau,$$

$$\phi_{33} = \int h_3(\tau) d\tau,$$

$$\phi_{44} = \phi_1 + \psi^+ + \int h_4(\tau) d\tau,$$

$$\phi_{14} = \phi_{41} = \phi_1 + \psi^+ + \int h^+(\tau) d\tau,$$

where

$$\psi^\pm = (\psi_1 \pm \psi_2)/2,$$

$$\psi_1 = -\int \left[\frac{\Delta - \delta}{2} - \sqrt{\frac{(\Delta - \delta)^2}{4} + H^2(\tau) + 2V^2(\tau)} \right] d\tau,$$

$$\psi_2 = -\int \left[\frac{\Delta - \delta}{2} - \sqrt{\frac{(\Delta - \delta)^2}{4} + H^2(\tau)} \right] d\tau,$$

and

$$h_1(\tau) = -\frac{V^2(\tau)}{2\Pi + \delta} - \frac{H^2(\tau)}{\Delta - \delta + 2\Sigma},$$

$$h_2(\tau) = \frac{V^2(\tau)}{2\Pi - \delta} - \frac{H^2(\tau)}{\Delta - \delta - 2\Sigma},$$

$$h_3(\tau) = -\frac{H^2(\tau)}{\Delta - \delta + 2\Sigma} - \frac{H^2(\tau)}{\Delta - \delta - 2\Sigma},$$

$$h_4(\tau) = -\frac{V^2(\tau)}{2\Pi + \delta} + \frac{V^2(\tau)}{2\Pi - \delta},$$

$$h^\pm(\tau) = h_1(\tau) \pm h_4(\tau).$$

*saykin@fas.harvard.edu

[1] E. Farhi, J. Goldstone, S. Gutmann, J. Lapan, A. Lundgren, and D. Preda, Science **292**, 472 (2001).

[2] J. Oreg, F. T. Hioe, and J. H. Eberly, Phys. Rev. A **29**, 690 (1984); K. Bergmann, H. Theuer, and B. W. Shore, Rev. Mod. Phys. **70**, 1003 (1998).

[3] Z. Kis and F. Renzoni, Phys. Rev. A **65**, 032318 (2002).

[4] C. Emary and L. J. Sham, J. Phys.: Condens. Matter **19**, 056203 (2007).

[5] R. G. Unanyan, B. W. Shore, and K. Bergmann, Phys. Rev. A **63**, 043405 (2001).

[6] D. Loss and D. P. DiVincenzo, Phys. Rev. A **57**, 120 (1998).

[7] A. Greilich, D. R. Yakovlev, A. Shabaev, Al. L. Efros, I. A. Yugova, R. Oulton, V. Stavarache, D. Reuter, A. Wieck, and M. Bayer, Science **313**, 341 (2006).

[8] J. R. Petta, A. C. Johnson, J. M. Taylor, E. A. Laird, A. Yacoby, M. D. Lukin, C. M. Marcus, M. P. Hanson, and A. C. Gossard, Science **309**, 2180 (2005); F. H. L. Koppens, C. Buizert, K. J. Tielrooij, I. T. Vink, K. C. Nowack, T. Meunier, L. P. Kouwenhoven, and L. M. K. Vandersypen, Nature (London) **442**, 766 (2006).

[9] A. Imamoğlu, D. D. Awschalom, G. Burkard, D. P. DiVincenzo, D. Loss, M. Sherwin, and A. Small, Phys. Rev. Lett. **83**, 4204 (1999).

[10] C. Piermarocchi, Pochung Chen, L. J. Sham, and D. G. Steel, Phys. Rev. Lett. **89**, 167402 (2002).

[11] R. J. Warburton, C. Schflein, D. Haft, F. Bickel, A. Lorke, K. Karrai, J. M. Garcia, W. Schoenfeld, and P. M. Petroff, Nature (London) **405**, 926 (2000).

[12] X. Xu, Y. Wu, Bo Sun, Q. Huang, J. Cheng, D. G. Steel, A. S. Bracker, D. Gammon, C. Emary, and L. J. Sham, Phys. Rev. Lett. **99**, 097401 (2007).

[13] M. Atatüre, J. Dreiser, A. Badolato, A. Högele, K. Karrai, and A. Imamoğlu, Science **312**, 551 (2006).

[14] M. Atatüre, J. Dreiser, A. Badolato, and A. Imamoğlu, Nat. Phys. **3**, 101 (2007).

[15] J. Berezovsky, M. H. Mikkelsen, N. G. Stoltz, L. A. Coldren, and D. D. Awschalom, Science **320**, 349 (2008).

[16] B. D. Gerardot, S. Strauf, M. J. A. de Dood, A. M. Bychkov, A. Badolato, K. Hennessy, E. L. Hu, D. Bouwmeester, and P. M. Petroff, Phys. Rev. Lett. **95**, 137403 (2005).

[17] M. Scheibner, I. V. Ponomarev, E. A. Stinaff, M. F. Doty, A. S. Bracker, C. S. Hellberg, T. L. Reinecke, and D. Gammon, Phys. Rev. Lett. **99**, 197402 (2007).

[18] C. Emary and L. J. Sham, Phys. Rev. B **75**, 125317 (2007).

[19] B. W. Lovett, A. Nazir, E. Pazy, S. D. Barrett, T. P. Spiller, and G. A. Briggs, Phys. Rev. B **72**, 115324 (2005).

[20] S. M. Clark, Kai-Mei C. Fu, T. D. Ladd, and Y. Yamamoto, Phys. Rev. Lett. **99**, 040501 (2007).

[21] T. Calarco, A. Datta, P. Fedichev, E. Pazy, and P. Zoller, Phys. Rev. A **68**, 012310 (2003).

[22] E. Biolatti, I. D'Amico, P. Zanardi, and F. Rossi, Phys. Rev. B **65**, 075306 (2002).

[23] C. Emary, Xiaodong Xu, D. G. Steel, S. Saikin, and L. J. Sham, Phys. Rev. Lett. **98**, 047401 (2007).

[24] D. Jaksch, J. I. Cirac, P. Zoller, S. L. Rolston, R. Côté, and M. D. Lukin, Phys. Rev. Lett. **85**, 2208 (2000).

[25] F. T. Hioe and C. E. Carroll, Phys. Rev. A **37**, 3000 (1988).

[26] W. K. Wootters, Phys. Rev. Lett. **80**, 2245 (1998).

[27] J. F. Poyatos, J. I. Cirac, and P. Zoller, Phys. Rev. Lett. **78**, 390 (1997).

[28] C. F. Roos, G. P. T. Lancaster, M. Riebe, H. Häffner, W. Hänsel, S. Gulde, C. Becher, J. Eschner, F. Schmidt-Kaler, and R. Blatt, Phys. Rev. Lett. **92**, 220402 (2004).

PHYSICAL REVIEW LETTERS

Single Charged Quantum Dot in a Strong Optical Field: Absorption, Gain, and the ac-Stark Effect

Xiaodong Xu,[1] Bo Sun,[1] Erik D. Kim,[1] Katherine Smirl,[1] P. R. Berman,[1] D. G. Steel,[1,*] A. S. Bracker,[2]
D. Gammon,[2] and L. J. Sham[3]

[1]*The H. M. Randall Laboratory of Physics, The University of Michigan, Ann Arbor, Michigan 48109, USA*
[2]*The Naval Research Laboratory, Washington D.C. 20375, USA*
[3]*Department of Physics, The University of California–San Diego, La Jolla, California 92093, USA*
(Received 25 February 2008; published 25 November 2008)

We investigate a singly charged quantum dot under a strong optical driving field by probing the system with a weak optical field. We observe all critical features predicted by Mollow for a strongly driven two-level atomic system in this solid state nanostructure, such as absorption, the ac-Stark effect, and optical gain. Our results demonstrate that even at high optical field strengths the electron in a single quantum dot with its dressed ground state and trion state behaves as a well-isolated two-level quantum system.

Quantum dot (QD) nanostructures have been proposed for numerous quantum mechanical applications due to their customizable atomlike features [1]. One important application involves using these QDs as the building blocks for quantum logic devices [2]. An electron spin trapped inside a QD is a good candidate for a quantum bit (qubit) since it is known to have long relaxation [3] and decoherence times [4,5]. Recently, the electron spin coherence has been optically generated and controlled [5–7] in ensembles of QDs. The initialization of the electron spin state in a single QD has also been realized by optical cooling techniques [8,9].

One important task is to understand and control the physical properties of a singly charged QD in the strong optical field regime, i.e., the light-matter interaction strength is much larger than the transition linewidth, under both resonant and nonresonant excitation. For an ideal two-level atomic system, it has been shown theoretically [10–12] and demonstrated experimentally [13,14] that the strong coupling leads to interesting spectral features, such as Rabi side bands in the absorption, and strikingly, the amplification of a probe beam, which is known as the Mollow absorption spectrum (MAS).

Because of the unique atomic properties of the QD system, many body effects which dominate the nonlinear optical response in higher dimensional heterostructures are strongly suppressed. Recently, the optical ac-Stark effect has been seen by exciting a neutral QD with a detuned strong optical pulse [15] while the MAS and Mollow triplets [16] have been observed in a single neutral QD [17,18] and a single molecule with intense resonant pumping [19].

It is clear that a negatively charged quantum dot has similarities to a negative ion. However, the excited state of a dot is a many body system comprised of two electrons and a hole. The Fano interference effect, which arises from the coupling between a two-level system with a continuum [20], has been observed in a negatively charged QD [9,21].

The recent study of a single charged QD in the strong coupling regime does not exhibit the typical MAS [22]. All these indicate that interactions with a single charged QD could be more complex due to many-body effects than the electron-hole system reported earlier in neutral dots [17,18]. Interestingly, the results in this Letter show that strong field excitation tuned near resonance in a negatively charged dot leads to changes in the absorption spectrum that are in excellent agreement with theory for a strongly driven two-level system.

In this Letter, we investigate a singly charged QD under a strong optical driving field with both on- and off-resonant pumping. When the strong pump is on resonance with the trion transition, a triplet appears in the probe absorption spectrum with a weak center peak and two Rabi side bands with dispersive line shapes. As the pump beam is detuned from the trion transition, we observe three spectral features: a weak dispersive line shape centered at the driving field frequency flanked by an ac-Stark shifted absorption peak and a Raman gain side band. Our results reflect the coherent nonlinear interaction between light and a single quantum oscillator, and demonstrate that even at high optical field strengths, the electron in a single quantum dot with its ground state and trion state behaves as a well-isolated two-level quantum system. It is a step forward toward spin-based QD applications.

Assuming the trion can be considered as a simple two-level system in the absence of the magnetic field, the only optically allowed transitions are from the spin ground states ($|\pm \frac{1}{2}\rangle$) to the trion states ($|\pm \frac{3}{2}\rangle$) with $\sigma\pm$ polarized light excitations. Since the Zeeman sublevels of the electron spin ground state are degenerate, as are the trion states, both trion transitions are degenerate. We then use the two-level optical Bloch equations to model the trion system. For simplicity, we labeled the electron spin ground state as state $|S\rangle$ and the excited state as $|T\rangle$, as shown in Fig. 1(a).

It is known that in a two-level system driven by a strong optical field, the absorption of the weak probe beam is
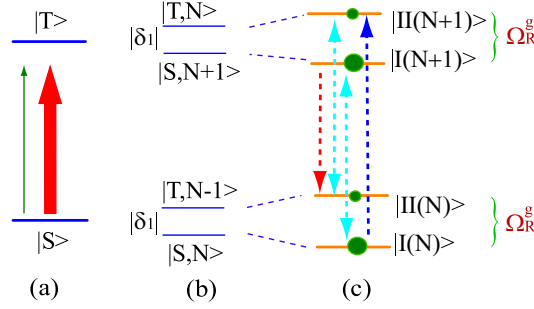
FIG. 1 (color online).   (a) The energy level diagram of a trion state at zero magnetic field. The absorption spectrum of the weak probe (thin arrow) is modified by a strong pump field (thick arrow). (b) The uncoupled atom-field states. (c) Dressed state picture of a two-level system driven by a strong optical field. The energy levels outside the picture are not shown. The energy splitting between the dressed states with the same photon number is $\hbar\Omega_R^g$, where Ω_R^g is the generalized Rabi frequency.

significantly modified [10–12]. The absorption coefficient can be obtained by solving the optical Bloch equations to all orders in the pump field and first order in the probe field, as shown in Ref. [11,17]. When the strong pump is on resonance with the trion transition, i.e., the pump detuning $\delta_1 = 0$ and the Rabi frequency Ω_R is much larger than the transition linewidth 2γ, the probe will show a complex Mollow absorption spectrum, which has been discussed in detailed in Ref. [17], where a neutral exciton has been studied with a strong resonant pumping.

When the pump detuning is larger than the transition linewidth, the physics can be understood in the fully quantized dressed state picture. The uncoupled QD-field states [Fig. 1(b)] map into the dressed states [Fig. 1(c)] when the QD-field interaction is included. In Fig. 1, we assume the pump detuning δ_1 to be negative, $|S\rangle$ and $|T\rangle$ are the quantum dot states, and N is the photon number. Because of the light-matter interaction, one set of the dressed states can be written as [23]

$$|I(N)\rangle = c|S, N\rangle - s|T, N - 1\rangle,$$
$$|II(N)\rangle = s|S, N\rangle + c|T, N - 1\rangle$$

where $c = \sqrt{\frac{1}{2}(1 - \frac{\delta_1}{\Omega_R^g})}$, $s = \sqrt{\frac{1}{2}(1 + \frac{\delta_1}{\Omega_R^g})}$, and $\Omega_R^g = \sqrt{\Omega_R^2 + \delta_1^2}$ is the generalized Rabi frequency. The energy separation between the dressed states $|I(N)\rangle$ and $|II(N)\rangle$ is $\hbar\Omega_R^g$. As shown in Fig. 1(c), there are three transition frequencies: one centered at the pump frequency ω_1, and two Rabi side bands centered at frequency $\omega_1 \pm \Omega_R^g$.

Assuming $\Omega_R^g \gg \gamma$ and using the secular approximation, the steady state solutions for the dressed state population are

$$\rho_{I,I} = \frac{c^4}{c^4 + s^4}, \qquad \rho_{II,II} = \frac{s^4}{c^4 + s^4}.$$

It is clear when $\delta_1 < 0$, the dressed state $|I(N)\rangle$ is more populated than the dressed state $|II(N)\rangle$. In Fig. 1(c), the size of the dots on states $|I(N)\rangle$ ($|I(N + 1)\rangle$ and $|II(N)\rangle$ ($|II(N + 1)\rangle$ indicates their population. Therefore, the transition centered at $\omega_1 + \Omega_R^g$ represents probe absorption [the rightmost dashed line in Fig. 1(c)], and the transition centered at $\omega_1 - \Omega_R^g$ is probe gain due to the population inversion of the dressed states [the leftmost dashed line in Fig. 1(c)]. The gain process, in its simplest form, can also be considered as a three photon process, in which two pump photons are absorbed at frequency ω_1 and a third photon is emitted at frequency $\omega_1 - \Omega_R^g$ [14]. The middle dashed lines indicate transitions where the probe frequency is close to the pump frequency and the secular approximation fails. These can give rise to a dispersive line shape [14,24].

The experiment is performed on a singly charged self-assembled InAs QD embedded in a Schottky diode structure. The detailed sample information can be found in Ref. [17,25]. The sample is located in a continuous helium flow magneto cryostat at a temperature of 5 K. By varying the dc gate voltage across the sample, the charge state of the dot can be controlled [25,26] and the transition energies can be electrically tuned using the dc Stark effect [27]. When the dc Stark shift is modulated by a small ac voltage, the changes in the transmission signal can be detected at the modulation frequency by a phase-sensitive lock-in amplifier.

By setting the voltage modulation amplitude to about 16 times the transition linewidth, we avoid complexities associated with smaller modulations [27]. The data taken directly correspond to the absorption. To obtain the Mollow absorption spectrum, two continuous wave (cw) lasers are used. In the pump-probe experiment, we set both beams to be linearly polarized with orthogonal polarization. By filtering out the pump beam with a polarizer in front of the detector, we can measure the probe absorption only.

We first set the pump detuning δ_1 to be zero and scan the probe frequency across the trion transition frequency ω_o. Figure 2(a) shows the probe absorption line shape with a pump intensity of 95 W/cm². Instead of a Lorentzian absorption line shape in the absence of the pump, as shown at the bottom of the Fig. 2(a), the line shape of the probe beam in the presence of a strong pump beam shows a complex structure [28]: a tripletlike absorption pattern appears with one weak central structure and two Rabi side bands with dispersive line shape. The observation of the Rabi side bands is a signature of the optical generation of single dot trion Rabi oscillations. The inset in Fig. 2(a) shows the Rabi splitting of the side bands as a function of the pump intensity. The largest Rabi splitting we achieved in the experiment is about $2 \times \hbar\Omega_R = 13.2 \mu$eV, which corresponds to switching between the ground and trion states at a frequency of 1.6 GHz and is limited only by the current experimental configuration.
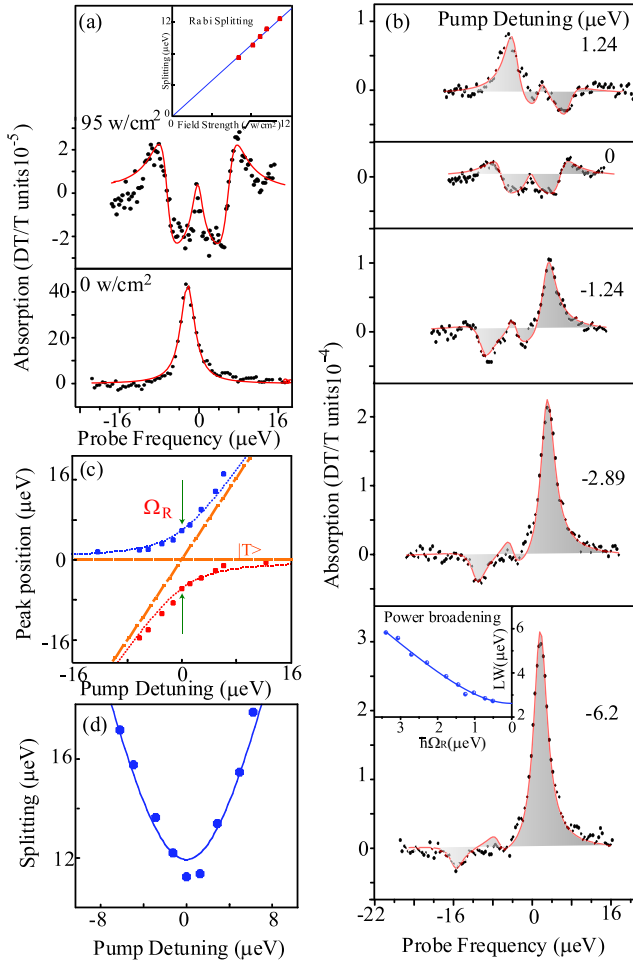
FIG. 2 (color online). The zero of the laser energy scale is
1318.797 meV. (a) Top curve: trion Mollow absorption spectrum
at a pump intensity of 95 W/cm^2 with resonant pumping.
Bottom curve: a probe beam absorption spectrum with no
pump. Inset: the Rabi splitting of the side bands as a function
of the pump intensity. (b) Trion Mollow absorption spectrum
with various pump detuning with a fixed pump intensity of
95 W/cm^2. Two Rabi side bands are clearly observed, where
one is the ac-Stark shifted absorption peak and the other shows
gain. Inset: the trion linewidth of the one beam absorption
spectrum as a function of laser Rabi frequency. It clearly shows
the power broadening effect. (c) The spectral position of the Rabi
side bands as a function of the pump detuning. We use the trion
transition energy as the zero point. The anticrossing feature of
the Rabi side bands is demonstrated as the pump is detuned from
the red to the blue of the trion transition. (d) The energy
separation of the Rabi side bands as a function of the pump
detuning. The solid line is the fit.

The negative part of the absorption line shape demon-
strates gain of the probe beam. Since the pump is resonant
with the trion transition, there is no population inversion in
the steady state of the trion system in any picture. The gain
effect comes from the coherent energy exchange between
the pump and probe beams through the QD nonlinearity.
We define the efficiency of the probe gain as the ratio of the
amplitude of the negative absorption to the probe absorp-
tion in the absence of the strong pump. The probe gain
efficiency corresponding to a pump intensity of 95 W/cm^2
is 5.3%. The earlier work by Kroner *et. al.* [22] did not
observe the typical spectral features for a isolated two-level
system, such as the dispersive side bands with optical gain
effect, and they attribute this difference to possible effects
of dephasing.

As we tune the pump laser frequency away from the
trion transition, the dispersionlike line shapes of the Rabi
side bands evolve into three spectral features: one weak
central structure with a dispersive line shape and two Rabi
side bands with Lorentzian line shapes. Figure 2(b) dis-
plays the probe absorption spectrum as a function of the
pump detuning with a fixed pump intensity of 95 W/cm^2.

A distinct feature of the probe absorption spectrum is
that one of the side bands shows purely negative "absorp-
tion," which is the gain effect. Using the pump detuning
$\hbar\delta_1 = -6.2$ μeV as an example [the bottom curve of
Fig. 2(b)], there is an absorption peak located at $\omega_1 +
\Omega_R^g$. This is an ac-Stark shifted absorption peak. The side
band centered at $\omega_1 - \Omega_R^g$ is negative, which signifies the
amplification of the probe beam. In lowest order perturba-
tion theory, this reflects a three photon Raman gain effect:
the QD absorbs two pump photons at frequency ω_1 and
emits a photon at $\omega_1 - \Omega_R^g$. The frequency at which gain
occurs can be tuned by adjusting the pump detuning. As
expected, if the pump detuning is positive, the probe sees
gain at $\omega_1 + \Omega_R^g$. The data with pump detuned $\hbar\delta_1 =
1.24$ μeV are shown at the top of Fig. 2(b). A gain peak
is clearly observed for the positive detuning of the probe. It
has been shown theoretically that the maximum gain oc-
curs at the absolute value of the pump detuning $|\delta_1| =
\Omega_R^g/3$ provided $\Omega_R^g \gg \gamma$ [29]. For the pump detuning
$\hbar\delta_1 = -1.24$ μeV, the data shows a probe gain of 9.7%,
which is much larger than under resonant pumping with the
same intensity. When the probe frequency is nearly degen-
erate with the pump beam, there is also a small dispersive
structure in the probe absorption spectrum, as shown in
Fig. 2(b).

The solid lines in Fig. 2(b) are theoretical fits of the data
to Eq. (1). The fits yield trion decay rate $\hbar\gamma_T$ and decoher-
ence rate $\hbar\gamma$ of (2.4 ± 0.4) μeV and (1.45 ± 0.15) μeV,
respectively. We also performed power dependent one
beam absorption measurements. The extracted linewidth
is plotted in the inset of Fig. 2(b) as a function of laser
Rabi frequency, which clearly shows the power broaden-
ing effect. The fit with a equation of FWHM =
$2\hbar\gamma\sqrt{1 + \Omega_R^2/(\gamma\gamma_T)}$ yields respectively $\hbar\gamma_T$ and $\hbar\gamma$ of
(2.2 ± 0.1) μeV and (1.35 ± 0.1) μeV, which agrees
well with the extracted parameters from the MAS. Since
γ_T is almost twice γ, these fits show that our results can be
well reproduced by the optical Bloch equations and that
there is no significant pure dephasing in the QDs.

Figure 2(c) shows the spectral positions of the Rabi side bands as a function of the pump detuning. In the plot, we use the trion transition frequency ω_o as the zero energy point. Figure 2(c) clearly illustrates the anticrossing behavior of the Rabi side bands. The separation between the two peaks at zero pump detuning represents the interaction strength between the light and QD, equal to the Rabi frequency. The dotted curves in the plot are the theoretical predictions of the peak positions as a function of the detuning, which is in good agreement with the measurements. The laser light induced transition energy shifts at the large pump detuning are a demonstration of the dynamic, or ac-Stark effect.

We extracted the energy separation of the side bands from the data and plotted it as a function of the pump detuning in Fig. 2(d). The solid line is a fit by the expression $2\sqrt{\Omega_R^2 + \delta_1^2}$ and gives $\hbar\Omega_R = (6.2 \pm 0.4~\mu\text{eV})$. Since $\Omega_R = \mu E_{\text{pump}}/\hbar$, we infer the trion dipole moment of $(25 \pm 2)~D$. The trion dipole moment we calculated is similar to the reported neutral exciton dipole moment [17].

The Einstein A coefficient, or spontaneous emission rate, is [30]

$$\gamma_{\text{sp}} = \frac{9n^5}{(2n^2 + n_{\text{QD}}^2)^2} \frac{\omega_o^3 \mu^2}{3\pi\varepsilon_o \hbar c^3} = \frac{9n^5}{(2n^2 + n_{\text{QD}}^2)^2} \gamma_{\text{spo}} \quad (1)$$

where γ_{spo} is the spontaneous emission rate in the vacuum, n and n_{QD} are the refractive index of the medium and the QD, respectively. By inserting the parameters into Eq. (1), we obatin a spontaneous emission rate of $\hbar\gamma_{\text{sp}} = 0.54~\mu\text{eV}$, which corresponds to a trion radiative lifetime of 1.2 ns. Assuming there is no pure dephasing in the QD, as we have shown earlier, then the trion transition linewidth is about $\hbar\Gamma_T = 0.54~\mu\text{eV}$, which is smaller than what we extracted from our previous fits from MAS or power broadening data. This discrepancy could come from the spectral diffusion process, which broadens the trion transition linewidth [17,31].

*dst@umich.edu

[1] D. Gammon and D. G. Steel, Phys. Today **55**, 36 (2002).

[2] D. Loss and D. P. DiVincenzo, Phys. Rev. A **57**, 120 (1998).

[3] Miro Kroutvar et al., Nature (London) **432**, 81 (2004).

[4] J. R. Petta et al., Science **309**, 2180 (2005).

[5] A. Greilich et al., Science **313**, 341 (2006).

[6] M. V. Gurudev Dutt et al., Phys. Rev. Lett. **94**, 227403 (2005).

[7] A. Greilich et al., Science **317**, 1896 (2007).

[8] Mete Atature et al., Science **312**, 551 (2006).

[9] Xiaodong Xu et al., Phys. Rev. Lett. **99**, 097401 (2007).

[10] E. V. Baklanov and V. P. Chebotaev, Sov. Phys. JETP **34**, 490 (1972).

[11] B. R. Mollow, Phys. Rev. A **5**, 2217 (1972).

[12] S. Haroche and F. Hartmann, Phys. Rev. A **6**, 1280 (1972).

[13] F. Y. Wu, S. Ezekiel, M. Ducloy, and B. R. Mollow, Phys. Rev. Lett. **38**, 1077 (1977).

[14] M. T. Gruneisen, K. R. MacDonald, and R. W. Boyd, J. Opt. Soc. Am. B **5**, 123 (1988).

[15] T. Unold et al., Phys. Rev. Lett. **92**, 157401 (2004).

[16] B. R. Mollow, Phys. Rev. **188**, 1969 (1969).

[17] Xiaodong Xu et al., Science **317**, 929 (2007).

[18] A. Muller et al., Phys. Rev. Lett. **99**, 187402 (2007).

[19] G. Wrigge, I. Gerhardt, J. Hwang, G. Zumofen, and V. Sandoghdar, Nature Phys. **4**, 60 (2008).

[20] U. Fano, Phys. Rev. **124**, 1866 (1961).

[21] M. Kroner et al., Nature (London) **451**, 311 (2008).

[22] M. Kroner et al., Appl. Phys. Lett. **92**, 031108 (2008).

[23] J. Dupont-Roc, G. Grynberg, and C. Cohen-Tannoudji, *Atom-Photon Interactions: Basic Processes and Applications* (John Wiley and Sons, New York, 1998).

[24] G. Grynberg and C. Cohen-Tannoudji, Opt. Commun. **96**, 150 (1993); P. R. Berman and G. Khitrova, Opt. Commun. **179**, 19 (2000).

[25] M. E. Ware et al., Phys. Rev. Lett. **95**, 177403 (2005).

[26] R. J. Warburton et al., Nature (London) **405**, 926 (2000).

[27] Benito Alen et al., Appl. Phys. Lett. **83**, 2235 (2003).

[28] There is a small energy shift of the weak probe absorption spectra between the presence and the absence of the pump, which is probably due to a small screening of the applied field by photoexcited charge in the diode. This shift saturates at a power between the lowest-intensity curve and the next higher-power spectrum. In the experiment, the pump laser is adjusted to follow the shift of the resonance.

[29] C. Cohen-Tannoudji and S. Reynaud, J. Phys. B **10**, 345 (1977).

[30] A. Thranhardt, C. Ell, G. Khitrova, and H. M. Gibbs, Phys. Rev. B **65**, 035327 (2002); J. R. Guest et al., Phys. Rev. B **65**, 241310(R) (2002).

[31] A. Hogele et al., Phys. Rev. Lett. **93**, 217401 (2004).

field of the form $M(y)P_\ell(y)$ can be obtained by introducing a slowly varying modulation in, say, the width or the properties of the material of which an element is made. Similarly, in the case of azimuthal symmetry, a Bessel beam can be used together with a set of concentric rings of properly modulated width placed at radii satisfying $J_1(q_0\rho) = 0$. The technology for manufacturing plates of this kind for microwave applications has been available for quite some time, whereas nanofabrication methods involving, for example, electron and focused ion beam lithography, can be used for the infrared and optical range. An important consideration in the design of a near-field plate is to avoid as much as possible the presence of terms giving a background that could overwhelm the sharp features of the field. An example of background-free focusing is shown in Fig. 2. These results are for the diffraction of a plane wave by a set of ribbons of very narrow width $\ll \ell$ and parameters such that the total current density is $\mathbf{j} = (j_x, 0, 0)$ where

$$j_x \propto \delta(z) \sum_{s=-\infty}^{\infty} \frac{(-1)^s \delta(y - s\ell)}{(1 + s^2\ell^2/L^2)} \qquad (7)$$

(the incident electric field is parallel to the cylindrical axis). Such an array of currents, with the sign varying from one element to the next, can be realized at infrared and optical frequencies by alternating material with positive and negative permittivity and, in the microwave re-

gime, by using a set of interchanging capacitive and inductive elements. Figure 2B shows a contour plot of the y component of the diffracted magnetic field (logarithmic scale). These results are similar to those reported for negative-index slabs (*14*, *25*), thereby revealing the close relationship between the two phenomena (*26*). Finally, to help ascertain the origin of radiationless interference, we show in Fig. 2C a linear plot of the field intensity, normalized to its largest value at a given z. Reflecting a property of the zeros of H_y, the figure clearly shows behavior reminiscent of beam coupling in that the diffraction of the beam produced by a particular current source is prevented by the presence of its neighbors. It is only after the intensity of its neighbors has decreased a sufficient amount that the central beam is allowed to spread, and the point at which this happens determines the focal length.

References and Notes

1. E. Abbe, *Arch. Mikrosk. Anat.* **9**, 413 (1873).
2. E. Betzig, J. K. Trautman, *Science* **257**, 189 (1992).
3. A. Tselev *et al.*, *Rev. Sci. Instrum.* **74**, 3167 (2003).
4. F. Zenhausern, Y. Martin, H. K. Wickramasinghe, *Science* **269**, 1083 (1995).
5. R. Hillenbrand, T. Taubner, F. Keilmann, *Nature* **418**, 159 (2002).
6. M. I. Stockman, S. V. Faleev, D. J. Bergman, *Phys. Rev. Lett.* **88**, 067402 (2002).
7. G. Lerosey, J. de Rosny, A. Tourin, M. Fink, *Science* **315**, 1120 (2007).
8. P. C. M. Planken, N. C. J. van der Valk, *Opt. Lett.* **29**, 2306 (2004).
9. D. R. Smith, J. B. Pendry, M. C. K. Wiltshire, *Science* **305**, 788 (2004).
10. D. R. Smith, *Science* **308**, 502 (2005).
11. J. B. Pendry, *Phys. Rev. Lett.* **85**, 3966 (2000).
12. N. A. P. Nicorovici, R. C. McPhedran, G. W. Milton, *Phys. Rev. B* **49**, 8479 (1994).
13. G. W. Milton, N. A. P. Nicorovici, R. C. McPhedran, V. A. Podolskiy, *Proc. R. Soc. London Ser. A* **461**, 3999 (2005).
14. R. Merlin, *Appl. Phys. Lett.* **84**, 1290 (2004).
15. R. Shelby, D. R. Smith, S. Schultz, *Science* **292**, 77 (2001).
16. A. Grbic, G. V. Eleftheriades, *Phys. Rev. Lett.* **92**, 117403 (2004).
17. N. Fang, H. Lee, C. Sun, X. Zhang, *Science* **308**, 534 (2005).
18. T. Taubner, D. Korobkin, Y. Urzhumov, G. Shvets, R. Hillenbrandt, *Science* **313**, 1595 (2006).
19. E. Hecht, *Optics* (Addison Wesley, San Francisco, 2002).
20. J. A. Stratton, *Electromagnetic Theory* (McGraw-Hill, New York, 1941).
21. P. C. Clemmow, *The Plane Wave Spectrum Representation of Electromagnetic Fields* (Pergamon, Oxford, 1966).
22. J. H. McLeod, *J. Opt. Soc. Am.* **44**, 592 (1954).
23. J. Durnin, J. J. Miceli Jr., J. H. Eberly, *Phys. Rev. Lett.* **58**, 1499 (1987).
24. D. R. Smith *et al.*, *Appl. Phys. Lett.* **82**, 1506 (2003).
25. G. Shvets, *Phys. Rev. B* **67**, 035109 (2003).
26. We emphasize that, although our plates and negative-index slabs create comparable field distributions, the physical origins are very different in that the plates transform, propagating into evanescent modes, whereas the slabs amplify the near field.
27. The author acknowledges discussions with A. Grbic. This work was supported by the Air Force Office of Scientific Research under contract FA 9550-06-01-0279 through the Multidisciplinary University Research Initiative Program.

Coherent Optical Spectroscopy of a Strongly Driven Quantum Dot

Xiaodong Xu,[1] Bo Sun,[1] Paul R. Berman,[1] Duncan G. Steel,[1]* Allan S. Bracker,[2] Dan Gammon,[2] L. J. Sham[3]

Quantum dots are typically formed from large groupings of atoms and thus may be expected to have appreciable many-body behavior under intense optical excitation. Nonetheless, they are known to exhibit discrete energy levels due to quantum confinement effects. We show that, like single-atom or single-molecule two- and three-level quantum systems, single semiconductor quantum dots can also exhibit interference phenomena when driven simultaneously by two optical fields. Probe absorption spectra are obtained that exhibit Autler-Townes splitting when the optical fields drive coupled transitions and complex Mollow-related structure, including gain without population inversion, when they drive the same transition. Our results open the way for the demonstration of numerous quantum level–based applications, such as quantum dot lasers, optical modulators, and quantum logic devices.

The quantum optoelectronic properties of semiconductor quantum dots (QDs) have featured prominently in numerous proposals, including quantum computing, single-photon sources, and quantum repeaters (*1–3*). QDs are particularly attractive for these applications because they behave in many ways as simple stationary atomic or molecular systems (*4*) with discrete states where the electron-hole pair can be treated as a well-defined composite-particle state (*5*).

Whereas strong optical excitation of a semiconductor creates a many-body problem because

of the extended nature of the wave function (*6*), confinement of the wave function in QDs leads to strong energy-level shifts between one exciton and two or more exciton states, enabling the system to be considered as a relatively simple few-level problem. The strong-field excitation regime of the transition from the ground state to an excited state such as the exciton, a Coulomb bound electron-hole pair, is then defined by $\Omega_R \gg 2\gamma$ where the Rabi frequency $\Omega_R = \frac{\mu E}{h}$, $\frac{\gamma}{\pi}$ is a transition linewidth (full width at half-maximum, in Hz), μ is the transition dipole moment, and E is the amplitude of the optical electric field. For time scales less than γ^{-1}, strong excitation leads to Rabi oscillations (*7–10*) in time. The effect of vacuum Rabi splitting (*11*) has also been observed in a single QD embedded in a nanocavity (*12–14*).

Under strong continuous wave (CW) narrow-band resonant optical excitation of a simple atomic system, the fluorescence emission spectrum, which is a narrow emission line at low power (the emission width is the laser bandwidth), consists of three peaks referred to as the Mollow triplet (*15*). A simple picture of the origin of this emission pattern is understood from a dressed-atom picture (*16*). Figure 1B shows the dressed-state picture with fully quantized atom-field states, when the driving-field frequency ω is equal to the electronic frequency ω_0. In this limit,

[1]The H. M. Randall Laboratory of Physics, The University of Michigan, Ann Arbor, MI 48109, USA. [2]The Naval Research Laboratory, Washington, DC 20375, USA. [3]Department of Physics, University of California–San Diego, La Jolla, CA 92093, USA.

*To whom correspondence should be addressed. E-mail: dst@umich.edu

the "bare" states $|3, N-1\rangle$ and $|2, N\rangle$ are degenerate, where N labels the photon number of the driving field. The atom-field interaction lifts this degeneracy and produces "dressed" states $|\alpha(N-1)\rangle$ and $|\beta(N-1)\rangle$ having energy separation $\hbar\Omega_R$ as shown. The dressed states are linear combinations of the bare states. The dashed lines in the figure indicate a triplet of possible emission frequencies, occurring at ω and $\omega \pm \Omega_R$.

In absorption, the spectrum can be more complex. For the three-level V system (Fig. 1A), where the strong field couples levels 2 and 3, theory predicts that the probe absorption from level 2 to level 1 is strongly modified from the usual simple Lorentzian seen in the absence of strong-field excitation. The probe absorption splits into two resonances, known as the Autler-Townes (AT) splitting (17). When the probe absorption on the strongly driven transition (between levels 2 and 3) is measured, the spectrum is much richer. New physics beyond that seen in the Mollow fluorescence triplet is observed (18–22) and arises from the coherent coupling between the two optical fields. When the Rabi frequency of the strong pump field is sufficiently large, the absorption spectrum shows gain without population inversion.
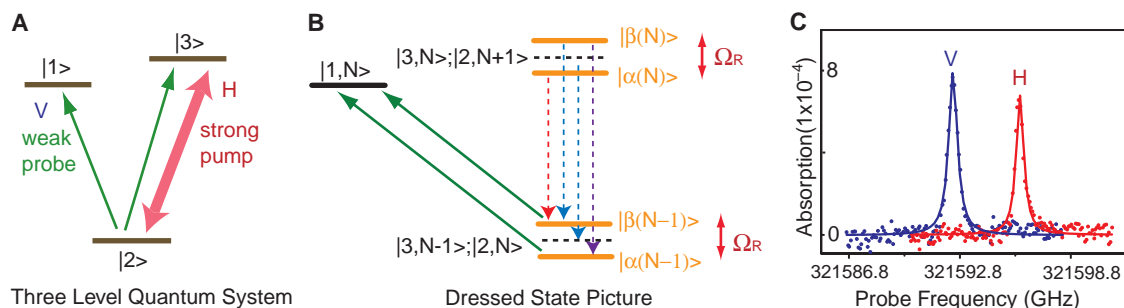
We present experimental results of the AT splitting and complex Mollow absorption spectrum (MAS) using a single semiconductor QD. We coherently control the probe absorption with a strong optical field, thus demonstrating that the single QD coupled with the strong pump can function as a modulator of the probe absorption (23). In addition, the spectrum as a function of the probe frequency shows Rabi splitting and gain without population inversion. The results are in good agreement with the standard theory based on the optical Bloch equations. Our work demonstrates that on long time scales, the discrete energy-level spectrum of the dot is maintained even at the high field strengths needed for quantum logic operations (e.g., qubit rotations) and single-photon devices, and that the system behaves in a manner similar to that of a trapped atom. The results suggest that it should be possible to demonstrate numerous quantum level–based applications, such as dressed-state lasers (24), QD optical modulators (23), and quantum logic devices (4).

The system of interest is a single, neutral InAs self-assembled QD embedded in a Schottky diode structure at 5K (25). The typical single-beam, linear absorption spectrum of a single QD

(Fig. 1C), taken with a CW laser with a 300-KHz linewidth, shows that the neutral exciton has two linearly polarized quantum transitions with orthogonal polarizations. The fine-structure splitting of the exciton states, due to the QD in-plane anisotropy (26), is about 15 μeV. In the corresponding energy-level diagram of the states (Fig. 1A), states $|1\rangle$ and $|3\rangle$ represent the exciton states, state $|2\rangle$ is the crystal ground state, and the two linearly polarized transitions are labeled V and H.

To analytically describe our experiments, we follow the approach used in (17, 19), describing the system with the optical Bloch equations $i\hbar\frac{d\rho}{dt} = [H, \rho] + \text{Decay}$ (27, 28), where ρ and H are the density matrix and Hamiltonian of the light-coupled QD system, respectively. The Hamiltonian is given by $H = H_0 - \vec{\mu} \cdot \vec{E}$ where $\vec{E} = \vec{E}_0 + \vec{E}_1$. $\vec{E}_0$ is the strong pump field and $\vec{E}_1$ is the weak probe field. For calculations of the absorption spectrum, we can use the semi-classical approach where the fields are taken to be classical. H_0 is the diagonalized Hamiltonian for the QD structure (Fig. 1A). The results of calculations in the limits appropriate to this work are provided in the Supporting Online Material (25). The theory is fit to experimental data with

Fig. 1. (A) The energy-level diagram of a single neutral QD. The absorption of the weak probe beam by scanning either transition V or H is modified by the strong pump beam, which is near resonant with transition H. **(B)** The dressed-state picture of the system shown in (A). The transitions between states $|\alpha,N\rangle$ ($|\beta,N\rangle$) and $|1,N+1\rangle$, outside the energy range of the diagram, are not shown. If a weak beam probes transition 2-1 as shown by the green arrows, the absorption spectrum consists of a doublet. Ignoring the state $|1\rangle$, the emission spectrum of transition 3-2 consists of three peaks (Mollow triplet): a peak centered at the electronic transition ω, and two Rabi side bands located at $\omega \pm \Omega_R$ (shown by the dashed lines). **(C)** Single-beam, linear absorption profile of a single exciton state. The horizontally (or vertically) polarized light only excites the corresponding linearly polarized exciton transition.

Fig. 2. Autler-Townes splitting by means of a single QD. A strong pump drives transition H, and a weak probe scans across transition V. **(A)** Probe absorption spectra as a function of the pump intensity when the pump is on resonance. I_0 equals 1.2 W/cm². The solid lines are theoretical fits to the data. The inset shows the AT splitting (Rabi splitting) as a function of the square root of the pump intensity. A linear fit (solid line) matches the data very well. **(B)** The probe absorption spectra as a function of the pump frequency detuning with fixed pump intensity. The lines are the theoretical fits to the data.
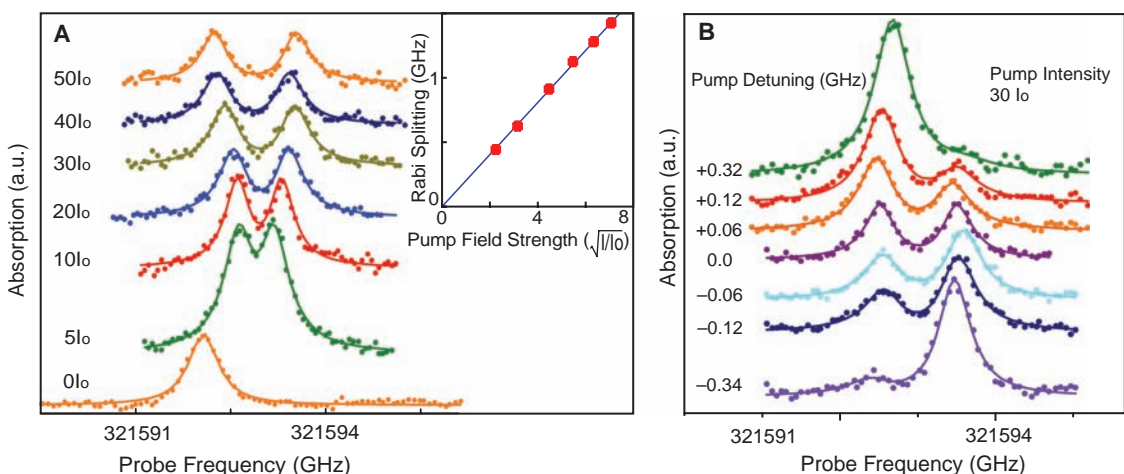
only the linewidth and amplitude as free parameters. The dipole moment is extracted from the linear dependence of the splitting on the field strength.

To experimentally demonstrate the AT effect (17), we use two frequency-locked but independently tunable CW lasers with a mutual coherence bandwidth of a few MHz (25). We set a horizontally polarized pump beam resonant with the H transition. A weak, vertically polarized probe beam then scans across transition V. The probe absorption spectra for different pump laser intensities are plotted in Fig. 2A with increasing pump intensity. The data are shifted vertically for clarity. In agreement with theory (solid lines) (25), the probe absorption splits into a doublet where each peak has equal strength. There is a small energy shift of the response relative to the low-intensity excitation that is probably due to a small screening of the applied field by photo-excited charge in the diode. The shift saturates at a power between the lowest-intensity curve and the next higher-power spectrum. The pump laser is adjusted to follow the shift of the resonance.

The frequency separation between the absorption peaks shows a strong dependence on the pump intensity. We plot the measured splitting as a function of the square root of the pump intensity in the inset of Fig. 2A. The splitting clearly depends linearly on the pump field strength and goes to zero in the absence of the pump, as expected for the dependence of the AT splitting on the Rabi frequency.

Figure 2B shows the probe absorption as a function of the pump detuning with a fixed pump intensity of $30I_0$ (the corresponding photon number per unit volume is $\sim 1.4 \times 10^{10}/\text{cm}^3$), where $I_0 = 1.2$ W/cm^2, corresponding to a Rabi frequency of $\sim \frac{\Omega_R}{2\pi} = 1.1$ GHz. Again, the data are shifted for clarity, and the solid lines are the fit of the data to the theory (25) and show good agreement.

In the MAS, where the pump and probe beams coherently couple to the same transition and the pump field is tuned to resonance, we observe a relatively weak maximum centered at zero probe detuning and two Rabi side bands with dispersive line shapes. The pump power dependence of the probe absorption spectra is shown in Fig. 3A. The single-beam absorption data are plotted at the bottom. The spectral shift of the data with the high-power optical field is due to the excitation of the charge states in the buffer layer. The complex line shape of the MAS depends strongly on the pump intensity. The splitting between the two side bands is plotted as a function of the square root of the pump intensity in Fig. 3B, again showing that the splitting linearly depends on the pump field strength and is zero in the absence of the pump field.

The data confirm that the probe beam experiences optical gain in the pump-probe configuration for strong excitation. The MAS data in Fig. 3A show that part of the probe absorption curve is below zero, which is the "gain" effect. Using the data corresponding to

$15I_0$ as an example, the absorption/gain ratio is about 0.066%/0.0024% = 27.5. This gain is from the pump and probe beams coherently exchanging energy through the QD and corresponds to gain without inversion because there is no population inversion either in the dressed- or bare-atom pictures.

The AT splitting can provide a method to measure the dipole moment, as the Rabi frequency is a product of the transition dipole moment with the optical field. From the extracted Rabi splitting with the corresponding optical field strength, we can infer a transition dipole moment of about 30 D for this particular QD. The Einstein A coefficient (spontaneous emission rate) of a QD in a medium is given as $\gamma_{sp} = \frac{9n^5}{(2n^2 + n_{QD}^2)^2} \times \frac{\omega_0^3 \mu^2}{3\pi\varepsilon_0 hc^3} = \frac{9n^5}{(2n^2 + n_{QD}^2)^2}\gamma_{spo}$, where n (n_{QD}) is the refractive index of the medium (QD) and γ_{spo} is the spontaneous emission rate of a two-level quantum system in the vacuum (29). By taking $n = n_{QD} = 3.44$ and inserting the experimental parameters and the extracted dipole moment into the equation, we obtain $\frac{\gamma_{sp}}{2\pi} = 190$ MHz, which corresponds to a life time of about 840 ps. Assuming there is no other decay and no pure dephasing, this would lead to a natural linewidth expected in the low-power absorption spectrum also equal to $\frac{\gamma_3}{2\pi} = 190$ MHz, where γ_j is the decay rate of level j in Fig. 1A. Compared to the extracted linewidth from the single-beam, low-power absorption data, which is about 500 MHz, γ_{sp} is smaller by a factor of about 2.5. This discrepancy indicates that there is possibly a spectral wandering process that broadens the transition linewidth (30). This interpretation agrees with our previous study on a single charged QD, which also suggested the absence of pure dephasing.

We can also extract the exciton decay and dephasing rates from the AT splitting and MAS data. The solid lines in Fig. 2A are the theoretical fit of the AT splitting data assuming that $\gamma_3 = \gamma_1$ and $\Gamma_{13} = 0$, where $\gamma_{ij} = (\gamma_i + \gamma_j)/2 + \Gamma_{ij}$, γ_{ij} is the total dephasing rate, and Γ_{ij} is the contribution to the dephasing rate of the ij transition from sources other than spontaneous emission. From the fits, we find $\frac{\gamma_{23}}{2\pi}$ and $\frac{\gamma_1}{2\pi}$ of (176 ± 16) MHz and (357 ± 16) MHz, respectively. The theory fits the data very well and indicates that under these experimental conditions, the single QD behaves like a single atomic system. We also fit the MAS data to theory (25) (solid lines in Fig. 3A). The fitting yields $\frac{\gamma_{23}}{2\pi}$ and $\frac{\gamma_1}{2\pi}$ of (230 ± 12) MHz and (315 ± 45) MHz, respectively. The value of $\frac{\gamma_{23}}{2\pi}$ is within 10% of that extracted from the low-pump field profile. The physical parameters from the MAS and AT splitting data show that the decay rate is almost twice the dephasing rate, indicating no appreciable pure dephasing. We speculate that the reason for the discrepancy between the Einstein A coefficient determined from the dipole moment (above) and the fitting parameters is again due to spectral wandering, which leads to a fit of the theory that over-
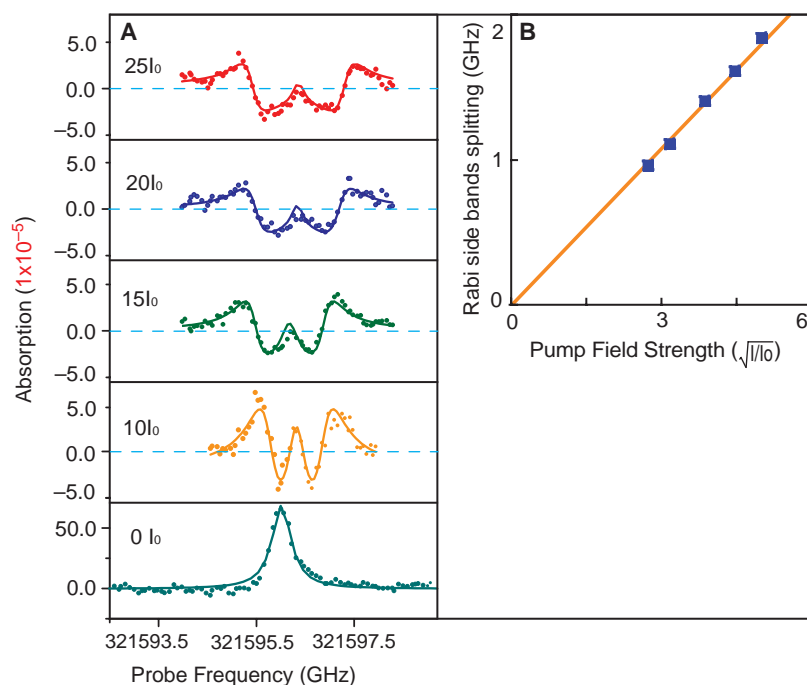

Fig. 3. Mollow absorption spectrum when the strong pump and weak probe beams couple to the same transition. (**A**) Measured probe absorption versus pump field intensity when the pump is on resonance. The lines are the fits to the probe absorption function obtained by solving optical Bloch equations. The MAS data show that the part of the absorption signal is "negative." Using the data corresponding to $15I_0$ as an example, the absorption/gain ratio is about 0.066%/0.0024% = 27.5. (**B**) The splitting between the Rabi side bands versus pump field strength. The solid line is the linear fit to the data.

estimates the population relaxation rate. However, this remains under investigation.

The AT splitting and gain without inversion in the Mollow absorption spectrum imply that the absorption and gain inside a single QD are tunable. In the AT configuration, the absorption of the probe beam can be switched on and off by applying a strong optical field. In contrast, in the MAS experiment, the absorption of the frequency fixed probe beam can be tuned to be positive or negative (gain) by adjusting the pump field strength. Our results are the first step toward the realization of electromagnetically induced transparency and lasing without inversion in the spin-based lambda system and suggest that QDs offer the potential to be used as elements in opto-electronics and quantum logic devices (*4*, *27*).

Note added in proof: Since the submission of this paper, two papers have appeared on http://arxiv.org that report studies of the resonant excitation of quantum dots in the strong excitation regime. The first (*31*) reports a measurement of the fluorescence correlation function that Mollow first calculated, and the second (*32*) reports Rabi oscillations.

References and Notes

1. D. Loss, D. P. DiVincenzo, *Phys. Rev. A.* **57**, 120 (1998).
2. Z. Yuan *et al.*, *Science* **295**, 102 (2002).
3. H.-J. Briegel, W. Duer, J. I. Cirac, P. Zoller, *Phys. Rev. Lett.* **81**, 5932 (1998).
4. D. Gammon, D. G. Steel, *Phys. Today* **55**, 36 (2002).
5. L. J. Sham, T. M. Rice, *Phys. Rev.* **144**, 708 (1966).
6. V. M. Axt, A. Stahl, *Z. Phys. B* **93**, 195 (1994).
7. T. H. Stievater *et al.*, *Phys. Rev. Lett.* **87**, 133603 (2001).
8. H. Kamada, H. Gotoh, J. Temmyo, T. Takagahara, H. Ando, *Phys. Rev. Lett.* **87**, 246401 (2001).
9. H. Htoon *et al.*, *Phys. Rev. Lett.* **88**, 087401 (2002).
10. A. Zrenner *et al.*, *Nature* **418**, 612 (2002).
11. J. J. Sanchez-Mondragon, N. B. Narozhny, J. H. Eberly, *Phys. Rev. Lett.* **51**, 550 (1983).
12. J. P. Reithmaier *et al.*, *Nature* **432**, 197 (2004).
13. T. Yoshie *et al.*, *Nature* **432**, 200 (2004).
14. K. Hennessy *et al.*, *Nature* **445**, 896 (2007).
15. B. R. Mollow, *Phys. Rev.* **188**, 1969 (1969).
16. J. Dupont-Roc, G. Grynberg, C. Cohen-Tannoudji, *Atom-Photon Interactions: Basic Processes and Applications* (Wiley, New York, 1998).
17. S. H. Autler, C. H. Townes, *Phys. Rev.* **100**, 703 (1955).
18. E. V. Baklanov, V. P. Chebotaev, *Sov. Phys. JETP* **34**, 490 (1972).
19. B. R. Mollow, *Phys. Rev. A.* **5**, 2217 (1972).
20. S. Haroche, F. Hartmann, *Phys. Rev. A.* **6**, 1280 (1972).
21. F. Y. Wu, S. Ezekiel, M. Ducloy, B. R. Mollow, *Phys. Rev. Lett.* **38**, 1077 (1977).
22. M. T. Gruneisen, K. R. MacDonald, R. W. Boyd, *J. Opt. Soc. Am. B* **5**, 123 (1988).
23. S. G. Carter *et al.*, *Science* **310**, 651 (2005).
24. N. Lu, P. R. Berman, *Phys. Rev. A.* **44**, 5965 (1991).
25. Materials and methods are available as supporting material on *Science* Online.
26. D. Gammon, E. S. Snow, B. V. Shanabrook, D. S. Katzer, D. Park, *Phys. Rev. Lett.* **76**, 3005 (1996).
27. M. O. Scully, M. S. Zubairy, *Quantum Optics* (Cambridge Univ. Press, Cambridge, 1997).
28. P. Meystre, M. Sargent, *Elements of Quantum Optics* (Springer-Verlag, Heidelberg, Germany, ed. 3, 1998) chap. 9.
29. A. Thranhardt, C. Ell, G. Khitrova, H. M. Gibbs, *Phys. Rev. B* **65**, 035327 (2002).
30. A. Hogele *et al.*, *Phys. Rev. Lett.* **93**, 217401 (2004).
31. A. Muller *et al.*, http://arxiv.org/abs/0707.0656.
32. R. Melet *et al.*, http://arxiv.org/abs/0707.3061.
33. This work is supported by the U.S. Army Research Office, Air Force Office of Scientific Research, Office of Naval Research, NSA/LPS, and FOCUS-NSF.

Deep Ultraviolet Light–Emitting Hexagonal Boron Nitride Synthesized at Atmospheric Pressure

Yoichi Kubota,* Kenji Watanabe, Osamu Tsuda, Takashi Taniguchi

Materials emitting light in the deep ultraviolet region around 200 nanometers are essential in a wide-range of applications, such as information storage technology, environmental protection, and medical treatment. Hexagonal boron nitride (hBN), which was recently found to be a promising deep ultraviolet light emitter, has traditionally been synthesized under high pressure and at high temperature. We successfully synthesized high-purity hBN crystals at atmospheric pressure by using a nickel-molybdenum solvent. The obtained hBN crystals emitted intense 215-nanometer luminescence at room temperature. This study demonstrates an easier way to grow high-quality hBN crystals, through their liquid-phase deposition on a substrate at atmospheric pressure.

Hexagonal boron nitride (hBN) and cubic boron nitride (cBN) are known as the representative crystal structures of BN. hBN is chemically and thermally stable and has been widely used as an electrical insulator and heat-resistant material for several decades; cBN, which is a high-density phase, is almost as hard as diamond (*1*).

Promising semiconductor characteristics due to a direct band gap of 5.97 eV were recently discovered in high-purity hBN crystals obtained by a high-pressure flux method,

National Institute for Materials Science (NIMS), Tsukuba, Ibaraki 305-0044, Japan.

*To whom correspondence should be addressed. E-mail: kubota.yoichi@nims.go.jp

paving the way for a material that efficiently emits deep ultraviolet (DUV) light (*2*, *3*). Similar to aluminum nitride (AlN) (*4*) and gallium nitride (GaN) (*5*), hBN may have attractive potential as a wide–band gap material. The layered structure of hBN makes the material mechanically weak, but it has greater chemical and thermal stability than GaN and AlN. The interesting optical properties of hBN, such as its huge exciton-binding energy (*2*), are due to its anisotropic structure, whereas a single crystal's basal plane in hBN is not easily broken because of its strong in-plane bonds. Thus far, the excitation of hBN by an accelerated electron beam or by far-UV light above the band-gap energy shows various efficient luminescence bands near the band edge.

However, the electronic properties of hBN near the band gap, which is fundamental information for developing DUV light–emission applications, are not yet fully understood, as seen by the fact that the origins of the luminescence bands are still controversial (*2*, *6*, *7*). Two opposed models, a Wannier exciton model and a Frenkel exciton model, have been proposed. The former model is based on results of the intrinsic absorption spectra near the band edge from pure single crystals (*2*), and the latter model is based on theoretical calculations and a luminescence study that used powder samples (*7*) showing very intense impurity bands around 4.0 eV (*8*). According to work examining the correlation between impurities and defects and luminescence properties (*8*, *9*), the intrinsic optical properties of samples are hindered by the extrinsic ones if experimenters do not have careful control of the samples' crystallinity and polymorphic purity. In (*7*), the strong 5.46-eV luminescence band, which is attributed to stacking faults (*9*), dominated in the region of the band gap, and the most intense photoluminescence band at 215 nm, observed in a pure single crystal, was not observed from the powder sample. Pure samples with high crystallinity must be indispensable for developing this new material for DUV light–emitting applications. Because high-quality hBN crystals have so far been produced only by high-pressure processes, it is important to discover an alternative synthesis scheme for conventional crystal growth at atmospheric pressure.

DUV-luminous single-crystalline hBN has been created through the reduction of O and C impurities with the use of a reactive solvent of the Ba-BN system under high pressure (*2*, *3*, *8*).

P H Y S I C A L R E V I E W L E T T E R S

Selective Optical Control of Electron Spin Coherence in Singly Charged GaAs-Al$_{0.3}$Ga$_{0.7}$As Quantum Dots

Yanwen Wu,[1] Erik D. Kim,[1] Xiaodong Xu,[1] Jun Cheng,[1] D. G. Steel,[1,*] A. S. Bracker,[2] D. Gammon,[2]
Sophia E. Economou,[3,†] and L. J. Sham[3]

[1]*The H. M. Randall Laboratory of Physics, University of Michigan, Ann Arbor, Michigan 48109, USA*
[2]*The Naval Research Laboratory, Washington D.C. 20375, USA*
[3]*Department of Physics, University of California, San Diego, La Jolla, California, 92093-0319, USA*
(Received 22 February 2007; published 29 August 2007)

Coherent transient excitation of the spin ground states in singly charged quantum dots creates optically coupled and decoupled states of the electron spin. We demonstrate selective excitation from the spin ground states to the trion state through phase sensitive control of the spin coherence via these three states, leading to partial rotations of the spin vector. This progress lays the ground work for achieving complete ultrafast spin rotations.

The two spin states of an electron inside a semiconductor quantum dot (QD) can be mapped directly to the two operational states in quantum information processing. The lifetime of the spin states is on the order of milliseconds [1–3], making the electron spin an ideal realization of a quantum bit (qubit). Electron spin rotations have already been demonstrated in surface gated dots using electrical gates [4], but the operation time is limited to a few microseconds by the microwave control resonant with the spin states. Alternatively, ultrafast optical pulses are readily available. Manipulating the spin states with these pulses increases the gate operation speed and hence the number of operations during the spin coherence lifetime. Fast operation rates are crucial for practical quantum information processing.

In this Letter, we demonstrate phase sensitive partial rotations of the electron spin vector in an ensemble of singly charged QDs using picosecond pulses. Similar rotations have been performed on electrons in quantum wells [5,6]. The rotations are achieved through optically coupling the spin ground states to the charged exciton (trion) state. The accomplishment of the partial rotations prepares the way for the demonstration of complete rotations of a single spin, which would encompass arbitrary qubit rotations.

The sample used in this study contains an ensemble of interface fluctuation GaAs/Al$_{0.3}$Ga$_{0.7}$As QDs (IFQD) [7–9] charged with single electrons through modulation silicon δ-doping. The number of electrons in each dot is determined by the doping density of the sample. In this case, the doping density is $10^{10}/cm^2$, which gives an average of one electron per dot [10]. The sample is placed inside a magnetic cryostat cooled to 5 K. The magnetic field applied in the experiments is aligned in the Voigt geometry, perpendicular to the sample growth axis, z. The magnitude of the field is fixed at $B = 6.6$ T.

The population and coherence decay times in these QDs range from 30 ps for the trion population to a T_2^* of about

400 ps for the ensemble spin coherence at $B = 6.6$ T [11]. As a compromise between temporal and spectral resolution, 3 ps pulses are chosen for the experiments. Three pulses are used to excite, control, and measure the QD system, denoted as the pump pulse, the control pulse with tunable delay (τ_c) and pulse area (θ_c), and the temporally scanning probe pulse. The pump and probe pulses are each modulated at 1 MHz and 1.05 MHz, respectively, while the control pulse is unmodulated. The nonlinear optical signal in differential transmission (DT) is homodyne-detected along the probe path at the difference frequency of 50 kHz.

The energy structure of the singly charged QD at $B = 0$ T can be described by two degenerate two-level systems, each consisting of one spin ground state and one trion excited state, as shown in Fig. 1(a). The total angular momentum projections along the z axis of the spin ground
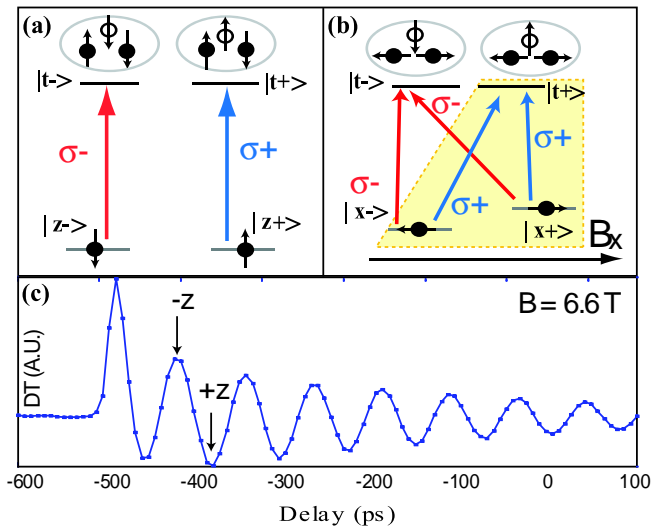

FIG. 1 (color online). Energy level diagrams of a charged QD at (a) $B = 0$ T and (b) $B \neq 0$ T in the Voigt geometry. (c) Two-beam (pump and probe) quantum oscillation signal of the initialized spin polarization at $B = 6.6$ T.

states $|z\pm\rangle$ are $\pm\frac{1}{2}$, defined by the electron spin, while those of the singlet trion states $|t\pm\rangle$ are $\pm\frac{3}{2}$, defined by the hole spin. The electron spins do not contribute to the total angular momentum of the trion due to the antipairing. The allowed optical transitions are then restricted to $\triangle m = \pm 1$ for $\sigma_\pm$ polarized excitations. This angular momentum restriction inhibits optical coupling between the two spin states.

Indirect optical coupling between the spin states is enabled by applying a magnetic field in the Voigt geometry, which produces two new eigenstates of the electron spin, $|x\pm\rangle = (|z+\rangle \pm |z-\rangle)/\sqrt{2}$ parallel or antiparallel to $\vec{x}$, the magnetic field direction [Fig. 1(b)]. The in-plane electron g factor in this sample is 0.13 [9,12], and thus the Zeeman splitting is approximately $\Delta \sim 50\ \mu$eV at 6.6 T.

In contrast, the highly suppressed mixing of the light and heavy hole states at even 6.6 T by the strong spin orbit coupling in this particular sample leads to a negligibly small in-plane hole g factor [9]. This causes the hole spins to be pinned along the z axis. Consequently, the trion states remain unaffected by the magnetic field. The spin ground states are now optically coupled through the trion states by either σ_+ or σ_- polarized optical pulses. Since the two Λ systems are essentially equivalent, without loss of generality, we concentrate on the σ_+ polarized Λ system highlighted in Fig. 1(b).

In the presence of the σ_+ pulses, stimulated Raman transitions are driven through the trion state $|t+\rangle$. The σ_+ pulses have a bandwidth of $\Omega \sim 400\ \mu$eV $\gg \Delta$, which couple both spin states, $|x\pm\rangle$, to $|t+\rangle$ simultaneously and equally. The equations of motion in the field interaction representation are then

$$\dot{C}_{|x+\rangle} = -i\chi * C_{|t+\rangle}, \qquad \dot{C}_{|x-\rangle} = -i\chi * C_{|t+\rangle},$$
$$\dot{C}_{|t+\rangle} = -i\chi(C_{|x+\rangle} + C_{|x-\rangle}), \qquad (1)$$

where the C's are the probability amplitudes of the different states and χ is the optical field. Two optically coupled and decoupled states, $|z\pm\rangle = (|x+\rangle \pm |x-\rangle)/\sqrt{2}$, are formed for the σ_+ polarization chosen. The $|z-\rangle$ state has no χ dependence, indicating that it is completely decoupled from the optical field. Conversely, $|z+\rangle$ is fully coupled to the σ_+ optical excitation. Spin initialization and polarization control are achieved utilizing this state pair. Decay terms are not included in the equations as long as the pulse duration is short compared to the trion and spin decay times. For evolution of the system after the pulses, trion decay is important, as discussed later.

At a temperature of 5 K, the thermal excitation energy is 430 μeV, which is an order of magnitude larger than the electron Zeeman splitting energy, Δ. This results in a completely mixed state of the electron spin, which also means equal population in both spin ground states and zero spin coherence in any basis. This completely mixed spin subspace is inoperable using only unitary transformations within this two-level system.

The initialization of the spin out of the completely mixed state is accomplished with a single pump pulse. A probe pulse reads out the result. The pump pulse transfers population from state $|z+\rangle$ to the trion $|t+\rangle$ state, leaving a net population difference of magnitude ξ in the optically decoupled state $|z-\rangle$. This population difference in the spin subspace signifies a net spin polarization in the $-\vec{z}$ direction. The net spin polarization precesses at the Larmor frequency, $\omega_L = \frac{\Delta}{\hbar}$, around the magnetic field in the z-y plane, corresponding to population cycling through the $|z\pm\rangle$ states. The beat signal in Fig. 1(c) traces the projected magnitude of the spin polarization along $\vec{z}$, the optical readout axis. The peaks and troughs of the beats represent net spin polarization pointing along the $-\vec{z}$ (spin population in the $|z-\rangle$ state) and $\vec{z}$ (spin population in the $|z+\rangle$ state) directions, respectively.

The density matrix ρ_z in the z basis after initialization and trion decay can be written as a sum of the coherent and incoherent components in the absence of spin relaxation.

$$\rho_z = \rho_{\text{inc}} + \rho_{\text{coh}}$$
$$= \begin{bmatrix} \frac{1-\xi}{2} & 0 \\ 0 & \frac{1-\xi}{2} \end{bmatrix} + \xi \begin{bmatrix} \cos^2\frac{\omega_L\tau}{2} & \frac{i}{2}\sin\omega_L\tau \\ \frac{-i}{2}\sin\omega_L\tau & \sin^2\frac{\omega_L\tau}{2} \end{bmatrix} \quad (2)$$

where the delay time τ is measured from a peak of the Larmor oscillations. The incoherent part of the density matrix ρ_{inc} describes the equal distribution of the uninitialized spin population $1 - \xi$ between the $|z\pm\rangle$ states. The coherent part ρ_{coh} describes the time evolution of the initialized spin population ξ. The initialized spin polarization with unit $\hbar/2$ in Cartesian coordinates is then given by

$$\vec{S}_{\text{coh}} = \xi(0, -\sin\omega_L\tau, \cos\omega_L\tau) \quad (3)$$

representing the precession of the spin vector around the x axis on the z-y plane.

We note here that at 6.6 T, the contribution from spontaneously generated coherence (SGC) [11] is negligible in the initialization process. The maximum initialized population is 0.5 via a π pulse excitation to the trion. A more detailed discussion of the initialization process has been reported theoretically [13] and experimentally [12] using multiple pump pulses. The ensemble spin coherence time of about 400 ps at 6.6 T is limited by the inhomogeneous broadening of the electron g factor and the spectral diffusion process.

The initialized spin polarization described by ρ_{coh} can now be controlled through an optical pulse. Arbitrary rotations of the spin are achieved through selective excitations at different positions on the z-y plane during the precession of the net spin polarization. By controlling this excitation, we can control both the relative population and phase between the $|z\pm\rangle$ components in the pure state. If the optical field performs a coherent Rabi rotation on $|z+\rangle$ via the trion and back with a net phase change, ϕ, a general spin state, $|\psi\rangle$, will have the phase change in its $|z+\rangle$ component without affecting its $|z-\rangle$ component, i.e.,

its spin vector rotates about the z axis. The general spin state for the initialized and properly controlled spin polarization has the form

$$|\psi\rangle = \sqrt{\xi}\left[e^{i\phi}\cos\frac{\omega_L\tau}{2}|z+\rangle - i\sin\frac{\omega_L\tau}{2}|z-\rangle \right] \quad (4)$$

where ϕ is the net phase between states $|z\pm\rangle$ induced by the control pulse. For $\omega_L\tau = \frac{\pi}{2}$ and $\phi = \mp\frac{\pi}{2}$, the spin state $|\psi\rangle$ is proportional to $|x\pm\rangle$ along the x axis. Similarly, a zero or π value of ϕ puts the spin state in $|y\pm\rangle$ along the y axis. If the optical Rabi rotation is π, bringing state $|z+\rangle$ to the trion state, followed by the trion decaying equally to the $|x\pm\rangle$ states thus annihilating a portion of the spin coherence, then the net result is a rotation together with a reduction of the magnitude of the spin vector. This is a partial rotation.

We first consider using a pulse area $\theta_c = \pi$ control pulse delayed at different τ_c from the pump pulse to rotate the initialized spin polarization at different times during the Larmor precession. When the control pulse arrives at $\tau_c = \tau_{+z} = \frac{\pi}{\omega_L}$, the entire initialized spin population ξ is in state $|z+\rangle$ as shown in Fig. 2(a). The π pulse excites all of ξ from $|z+\rangle$ to the trion state $|t+\rangle$. After the decay of $|t+\rangle$, the system returns to the completely mixed state, as the excited population ξ redistributes equally and incoherently between the two spin ground states. As a result, the quantum beats are annihilated and the simulated signal exhibits
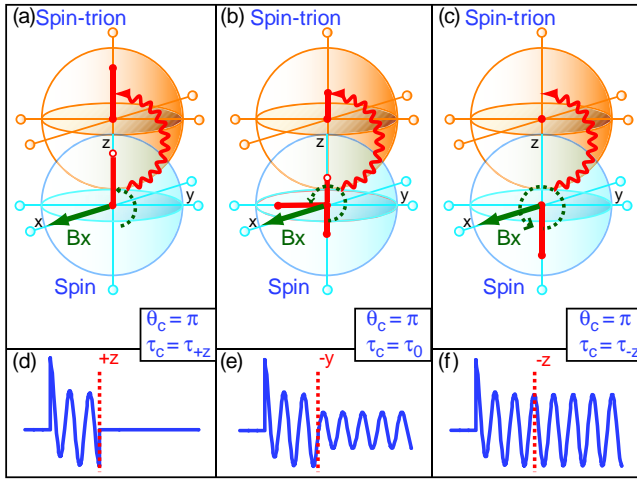

FIG. 2 (color online).   Evolution of the spin polarization vector at control pulse delays of (a) $\tau_c = \tau_{+z}$, (b) $\tau_c = \tau_0$, and (c) $\tau_c = \tau_{-z}$. The upper (lower) sphere is the trion-spin (spin) subspace. The zig-zagged lines represent the σ_+ polarized optical control field. The solid arrows indicate the magnetic field directions, and the dotted curves are the paths of the precession of the spin polarization vector prior to the arrival of the control pulse. The solid bars represent the spin polarization alignment. (d), (e), and (f) are simulated quantum oscillation signals before and after the control pulse at the different τ_c indicated in (a), (b), and (c), respectively.

a flat line following the control pulse at $\tau_c = \tau_{+z}$ as shown in Fig. 2(d).

By moving the control pulse to $\tau_c = \tau_0 = \frac{3\pi}{2\omega_L}$, where the optical signal or the z component of the spin polarization is zero as shown in Fig. 2(b), the spin polarization is along $-\vec{y}$, and states $|z\pm\rangle$ have equal populations. The oscillation amplitude is decreased by half after the control pulse as expected in Fig. 2(e) because half of ξ is being "protected" in state $|z-\rangle$ and is not destroyed by the decay and redistribution process.

Finally, when the spin polarization is along $-\vec{z}$ at $\tau_c = \tau_{-z} = \frac{2\pi}{\omega_L}$, all of ξ is preserved in the optically decoupled state $|z-\rangle$ as illustrated in Fig. 2(c). The quantum beats are unaffected by the control pulse and continue to oscillate uninterrupted as pictured in Fig. 2(f).

Overall then, as this delay τ_c of the control optical pulse is scanned, the beat amplitude, which is also the magnitude of the spin polarization $|\vec{S}(\tau_c)|$ from Eq. (3) after the control pulse, follows an oscillatory behavior

$$|\vec{S}_{\text{coh}}(\tau_c)| = \frac{\xi}{2}(1 + \cos\omega_L\tau_c). \quad (5)$$

This discussion has treated the optical excitations and precession dynamics in the magnetic field separately. The assumption is valid since the temporal pulse width (3 ps) is much shorter than the oscillation period of the quantum beats (85 ps). Therefore, we can approximate the excitation to the trion state as instantaneous so that precession around the magnetic field during the optical pulse duration is negligible.

Experimentally, we need to consider the effect of the control on the uninitialized population in addition to the initialized population. In the two-frequency modulation spectroscopy used in the experiments, the DT signal detected at the difference modulation frequency is equivalent to the signal taken with the pump pulse on minus pump pulse off. When the pump beam is off, the $\theta_c = \pi$ control pulse produces quantum beats with an amplitude of $|\vec{S}_{\text{off}}| = \frac{1}{2}$ from the completely mixed spin states, regardless of the control delay τ_c. However, when the pump pulse is turned on, the position of the control delay τ_c becomes significant. The beat amplitude after both the pump and control pulses consists of two terms, where the first is a τ_c dependent controlled term, $|\vec{S}_{\text{coh}}(\tau_c)|$, due to both the pump and control pulses as described in Eq. (5), and the second term is a noncontrolled term, $|\vec{S}_{\text{inc}}| = \frac{1-\xi}{2}$, due to the redistributed uninitialized spin population. The final amplitude of the normalized quantum beat signal detected after the control pulse, determined by the function $I_{\text{on-off}}$ for pump pulse on minus off, is the sum of the controlled ($|\vec{S}_{\text{coh}}(\tau_c)|$) and noncontrolled terms ($|\vec{S}_{\text{inc}}|$) minus $|\vec{S}_{\text{off}}|$,

$$I_{\text{on-off}}(\tau_c) = \frac{\xi}{2}\cos\omega_L\tau_c. \quad (6)$$
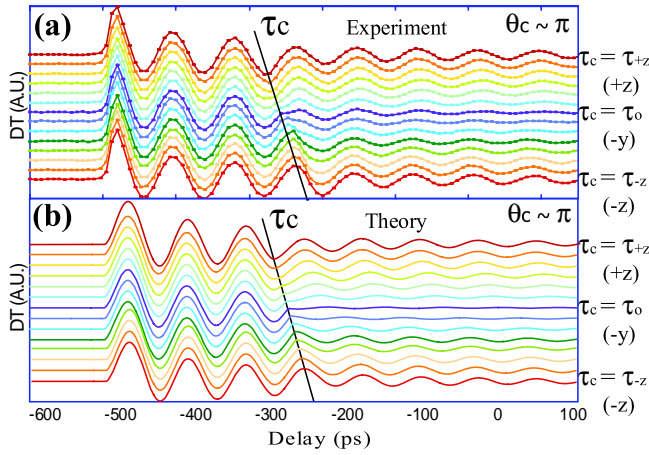
PHYSICAL REVIEW LETTERS

FIG. 3 (color online). (a) Experimental result of the three-beam (initialization, control, and probe) quantum oscillation signal at different control delays τ_c. The solid line indicates the position of the control pulse. (b) Theoretical simulations of the same experimental set up in (a).

Data of the three-beam control experiment are shown in Fig. 3(a). The $\cos\omega_L\tau_c$ dependence observed in the signal beat amplitudes after τ_c (solid line) in Fig. 3(a) is in contrast with the $1 + \cos\omega_L\tau_c$ dependence of the physical pictures in Figs. 2(d)–2(f) as anticipated in Eq. (6). For example, at $\tau_c = \tau_{+z}$, Fig. 2(d) shows vanishing quantum beats after τ_c, while the quantum beat signal corresponding to $\tau_c = \tau_{+z}$ in Fig. 3(a) persists due to the nonzero $I_{\text{on-off}}$. Numerical simulations in Fig. 3(b) take into account the experimental parameters, such as the pulse width, beam modulations, and decoherence times of the system. The theoretical results are in excellent agreement with the experiment.

We note that unlike the work in Ref. [12], where the observed signal is a result of the quantum interference between two independently initialized spin coherences induced by the pump and control pulses, the behavior described here is due to the subsequent rotation by the control pulse of the actual pump-induced spin coherence. In terms of optical pulses as transformation matrices for the state vector of the quantum system, the former is a sum of two matrices while the latter is a product.

To completely control the rotations of the electron spin in the spin subspace without populating the trion, we need to use a $\theta_c = 2\pi$ pulse to control the relative phase ϕ between states $|z\pm\rangle$ in addition to the populations. This phase control performs a complete Rabi rotation of state $|z+\rangle$. As a result, the population in $|z+\rangle$ is unaffected by the 2π pulse, but the state gains an overall phase depending on the detuning of the pulse from the trion state [14]. For example, the overall phase gained for an on resonance 2π control pulse is $\phi = \pi$. At $\tau_c = \tau_0$, the spin state is rotated from $|y-\rangle$ to $|y+\rangle$, representing a spin flip. Similarly, $\phi = \frac{\pi}{2}$ rotates the spin state from $|y-\rangle$ to $|x+\rangle$. The magnetically induced Larmor precession about $\vec{x}$ and optically induced rotation about $\vec{z}$ are sufficient for creating any

arbitrary spin state. For an all-optical ultrafast spin rotation scheme, optically induced rotation around $\vec{x}$ [15] can replace the Larmor precession.

Our data shows a partial rotation. The reason for the limitation in IFQDs, namely, the difficulty in completing a trion Rabi rotation, is not fully understood, especially in light of the fact that Rabi oscillations in neutral IFQDs have been observed [16]. However, the demonstration of Rabi oscillations of trions in self-assembled QDs [3] shows that the result in this experiment should be readily applicable in those structures.

*dst@umich.edu
†Present address: Naval Research Laboratory, WA, DC 20375, USA

[1] M. Kroutvar, Y. Ducommun, D. Heiss, M. Bichler, D. Schuh, G. Abstreiter, and J. J. Finley, Nature (London) **432**, 81 (2004).

[2] J. M. Elzerman, R. Hanson, L. H. W. van Beveren, B. Witkamp, L. M. K. Vandersypen, and L. P. Kouwenhoven, Nature (London) **430**, 431 (2004).

[3] A. Greilich, R. Oulton, E. A. Zhukov, I. A. Yugova, D. R. Yakovlev, M. Bayer, A. Shabaev, A. L. Efros, I. A. Merkulov, and V. Stavarache et al., Phys. Rev. Lett. **96**, 227401 (2006).

[4] F. H. L. Koppens, C. Buizert, K. J. Tielrooij, I. T. Vink, K. C. Nowack, T. Meunier, L. P. Kouwenhoven, and L. M. K. Vandersypen, Nature (London) **442**, 766 (2006).

[5] J. A. Gupta, R. Knobel, N. Samarth, and D. D. Awschalom, Science **292**, 2458 (2001).

[6] Y. Shen, A. M. Goebel, and H. Wang, Phys. Rev. B **75**, 045341 (2007).

[7] D. Gammon, E. S. Snow, B. V. Shanabrook, D. S. Katzer, and D. Park, Phys. Rev. Lett. **76**, 3005 (1996).

[8] D. Gammon, E. S. Snow, B. V. Shanabrook, D. S. Katzer, and D. Park, Science **273**, 87 (1996).

[9] J. G. Tischler, A. S. Bracker, D. Gammon, and D. Park, Phys. Rev. B **66**, 081310(R) (2002).

[10] A. S. Bracker, E. A. Stinaff, D. Gammon, M. E. Ware, J. G. Tischler, D. Park, D. Gershoni, A. V. Filinov, M. Bonitz, and A. V. Filinov et al., Phys. Rev. B **72**, 035332 (2005).

[11] M. V. G. Dutt, J. Cheng, B. Li, X. Xu, X. Li, P. R. Berman, D. G. Steel, A. S. Bracker, D. Gammon, and S. E. Economou et al., Phys. Rev. Lett. **94**, 227403 (2005).

[12] M. V. G. Dutt, J. Cheng, Y. Wu, X. Xu, D. G. Steel, A. S. Bracker, D. Gammon, S. E. Economou, R.-B. Liu, and L. J. Sham, Phys. Rev. B **74**, 125306 (2006).

[13] A. Shabaev, A. L. Efros, D. Gammon, and I. A. Merkulov, Phys. Rev. B **68**, 201305(R) (2003).

[14] S. E. Economou, L. J. Sham, Y. Wu, and D. G. Steel, Phys. Rev. B **74**, 205415 (2006).

[15] C. Emary and L. J. Sham, J. Phys. Condens. Matter **19**, 056203 (2007).

[16] T. H. Stievater, X. Li, D. G. Steel, D. Gammon, D. S. Katzer, D. Park, C. Piermarocchi, and L. J. Sham, Phys. Rev. Lett. **87**, 133603 (2001).

P H Y S I C A L R E V I E W L E T T E R S

Fast Spin State Initialization in a Singly Charged InAs-GaAs Quantum Dot by Optical Cooling

Xiaodong Xu,[1] Yanwen Wu,[1] Bo Sun,[1] Qiong Huang,[1] Jun Cheng,[1] D. G. Steel,[1,*] A. S. Bracker,[2] D. Gammon,[2]
C. Emary,[3] and L. J. Sham[3]

[1]*The H. M. Randall Laboratory of Physics, The University of Michigan, Ann Arbor, Michigan 48109, USA*
[2]*The Naval Research Laboratory, Washington D.C. 20375, USA*
[3]*Department of Physics, The University of California-San Diego, La Jolla, California 92093, USA*
(Received 1 February 2007; published 28 August 2007)

Quantum computation requires a continuous supply of rapidly initialized qubits for quantum error correction. Here, we demonstrate fast spin state initialization with near unity efficiency in a singly charged quantum dot by optically cooling an electron spin. The electron spin is successfully cooled from 5 to 0.06 K at a magnetic field of 0.88 T applied in Voigt geometry. The spin cooling rate is of order 10^9 s^{-1}, which is set by the spontaneous decay rate of the excited state.

The use of electron spins in semiconductor quantum dots (QDs) as quantum bits (qubits) is being widely explored for quantum information and quantum computation (QIQC) [1–6]. A key element for QIQC is the initial quantum state preparation. QIQC requires not only qubits initialized in a known state for computation and gate operations, but also a continuous supply of low-entropy ancillary qubits for quantum error correction (QEC) [7,8]. A fault-tolerant quantum computation requires about 10^4 quantum operations before the qubits lose their coherence [7,8]. This requirement demands that the state initialization speed must be much faster than the quantum state decoherence rate.

The spin relaxation time ($T1$) of an electron spin trapped in a self-assembled In(Ga)As QD has been measured to be on the order of 20 ms [3], which sets an upper limit for the spin decoherence time in the absence of other interactions (e.g., phonon scattering, hyperfine interaction). The initialization of an electron spin state has been demonstrated recently in a singly charged QD by applying magnetic fields in the Faraday geometry [2]. Although near unity fidelity is successfully achieved, the initialization rate is about 3×10^5 s^{-1} [9], making it challenging for this scheme to satisfy the QEC requirement. A fast state initialization method with a high efficiency is essential for practical QEC processes.

In this Letter, we demonstrate fast spin state initialization (optical pumping or laser cooling of an electron spin [2]) in a singly charged InAs/GaAs self-assembled QD (SAQD) in the presence of a magnetic field in the Voigt geometry. The fast spin cooling with near unity efficiency is achieved at the spin cooling rate of about 10^9 s^{-1} via the resonant excitation of a trion state. The spin state is cooled from 5 to 0.06 K at a magnetic field of 0.88 T at a rate considerably faster than the spin decoherence rate.

The sample under study contains InAs SAQDs embedded in a Schottky diode structure. An aluminum mask with 1 μm apertures on the surface provides the spatial resolution to study a single QD. The number of electrons in

a QD can be controlled by varying the bias voltages across the sample. The experiment is performed at 5 K. Figure 1(a) displays a bias dependent photoluminescence (PL) intensity map of a single QD showing the charging effects. The state of interest is a single negatively charged exciton (X^-), which is called a trion and about 5.5 meV lower in energy than the neutral exciton state. Details regarding the physics of the bias dependent PL and discussion of the transition assignments are found in Ref [10–12].

The projection of the hole angular momentum on the sample growth direction determines the angular momentum of the trion state to be $| \pm \frac{3}{2}\rangle$. At zero magnetic field, the electron spin ground states $| \pm \frac{1}{2}\rangle$ are twofold degenerate. The only dipole allowed transitions are from the spin states $| \pm \frac{1}{2}\rangle$ to the trion states $| \pm \frac{3}{2}\rangle$ with σ^+ and σ^- excitations, respectively. Figure 1(b) shows the spin flip
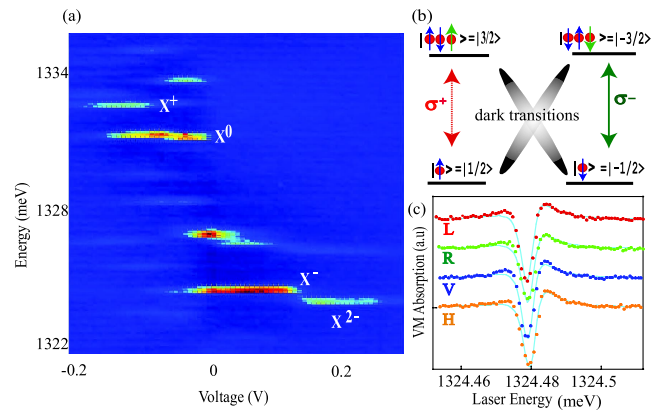

FIG. 1 (color online). (a) Bias dependent PL intensity map of a single InAs SAQD, where $X^{n\pm}$ denotes the charged exciton with n excess electrons ($-$) or holes ($+$). (b) Trion energy level diagram at zero magnetic field. (c) Polarization dependent VM spectra of a singly charged QD at zero magnetic field. L, R, V, and H denote left circular, right circular, vertical, and horizontal polarization, respectively. Curves are the fittings of the data.

Raman scattering transitions are ideally dark [13]. The imperfect selection rules will lead to finite spontaneous emission rates for the dark transitions [2], which ultimately limit the spin cooling speed under these conditions [14].

Figure 1(c) shows a polarization dependent study on a trion by voltage modulation (VM) spectroscopy [15] with a modulation amplitude about a quarter of the trion linewidth. No fine structure splitting was observed [16]. Analysis of the line shape shows an asymmetry that could arise from some kind of interference. Independent experiments [17] have suggested it arises from a coupling of the hole to the cap layer when the thickness of the cap layer exceeds a critical value. The effect, still under investigation, complicates the exact determination of the linewidth, but does not interfere with the qualitative features described below. Fitting yields a trion linewidth of 1.5 GHz.

In order to implement a fast spin state initialization, the dark transitions have to become bright, since the optical pumping rate depends on the spin flip Raman scattering process. This can be realized by applying a magnetic field perpendicular to the sample growth direction [001]. Figure 2(a) shows the VM absorption map [18,19] as a function of the applied bias at a magnetic field of 0.88 T along the [110] axis. The laser field is linearly polarized and 45° to the polarization axis ($\vec{\rho}$) of the quantum dot. In bias region II, the optical pumping rate is larger than the spin relaxation rate. Fast spin cooling is demonstrated, where the absorption of the laser beam is strongly suppressed by optical pumping. In region I, cotunneling (the tunneling of the electron between the quantum dot and the Fermi sea [2,20]) induced spin relaxation rate is comparable or larger than the optical pumping rate, so the depletion of the spin ground states is not achieved. Thus, the strong suppression of the absorption disappears in region I and a quartet transition pattern appears. The physics of the two bias regions is discussed below along with the bias dependent g factor associated with transition H1 and H2.

We first start with the bias region I of Fig. 2(a). As a magnetic field is applied along the [110] axis, it induces off diagonal terms in the Hamiltonian that couple both electron and hole states. The coupling leads to linearly polarized transitions from the spin ground states to the trion states. Figure 2(b) shows the corresponding four level trion model, where $|x\pm\rangle$ ($|t\pm\rangle$) are the spin (trion) eigenstates in the magnetic field. The Zeeman splitting of the electron spin (trion) states is $|g_{e\perp}\mu_B B_x|$ ($|g_{h\perp}\mu_B B_x|$), where $g_{e\perp}$ ($g_{h\perp}$) is the electron (hole) spin in-plane g factor, μ_B is Bohr magneton, and B_x is the applied magnetic field. The four linearly polarized transitions are labeled as V1, H1, H2, and V2, where $\overrightarrow{V1}\|\overrightarrow{V2} \perp \vec{\rho}$ and $\overrightarrow{H1}\|\overrightarrow{H2}\|\vec{\rho}$.

Our measurements confirm that the dark transitions become bright and all four transitions are linearly polarized. However, the polarization axis ($\vec{\rho}$) of the QD is not parallel or perpendicular to the applied magnetic field direction, rather it is 45° to $\vec{B}$ in the X-Y plane for this
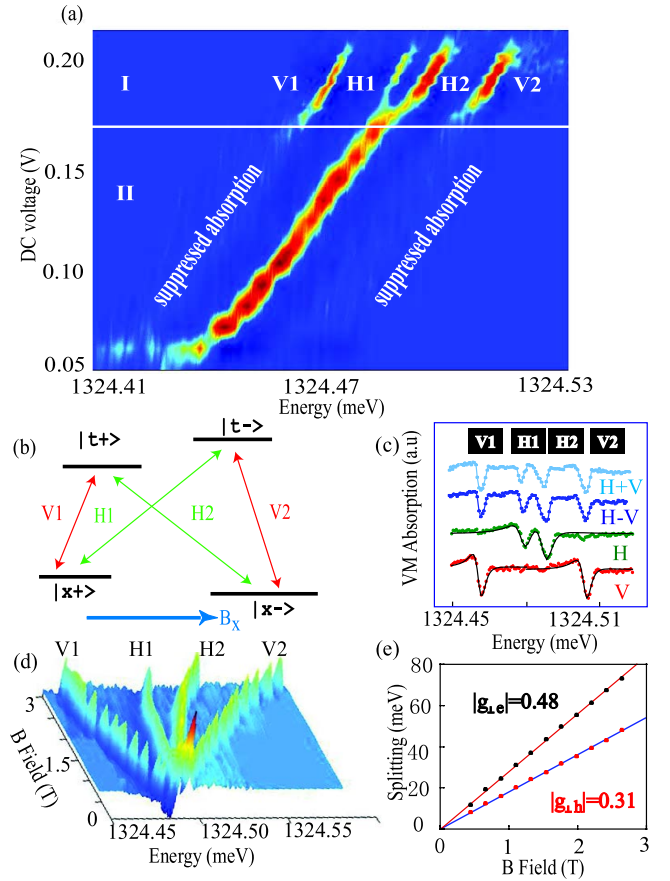

FIG. 2 (color online). (a) Bias dependent VM absorption map of a singly charged SAQD at a magnetic field of 0.88 T. The laser is 45° polarized. Voltage region I shows all four trion transitions. Spin state preparation is achieved in Voltage range II. (b) Energy level diagram of a trion. The gate voltage is set at 0.19 V for plots (c), (d), and (e). (c) Polarization dependent VM spectra of a singly charged QD at magnetic fields 0.88 T. The black curves are the fittings. (d) 3d plot of the trion evolution with various magnetic fields. The laser is 45° polarized. The data are inverted for clarity. (e) The electron (black dots) and hole (orange dots) Zeeman splitting as a function of the magnetic fields.

particular QD ($\vec{\rho}$ may vary from dot to dot). This observation indicates the existence of heavy and light hole mixing in our QDs caused by the QD in-plane anisotropy. The mixing effects observed here agree with the previous reports on the CdSe/ZnSe SAQDs [21]. The hole mixing only affects the intermediate trion states, but not the spin ground states. The only change introduced by the mixing effect is that $\vec{\rho}$ rotates away from $\vec{B}$, which is not essential to our optical pumping scheme. For simplicity, the light polarized along (perpendicular to) $\vec{\rho}$ is referred to as horizontally (vertically) polarized.

Figure 2(c) shows the polarization study of the trion state at gate voltage 0.19 V. A quartet transition pattern is excited with a 45° linearly polarized light. When the light is vertically (horizontally) polarized, the optical field only excites the outer (inner) two transitions of the quartet.

Thus, the inner and outer transitions are strictly linearly polarized and orthogonal to each other, which inhibits spontaneously generated coherence (SGC) [13]. The observation of the quartet demonstrates that under a transverse magnetic field, all four trion transitions are optically allowed and obey well defined polarization selection rules.

The evolution of the trion states as a function of the magnetic field is illustrated with the fan diagram in Fig. 2(d). The trion states start with a single peak at zero magnetic field and split into four lines at finite magnetic fields. The energy difference between transitions $V1$ and $H1$ ($H2$) corresponds to the hole (electron) Zeeman splitting. The electron and hole Zeeman splittings are plotted in Fig. 2(e) as a function of the applied magnetic fields. The linear fittings yield $|g_{e\perp}|$ and $|g_{h\perp}|$ of 0.48 and 0.31, respectively. Although the absolute signs of $|g_{e\perp}|$ and $|g_{h\perp}|$ are not identified experimentally, we are able to tell that $|g_{e\perp}|$ and $|g_{h\perp}|$ have the same sign.

In region II of Fig. 2(a), spin relaxation is inhibited. When the laser beam is resonant with transition $V1$, as shown in Fig. 3(a), the electron spin in $|x+\rangle$ state will be excited to the trion state $|t+\rangle$ and then relax equally to the two spin ground states as suggested by the comparable absorption strengths and linewidths. That is to say, because the spin flip resonant Raman scattering process is now allowed in the Voigt profile, the optical induced spin flip
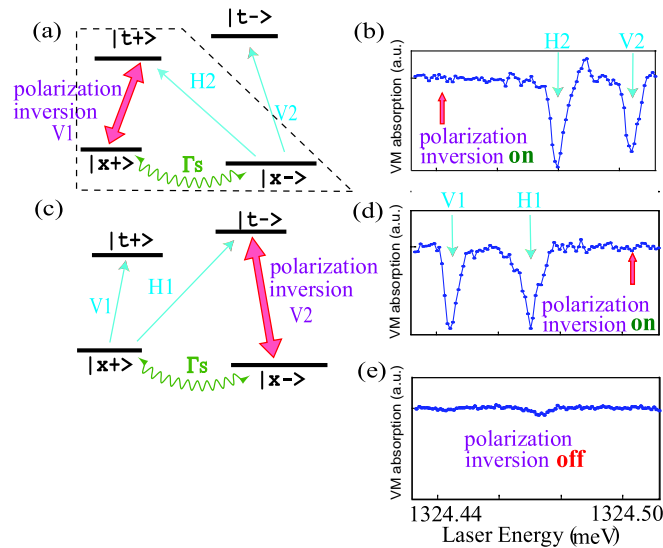

FIG. 3 (color online). Demonstration of the spin state preparation in $|x+>$ ($|x->$) state at magnetic field 1.32 T and gate voltage 0.12 V. The scanning laser is 45° polarized and the PIB is vertically polarized. (a) and (b) [(c) and (d)]. The PIB is resonant with the transition $V1$ ($V2$) while probing the transitions $H2$ and $V2$ ($H1$ and $V1$). (e) One beam absorption spectrum of the trion state in the absence of the PIB. The absorption of transitions $V1$ and $V2$ are strongly suppressed due to the optical pumping effect. Since the degeneracy of transitions $H1$ and $H2$ are lifted by increasing the magnetic field to 1.32 T, the central peak is also suppressed.

process is dramatically "sped up", ensuring fast spin cooling. Since the electron spin in the ground state has a much slower relaxation rate than the trion spontaneous decay rate, the electron spin will be optically pumped into the $|x-\rangle$ spin state within a few radiative cycles. The signature of optical pumping is that transition $V1$ becomes transparent to the laser beam. The preparation of $|x+\rangle$ works in a similar way. This is clearly demonstrated in bias range II of Fig. 2(a). When the laser is on resonance with $V1$ ($V2$), the absorption is strongly suppressed and the transition becomes transparent. Thus, the polarized spin states can be selectively prepared in either the $|x-\rangle$ or $|x+\rangle$ spin state.

The mechanism of the spin state preparation can also be explained in terms of saturation spectroscopy. A simple rate equation calculation for a three level lambda system gives the saturation intensity for a trion transition as $I_{\text{SAT}} \simeq I_{\text{SAT}_0} \frac{\Gamma_s}{\Gamma}$, where I_{SAT_0} is the trion saturation intensity at zero magnetic field, Γ_s is the spin relaxation rate, and Γ is the trion spontaneous decay rate. The spin relaxation time $\frac{1}{\Gamma_s}$ has been reported to be on the order of tens of milliseconds [3]. It is much longer than the trion decay time $\frac{1}{\Gamma}$, which is about a few hundred picoseconds [20]. Therefore, in the presence of the transverse magnetic fields, the saturation intensity I_{SAT} of the trion system could be about 6 to 7 orders of magnitude weaker than I_{SAT_0}. Thus, the trion transition is easily saturated and becomes transparent to the optical beam.

The data in the transition region from I to II in Fig. 2(a) show the signature of a bias dependent electron g factor, which leads to transitions $H1$ and $H2$ evolving from two well-resolved lines in region I into a central absorption peak in region II. Since transitions $H1$ and $H2$ are nearly degenerate in region II, when the laser is on resonance with transition $H1$, it is also nearly resonant with $H2$. Therefore, the optical pumping effect is partially canceled by the bidirectional pumping induced by the same optical field. Hence, the optical pumping effect is suppressed and results in the central absorption peak. The origin of this behavior remains under investigation, but it is likely that the strong bias dependence is more complex than the bias dependent g factors reported earlier in quantum wells [22] and for hole in QDs [23]. Fortunately, the behavior does not impact the main qualitative conclusion of the work.

In order to prove that the laser beam leads to nearly complete spin polarization and prepares the spin state as $|x-\rangle$ ($|x+\rangle$) by pumping transition $V1$ ($V2$), a polarization inversion beam (PIB) is tuned to be on resonance with transition $V2$ ($V1$). As shown in Fig. 3(a), while the PIB is tuned to be on resonance with transition $V1$, it repolarizes the spin ground states prepared by pumping transition $V2$ (i.e., redistributes the population between the spin ground states). This leads to the recovery of the absorption peaks at transitions $V2$ and $H2$. Figure 3(c) and 3(d) show that transitions $V1$ and $H1$ can also be recovered by tuning

the PIB to be on resonance with transition *V*2. Considering that the spin cooling process prepares a low-entropy polarized spin state, depending on the intensity of the PIB, the effect of the PIB is to increase the entropy of the system by generating a mixed spin ground state at low intensity, or reversing the spin polarization at high intensity.

The excited state decay rate is 2π times the absorption linewidth in the absence of pure dephasing or spectral wandering. Nearly degenerate differential transmission (NDT) is particularly sensitive to these latter two effects [24,25]. We have performed NDT on the trion state (data not shown), and while the data are complicated by the effect of the Fano interference, they show no evidence of either significant pure dephasing or spectral wandering.

The optical pumping rate is analyzed by the method developed in Ref. [14]. When the laser is on resonance with one trion transition, the four level model can be reduced to a three level lambda system, as shown in the dashed box in Fig. 3(a). To keep the discussion general, the trion decay rates to the two spin ground states $|x+\rangle$ and $|x-\rangle$ are Γ_{t+x+} and Γ_{t+x-}, respectively. The optical pumping rate is calculated to be

$$\lambda = \frac{-\Gamma_{t+x-}}{6b\kappa^{1/3}}(3^{2/3} + 2 \times 3^{2/3}b + 3^{2/3}b^2 - 16 \times 3^{2/3}r^2$$
$$- 3\kappa^{1/3} - 3b\kappa^{1/3} + 3^{1/3}\kappa^{2/3}), \qquad (1)$$

$\kappa = 72r^2 + \frac{1}{3}[46\,656r^4 - 27(1 + 2b + b^2 - 16r^2)^3]^{1/2}$, where $r = \frac{\Omega}{\Gamma_{t+x+}}$, Ω is the Rabi frequency, the branching ratio b is $\frac{\Gamma_{t+x-}}{\Gamma_{t+x+}}$. If we take $b = 1$ and $r \gg 1$, the optical pumping rate is $\Gamma_{t+x-}/2$, as shown in Ref. [14].

Using the line shape data in Fig. 3, a linewidth of order 1.2 GHz (1.5 GHz), in the absence of pure dephasing or spectral wandering, corresponds to Γ_{t+x+} (Γ_{t+x-}) of 7.5×10^9 s^{-1} (9.4×10^9 s^{-1}). In the spin state preparation experiment, the Rabi frequency of the pump beam approximately equals Γ_{t+x+}. Thus, by inserting $b = 1.25$ and $r = 1$ into Eq. (1), we infer an optical pumping rate of order 4×10^9 s^{-1}. The optical pumping rate inferred from the measured linewidth may be an upper limit if the linewidth is broadened by the spectral diffusion process [16]. The hole coupling to the continuum states might also result uncertainty in the radiative lifetime (at most a factor of 3) but not affect the qualitative speed up by a few orders of magnitude due to the magnetic field induced state mixing. Using a more conservative trion relaxation rate of 1×10^9 s^{-1} reported by Ref [26], our scheme infers an spin state initialization rate of order 5×10^8 s^{-1}.

The Voigt profile introduces a limitation to the optical pumping efficiency [14]. This arises from the fact that transitions *V*1 and *V*2 have the same polarization selection rules. When the laser is resonant with transition *V*1 (*V*2), transition *V*2 (*V*1) will be off-resonantly coupled, which causes a small amount of the spin population to be pumped back. As mentioned above, this type of off-resonant coupling is responsible for the central absorption peak in Fig. 2(a). At a magnetic field of 0.88 T, a spin state preparation efficiency of $(98.9 \pm 0.4)\%$ (the error comes from the measurement noise) is achieved experimentally, which corresponds to a spin temperature of 0.06 K [2,27,28]. This demonstrates laser cooling of an electron spin from 5 (the experimental temperature) to 0.06 K in a singly charged QD. To reach the same efficiency at 5 K by thermal equilibration, the applied magnetic field would need to be 69 T at a much slower initialization speed as well.

*dst@umich.edu

[1] D. Loss and D. P. DiVincenzo, Phys. Rev. A **57**, 120 (1998).
[2] Mete Atature *et al.*, Science **312**, 551 (2006).
[3] Miro Kroutvar *et al.*, Nature (London) **432**, 81 (2004).
[4] A. S. Bracker *et al.*, Phys. Rev. Lett. **94**, 047402 (2005).
[5] J. G. Tischler *et al.*, Phys. Rev. B **66**, 081310(R) (2002).
[6] A. Greilich *et al.*, Science **313**, 341 (2006).
[7] D. P. DiVincenzo, Fortschr. Phys. **48**, 771 (2000).
[8] J. Preskill, Proc. R. Soc. A **454**, 385 (1998).
[9] This is calculated by the numbers provided in Ref. [2].
[10] R. J. Warburton *et al.*, Nature (London) **405**, 926 (2000).
[11] M. E. Ware *et al.*, Phys. Rev. Lett. **95**, 177403 (2005).
[12] M. Ediger *et al.*, Phys. Rev. Lett. **98**, 036808 (2007).
[13] M. V. G. Dutt *et al.*, Phys. Rev. Lett. **94**, 227403 (2005).
[14] C. Emary *et al.*, Phys. Rev. Lett. **98**, 047401 (2007).
[15] Benito Alen *et al.*, Appl. Phys. Lett. **83**, 2235 (2003).
[16] A. Hogele *et al.*, Phys. Rev. Lett. **93**, 217401 (2004).
[17] R. Warburton (personal communication); M. Atature (personal communication).
[18] The difference in the range of the applied bias between PL and VM maps arises from the local electric field effect, which depends on the excitation wavelength [19].
[19] S. Seidl *et al.*, Phys. Rev. B **72**, 195339 (2005).
[20] J. M. Smith *et al.*, Phys. Rev. Lett. **94**, 197402 (2005).
[21] A. V. Koudinov *et al.*, Phys. Rev. B **70**, 241305(R) (2004).
[22] G. Salis *et al.*, Nature (London) **414**, 619 (2001).
[23] M. F. Doty *et al.*, Phys. Rev. Lett. **97**, 197202 (2006).
[24] N. H. Bonadeo *et al.*, Phys. Rev. Lett. **81**, 2759 (1998).
[25] H. Wang *et al.*, Phys. Rev. Lett. **65**, 1255 (1990).
[26] W. Langbein *et al.*, Phys. Rev. B **70**, 033301 (2004).
[27] A. Hogele *et al.*, Appl. Phys. Lett. **86**, 221905 (2005).
[28] Assuming the spin state is prepared in the $|x-\rangle$ state, the preparation efficiency is defined as $1 - \rho_{x+x+}/(\rho_{x+x+} + \rho_{x-x-})$. The spin temperature can be calculated by assuming Maxwell-Boltzmann distribution.

P H Y S I C A L   R E V I E W   L E T T E R S

Fast Initialization of the Spin State of an Electron in a Quantum Dot in the Voigt Configuration

C. Emary,[1] Xiaodong Xu,[2] D. G. Steel,[2] S. Saikin,[1] and L. J. Sham[1]

[1]*Department of Physics, The University of California–San Diego, La Jolla, California 92093, USA*
[2]*The H. M. Randall Laboratory of Physics, The University of Michigan, Ann Arbor, Michigan 48109, USA*

We consider the initialization of the spin state of a single electron trapped in a self-assembled quantum dot via optical pumping of a trion level. We show that with a magnetic field applied perpendicular to the growth direction of the dot, a near-unity fidelity can be obtained in a time equal to a few times the inverse of the spin-conserving trion relaxation rate. This method is several orders of magnitude faster than with the field aligned parallel, since this configuration must rely on a slow hole spin-flip mechanism. This increase in speed does result in a limit on the maximum obtainable fidelity, but we show that for InAs dots, the error is very small.

In a recent experiment [1], Atatüre and co-workers demonstrated high fidelity spin-state preparation of an electron in a self-assembled InAs/GaAs quantum dot (QD). Their purifying mechanism coupled the resonant laser excitation of the QD with heavy-light hole mixing to induce a small, but finite, degree of spin-flip Raman scattering. These experiments were performed with the magnetic field aligned in the growth direction of the QD (the Faraday configuration), and this was shown to be effective in suppressing deleterious spin flips caused by the nuclear hyperfine field.

Although fidelities very close to unity ($\geq 99.8\%$) were obtained through this mechanism, for quantum information processing purposes one would also like state preparation to be fast. The speed of the scheme in Ref. [1] is limited by the rate of hole-mixing spin-flip trion relaxation, which was determined to have a characteristic time of ~ 1 μs, corresponding to the measured rate of 100 kHz. This is slow compared with the picosecond time scale on which it is hoped that quantum operations will be performed in such dots [2–6].

It is the purpose of this Letter to show that a magnetic field aligned perpendicular, rather than parallel, to the growth axis allows the purification of the spin to near-unity fidelities with a characteristic time scale of $2\Gamma^{-1} \approx 1$ ns, where $\Gamma = 300$ MHz is the trion relaxation rate without spin flip as measured by Atatüre. This Voigt configuration is therefore some 3 orders-of-magnitude quicker than the Faraday configuration of Ref. [1].

The price paid for this dramatic speedup is that now both ground states are optically coupled to the trion. This inevitably leads to a reduction in the maximum obtainable fidelity, as it provides a path back for the population localized in the desired level. However, as we will show, this effect decreases with increasing field strength such that, for a typical InAs QD, the maximum obtainable fidelity typically differs from unity by only 0.3% at a field of 1 T and 0.005% at 8 T.

We consider a singly charged self-assembled InAs QD with growth direction z. Figure 1 shows our four-level model that describes the pertinent features of the system. With B field aligned in the x direction, the Zeeman energy of a QD electron is $\mathcal{H}_B^e = g_x^e \mu_B B_x s_x^e \equiv E_B^e s_x^e$, where g_x^e is the electronic g factor, μ_B is the Bohr magneton, B_x is the magnitude of the field, and $s_x^e = \pm 1/2$ corresponds to the
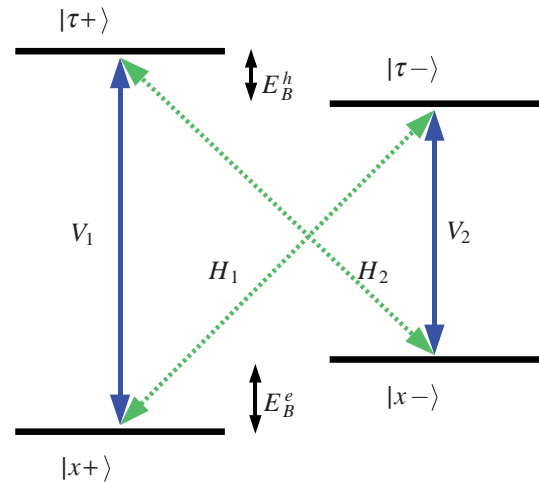

FIG. 1 (color online). The four levels of the electron-trion system in the Voigt basis consists of two Zeeman-split single-electron ground states $|x\pm\rangle$ with spins in the x direction, and two trion levels $|\tau\pm\rangle$ with heavy-hole spins also in the x direction. Arrows indicate allowed optical transitions with H, V denoting two orthogonal linear polarizations. State preparation is achieved by resonantly pumping the V_1 transition. This populates the trion level $|\tau_+\rangle$, which subsequently relaxes with rate Γ back to both ground states, resulting in a partial transfer of population from $|x+\rangle$ to $|x-\rangle$. This simple picture is complicated by the fact that the same laser also drives the V_2 transition, albeit off resonantly. This results in a small pumping of population in the opposite direction and hence a slight decrease in the maximum obtainable purity. We take the relaxation rate $\Gamma = 1.2$ μeV and g factors $g_x^e = -0.46$ and $g_x^h = -0.29$. For a field of 1 T, the Zeeman splitting are then $E_B^e = -27$ μeV and $E_B^h = 17$ μeV.

047401-1

electron spin. We have measured the magnitude of the electron g factor to be $|g_x^e| = 0.46$ [7], which is similar to values in the literature [1,8].

Our measurements also indicate that the behavior of the heavy-hole component of the trion in this field can be described with a Zeeman Hamiltonian $\mathcal{H}_B^h = -g_x^h \mu_B B_x s_x^h \equiv E_B^h s_x^h$, where $s_x^h = \pm 1/2$ are the eigenvalues of a pseudospin, the components of which correspond to heavy-hole states aligned in the x direction, and g_x^h is the hole g factor, which we determine to have a magnitude of $|g_x^h| = 0.29$. Our measurements do not give us access to the signs of these two g factors, but here we take both to be negative as suggested by some recent results [1,9]. Our scheme relies neither on this assumption about the signs, nor indeed even on g_x^h being nonzero.

The four levels of our model are then the two electron ground states with spins in the x direction, $|x\pm\rangle \equiv 2^{-1/2}(|\downarrow\rangle \pm |\uparrow\rangle)$, where $|\downarrow\rangle$ and $|\uparrow\rangle$ represent electron spins in the z direction, and the two trion levels, $|\tau\pm\rangle \equiv 2^{-1}(|\downarrow\uparrow\rangle - |\uparrow\downarrow\rangle)(|\Downarrow\rangle \pm |\Uparrow\rangle)$, where $|\Downarrow\rangle$ and $|\Uparrow\rangle$ denote heavy-hole states also aligned in the z direction. Figure 1 shows the allowed optical transitions between these levels. These transitions are linearly polarized and we have defined the polarization vectors in terms of $\sigma_\pm$ circular polarizations as $V = 2^{-1/2}(\sigma_- + \sigma_+)$ and $H = 2^{-1/2}(\sigma_- - \sigma_+)$. Our experiments [7] confirm that the level diagram of Fig. 1 provides an accurate description of the system up to a field strength of a few Tesla, and we expect this model to hold for even higher fields [10].

We drive the system with a V-polarized laser tuned on resonance with the transition from $|x+\rangle$ to $|\tau+\rangle$, which is denoted V_1 in Fig. 1. This illumination will also drive the V_2 transition and this off-resonant driving is the main source of nonideality considered in our model. We elect to drive the V_1 transition because, since we take the sign of both electron and hole g factors to be the same, the detuning of V_2 with respect to driving transition V_1 is $\Sigma_B = (g_x^e + g_x^h)\mu_B B_x = E_x^e - E_x^h$. The magnitude of this detuning is greater than that of $\Delta_B = (g_x^e - g_x^h)\mu_B B_x = E_x^e + E_x^h$, which is the detuning of transition H_2 with respect to transition H_1. As we will show, the larger this detuning, the smaller the deleterious effects of the off-resonant transition [11].

In the rotating frame then, the Hamiltonian of our system with driven V_1 transition in the basis $\{|x+\rangle, |x-\rangle, |\tau+\rangle, |\tau-\rangle\}$ is

$$\mathcal{H} = \begin{pmatrix} 0 & 0 & \Omega & 0 \\ 0 & 0 & 0 & \Omega e^{-i\Sigma_B t} \\ \Omega & 0 & 0 & 0 \\ 0 & \Omega e^{i\Sigma_B t} & 0 & 0 \end{pmatrix}, \qquad (1)$$

where Ω is the Rabi energy of the V_1 transition, which we assume to be independent of magnetic field strength and identical with that of the V_2 transition. We have set $\hbar = 1$. As this Hamiltonian shows, the laser drives not only the

transition with which it is resonant, but also the unintended transition with terms oscillating with frequency $\pm\Sigma_B$. In writing this Hamiltonian, we have neglected hole mixing since it is both expected to be small [1], and can in any case be incorporated into the current scheme without significant change [12].

We will determine the properties of this system through the master equation for the density matrix ρ in the Lindblad form

$$\dot{\rho} = -i[\mathcal{H}, \rho] + \sum_i \mathcal{L}_i[\rho], \qquad (2)$$

where the sum is over all trion relaxation channels, each of which is described by a Lindblad superoperator

$$\mathcal{L}_i[\rho] = D_i \rho D_i^\dagger - \tfrac{1}{2} D_i^\dagger D_i \rho - \tfrac{1}{2} \rho D_i^\dagger D_i. \qquad (3)$$

Since the trion can relax through all four optical transitions shown in Fig. 1, we need to consider the four independent jump operators: $D_1 = \sqrt{\Gamma}|x+\rangle\langle\tau+|$, $D_2 = \sqrt{\Gamma}|x-\rangle\langle\tau+|$, $D_3 = \sqrt{\Gamma}|x+\rangle\langle\tau-|$, and $D_4 = \sqrt{\Gamma}|x-\rangle \times \langle\tau-|$. In writing these operators, we have assumed that the relaxation channels proceed incoherently. This is justified since we will work in a regime where the Zeeman splittings are large enough that $|\Delta_B|, |\Sigma_B| > \Omega$ and the degree of spontaneously generated coherence [13] is negligible. We also assume, for the sake of simplicity and ease of presentation, that the rate Γ is the same for all channels. On the time scales considered here, the hole-mixing spin-flip relaxation, central to the mechanism of Ref. [1], is negligible. Furthermore, since we will work at significant magnetic fields ($\gtrsim 1$ T), ground-state spin flips caused by the nuclear hyperfine interaction are suppressed, as demonstrated by Atatüre *et al.* [1], and further effects of the nuclear spins are negligible, since they are operative over time scales far longer than our initialization time [14]. Finally, we assume that the initial state of the spin is unpolarized with $\rho_{++} = \rho_{--} = 1/2$ and all other elements of ρ zero.

Our elucidation of the properties of this system consists of two parts. First, we derive the time taken for the system to reach its asymptotic limit. This we do by neglecting the effects of the off-resonant transition. Second, we include the off-resonant effects and derive a limit on the maximum fidelity obtainable imposed by this nonideality.

With a trion relaxation rate of $\Gamma = 1.2 \ \mu$eV and g factors as stated, then even with a small applied magnetic field, we work in a regime in which the detuning of the off-resonant transition $|\Sigma_B|$ is much greater than both Γ and the Rabi energy Ω. In this limit we can assume that the terms $\Omega e^{\pm i\Sigma_B t}$ in the Hamiltonian of Eq. (1) oscillate sufficiently rapidly that they approximate as self-averaging to zero. In this case, the state $|\tau-\rangle$ decouples from the rest of the system and the Hamiltonian reduces to $\mathcal{H} = \Omega|x+\rangle\langle\tau+| + \text{H.c.}$ Physically this means that the off-resonant transition is so far off resonance that the laser

induces no transitions from it. We will derive a correction to this behavior later.

With this simplified Hamiltonian, there are only three independent nonzero density matrix elements to consider and these we organize into the vector $\mathbf{v} = (\rho_{x+,x+}, \rho_{x-,x-}, \mathrm{Im}\rho_{x+,\tau+})$. We have utilized the normalization condition $1 = \mathrm{Tr}\rho$ to eliminate $\rho_{\tau+,\tau+}$.

The equation of motions for these components can then be rephrased in terms of this vector as

$$\dot{\mathbf{v}} = \mathbf{X} \cdot (\mathbf{v} - \mathbf{v}_\infty), \tag{4}$$

where

$$X = \begin{pmatrix} -\Gamma & -\Gamma & -2\Omega \\ -\Gamma & -\Gamma & 0 \\ 2\Omega & \Omega & -\Gamma \end{pmatrix}, \tag{5}$$

and $\mathbf{v}_\infty = (0, 1, 0)$ is the stationary solution of this model, which represents the qubit population completely localized in state $|x-\rangle$ and hence 100% purified.

The time taken to reach this limit can be derived in the following way [15]. The solution of Eq. (4) is

$$\mathbf{v}(t) = \mathbf{v}_\infty + e^{\mathbf{X}t}(\mathbf{v}_0 - \mathbf{v}_\infty) \tag{6}$$

with initial vector $\mathbf{v}_0 = (\frac{1}{2}, \frac{1}{2}, 0)$. In the long time limit this can be approximated as

$$\mathbf{v} \sim \mathbf{v}_\infty + (\mathbf{v}_0 - \mathbf{v}_\infty)e^{-t/T_0} \tag{7}$$

with the characteristic time defined through $T_0^{-1} = \min\{|\mathrm{Re}(\lambda_i)|\}$, where $\{\lambda_i\}$ are the eigenvalues of matrix $\mathbf{X}$, all of which have negative real parts. This characteristic time is found to be

$$T_0 = \frac{3\lambda^{1/3}}{\Gamma}[3^{2/3}(1 - 4r^2) + 3^{1/3}\lambda^{2/3} - 3\lambda^{1/3}]^{-1} \tag{8}$$

with $\lambda = 9r^2 + \sqrt{192r^6 - 63r^4 + 36r^2 - 3}$ and $r = \Omega/\Gamma$. In Fig. 2, we plot this characteristic time as a function of the laser Rabi frequency in units of linewidth and the inset shows a typical evolution of the system and shows how well the behavior of the full system is approximated by Eq. (7) with T_0 as above.

The characteristic time T_0 has the following simple limits:

$$T_0 = \begin{cases} \Gamma/\Omega^2 & \text{if } \Omega \ll \Gamma, \\ 2/\Gamma & \text{if } \Omega \gg \Gamma. \end{cases} \tag{9}$$

If the driving is weak $\Omega \ll \Gamma$ then the time to reach the asymptotic population is slow. However, for laser amplitudes greater than the relaxation rate, the characteristic time saturates at a value twice that of the trion lifetime. This makes sense since, in this limit, the speed of the system is limited by trion relaxation, in which case, one half of the spin population is transferred to $|x-\rangle$ in time Γ^{-1}, whence $T_0 = 2\Gamma^{-1}$. With the value $\Gamma = 1.2\ \mu$eV we obtain $T_0 \approx 1.1$ ns, which is far shorter that the hole-
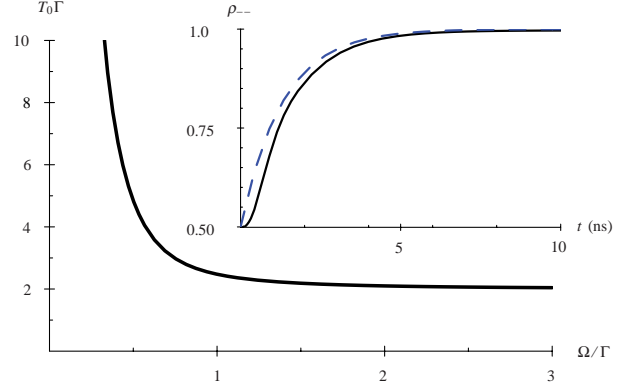

FIG. 2 (color online). The characteristic time T_0 describing the approach of the system to its asymptotic limit as a function of the Rabi frequency Ω. When $\Omega/\Gamma \gtrsim 1$, $T_0 \approx 2/\Gamma$. Inset: The population of the state $|x-\rangle$ as a function of time under continuous illumination. The solid black line shows the result of numerical integration of the master equation, whereas the dashed blue line shows the analytic result of Eq. (7). Near-unity fidelity is approached with a characteristic time of $T_0 \approx 1$ ns. For both plots, the parameters are the same as in Fig. 1 and for the inset we have further set $\Omega = \Gamma$.

mixing spin-flip transition time of $\gamma^{-1} \approx 1.6\ \mu$s of Ref. [1]. Figure 2 also shows that this limit of $T_0 = 2\Gamma^{-1}$ is a good approximation for all $\Omega/\Gamma \gtrsim 1$.

We now consider the inclusion of the off-resonant transition, which acts to reduce the asymptotic value of ρ_{--} away from unity. The full Hamiltonian of Eq. (1) depends on time, and therefore we cannot simply set $\dot{\rho} = 0$ to find the asymptotic solutions. Rather, we proceed by making the following ansatz for the asymptotic density matrix elements [16]:

$$\rho_{ij}(t \to \infty) = \rho_{ij}^{(0)} + \sum_{\pm} \rho_{ij}^{(\pm)} e^{\pm i\Sigma_B t}, \tag{10}$$

where the coefficients $\rho_{ij}^{(0,\pm)}$ are stationary. We place this ansatz into Eq. (2) and neglect terms oscillating as frequencies faster than Σ_B. This results in a set of algebraic equation for the coefficients $\rho_{ij}^{(0,\pm)}$ which we simply solve. We obtain the following expressions for the steady-state coefficients:

$$\begin{aligned}
\rho_{x+,x+}^{(0)} &= \frac{\Gamma^2 + \Omega^2}{D}; \\
\rho_{x-,x-}^{(0)} &= 1 - \frac{\Gamma^2 + 3\Omega^2}{D} \\
\rho_{\tau-,\tau-}^{(0)} &= \rho_{\tau+,\tau+}^{(0)} = \Omega^2/D; \\
\rho_{x+,\tau+}^{(0)} &= i\Gamma\Omega/D; \\
\rho_{x-,\tau-}^{(-)} &= (\rho_{\tau-,x-}^{(+)})^* = \Omega(i\Gamma - \Sigma_B)/D,
\end{aligned} \tag{11}$$

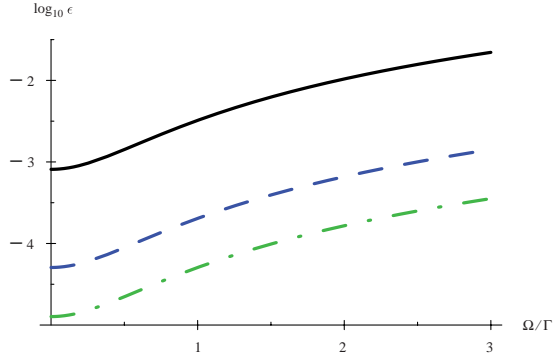where the denominator $D = \Sigma_B^2 + 2\Gamma^2 + 4\Omega^2$, and all the other coefficients are zero.

FIG. 3 (color online).   The logarithm of the error $\epsilon = 1 - F$, with F the fidelity, as a function of the Rabi energy Ω. Results are shown for three different fields: 1 T (black, solid), 4 T (blue, dash), and 8 T (green, dash-dot). Other parameters as Fig. 1.

Let us define the fidelity of the state preparation as $F = \langle\Psi|\rho|\Psi\rangle$, where $|\Psi\rangle$ is the desired target state with population localized in the state $|x-\rangle$ and ρ is the actual density matrix of the final states. This evaluates simply as $F = \rho_{x-,x-} = \rho^{(0)}_{x-,x-}$ and starts with a value of $\frac{1}{2}$ in the initial unpolarized state, and is unity for 100% purification [17]. Let us define as ϵ the amount by which F differs from unity: $\epsilon = 1 - F$. From Eqs. (11), we therefore find that the state-preparation error is

$$\epsilon = \frac{\Gamma^2 + 3\Omega^2}{\Sigma_B^2 + 2\Gamma^2 + 4\Omega^2} \approx \frac{\Gamma^2 + 3\Omega^2}{\Sigma_B^2}, \qquad (12)$$

where we have made use of $|\Sigma_B| \gg \Omega, \Gamma$.

In Fig. 3 we plot the full result for ϵ as a function of the Rabi frequency. The most salient point is that for a field of the order of 1 T, and with $\Omega/\Gamma = 1$, the error ϵ is of the order of 3×10^{-3}, which is very small, and of the order of the measurement threshold described in Ref. [1]. Increasing the field, decreases the error and at a high laboratory field such as 8 T the error is reduced to $\epsilon = 5 \times 10^{-5}$. These estimates agree very well with the results of numerical integration of the equations of motion. It should be noted that these values apply while the CW illumination is still in effect. Turning off the laser allows population trapped in the trion states to relax back to the ground-state sector with rate Γ. Half of this population ends up in the required state $|x-\rangle$, reducing the error by a factor of $2/3$.

In summary then, we have considered the advantages of using the Voigt configuration for the preparation of the spin state of an electron in a self-assembled QD. Provided that the Rabi frequency of the laser is greater than the trion relaxation rate, the state preparation is fast, proceeding with a time scale of $2\Gamma^{-1} \approx 1$ ns, which is orders of magnitude faster than in the Faraday configuration. Use of the Voigt configuration does, however, impose an upper limit on the maximum obtainable fidelity, but this is small, with the deviation from unity being $\epsilon \approx (\Gamma^2 + 3\Omega^2)/\Sigma_B^2 \approx 10^{-3}$ at 1 T. This approach therefore represents a fast way of initializing an electron spin to high fidelities for quantum information processing.

[1] M. Atatüre, J. Dreiser, A. Badolato, A. Högele, K. Karrai, and A. Imamoglu, Science **312**, 551 (2006).
[2] C. Piermarocchi, Pochung Chen, L. J. Sham, and D. G. Steel, Phys. Rev. Lett. **89**, 167402 (2002).
[3] T. Calarco, A. Datta, P. Fedichev, E. Pazy, and P. Zoller, Phys. Rev. A **68**, 012310 (2003).
[4] B. W. Lovett, A. Nazir, E. Pazy, S. D. Barrett, T. P. Spiller, and G. A. D. Briggs, Phys. Rev. B **72**, 115324 (2005).
[5] P. Chen, C. Piermarocchi, L. J. Sham, D. Gammon, and D. G. Steel, Phys. Rev. B **69**, 075320 (2004).
[6] C. Emary and L. J. Sham, cond-mat/0608518; cond-mat/0609094.
[7] Xiaodong Xu *et al.* (unpublished).
[8] I. Hapke-Wurst, U. Zeitler, R. J. Haug, and K. Pierz, Physica (Amsterdam) **12E**, 802 (2002).
[9] M. Bayer, O. Stern, A. Kuther, and A. Forchel, Phys. Rev. B **61**, 7273 (2000).
[10] M. V. Gurudev Dutt, Jun Cheng, Bo Li, Xiaodong Xu, Xiaoqin Li, P. R. Berman, D. G. Steel, A. S. Bracker, D. Gammon, S. E. Economou, Ren-Bao Liu, and L. J. Sham, Phys. Rev. Lett. **94**, 227403 (2005).
[11] If the g factors had opposite signs, we would have $|\Delta_B| > |\Sigma_B|$ and therefore driving one of the H transitions instead would be the best strategy to minimize initialization error.
[12] The dominant hole mixing here is between heavy hole $|\frac{3}{2}; \pm\frac{3}{2}\rangle$ and light hole $|\frac{3}{2}; \mp\frac{1}{2}\rangle$. By adjusting the relative phase between circular-polarized components of the applied laser, the effect of this mixing can be reduced to only altering the Hamiltonian of Eq. (1) through a rescaling of the Rabi frequency.
[13] S. E. Economou, R.-B. Liu, L. J. Sham, and D. G. Steel, Phys. Rev. B **71**, 195327 (2005).
[14] A. Greilich, D. R. Yakovlev, A. Shabaev, Al. L. Efros, I. A. Yugova, R. Oulton, V. Stavarache, D. Reuter, A. Wieck, and M. Bayer, Science **313**, 341 (2006).
[15] B. Michaelis, C. Emary, and C. W. J. Beenakker, Europhys. Lett. **73**, 677 (2006).
[16] T. H. Stoof and Yu. V. Nazarov, Phys. Rev. B **53**, 1050 (1996).
[17] In the limit that $1 - \rho_{x-,x-} \ll 1$, this fidelity is approximately the same as the definition $F = 1 - \rho_{x+,x+}/\rho_{x-,x-}$ used in Ref. [1] [M. Atatüre (private communication)].

Theory of nonlinear optical spectroscopy of electron spin coherence in quantum dots

Ren-Bao Liu,[1] S. E. Economou,[2] L. J. Sham,[2] and D. G. Steel[3]

[1]*Department of Physics, The Chinese University of Hong Kong, Shatin, New Territories, Hong Kong, China*
[2]*Department of Physics, University of California San Diego, La Jolla, California 92093-0319, USA*
[3]*The H. M. Randall Laboratory of Physics, University of Michigan, Ann Arbor, Michigan 48109, USA*

We study in theory the generation and detection of electron spin coherence in nonlinear optical spectroscopy of semiconductor quantum dots doped with single electrons. In third-order differential transmission spectra, the inverse width of the ultranarrow peak at degenerate pump and probe frequencies gives the longitudinal spin relaxation time (T_1), and that of the Stokes and anti-Stokes spin resonances gives the spin dephasing time including the inhomogeneous broadening (T_2^*). The transverse spin relaxation time excluding the inhomogeneous broadening effect (T_2) can be measured by the inverse width of ultranarrow hole-burning resonances in fifth-order differential transmission spectra.

I. INTRODUCTION

Electron spin coherence in semiconductor quantum dots (QDs) is a quantum effect to be exploited in emerging technologies such as spin-based electronics (spintronics) and quantum computation.[1] The electron spin decoherence is a key issue for practical application of the electron spin freedom and is also of fundamental interest in mesoscopic physics and in quantum physics. The electron spin decoherence in QDs, however, is yet poorly characterized. By convention, the spin decoherence is classified into the longitudinal and the transverse parts, which correspond to the spin population flip and the Zeeman energy fluctuation processes and are usually characterized by the longitudinal relaxation time T_1 and the transverse relaxation time T_2, respectively. Most current experiments are carried out on ensembles of spins, composed of either many similar QDs (Refs. 2–5) or many repetitions of (approximately) identical measurements on a single QD.[6–14] The ensemble measurements are subjected to the inhomogeneous broadening of the Zeeman energy, which results from the fluctuation of the QD size, shape, and compound composition (and in turn the electron g-factor) and from the random distribution of the local Overhauser field (due to the hyperfine interaction with nuclear spins in thermal states). The inhomogeneous broadening leads to a dephasing time T_2^*.[15–17] The three time scales characterizing the electron spin decoherence can differ by orders of magnitude usually in the order of $T_1 \gg T_2 \gg T_2^*$. For example, in a typical GaAs QD at a low temperature ($\lesssim 4$ K) and under a moderate to strong magnetic field ($0.1–10$ T), the longitudinal relaxation time T_1 can be in the order of milliseconds,[6–11,18] the transverse relaxation time T_2 is up to several microseconds,[5,12,14] and the dephasing time T_2^* can be as short as a few nanoseconds.[3,5,12,13]

The issue is how to measure the characteristic times of electron spin decoherence in QDs. There have been many experiments both in optics[4,9–11,18] and in transport,[6–8] which establish the longitudinal spin relaxation time T_1 in QDs of different materials. The dephasing time T_2^* has also been measured for QD ensembles,[2,3,5,12,13] giving a lower bound of T_2. Spin echo in microwave electron spin resonance (ESR)

experiments is a conventional approach to measuring the transverse spin relaxation time T_2 excluding the inhomogeneous broadening,[19–21] which, however, is less feasible for III-V compound quantum dots due to the fast time scales in such systems ($T_2 \lesssim 10^{-6}$ s and $T_2^* \lesssim 10^{-9}$ s). Indeed, the remarkable spin echo experiments in coupled QDs done by Petta *et al.* are performed with rather long dc voltage pulses instead of instantaneous microwave pulses.[12] Alternatively, picosecond optical pulses may be used to manipulate electron spins via Raman processes[22] and realize the spin echo, which, however, still need to overcome the difficulty of stabilizing and synchronizing picosecond pulses in microsecond time spans. A recent experiment by Greilich *et al.* also shows that the inhomogeneous broadening effect can be filtered out from the spin coherence mode locked by a periodic train of laser pulses.[5]

In this paper, we will study the frequency-domain nonlinear optical spectroscopy as another approach to measuring the electron spin decoherence times. Particularly, the transverse relaxation rate T_2^{-1} is correlated to the width of ultranarrow hole-burning peaks in fifth-order differential transmission (DT) spectra. This hole-burning measurement of the spin relaxation time is analogous to the exploration of slow relaxation of optical coherence in atomic systems by the third-order hole-burning spectroscopy.[23] Here, the fifth-order nonlinearity is needed because the creation of spin coherence by Raman processes involves at least two orders of optical field and hole-burning two more. The state-of-the-art spectroscopy already has the ultrahigh resolution (much better than megahertz-resolution) to resolve the slow spin decoherence in microsecond or even millisecond time scales.[24–26]

The organization of this paper is as follow. After this introductory section, Sec. II describes the model for the QD system and the master-equation approach to calculating the nonlinear optical susceptibility. Section III presents the results and discussion. Section IV concludes this paper. The solution of the master equation in the frequency domain is presented in the Appendix.

II. MODEL AND THEORY

The system to be studied is a semiconductor QD doped with a single electron. The geometry of the QD under an
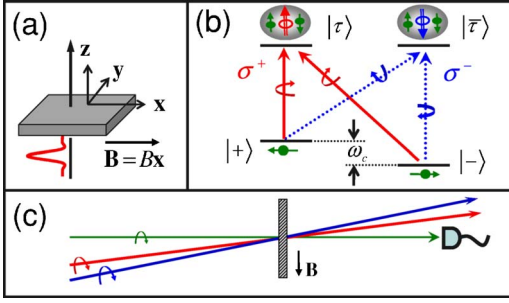
FIG. 1. (Color online) Schematics of (a) the quantum dot, (b) the selection rules for optical transitions, and (c) the optical detection geometry.

external magnetic field and optical excitation is shown in Figs. 1(a) and 1(c). The QD is assumed to be a shape with small thickness in the growth direction and relatively large radius in the lateral directions, as in the usual cases of fluctuation GaAs QDs.[3,10] To enable the generation and manipulation of the electron spin coherence through Raman processes, a magnetic field is applied along a lateral direction (x axis). The propagation directions of the pump and probe laser beams are close to the growth direction (z axis). The two electron spin states $|\pm\rangle$ are split by the magnetic field with Zeeman energy ω_0. The strong confinement along the z axis induces a large splitting between the heavy hole and the light hole states, thus the relevant exciton states are the ground trion states $|\tau\rangle$ and $|\bar{\tau}\rangle$, which consist of two electrons (including the doped one and one created by optical excitation) in the singlet spin state and one heavy hole in the spin states $|+3/2\rangle$ and $|-3/2\rangle$ (quantized along the z axis with nearly zero Zeeman splitting), respectively. Similarly, we can also neglect the excitation of higher-lying trions, biexciton, and multiexciton states since the energy of adding an exciton in each case is well separated from energy of the lowest trion states. The selection rules for the optical transitions are determined by the (approximate) conservation of the angular momentum along the growth direction so that a circularly polarized light with polarization σ^+ or σ^- connects the two electron spin states to the trion state $|\tau\rangle$ or $\bar{\tau}\rangle$, respectively [see Fig. 1(b)]. The relaxation processes in the system are parametrized by the exciton recombination rate Γ_1, the exciton dephasing rate Γ_2, the longitudinal spin relaxation time T_1, and the transverse spin relaxation time T_2. The inhomogeneous broadening leads to a random component ϵ to the Zeeman splitting: $\omega_c = \omega_0 + \epsilon$, which is assumed to be a Gaussian distribution $g(\epsilon) = e^{-\epsilon^2/(2\gamma^{*2})}/(\sqrt{2\pi}\gamma^*)$. The spin dephasing time including the inhomogeneous broadening $T_2^* \cong 1/\gamma^* \ll T_2$, unless it is artificially set to be $T_2^* = T_2$ (by setting $\gamma_2^* = 0$). The hole spin relaxation is neglected since it is extremely slow when the hole is confined in the trion states.[11] The theory presented here can be extended straightforwardly to include the hole spin relaxation, the light-hole states, the hole mixing effect (which leads to the imperfection in the selection rules, for example, in InAs QDs), the multiexciton states, the inhomogeneous broadening of the trion states, and so on, but we expect no qualitative modification of the resonance features related to the electron spin coherence in the nonlinear optical spectra. For simplicity, we

shall consider only σ^+-polarized optical fields (extension to other polarization configurations may provide some flexibility for experiments and is trivial in the theoretical part). Thus, the model is reduced to a Λ-type three-level system, consisting of the two electron spin states $|\pm\rangle$ and the trion state $|\tau\rangle$. The Λ-type three-level model, in spite of its simplicity, is the basis of a wealth of physical effects, including electromagnetically induced transparency,[27] lasing without inversion,[28] and stimulated Raman adiabatic passage,[29] and it has been successfully applied to study transient optical signals of doped QDs.[3,30]

The dynamics of the system is described in the density matrix formalism with $\rho_{\alpha,\beta}$ as the density matrix elements between the states $|\alpha\rangle$ and $|\beta\rangle$. The optical excitation and relaxation are accounted for in the master equation as

$$\partial_t \rho_{\tau,\pm} = -i[\mathcal{E}_g \mp (\omega_0 + \epsilon)/2 - i\Gamma_2]\rho_{\tau,\pm} - iE(t)\rho_{\tau,\tau} + iE(t)\rho_{\mp,\pm} \\ + iE(t)\rho_{\pm,\pm}, \tag{1a}$$

$$\partial_t \rho_{\tau,\tau} = -2\Gamma_1 \rho_{\tau,\tau} + 2\Im[E^*(t)\rho_{\tau,+} + E^*(t)\rho_{\tau,-}], \tag{1b}$$

$$\partial_t \rho_{\pm,\pm} = -(p_\mp \rho_{\pm,\pm} - p_\pm \rho_{\mp,\mp})/T_1 + \Gamma_1 \rho_{\tau,\tau} - 2\Im[E^*(t)\rho_{\tau,\pm}], \tag{1c}$$

$$\partial_t \rho_{\pm,\mp} = \Gamma_1 \rho_{\tau,\tau} - i[\pm(\omega_0 + \epsilon) - i/T_2]\rho_{\pm,\mp} + iE^*(t)\rho_{\tau,\mp} \\ - iE(t)\rho_{\tau,\pm}^*, \tag{1d}$$

where $\mathcal{E}_g$ is the energy gap and $p_\pm$ is the equilibrium population of the spin states in the absence of the optical excitation; the optical field $E(t) = \sum_j E_j e^{-i\Omega_j t}$ contains different frequency components. The transition dipole moment is understood to be absorbed into the field quantities. In the rotating wave reference frame, the energy gap $\mathcal{E}_g$ is set to be zero and the optical frequencies Ω_j are measured from the gap. The first term in the right-hand side of Eq. (1d) is the spin coherence generated by spontaneous emission,[30–32] which has been demonstrated in time-domain experiments with significant effects on spin beats.[3] We will show that it produces extra resonances in the fifth-order DT spectra.

To calculate the nonlinear optical susceptibility, the master equation is obtained in the frequency domain (as given in the Appendix). With the spectrum of the optical field given by $E(\Omega) = \sum_j 2\pi E_j \delta(\Omega - \Omega_j)$, the density matrix can be expanded as

$$\rho_{\alpha,\beta}(\Omega) = \sum_{j,\ldots,k;m,\ldots,l} 2\pi E_j \cdots E_k E_m^* \cdots E_l^* \rho_{\alpha,\beta}^{(j\cdots k\bar{m}\cdots\bar{l})} \delta(\Omega \\ - \Omega_{j\cdots k\bar{m}\cdots\bar{l}}), \tag{2}$$

where $\Omega_{j\cdots k\bar{m}\cdots\bar{l}} \equiv \Omega_j + \cdots + \Omega_k - (\Omega_m + \cdots + \Omega_l)$. The derivation of the density matrix component $\rho^{(j\cdots k\bar{m}\cdots\bar{l})}$ up to the fifth order is lengthy but straightforward. The final result is averaged with the inhomogeneous broadening distribution $g(\epsilon)$.
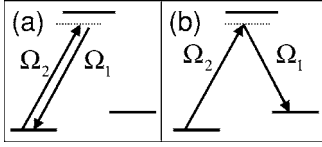
FIG. 2. Schematics of Raman processes generating (a) the spin population and (b) the off-diagonal spin coherence.

III. RESULTS AND DISCUSSIONS

The linear optical susceptibility is given by

$$\rho^{(j)} = \int \frac{g(\epsilon)}{\Omega_j - \mathcal{E}_g \pm (\omega_0 + \epsilon)/2 + i\Gamma_2} d\epsilon. \qquad (3)$$

In fluctuation GaAs QDs, the exciton dephasing is much faster than the spin dephasing due to the inhomogeneous broadening $(\Gamma_2^{-1} \lesssim 0.1 \text{ ns} \ll T_2^* \sim 10 \text{ ns})$,[3] so the resonance width in linear optical spectra is usually dominated by the trion state broadening, revealing little information about the spin decoherence.

In third-order optical response, the population and off-diagonal coherence of the electron spin are generated by the Raman processes,

$$\rho_{\pm,\pm} \overset{E_2}{\to} \rho_{\tau,\pm}^{(2)} \overset{E_1^*}{\to} \rho_{\pm,\pm}^{(2\bar{1})} \propto \left(\Omega_{2\bar{1}} + \frac{i}{T_1}\right)^{-1}, \qquad (4a)$$

$$\rho_{\pm,\pm} \overset{E_2}{\to} \rho_{\tau,\pm}^{(2)} \overset{E_1^*}{\to} \rho_{\mp,\pm}^{(2\bar{1})} \propto \left[\Omega_{2\bar{1}} \pm (\omega_0 + \epsilon) + \frac{i}{T_2}\right]^{-1}, \qquad (4b)$$

corresponding to the illustrations in Figs. 2(a) and 2(b), respectively. Another optical field with frequency Ω_1 brings the second-order spin coherence into the third-order optical coherence $\rho_{\tau,\pm}^{(21\bar{1})}$. The DT spectrum as a function of the pump frequency Ω_1 and the probe frequency Ω_2 is

$$S_{\text{DT}}(\Omega_2, \Omega_1) \propto -\Im[\rho_{\tau,+}^{(21\bar{1})} + \rho_{\tau,-}^{(21\bar{1})}], \qquad (5)$$

which presents the ultranarrow resonances around $\Omega_{2\bar{1}} = 0$ and $\Omega_{2\bar{1}} = \pm\omega_0$, with resonance widths T_1^{-1} and T_2^{-1}, related to the spin population and off-diagonal coherence in Eqs. (4a) and (4b), respectively. Such resonances are shown in Fig. 3 (as dot black lines). Thus, the spin relaxation times T_1 and T_2 are measured, but when the inhomogeneous broadening is included, since usually $T_2 \gg T_2^*$, the Stokes and anti-Stokes Raman resonances at $\Omega_{2\bar{1}} = \pm\omega_0$ will be smeared to be a peak resembling the inhomogeneous broadening distribution as

$$\int \rho_{\pm,\mp}^{(2\bar{1})} g(\epsilon) d\epsilon \sim -i\pi g(\Omega_{2\bar{1}} \mp \omega_0). \qquad (6)$$

The effect of the inhomogeneous broadening is clearly seen in Fig. 3 (solid red lines). So in usual cases, the third-order DT spectra measure the T_2^* instead of the T_2. The resonance at degenerate pump and probe frequencies $(\Omega_{2\bar{1}} = 0)$ is related to the spin population and is immune to the random distribution of the electron Zeeman energy. So the longitudinal spin relaxation time T_1 can be deduced from the third-order DT spectra, regardless of the inhomogeneous broadening.
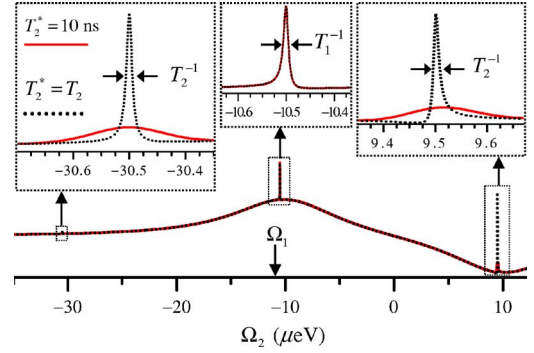

FIG. 3. (Color online) Third-order DT spectra of QDs doped with single electrons. The parameters are chosen such that the Zeeman energy $\omega_0 = 20 \ \mu\text{eV}$, the spin population $p_\pm = 0.5$, the pump frequency $\Omega_1 = \mathcal{E}_g - 10.5 \ \mu\text{V}$, $\Gamma_1 = 5 \ \mu\text{eV}$ $(\Gamma_1^{-1} \approx 0.12 \text{ ns})$, $\Gamma_2 = 6 \ \mu\text{eV}$ $(\Gamma_2^{-1} \approx 0.1 \text{ ns})$, $T_1 = 100 \text{ ns}$, $T_2 = 100 \text{ ns}$, and $T_2^* = 10 \text{ ns}$ for the solid (red) lines and $T_2^* = T_2$ (no inhomogeneous broadening) for the dot (black) lines. The insets are enlarged plots, showing details of the resonances.

We note that the resonance features of the third-order susceptibility shown in Fig. 3 are consistent with the recent experimental data.[18]

To measure the transverse relaxation time excluding the inhomogeneous broadening effect, the fifth-order nonlinearity can be used. In the fifth-order optical response, the spin coherence in the fourth order of optical field has very rich resonance structures. For instance, a double resonance such as

$$\rho_{+,-}^{(43\bar{2}\bar{1})} \sim \frac{1}{\left[\Omega_{3\bar{1}} - (\omega_0 + \epsilon) + \dfrac{i}{T_2}\right]\left[\Omega_{43\bar{2}\bar{1}} - (\omega_0 + \epsilon) + \dfrac{i}{T_2}\right]} \qquad (7)$$

arises from the excitation pathway

$$\rho_{-,-} \overset{E_3}{\to} \rho_{\tau,-}^{(3)} \overset{E_1^*}{\to} \rho_{+,-}^{(3\bar{1})} \overset{E_4}{\to} \rho_{\tau,-}^{(43\bar{1})} \overset{E_2^*}{\to} \rho_{+,-}^{(43\bar{2}\bar{1})}, \qquad (8)$$

as depicted in Fig. 4(a). The double resonance will manifest itself in a two-dimensional DT spectrum as an ultranarrow peak at $\Omega_{3\bar{1}} = \Omega_{43\bar{2}\bar{1}} = \omega_0 + \epsilon$ with width of $\sim T_2^{-1}$. When the inhomogeneous broadening is included, the ultranarrow resonance will be smeared into a broadened peak along the direction $\Omega_{3\bar{1}} = \Omega_{43\bar{2}\bar{1}}$ with width of $\sim 1/T_2^*$, but in the perpen-
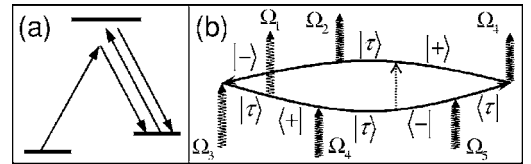

FIG. 4. (a) Schematics for a fourth-order optical process that generates spin coherence with a double resonance structure. (b) The Feynman diagram for the fifth-order optical response involving the spontaneous emission, in which the optical field and the vacuum field are represented by the wavy arrows and the dotted arrow, respectively.
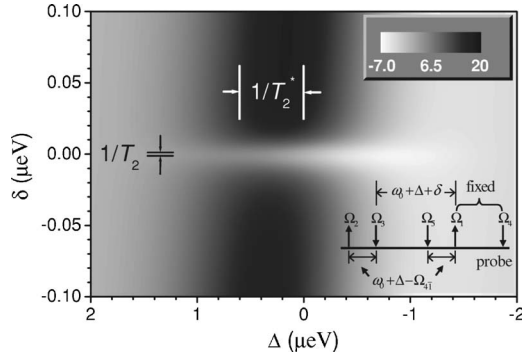
FIG. 5. Contour plot of the fifth-order DT spectrum of the QDs as a function of $\Delta \equiv \Omega_{43\bar{2}\bar{1}} - \omega_0$ and $\delta \equiv \Omega_{1\bar{3}} - \Omega_{43\bar{2}\bar{1}}$. The probe frequency is fixed to be $\Omega_4 = 22\,\mu$eV, the pump frequency Ω_1 is fixed at 9 μeV, and the other three pump frequencies are scanned with $\Omega_{53\bar{2}\bar{1}} = 0$ (which makes $\Omega_{1\bar{5}} = \Omega_{3\bar{2}} = \omega_0 + \Delta - \Omega_{4\bar{1}}$ and $\Omega_{1\bar{3}} = \Omega_{5\bar{2}} = \omega_0 + \Delta + \delta$, as indicated in the inset). The Zeeman energy $\omega_0 = 20$ μeV, the spin population $p_\pm = 0.5$, and the relaxation rates are such that $\Gamma_1 = 5$ μeV ($\Gamma_1^{-1} \approx 0.12$ ns), $\Gamma_2 = 6$ μeV ($\Gamma_2^{-1} \approx 0.1$ ns), $T_1 = 100$ ns, $T_2 = 100$ ns, and $T_2^* = 1$ ns.

dicular direction (defined by $\Omega_{3\bar{1}} = -\Omega_{43\bar{2}\bar{1}}$), the peak width remains unchanged. So when $\Omega_{43\bar{2}\bar{1}}$ is fixed around ω_0 and $\Omega_{3\bar{1}}$ is scanned, or vice versa, the DT spectrum will present a sharp peak whose width measures the inverse transverse relaxation time T_2^{-1}. This peak has the character of hole burning: The first frequency difference acts just as a selection of QDs with Zeeman energy $\omega_0 + \epsilon = \Omega_{43\bar{2}\bar{1}}$ from the inhomogeneously broadened ensemble. The hole-burning resonance resulting from the excitation pathway in Eq. (8), however, emerges together with the resonance associated with the spin population $(\Omega_{4\bar{2}} + i/T_1)^{-1}$, as given in Eq. (4a). To avoid the complication of mixing two types of resonance structures, we would rather make use of another mechanism for spin coherence generation, namely, the spontaneous emission that connects the trion state to the two spin states through the vacuum field [related to the first term in the right-hand side of Eq. (1d)].[3,30–32]

The generation of spin coherence in the fifth-order optical response involving the spontaneous emission can take a quantum pathway like

$$\rho_{-,-} \xrightarrow{E_3} \rho_{\tau,-}^{(3)} \xrightarrow{E_1^*} \rho_{+,-}^{(3\bar{1})} \xrightarrow{E_4} \rho_{\tau,-}^{(43\bar{1})} \xrightarrow{E_2^*} \rho_{\tau,\tau}^{(43\bar{2}\bar{1})} \xrightarrow{\Gamma_1} \rho_{-,+}^{(43\bar{2}\bar{1})}, \quad (9)$$

where the last step is the spontaneous emission. This optical process is illustrated by the Feynman diagram in Fig. 4(b). The spin coherence generated by the spontaneous emission and that by optical excitation can have opposite spin indices $[\rho_{+,-}^{(3\bar{1})} \rightarrow \rho_{-,+}^{(43\bar{2}\bar{1})}]$, which is impossible in quantum pathways without the spontaneous emission [as can be seen from Fig. 4(a)]. Thus, the double resonance becomes

$$\rho_{-,+}^{(43\bar{2}\bar{1})} \sim \frac{\Gamma_1/(\Omega_{43\bar{2}\bar{1}} + i2\Gamma_1)}{\left[\Omega_{3\bar{1}} + (\omega_0 + \epsilon) + \dfrac{i}{T_2}\right]\left[\Omega_{43\bar{2}\bar{1}} - (\omega_0 + \epsilon) + \dfrac{i}{T_2}\right]}, \quad (10)$$
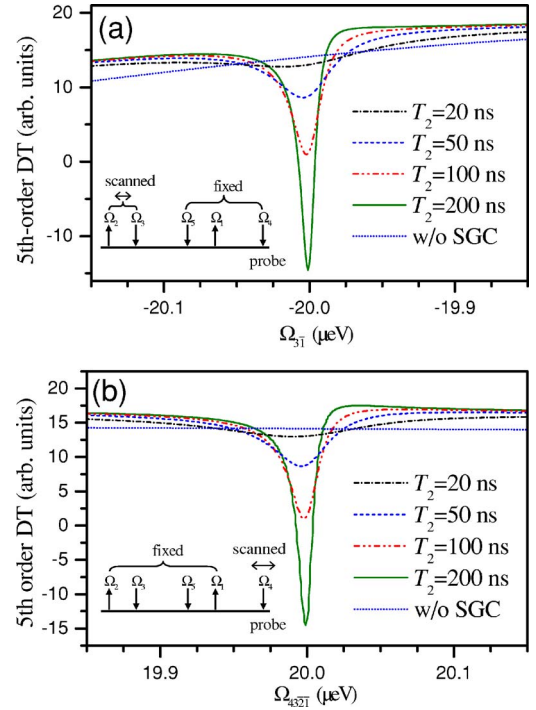

FIG. 6. (Color online) (a) The sectioned plot of Fig. 5 with $\Delta = 0$ (i.e., $\Omega_{43\bar{2}\bar{1}} = \omega_0$). (b) The fifth-order DT signal as a function of the probe frequency with pump frequencies fixed to be such that $\Omega_1 = 9$ μeV, $\Omega_5 = 2$ μeV, and $\Omega_{1\bar{3}} = \Omega_{5\bar{2}} = \omega_0 = 20$ μeV. In both figures, the transverse spin relaxation time $T_2 = 20$, 50, 100, and 200 ns for the dash-dot (black), dash (blue), dash-dot-dot (red), and solid (green) lines from top to bottom, respectively, and the dot (blue) line is calculated with the spontaneously generated spin coherence artificially switched off (for $T_2 = 100$ ns). The parameters are the same as in Fig. 5.

which is well separated from the spin population resonance. The spectrum is measured by fixing $\Omega_{43\bar{2}\bar{1}}$ to be the hole-burning frequency $\omega_0 + \Delta$ with $\Delta \lesssim 1/T_2^*$ and fine tuning $\Omega_{1\bar{3}}$ to be $\Omega_{43\bar{2}\bar{1}} + \delta$. As shown in the inset of Fig. 5, the optical frequencies can be configured such that Ω_4 and Ω_1 are fixed, Ω_3 are redshifted by $\omega_0 + \Delta + \delta$ from Ω_1, and Ω_5 and Ω_2 are redshifted by $\omega_0 + \Delta - \Omega_{4\bar{1}}$ from Ω_1 and Ω_3, respectively. Thus, the fifth-order optical response $\rho_{\tau,\pm}^{(543\bar{2}\bar{1})}$ oscillates at the probe frequency Ω_4, which enables the signal to be measured in the DT setup instead of six-wave mixing ones. We note that the resonance due to the spin population $\sim(\Omega_{53\bar{2}\bar{1}} + i/T_1)^{-1}$ contributes only a constant background since $\Omega_{53\bar{2}\bar{1}} \equiv 0$ in the above frequency configuration. As shown in Fig. 5, which plots the fifth-order DT spectrum as a function of $\Delta \equiv \Omega_{43\bar{2}\bar{1}} - \omega_0$ and the fine tuning $\delta \equiv \Omega_{1\bar{3}} - \Omega_{43\bar{2}\bar{1}}$, a very narrow hole in the spectrum as a function of $\Omega_{3\bar{1}}$ is burnt around $\Omega_{43\bar{2}\bar{1}}$, with width given by T_2^{-1}. Along the direction $\Omega_{3\bar{1}} = -\Omega_{43\bar{2}\bar{1}}$ ($\delta = 0$), the resonance is extended by the inhomogeneous broadening as expected. Sectioned plots of the DT signal with fixed Δ are shown in Fig. 6(a) for various transverse relaxation time. The resonance width is given by the transverse relaxation rate, demonstrating unambiguously that the T_2 is measured by the hole-burning effect. The hole-burning resonance can also be detected by varying the probe

frequency with the pump frequencies fixed, as demonstrated in Fig. 6(b). The role of the spontaneous emission-generated spin coherence is verified by the absence of the ultranarrow resonance with artificial switch-off of the relevant term in Eq. (1d).

IV. CONCLUSIONS

The spin coherence can be generated and detected in nonlinear optical spectroscopy of quantum dots doped with single electrons, which is studied in this paper up to the fifth-order nonlinearity with a Λ-type three-level model. The electron spin coherence is generated by the optical field through Raman processes as well as by spontaneous emission of the trion. The spin population and off-diagonal coherence manifest themselves in third-order differential transmission spectra as ultranarrow resonances. The inhomogeneous broadening smears out the sharp Stokes and anti-Stokes peaks related to the off-diagonal spin coherence. Thus, the longitudinal spin relaxation time T_1 and the dephasing time T_2^* are measured by the third-order spectra. In the fifth-order optical response, the generation of the spin coherence by both second- and fourth-order optical processes leads to double resonance structures in two-dimensional DT spectra, which are smeared by the inhomogeneous broadening along one direction in the frequency space but presents ultranarrow hole-burning resonances along the perpendicular direction. So the transverse spin relaxation time T_2 is measured as the inverse width of the hole-burning peak. The spontaneous emission-generated spin coherence[3,30] is useful to produce hole-burning resonances well separated from the spin-population resonances in the fifth-order spectra. The frequencies of the optical field can be configured properly to enable the detection of the signal in the DT setup instead of the multiwave mixing ones. In practice, the pump and probe frequencies may be generated from a single continuous-wave laser source by, e.g., acousto-optical modulation.[26] Since the ultranarrow hole-burning peaks are rather insensitive to the global shift of the laser frequencies and variation of the hole-burning frequency, nonstabilized laser sources may be used to resolve the slow spin decoherence.[26] In the present research, the electron spin decoherence and the inhomogeneous broadening are parametrized with a few time scales (T_1, T_2, and T_2^*). The theoretical framework in this paper can be readily extended to study the effect of the spectral diffusion[33–35] of the electron spin on the nonlinear optical spectroscopy. We expect that the leading-order effect of the spectral diffusion can also be eliminated in the fifth-order nonlinear optical susceptibility.

APPENDIX: SOLUTION OF THE MASTER EQUATION

The master equation in Eq. (1) can be solved in the frequency domain by Fourier transformation to be

$$\rho_{\tau,\pm}(\Omega) = \int \frac{-E(\Omega-\omega)\rho_{\pm,\pm}(\omega) - E(\Omega-\omega)\rho_{\mp,\pm}(\omega) + E(\Omega-\omega)\rho_{\tau,\tau}(\omega)}{\Omega - \mathcal{E}_g \pm (\omega_0+\epsilon)/2 + i\Gamma_2} \frac{d\omega}{2\pi}, \tag{A1a}$$

$$\rho_{\tau,\tau}(\omega) = \sum_{\pm} \int \frac{+E^*(\Omega-\omega)\rho_{\tau,\pm}(\Omega) - E(\Omega+\omega)\rho_{\tau,\pm}^*(\Omega)}{\omega + i2\Gamma_1} \frac{d\Omega}{2\pi}, \tag{A1b}$$

$$\rho_{\pm,\pm}(\omega) = p_\pm 2\pi\delta(\omega) - (\omega + i\Gamma_1 + ip_\pm/T_1) \int \frac{E^*(\Omega-\omega)\rho_{\tau,\pm}(\Omega) - E(\Omega+\omega)\rho_{\tau,\pm}^*(\Omega)}{(\omega + i/T_1)(\omega + i2\Gamma_1)} \frac{d\Omega}{2\pi}$$
$$+ (i\Gamma_1 - ip_\pm/T_1) \int \frac{E^*(\Omega-\omega)\rho_{\tau,\mp}(\Omega) - E(\Omega+\omega)\rho_{\tau,\mp}^*(\Omega)}{(\omega + i/T_1)(\omega + i2\Gamma_1)} \frac{d\Omega}{2\pi}, \tag{A1c}$$

$$\rho_{+,-}(\omega) = \frac{i\Gamma_1 \rho_{\tau,\tau}(\omega)}{\omega - (\omega_0+\epsilon) + i/T_2} + \int \frac{-E^*(\Omega-\omega)\rho_{\tau,-}(\Omega) + E(\Omega+\omega)\rho_{\tau,+}^*(\Omega)}{\omega - (\omega_0+\epsilon) + i/T_2} \frac{d\Omega}{2\pi}. \tag{A1d}$$

[1] *Semiconductor spintronics and quantum computation*, edited by D. D. Awschalom, D. Loss, and N. Samarth (Springer, New York, 2002).

[2] J. A. Gupta, D. D. Awschalom, A. L. Efros, and A. V. Rodina, Phys. Rev. B **66**, 125307 (2002).

[3] M. V. Gurudev Dutt, J. Cheng, B. Li, X. Xu, X. Li, P. R. Berman, D. G. Steel, A. S. Bracker, D. Gammon, S. E. Economou, R. B. Liu, and L. J. Sham, Phys. Rev. Lett. **94**, 227403 (2005).

[4] P. F. Braun, X. Marie, L. Lombez, B. Urbaszek, T. Amand, P. Renucci, V. K. Kalevich, K. V. Kavokin, O. Krebs, P. Voisin, and Y. Masumoto, Phys. Rev. Lett. **94**, 116601 (2005).

[5] A. Greilich, D. R. Yakovlev, A. Shabaev, A. L. Efros, I. A. Yugova, R. Oulton, V. Stavarache, D. Reuter, A. Wieck, and M. Bayer, Science **313**, 341 (2006).

[6] T. Fujisawa, D. G. Austing, Y. Tokura, Y. Hirayama, and S. Tarucha, Nature (London) **419**, 278 (2002).

[7] J. M. Elzerman, R. Hanson, L. H. Willems van Beveren, B. Witkamp, L. M. K. Vandersypen, and L. P. Kouwenhoven, Nature (London) **430**, 431 (2004).

[8] A. C. Johnson, J. R. Petta, J. M. Taylor, A. Yacoby, M. D. Lukin, C. M. Marcus, M. P. Hanson, and A. C. Gossard, Nature (London) **435**, 925 (2005).

[9] M. Kroutvar, Y. Ducommun, D. Heiss, M. Bichler, D. Schuh, D. Abstreiter, and J. J. Finley, Nature (London) **432**, 81 (2004).

[10] A. S. Bracker, E. A. Stinaff, D. Gammon, M. E. Ware, J. G. Tischler, A. Shabaev, A. L. Efros, D. Park, D. Gershoni, V. L. Korenev, and I. A. Merkulov, Phys. Rev. Lett. **94**, 047402 (2005).

[11] M. Atatüre, J. Dreiser, A. Högele, K. Karrai, and A. Imamoglu, Science **312**, 551 (2006).

[12] J. R. Petta, A. C. Johnson, J. M. Taylor, E. A. Laird, A. Yacoby, M. D. Lukin, C. M. Marcus, M. P. Hanson, and A. C. Gossard, Science **309**, 2180 (2005).

[13] F. H. L. Koppens, J. A. Folk, J. M. Elzerman, R. Hanson, L. H. W. van Beveren, I. T. Vink, H. P. Tranitz, W. Wegscheider, L. P. Kouwenhoven, and L. M. K. Vandersypen, Science **309**, 1346 (2005).

[14] F. H. L. Koppens, C. Buizert, K. J. Tielrooij, I. T. Vink, K. C. Nowack, T. Meunier, L. P. Kouwenhoven, and L. M. K. Vandersypen, Nature (London) **442**, 766 (2006).

[15] I. A. Merkulov, A. L. Efros, and M. Rosen, Phys. Rev. B **65**, 205309 (2002).

[16] Y. G. Semenov and K. W. Kim, Phys. Rev. B **67**, 073301 (2003).

[17] A. V. Khaetskii, D. Loss, and L. Glazman, Phys. Rev. Lett. **88**, 186802 (2002).

[18] J. Cheng, Y. W. Wu, X. D. Xu, D. Sun, D. G. Steel, A. S. Bracker, D. Gammon, W. Yao, and L. J. Sham, Solid State Commun. **140**, 381 (2006).

[19] A. M. Tyryshkin, S. A. Lyon, A. V. Astashkin, and A. M. Raitsimring, Phys. Rev. B **68**, 193207 (2003).

[20] E. Abe, K. M. Itoh, J. Isoya, and S. Yamasaki, Phys. Rev. B **70**, 033204 (2004).

[21] E. Abe, J. Isoya, and K. M. Itoh, J. Supercond. **18**, 157 (2005).

[22] P. Chen, C. Piermarocchi, L. J. Sham, D. Gammon, and D. G. Steel, Phys. Rev. B **69**, 075320 (2004).

[23] D. G. Steel and J. T. Remillard, Phys. Rev. A **36**, 4330 (1987).

[24] D. G. Steel and S. C. Rand, Phys. Rev. Lett. **55**, 2285 (1985).

[25] N. M. Strickland, P. B. Sellin, Y. Sun, J. L. Carlsten, and R. L. Cone, Phys. Rev. B **62**, 1473 (2000).

[26] S. Ohno, T. Ishii, T. Sonehara, A. Koreeda, and S. Saikan, J. Lumin. **107**, 298 (2004).

[27] S. E. Harris, J. E. Field, and A. Imamoğlu, Phys. Rev. Lett. **64**, 1107 (1990).

[28] S. E. Harris, Phys. Rev. Lett. **62**, 1033 (1989).

[29] K. Bergmann, H. Theuer, and B. W. Shore, Rev. Mod. Phys. **70**, 1003 (1998).

[30] S. E. Economou, R. B. Liu, L. J. Sham, and D. G. Steel, Phys. Rev. B **71**, 195327 (2005).

[31] J. Javanainen, Europhys. Lett. **17**, 407 (1992).

[32] A. Shabaev, A. L. Efros, D. Gammon, and I. A. Merkulov, Phys. Rev. B **68**, 201305(R) (2003).

[33] P. W. Anderson, J. Phys. Soc. Jpn. **9**, 316 (1954).

[34] R. Kubo, J. Phys. Soc. Jpn. **9**, 935 (1954).

[35] P. R. Berman and R. G. Brewer, Phys. Rev. A **32**, 2784 (1985).

Proposal for optical U(1) rotations of electron spin trapped in a quantum dot

Sophia E. Economou[*] and L. J. Sham

Department of Physics, University of California San Diego, La Jolla, California 92093-0319, USA

Yanwen Wu and D. G. Steel

The H. M. Randall Laboratory of Physics, University of Michigan, Ann Arbor, Michigan 48109, USA

We present a proposal to optically implement rotations of the electron spin in a quantum dot about the growth direction (z axis). In particular, we make use of the analytic properties of sech pulses in two-level systems to realize spin rotations about the growth direction by an arbitrary angle, for which we give an analytical expression. We propose to use this scheme to experimentally demonstrate this spin rotation. Using realistic system and pulse parameters we find the fidelity of the rotation to be more than 96% for pulses in the picosecond regime, and robust against small errors in pulse parameters. We design a feedback (adaptive) loop to correct for errors originating from unintended dynamics. The rotation is still evident—albeit with a large fidelity loss—in the ensemble case, providing the possibility of demonstration of this optical spin rotation in an ensemble of quantum dots.

PACS number(s): 78.67.Hc, 03.67.Lx, 42.50.Md

I. INTRODUCTION

A promising qubit candidate is the spin of an electron, trapped in a quantum dot (QD) and manipulated optically via Raman transitions involving a charged exciton (trion) state. Such a scheme combines the merits of the spin in the solid state environment (long coherence times, integrability) with advanced laser technology (speed, focusing, pulse shaping). Recently, there has been significant experimental progress towards the demonstration of the key DiVincenzo requirements for this qubit. In particular, the optical generation of spin coherence has been demonstrated[1–3] and the spin coherence time has been shown to have a lower bound of 10 ns.[1] The optically induced single-qubit rotation, however, has yet to be experimentally shown for this system. In this paper, after briefly reviewing other proposals for such a demonstration (Sec. II), we present a theoretical design of an experimental demonstration of spin rotations about the growth direction in Sec. III which lends itself more appropriately for an experimental demonstration, as it is tailored to the quantum dot Λ system. In Sec. IV we review the solution of the sech pulse in a two-level system. The spin rotation based on these pulses is presented in Sec. V. The numerical simulations are shown in Sec. VI with experimental details taken into account; fidelity loss mechanisms are discussed and quantified in Sec. VII and feedback loops are devised to correct for unintended dynamics or uncertainty in pulse parameters, in Sec. VIII. Finally, Sec. XI contains simulation of the spin rotation in an ensemble of dots.

II. REVIEW OF THE SYSTEM AND OTHER PROPOSALS

The relevant Hilbert space of the system consists of the two spin states of the trapped electron and the optically excited heavy-hole trion state. A static in-plane magnetic field splits the two spin states and defines the x direction. The growth axis of the dot is the z direction and the optical axis as well. The light used is circularly polarized along z. A peculiarity of this system is that the trion level, though spin polarized perpendicularly to the magnetic field, does not precess for fields of up to 5 T.[4] Also, the spin Zeeman splitting is typically small, on the order of tens of μeV's in GaAs (Ref. 1) and on the order of hundreds of μeV's in InAs.[5,6]

Thus we have a Λ-type system with both transitions having the same polarization and being very close in frequency, as depicted in Fig. 1. Therefore, common assumptions in Raman schemes such as polarization selectivity[7] cannot be used, whereas energy selectivity would require long pulses compared to the spin precession period. This could be an issue since the spin decoherence time should be long compared to the gate time. Moreover, when the excited state linewidth is large compared to the lower level splitting (spin Zeeman splitting)—which is the case with GaAs dots—energy selectivity is not well defined, even for long pulses.

A proposal which does not explicitly require selectivity between the two transitions is available,[8] but as will now be explained it implicitly requires long pulses when the spin Zeeman splitting is small. Specifically, in Ref. 8 two pulses with a definite phase relation are used. Both pulses act on both transitions. To remove fast oscillating terms, the condition
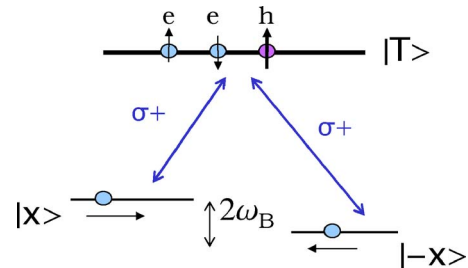

FIG. 1. (Color online) Energy levels of the three-level system, comprised by the two electron spin eigenstates of σ_x and by the trion.
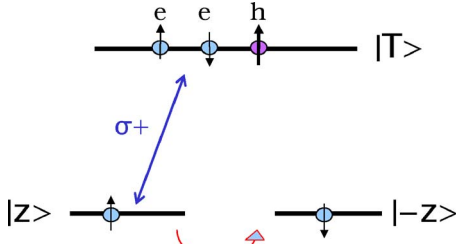
FIG. 2. (Color online) Alternative depiction of the Λ system: the two lower levels are the eigenstates of σ_z but not energy eigenstates, since they are perpendicular to the magnetic field. This basis is more suitable for imposing selection rules when circularly polarized light is used because it is just the one spin state ($|z\rangle$) that couples to the trion. The other one ($|\bar{z}\rangle$) is coupled through the magnetic field.

$$\omega_B \gg \Omega_j(t) \tag{1}$$

is imposed, where $2\omega_B$ is the spin Zeeman splitting and Ω_j is the Rabi frequency of pulse j. The axis of rotation depends on the ratio of the two Rabi frequencies and the phase between the two pulses. The angle of rotation is given by the time integral of

$$\lambda_2 = \frac{\Delta}{2} - \sqrt{\Omega_\uparrow^2 + \Omega_\downarrow^2 + \left(\frac{\Delta}{2}\right)^2}, \tag{2}$$

where Δ is the detuning. From the last relation, it is evident that in order to achieve large rotation angles, long pulses are needed, since the Rabi frequency is bounded from Eq. (1).

Another proposal[9] suggested to use a π pulse to populate the trion state for some time, during which the precession of the spin is used so that the $|\bar{z}\rangle$ state acquires a phase and subsequently a second π pulse recovers the $|z\rangle$ state population by stimulated emission. This method of rotating requires populating the trion state for a significant amount of time, so that trion decay will significantly deteriorate the fidelity. The operation will moreover be slowed down when the spin Zeeman splitting is small. It also provides a scheme for rotations only about the growth axis.

III. PROPOSAL OF ROTATIONS ABOUT Z

In the current proposal, contrary to the use of any kind of selectivity between the two transitions, we choose a pulse with sufficient bandwidth to act on both transitions. The Hamiltonian in the $\{|\bar{z}\rangle, |z\rangle, |\mathcal{T}\rangle\}$ basis has the form

$$H = \begin{bmatrix} 0 & \omega_B & 0 \\ \omega_B & 0 & \Omega(t)e^{i\omega_0 t} \\ 0 & \Omega(t)e^{-i\omega_0 t} & \epsilon_T \end{bmatrix}. \tag{3}$$

It is evident from the above form of the Hamiltonian, that the pulse only couples the $|z\rangle$ state to the excited trion state. The $|\bar{z}\rangle$ state is indirectly coupled through the B field, as shown schematically in Fig. 2. Therefore, for small spin Zeeman splitting compared to the pulse bandwidth we can view in our qualitative discussion the three-level system as two systems of dimensions 2 and 1, consisting of $\{|z\rangle, |\mathcal{T}\rangle\}$ and $\{|\bar{z}\rangle\}$,
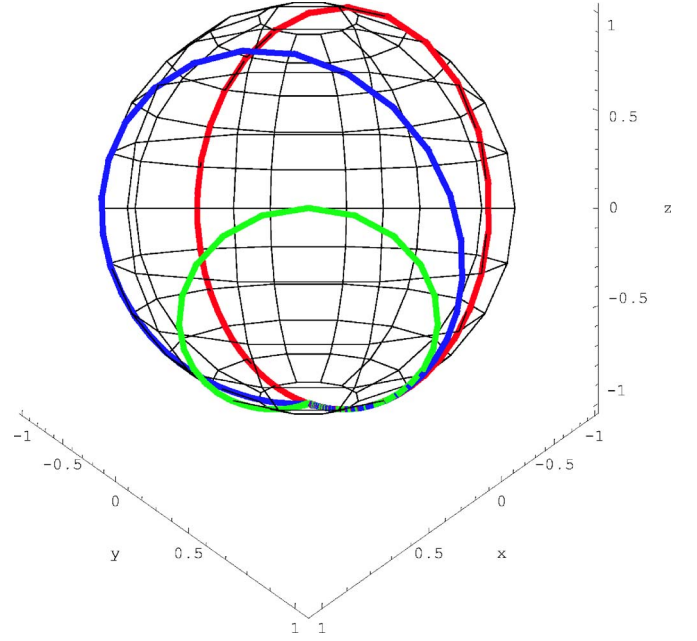
FIG. 3. (Color online) Bloch vector representation of the pseudospin; The pulse bandwidth is fixed ($\sigma=1$) and the detuning varies: $\Delta=0$ [red (dark grey) curve], $\Delta=1$ [blue (black) curve] and $\Delta=0.5$ [green (light grey) curve]. The plot is in the rotating frame of the laser, not that of the unperturbed system.

respectively. This of course is an approximation, strictly valid only in the $B \rightarrow 0$ limit. For finite B we really have two two-level systems sharing a common state. Clearly, fast resonant pulses of area 2π and arbitrary pulse shape will induce a minus sign to the $|z\rangle$ relative to the $|\bar{z}\rangle$ state, due to the SU(2) character of the pseudospin. This amounts to a π rotation of the spin about z.[3,10] We propose the use of analytically solvable off-resonant 2π pulses to design rotations about z by an *arbitrary* angle, for which we provide an analytical expression.

It is well known that for a two-level system the sech pulse shape of Rosen and Zener[11] (RZ) yields an exactly solvable evolution, for arbitrary detuning. As was more recently shown, the RZ pulse belongs to a class of exactly solvable pulse shapes.[12] In what follows, we will make use of the properties of the RZ pulses in the context of the three-level system to design z rotations.

IV. REVIEW OF THE ROSEN-ZENER SOLUTION

Consider a two-state system, initially in the ground state, $|g\rangle$, with the two levels coupled by a time dependent Hamiltonian with a sech envelope and central frequency ω_o:

$$\Omega \, \text{sech}(\sigma t) e^{i\omega_0 t} \equiv f(t) e^{i\omega_0 t}, \tag{4}$$

where Ω is the Rabi frequency, σ is the bandwidth of the pulse. Moving to the interaction picture, the problem reduces to solving two coupled first order equations or, equivalently, one second order equation of the form

$$\ddot{c}_e + (i\Delta - \dot{f}/f)\dot{c}_e + f^2 c_e = 0, \tag{5}$$

where c_g (c_e) is the coefficient of the ground (excited) state, Δ is the detuning, and with the initial condition $c_e(-\infty)=0$. By the change of variable

$$\zeta = \frac{1}{2}[\tanh(\sigma t) + 1], \tag{6}$$

RZ bring the equation into the form of the hypergeometric equation, where

$$a = \frac{\Omega}{\sigma}, \tag{7}$$

$$c = \frac{1}{2}\left(1 + i\frac{\Delta}{\sigma}\right). \tag{8}$$

After imposing the initial conditions, the coefficients of the ground ($|g\rangle$) and excited ($|e\rangle$) states are

$$c_g = F(a, -a, c^*, \zeta), \tag{9}$$

$$c_e = -i\frac{a}{c^*}\zeta^{1-c}F(a+1-c, 1-a-c, 2-c, \zeta). \tag{10}$$

We see from Eq. (10) and by use of the properties of the hypergeometric function that when

$$\sigma = \Omega \tag{11}$$

there is no population transfer to the excited state for $t \to \infty$, i.e., $c_e(\infty)=0$, and instead the pseudospin vector undergoes a full cycle from $|g\rangle$ to $|e\rangle$ and back to $|g\rangle$ with the ground state having acquired a phase factor

$$c_g(\infty) = -\frac{\sigma + i\Delta}{\sigma - i\Delta} \equiv e^{-i\phi}, \tag{12}$$

$$\tan\phi = \frac{2\sigma\Delta}{\Delta^2 - \sigma^2}. \tag{13}$$

For σ fixed, the path will be determined by the detuning, as shown in Fig. 3.

V. USE OF RZ PULSES FOR RAMAN QUBIT ROTATION

For an arbitrary sech pulse, the evolution operator of the whole three-level system, under the approximation of slow precession $\omega_B \ll \sigma$ is given by

$$U \simeq \begin{bmatrix} 1 & 0 & 0 \\ 0 & F(a,-a,c^*,\zeta) & -\frac{ia}{c}\zeta^c F(a+c,-a+c,1+c,\zeta) \\ 0 & -\frac{ia}{c^*}\zeta^{c^*}F(a+c^*,-a+c^*,1+c^*,\zeta) & F(a,-a,c,\zeta) \end{bmatrix}. \tag{14}$$

To have a unitary operation, it is necessary that Eq. (11) is satisfied, i.e., the trion state gets only virtually excited. We will refer to such pulses as "transitionless." Mathematically, this translates to $a=1$. We are also only interested in the form of U after the passage of the pulse, when $z=1$. Then U becomes

$$U \simeq \begin{bmatrix} 1 & 0 & 0 \\ 0 & 1-1/c^* & 0 \\ 0 & 0 & 1-1/c \end{bmatrix} \equiv \begin{bmatrix} 1 & 0 & 0 \\ 0 & e^{-i\phi} & 0 \\ 0 & 0 & e^{i\phi} \end{bmatrix}. \tag{15}$$

The truncated evolution operator, in the 2×2 spin space is described by the unitary matrix

$$U_{\text{spin}} \simeq \begin{bmatrix} 1 & 0 \\ 0 & e^{-i\phi} \end{bmatrix} = e^{-i\phi/2}\begin{bmatrix} e^{i\phi/2} & 0 \\ 0 & e^{-i\phi/2} \end{bmatrix}. \tag{16}$$

A phase between the $|z\rangle$ and $|\bar{z}\rangle$ states translates to a rotation about the z axis by an angle ϕ. So, while for a true two-level system the induced phase of a transitionless pulse is trivial when all the population is initially in the $|z\rangle$ state, for the three-level system it yields a nontrivial rotation about the z

axis. The expression for the angle of rotation may be simplified:

$$\tan\frac{\phi}{2} = \frac{\sin\phi}{1+\cos\phi} = \frac{\sigma}{\Delta} \Rightarrow \phi = 2\arctan\frac{\sigma}{\Delta}. \tag{17}$$

VI. NUMERICAL SIMULATION AND EXPERIMENTAL PROPOSAL

Equations (16) and (17) are our main theoretical results. To check how well this theory works for actual three level systems and with decoherence and unintended dynamics included, we simulate the spin beats of an optical experiment in the dots.

The optical experiments on quantum dots are usually performed at 4 K, which is well above the spin Zeeman splitting for GaAs.[1,13] We are thus starting with a completely mixed state of the qubit and initializing it with optical pumping.[1] We propose to use an RZ pulse which will probabilistically initialize the spin to −0.5 polarization, as in Ref. 3. A $\sigma+$ polarized pulse creates a spin vector (SV) initially pointing
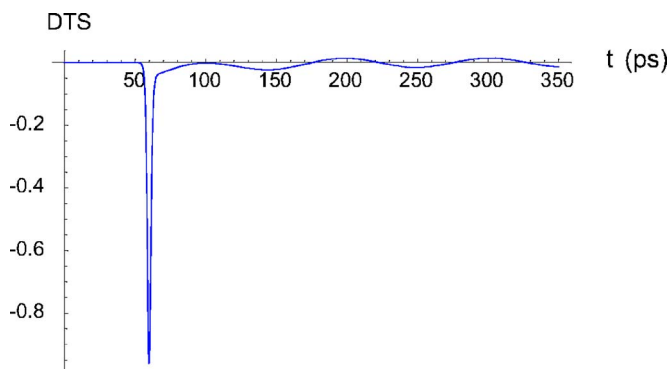
FIG. 4. (Color online) Differential transmission signal (DTS) of transitionless pulse on mixed state. Virtually no beats are generated when $\Omega = \sigma$. Here, $\sigma = 0.4$ meV and $\Delta = 0$.

FIG. 6. (Color online) DTS representing rotation of the spin in a InAs dot by π. The pulse is resonant with $\sigma = 0.8$ meV. The arrow indicates the incidence time of the control pulse.

along $-z$ and precessing about the static B field. We see that by setting $\Omega = \sigma/2$ and $\Delta = 0$ all the population of the $|z\rangle$ state is transferred to the trion, which subsequently decays incoherently to the two lower states provided that the trion state linewidth is small compared to the spin Zeeman splitting so that spontaneously generated coherence (SGC)[1,14] may be ignored. In Sec. VII we will investigate the effect of SGC along with the other deteriorating mechanisms. We also stress that SGC has been taken into account in all our numerical simulations.

Since the designed operation is a rotation about the z axis, the SV should not be affected when the incident control pulse finds it at a dip or peak, i.e., at $|\bar{z}\rangle$ or $|z\rangle$, respectively. On the other hand, the most prominent effect should be when the SV is pointing along the y direction, which is the case in our simulations.

To experimentally achieve a transitionless pulse, the Rabi frequency of the initializing pulse could be doubled or preferably a separate pump-probe experiment with the control pulse in place of the pump may be performed. The transitionless pulse induces a large initial spike and then the spin beats essentially vanish, as shown in Fig. 4. The physics is simple: the transitionless pulse only virtually excites the trion, ideally transferring no population, so that it may not be used for initialization via optical pumping. Once the pulse duration and Rabi frequency of the control pulse are fixed, the detuning will be varied from $\Delta = 0$, which renders a π rotation, to $\Delta = \sigma/\tan(\pi/8)$, which yields a $\pi/4$ rotation.
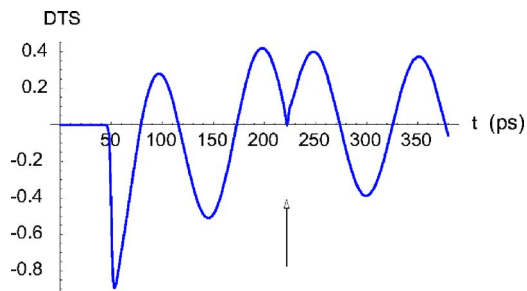
In our simulations we have used two or three pulses: an initializing pulse, a control pulse, and in the case of $\phi \neq \pi$ a second control pulse to recover the beats and prove unitarity. Experimentally, a third (or fourth) pulse, the probe, will be used to perform the measurement of the spin. The time re-

FIG. 5. (Color online) Differential transmission signal (DTS) representing rotation of the spin in a GaAs dot by π with a resonant pulse of $\sigma = 0.4$ meV. The time where the control pulse is centered is indicated by the arrow.
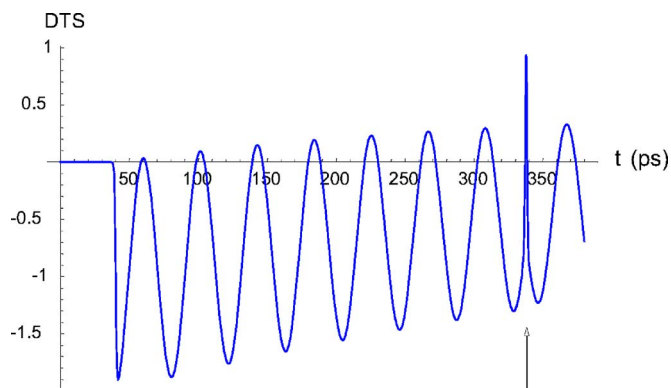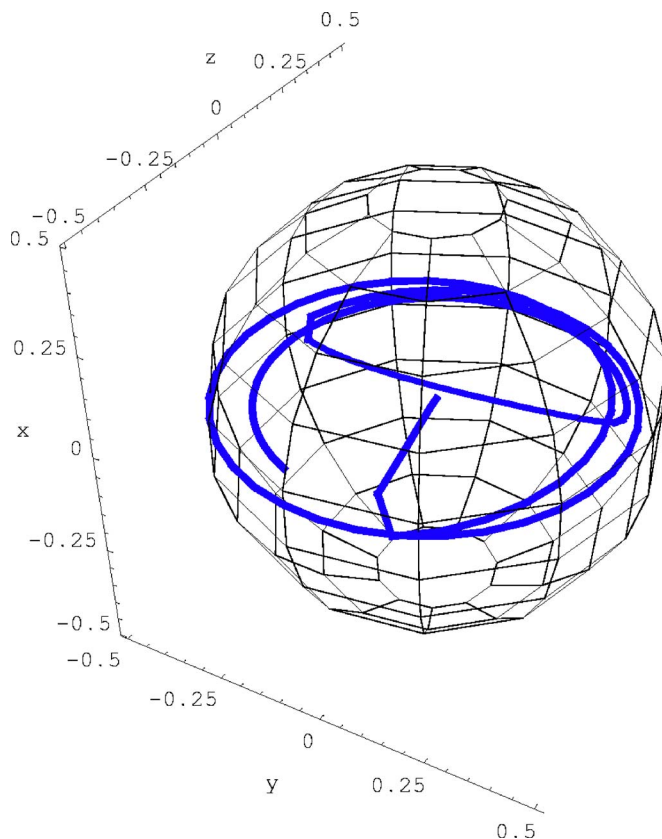

FIG. 7. (Color online) Bloch sphere depiction of the spin generation and rotation of Fig. 5. Initially there is no SV, and its generation along the $-z$ direction is shown. During the rotation the population is moved outside the 2×2 spin subspace and the SV shrinks (line inside the sphere, corresponding to the arrow of Fig. 5). The π rotation about the z axis is implemented when the SV is pointing along $-y$. Note that the Bloch sphere itself has been shrunk to a radius of 0.5 for clearer depiction.
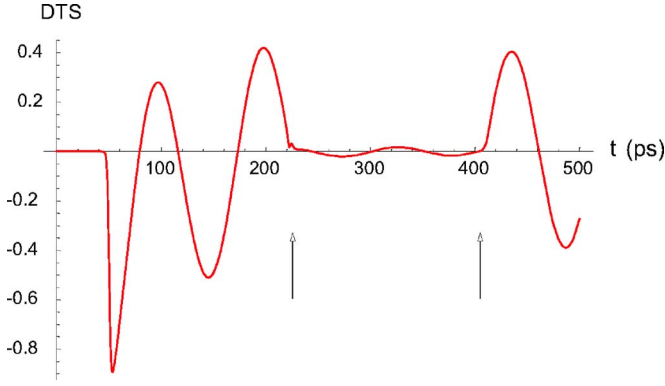
FIG. 8. (Color online) Differential transmission signal (DTS) representing spin rotation in a GaAs dot by $\pi/2$ with pulse of $\sigma = 0.4$ meV and $\Delta = \sigma$. The pump is centered at 50 ps, when the beats start and the central times of the control pulses are indicated by the arrows.

solved probe signal is called the differential transmission signal (DTS) as it measures the difference between the probe signal with the pump on and that with the pump off. When both a co-circularly and cross-circularly polarized probe is used and the difference is taken[1] the quantity measured is $\rho_{zz} - \rho_{TT} - \rho_{\bar{z}\bar{z}} + \rho_{TT}$. For a $\sigma+$ polarized pump, as in our case, and after the decay of the trion level ($\rho_{TT} = 0$) the quantity measured is $\rho_{zz} - \rho_{\bar{z}\bar{z}}$, i.e., the z component of the SV. The duration of the pulses is taken to be about 6 ps for GaAs, close to those used in Ref. 1, which translates to about $\sigma = 0.4$ meV. We take the spin Zeeman splitting to be 40 μeV, which corresponds to a B field of about 6.5 T.[1] For InAs dots, we take $\sigma = 0.8$ meV and the spin Zeeman splitting to be 0.1 meV, which corresponds to $B \sim 2.3$ T.[6] The trion decay rate for GaAs is also taken from Ref. 1, equal to 0.01 meV. For InAs dots it is about 0.6 μeV.[15] The spin dephasing has been chosen conservatively equal to 0.5 μeV for both kinds of dots.

For a π rotation of the spin, the degree of unitarity of the operation is evident in the beat amplitude after the control pulse, Figs. 5 and 6 for GaAs and InAs dots, respectively. In Fig. 7 a Bloch vector illustration of the spin generation and π rotation (corresponding to Fig. 5) is shown. To demonstrate the unitarity of the control pulse for a rotation angle other than π, a second control pulse is used to rotate the SV back to the yz plane and thus recover the initial beat amplitude, as shown in Fig. 8 for GaAs and in Fig. 9 for InAs. We note that the beats are not recovered completely due to errors originating from the trion decay and the (small but finite) precession of the spin during the operation. We will ignore spin dephasing in the following discussion on fidelity.

The spin will be measured via a weak probe. Given that a $\sigma+$ polarized probe measures the z component of the SV, the actual angle of rotation in the experiment will be given by

$$\phi_{exp} = \arccos \frac{A_1}{A_0}, \tag{18}$$

where A_0 and A_1 are the beat amplitudes before and after the control pulse respectively, as in Ref. 16.
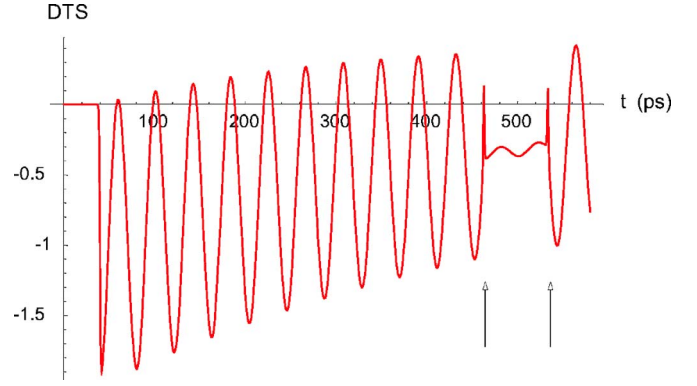

FIG. 9. (Color online) DTS showing the rotation of the spin in a InAs dot by $\pi/2$. The pulse parameters are $\sigma = \Delta = 0.8$ meV. The arrows indicate the incidence time of the two control pulses.

VII. FIDELITY

A. Initialization

The initialization process described above ideally yields a 50% fidelity. However, the mechanism that undermines the fidelity of the initialization is SGC, as mentioned above.[14] SGC is suppressed by making the spin Zeeman splitting larger.[1,14] Our numerical simulations show that the fidelity of initialization is about 40% for GaAs, even for relatively large Zeeman splittings. Since the initialization is far from perfect anyway, we will not worry about SGC effects.

A more important issue is a possible uncertainty in the Rabi frequency, stemming from limited knowledge of the dipole matrix element between $|z\rangle$ and $|t\rangle$. Deviation of the Rabi frequency from $\sigma/2$ will limit the generated polarization. In Sec. VIII we discuss how to maximize the polarization by use of adaptive feedback loops.

Finally, valence band mixing will affect the spin polarization by altering the selection rules. Again, by use of a feedback loop that scans through the polarization of the laser, a true Λ configuration is reached. This, also discussed in Sec. VIII, will also allow for correction due to valence band mixing in the subsequent control of the spin.
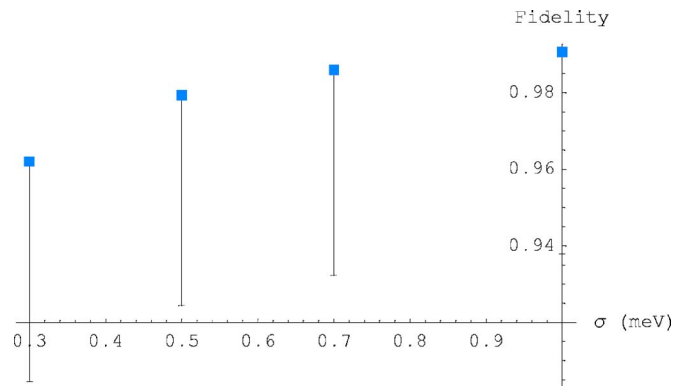

FIG. 10. (Color online) Fidelity of the operation as a function of the pulse bandwidth for GaAs dots. Large bandwidth corresponds to fast pulses, and therefore smaller time intervals of trion excitation. Here the angle of rotation equals π. The uncertainty in the laser electric field is 15%.
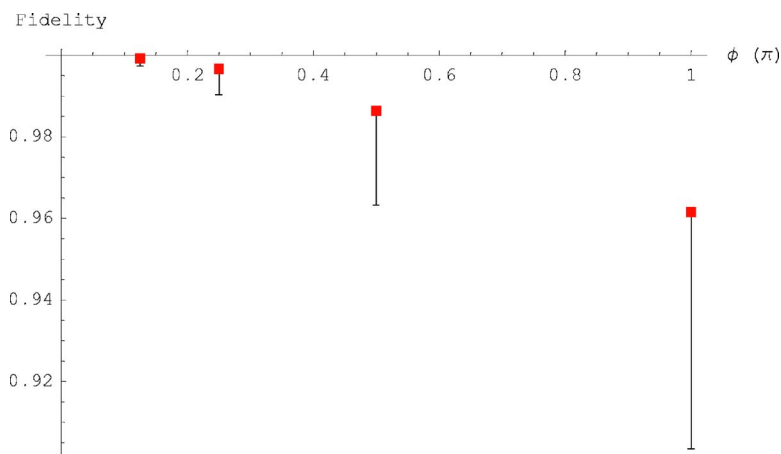
Fidelity

FIG. 11. (Color online) Fidelity of the operation as a function of the angle of rotation for GaAs dots. Large angles correspond to pulses closer to resonance, yielding loss of fidelity due to (real) trion excitation. Here the bandwidth has been taken equal to 0.3 meV and the uncertainty in the laser electric field is 15%.

B. Rotation

The fidelity is given by[16,17]

$$\mathcal{F} = \overline{|\langle \Psi | \widetilde{U}^\dagger U_{id} | \Psi \rangle|^2}, \tag{19}$$

where Ψ is the initial state, $\widetilde{U}$ and U_{id} are the actual and ideal operations, respectively, and the average is to be taken over the relevant (in our case 2×2) Hilbert space. If we define

$$I = \widetilde{U}^\dagger U_{id}, \tag{20}$$

then the fidelity becomes

$$\mathcal{F} = \frac{1}{3} \sum_i |I_{ii}|^2 + \frac{1}{6} \sum_{i \neq j} |I_{ij}|^2. \tag{21}$$

The purity of the operation is given by[17]

$$\mathcal{P} = \overline{\text{Tr}(\rho_{out}^2)} = \frac{1}{3} \sum_i \text{Tr} R_{ii}^2 + \frac{1}{6} \sum_{i \neq j} \text{Tr}(R_{ii} R_{jj} + R_{ij} R_{ji}), \tag{22}$$

where $R_{ij} = \widetilde{U} \rho_{ij} \widetilde{U}^\dagger$.

The fidelity of the operation deteriorates due to the following mechanisms: the decay of the trion state during the optical pulse, the spin precession during the pulse action, and the spin dephasing. The dominant mechanism is the former;

it is irreversible and will degrade the unitarity of the operation, with the effect being stronger for longer pulses and for pulses closer to resonance. Obviously, the shorter the pulse the higher the fidelity; however, there may be a lower bound to how short a pulse can be, as there seems to be an upper bound on pulse strength the system can accommodate. Figure 10 shows the fidelity as a function of the pulse bandwidth. Smaller detunings correspond to larger rotation angles, Eq. (17), so that the fidelity is lower for large rotation angles, and is close to perfect for small angles, as shown in Figs. 11 and 12 for GaAs and InAs dots, respectively.

On the other hand, the precession of the spin vector during the action of the control pulse is a reversible evolution, and will not affect the purity of the operation. It will, however, cause a tilt to the axis of rotation, affecting the fidelity. In principle, this can be taken into account by choosing this alternate axis of rotation instead of insisting on rotations about z. In our case, however, it does play a small role in the loss of fidelity, more so for longer pulses.

As in the initialization case, uncertainty in the Rabi frequency and valence band mixing will affect the fidelity of the rotation. In the next section we discuss how to overcome these effects by use of feedback loops. Once this process is carried out for initialization, the appropriate pulses will automatically be known for the rotation.
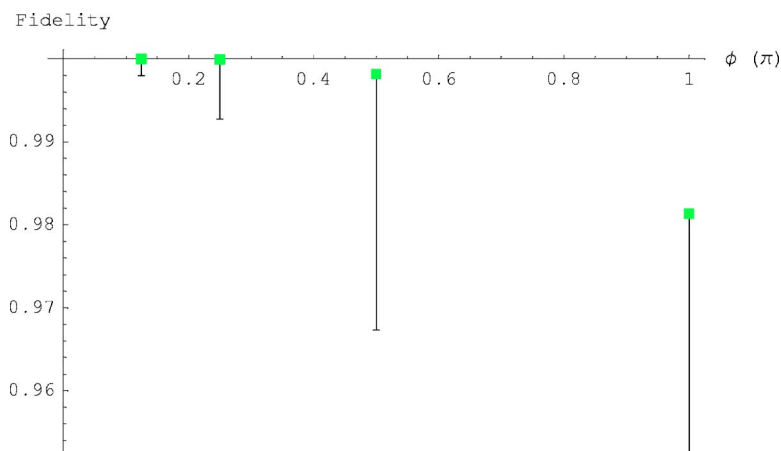
Fidelity

FIG. 12. (Color online) Fidelity of the operation as a function of the angle of rotation for InAs dots. Large angles correspond to pulses closer to resonance, yielding loss of fidelity due to (real) trion excitation. Here the bandwidth has been taken equal to 0.8 meV. The uncertainty in the laser electric field is 15%.
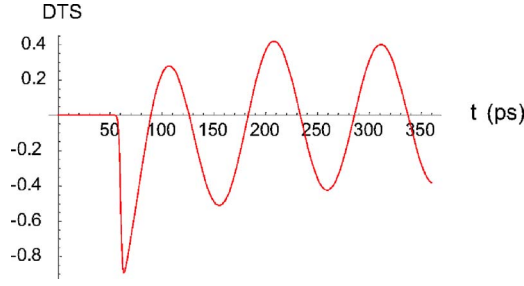
FIG. 13. (Color online) Initialization using a sech pulse with $\sigma=0.4$ meV and $\Omega=\sigma/2$.

FIG. 14. (Color online) Initialization with a pulse with $\sigma=0.4$ meV and $\Omega=1.5\ \sigma/2$.

VIII. OVERCOMING ERRORS WITH FEEDBACK LOOPS

A. Uncertainty in laser parameters

Experimentally, the Rabi frequency may not be exactly known if the polarization matrix element between $|z\rangle$ and $|T\rangle$ has not been measured; one way to find the optimal value of the Rabi frequency is fixing the pulse duration and scanning the intensity until the response (spin polarization) is maximized. Actually, even if the pulse duration is not precisely known, we can devise a feedback loop which combined with the analyticity of our solution will yield the maximum polarization, i.e., will pick the pulse with $\Omega=\sigma/2$. By use of the evolution operator of Eq. (14), we can find the trion population after the passage of the pulse. The truncated evolution operator for time $t\rightarrow\infty$ and for resonant pulses takes the form

$$\Lambda(\Delta=0)\simeq\begin{bmatrix}1 & 0\\ 0 & \cos\left(\dfrac{\Delta\theta}{2}\right)\end{bmatrix}, \tag{23}$$

where $\Delta\theta=2\pi\frac{\Omega}{\sigma}$ is the pulse area. Action of Λ on a mixed density matrix yields

$$\rho=\begin{bmatrix}1/2 & 0\\ 0 & 1/2\,\cos^2\left(\dfrac{\Delta\theta}{2}\right)\end{bmatrix}. \tag{24}$$

The feedback loop we propose consists of the laser, which is connected to a computer which also records the measurements from each run, and a pulse shaper. The pulse bandwidth is fixed but not precisely known. The initial value of the Rabi frequency (laser power) is also unknown, call it Ω_1. After the trion decays, the signal is proportional to the spin polarization. The maximum of the beats then is given by

$$P_1=\frac{A}{2}\sin^2\left(\frac{\Omega_1}{\sigma}\pi\right), \tag{25}$$

where A is some unknown constant related to the measurement process. The value P_1 is recorded and in the next run the Rabi frequency is doubled, $\Omega_2=2\Omega_1$. The next run will thus yield

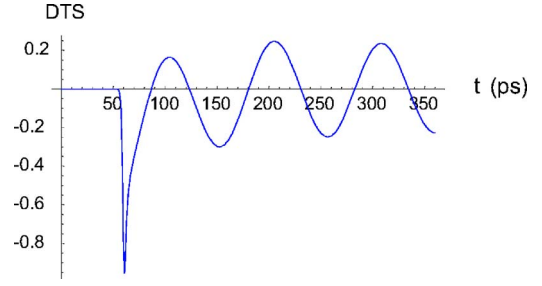$$P_2=\frac{A}{2}\sin^2\left(\frac{2\Omega_1}{\sigma}\pi\right). \tag{26}$$

The ratio is

$$P_1/P_2=\frac{\sin^2\left(\dfrac{\Omega_1}{\sigma}\pi\right)}{\sin^2\left(\dfrac{2\Omega_1}{\sigma}\pi\right)}\Rightarrow\sqrt{\frac{P_2}{P_1}}=\cos\left(\frac{\Omega_2\pi}{2\sigma}\right)\Rightarrow\Omega_2$$

$$=\frac{\sigma}{2\pi}\arccos\left(\frac{1}{2}\sqrt{\frac{P_2}{P_1}}\right). \tag{27}$$

Therefore, in the third run the Rabi frequency should be chosen to be

$$\Omega_3=\frac{\pi\Omega_2}{\arccos\left(\dfrac{1}{2}\sqrt{\dfrac{P_2}{P_1}}\right)}, \tag{28}$$

which is the target value, $\sigma/2$. This is the maximum SV that can be generated at a single shot, shown in Fig. 13 (compare to Figs. 14 and 15 for a stronger and weaker pulse, respectively). An advantage of this scheme is that knowledge of neither the pulse duration nor the Rabi frequency are required. It is also an indirect way of determining the dipole matrix element between $|z\rangle$ and $|T\rangle$.

B. Finite valence band mixing

In the presence of valence band mixing, the Hilbert space is no longer 3×3. We account here for mixing between the $\left|\frac{3}{2}\right\rangle\left(\left|\frac{\bar{3}}{2}\right\rangle\right)$ and the $\left|\frac{\bar{1}}{2}\right\rangle\left(\left|\frac{1}{2}\right\rangle\right)$ trions. Since in all cases the electrons are in the same orbital and in a spin singlet state, we list only the hole states
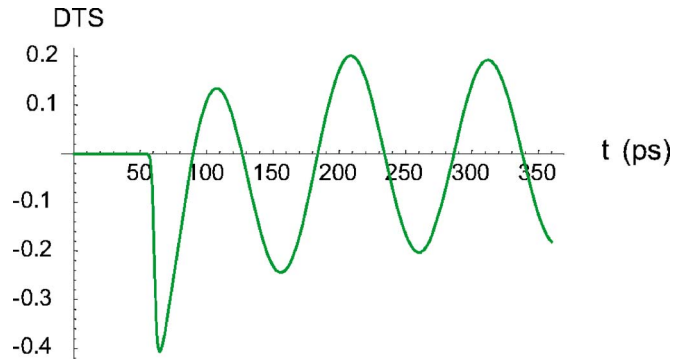

FIG. 15. (Color online) Initialization with a pulse with $\sigma=0.4$ meV and $\Omega=0.5\ \sigma/2$.

$$|HH+\rangle = -\frac{1}{\sqrt{2}}|(X+iY)\uparrow\rangle, \qquad (29)$$

$$|LH-\rangle = \frac{1}{\sqrt{6}}|(X-iY)\uparrow\rangle + \sqrt{\frac{2}{3}}|Z\downarrow\rangle, \qquad (30)$$

$$|LH+\rangle = -\frac{1}{\sqrt{6}}|(X+iY)\downarrow\rangle + \sqrt{\frac{2}{3}}|Z\uparrow\rangle, \qquad (31)$$

$$|HH-\rangle = \frac{1}{\sqrt{2}}|(X-iY)\downarrow\rangle, \qquad (32)$$

where $|X\pm iY\rangle$ and $|Z\rangle$ are the $l=1$ spherical harmonics with $m=\pm1$ and $m=0$, respectively. The corresponding trion states will be denoted by $|H\rangle\ (=|T\rangle), |\bar{L}\rangle, |L\rangle, |\bar{H}\rangle$.

When valence band mixing is included, the valence Hamiltonian in the $\{|H\rangle, |\bar{L}\rangle, |H\rangle, |L\rangle\}$ basis is

$$H = \begin{bmatrix} \epsilon_H & v & 0 & 0 \\ v^* & \epsilon_L & 0 & 0 \\ 0 & 0 & \epsilon_H & v \\ 0 & 0 & v^* & \epsilon_L \end{bmatrix}, \qquad (33)$$

where v is the coupling between heavy and light hole. The dot potential has been assumed such that the mixing between $|H\rangle\ (|\bar{H}\rangle)$ and $|L\rangle\ (|\bar{L}\rangle)$ is zero. To solve the eigenvalue equation, it helps to redefine the zero of energy by subtracting $\bar{\epsilon}/2 \equiv \frac{\epsilon_L+\epsilon_H}{2}$; then we get

$$H = \begin{bmatrix} -a & v & 0 & 0 \\ v^* & a & 0 & 0 \\ 0 & 0 & -a & v \\ 0 & 0 & v^* & a \end{bmatrix}, \qquad (34)$$

where $a = \frac{\epsilon_L-\epsilon_H}{2}$.

By diagonalizing within the blocks, the solution is given by the following eigenvalues and eigenstates:

$$\lambda_\pm = \pm\sqrt{a^2+v^2}, \qquad (35)$$

$$C_{1,-} = \begin{bmatrix} \cos\dfrac{\psi}{2} \\ -\sin\dfrac{\psi}{2} \\ 0 \\ 0 \end{bmatrix} \equiv |H\bar{l}\rangle, \qquad (36)$$

$$C_{1,+} = \begin{bmatrix} \sin\dfrac{\psi}{2} \\ \cos\dfrac{\psi}{2} \\ 0 \\ 0 \end{bmatrix} \equiv |\bar{L}h\rangle, \qquad (37)$$

$$C_{2,-} = \begin{bmatrix} 0 \\ 0 \\ \cos\dfrac{\psi}{2} \\ -\sin\dfrac{\psi}{2} \end{bmatrix} \equiv |H\bar{l}\rangle, \qquad (38)$$

$$C_{2,+} = \begin{bmatrix} 0 \\ 0 \\ \sin\dfrac{\psi}{2} \\ \cos\dfrac{\psi}{2} \end{bmatrix} \equiv |\bar{L}h\rangle. \qquad (39)$$

The angle ψ is defined through

$$\cos\psi = \frac{a}{\sqrt{a^2+v^2}}, \qquad (40)$$

and v is taken to be real.

Restoring the zero of energy, we can write the Hamiltonian in the new basis $\{|H\bar{l}\rangle, |\bar{L}h\rangle, |\bar{H}l\rangle, |L\bar{h}\rangle\}$ as

$$H = \begin{bmatrix} \dfrac{\bar{\epsilon}}{2}-\lambda & 0 & 0 & 0 \\ 0 & \dfrac{\bar{\epsilon}}{2}+\lambda & 0 & 0 \\ 0 & 0 & \dfrac{\bar{\epsilon}}{2}-\lambda & 0 \\ 0 & 0 & 0 & \dfrac{\bar{\epsilon}}{2}+\lambda \end{bmatrix}. \qquad (41)$$

If $\sigma+$ light is used, propagating along z and centered at the HH trions (with energy $\frac{\bar{\epsilon}}{2}-\lambda$) the trion states of higher energy can be ignored by frequency selectivity. In the presence of the mixing we will have a 4×4 Hamiltonian instead of the 3×3 from the previous sections, where mixing was ignored. In the $\{|z\rangle, |\bar{z}\rangle, |H\bar{l}\rangle, |\bar{H}l\rangle\}$ basis, where state $|H\bar{l}\rangle\ (|\bar{H}l\rangle)$ represents a state with largest contribution from the $|H\rangle\ (|\bar{H}\rangle)$ the total Hamiltonian, including the dipole interaction, is

$$H_4 = \begin{bmatrix} 0 & \omega_B & \Omega\cos\dfrac{\psi}{2} & 0 \\ \omega_B & 0 & 0 & \dfrac{1}{\sqrt{3}}\Omega\sin\dfrac{\psi}{2} \\ \Omega^*\cos\dfrac{\psi}{2} & 0 & \dfrac{\bar{\epsilon}}{2}-\lambda & 0 \\ 0 & \dfrac{1}{\sqrt{3}}\Omega^*\sin\dfrac{\psi}{2} & 0 & \dfrac{\bar{\epsilon}}{2}-\lambda \end{bmatrix}. \qquad (42)$$

From Eq. (42) it is clear that when a $\sigma+2\pi$ sech pulse is used, there is actually some error in the rotation scheme of

the previous sections, due to an incomplete Rabi cycle involving the new state $|H\bar{l}\rangle$, and also due to some population transfer to the $|\bar{H}l\rangle$ state. Although this is going to be a very small effect (compared, for example, to the decay of the trion state during the pulse action), we can compensate for it by changing the polarization of the applied field and recover a 3×3 Λ system, which will allow us to use our rotation scheme, as proposed in Sec. V. To find the target polarization, we assume elliptical polarization

$$c_x \hat{x} + i c_y \hat{y} \tag{43}$$

and require

$$\langle \bar{H}l | (c_x \hat{x} + i c_y \hat{y}) | \bar{z} \rangle = 0. \tag{44}$$

Solving Eq. (44) for the c's along with the normalization condition $c_x^2 + c_y^2 = 1$, we find

$$c_x^0 = \frac{\frac{1}{\sqrt{2}} \cos \frac{\psi}{2} - \frac{1}{\sqrt{6}} \sin \frac{\psi}{2}}{\left(\cos^2 \frac{\psi}{2} + \frac{1}{3} \sin^2 \frac{\psi}{2} \right)^{1/2}}, \tag{45}$$

$$c_y^0 = \frac{\frac{1}{\sqrt{2}} \cos \frac{\psi}{2} + \frac{1}{\sqrt{6}} \sin \frac{\psi}{2}}{\left(\cos^2 \frac{\psi}{2} + \frac{1}{3} \sin^2 \frac{\psi}{2} \right)^{1/2}}. \tag{46}$$

Then a three-level system is recovered, consisting of the states $|z\rangle$, $|\bar{z}\rangle$, and $|H\bar{l}\rangle$, and our rotation scheme may be carried out.

To determine the desired polarization, knowledge of ψ, and thus c_x^0, c_y^0, is not necessary. Instead, a feedback loop can be devised, in the spirit of the one described in Sec. VIII A

The Hamiltonian for arbitrary elliptical laser polarization $c_x \hat{x} + i c_y \hat{y}$ is given by

$$H = \begin{bmatrix} 0 & \omega_B & \Omega_+ & 0 \\ \omega_B & 0 & 0 & \Omega_- \\ \Omega_+^* & 0 & \frac{\bar{\epsilon}}{2} - \lambda & 0 \\ 0 & \Omega_-^* & 0 & \frac{\bar{\epsilon}}{2} - \lambda \end{bmatrix}, \tag{47}$$

where

$$\Omega_+ = -\Omega \frac{(c_x + c_y)}{\sqrt{2}} \cos \frac{\psi}{2} - \Omega \frac{(c_x - c_y)}{\sqrt{6}} \sin \frac{\psi}{2}, \tag{48}$$

$$\Omega_- = \Omega \frac{(c_x - c_y)}{\sqrt{2}} \cos \frac{\psi}{2} + \Omega \frac{(c_x + c_y)}{\sqrt{6}} \sin \frac{\psi}{2}. \tag{49}$$

Initially the density matrix is taken to be in a spin ensemble $\rho = \mathrm{diag}(1/2, 1/2, 0, 0)$. After the pulse we have

$\rho = \mathrm{diag}\left(\frac{1}{2} \cos^2 \frac{\theta_+}{2}, \frac{1}{2} \cos^2 \frac{\theta_-}{2}, \frac{1}{2} \sin^2 \frac{\theta_+}{2}, \frac{1}{2} \sin^2 \frac{\theta_-}{2} \right)$, where $\theta_\pm = \frac{2\pi\Omega_\pm}{\sigma}$. The signal then, ignoring SGC, will be

$$P = \frac{A}{2} \left(\cos^2 \frac{\theta_+}{2} - \cos^2 \frac{\theta_-}{2} \right) = \frac{A}{4} (\cos \theta_+ - \cos \theta_-)$$

$$= -\frac{A}{2} \sin \frac{\theta_+ + \theta_-}{2} \sin \frac{\theta_+ - \theta_-}{2}.$$

Inserting the expressions for the angles $\theta_\pm$, we get

$$P = \frac{A}{2} \sin\left(\frac{2\pi\Omega}{\sigma} c_y \left[\frac{1}{\sqrt{6}} n \frac{\psi}{2} - \frac{1}{\sqrt{2}} \cos \frac{\psi}{2} \right] \right)$$

$$\times \sin\left(\frac{2\pi\Omega}{\sigma} c_x \left[\frac{1}{\sqrt{6}} \sin \frac{\psi}{2} + \frac{1}{\sqrt{2}} \cos \frac{\psi}{2} \right] \right)$$

$$\equiv \frac{A}{2} \sin(\alpha_1 \pi c) \sin(\alpha_2 \pi \sqrt{1 - c^2}). \tag{50}$$

The feedback loop is designed as follows: First, we pick $c = c_x = 1/\sqrt{5}$ and the signal is

$$P_1 = \frac{A}{2} \sin\left(\frac{\alpha_1 \pi}{\sqrt{5}} \right) \sin\left(\frac{2\alpha_2 \pi}{\sqrt{5}} \right). \tag{51}$$

For the second run, we choose $c \to 2c$ we get

$$\frac{P_2}{P_1} = \frac{\cos(\alpha_1 \pi / \sqrt{5})}{\cos(\alpha_2 \pi / \sqrt{5})}, \tag{52}$$

which after some algebra becomes

$$\frac{P_2}{P_1} = \frac{\cos(\alpha_1 \pi / \sqrt{5})}{\cos\left(\frac{\alpha_1 \pi}{2\sqrt{5}} + \sqrt{\frac{2\pi^2 \Omega^2}{5\sigma^2} - \frac{3\alpha_1^2 \pi^2}{20}} \right)}, \tag{53}$$

where

$$\alpha_1 = \frac{2\Omega}{\sigma} \left(\frac{1}{\sqrt{6}} \sin \frac{\psi}{2} + \frac{1}{\sqrt{2}} \cos \frac{\psi}{2} \right). \tag{54}$$

Equations (53) and (54) can be solved numerically and thus determine ψ, from which the target polarization will be found from Eqs. (45) and (46), so that in the third run the ideal polarization will have been reached.

For small angle ψ, i.e., small mixing, the small-angle approximation may be employed to obtain an analytical solution for the polarization of the third run in terms of the signals from the first two runs. In this limit, we have for α_1

$$\alpha_1 \approx \frac{2\Omega}{\sigma} \left(\frac{\psi}{2\sqrt{6}} + \frac{1}{\sqrt{2}} \right), \tag{55}$$

and ψ is then

$$\psi = \frac{\sqrt{30}\sigma}{\pi\Omega} \cot\left(\frac{2\pi\Omega}{\sqrt{10}\sigma} \right) \frac{P_1 - P_2}{P_1 + P_2}. \tag{56}$$
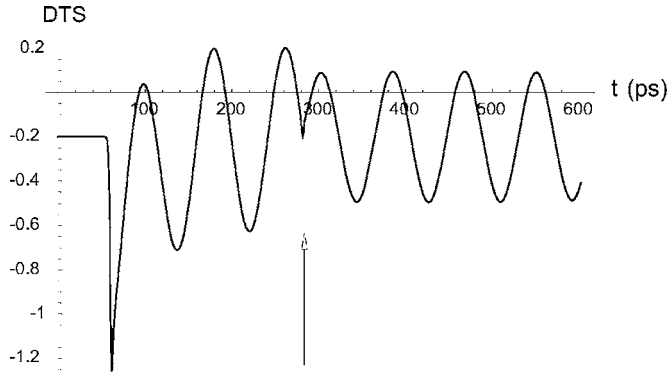
FIG. 16. DTS representing ensemble spin rotation by π using a resonant pulse with $\sigma=0.4$ meV. The fidelity of the rotation is a lot lower than the single-qubit case. The arrow indicates the time of incidence of the control pulse.

IX. ERRORS DUE TO INCOMPLETE RABI FLOP OF EXCITONS

A crucial feature in our scheme is the complete Rabi flop of the trion with a 2π pulse. Rabi oscillations for excitons in quantum dots have been demonstrated experimentally,[18] but they do exhibit distinct features compared to atoms. In Ref. 19 exciton population was measured as a function of the pulse area. For areas larger than π, the Rabi oscillations were shown to degrade considerably and the exciton was not flopped all the way back to the vacuum by a 2π pulse. This effect was seen by several groups,[19,20] and it was attributed to itinerant excitons, phonons, and coupling to wetting layer states.[21] Rabi oscillations between spins and trion states were demonstrated recently in ensemble experiments to have the same feature.[3] We note that for for practical use of our scheme this issue certainly has to be addressed, but for experimental demonstration the rotation should be evident (with a fidelity loss) even in the presence of the damped Rabi flop. In a future work, we will take into account the deteriorating mechanism and try to correct for it via pulse shaping and feedback loops.

X. ROTATIONS ABOUT OTHER AXES

A full set of rotations about one more axis would allow for an arbitrary rotation when combined with the rotations about z. Using the heavy-hole trion state, we can obtain rotations about x using again RZ pulses, albeit a lot slower ones, by frequency selectivity. If, e.g., a pulse is slow enough to excite only one of the two spin states along x, then a 2π RZ pulse, otherwise exactly the same as above, will cause a rotation about x. Clearly, we would have to pay the price of slow pulses, which is exactly what we set off to avoid. Possibly use of higher trion states (e.g., light hole trions) and/or tilting the optical axis away from z may allow for more efficient rotations about axes other than z.

XI. ENSEMBLE STUDY

The experiment may also be performed in an ensemble of dots. Both pump and probe pulses should be modulated at
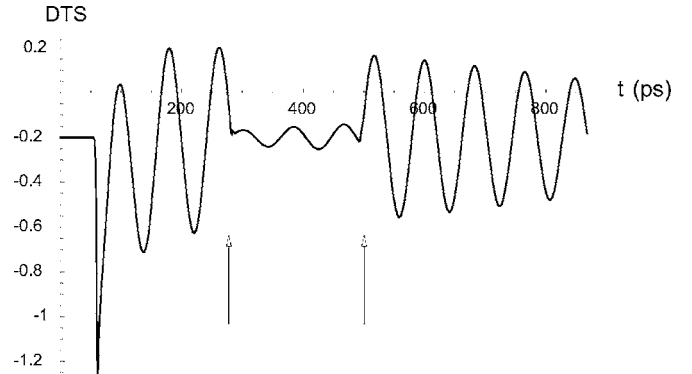

FIG. 17. DTS representing ensemble spin rotation by $\pi/2$. To demonstrate that the operation is a rotation, a second pulse is used to restore the beats. The two arrows indicate the incidence times of the two control pulses.

different frequencies,[22] whereas the control is left unmodulated, so that only the SV initialized by the pump is measured, and the control is measured to all orders in the control field.

In our simulations, we take into account the inhomogeneity of the g factors by an ensemble average over the Gaussian distribution with a full width at half maximum (FWHM) of $\Delta g=0.08g_0$,[1] and the inhomogeneity of the trion energies by a Gaussian, with a FWHM of about 3 meV.[23] The central spin Zeeman splitting is 50 μeV, so that it may represent GaAs dots in a high magnetic field. The pulse bandwidth is again chosen to be 0.3 meV. We have simulated the ensemble response for two different rotation angles, $\phi=\pi$, shown in Fig. 16 and $\phi=\pi/2$, shown in Fig. 17, cf to Figs. 5 and 8, respectively.

The first prominent feature of the plots is that the generated polarization drops by almost an order of magnitude compared to the single spin case. This is due to the contribution of the nonresonant dots to the beat signal. It also exhibits a spike, even for $\Omega=\sigma/2$. Moreover, the operation itself deteriorates significantly compared to the single dot, cf. Figs. 16 and 6 for example. However, the beat amplitude is found to be somewhat recovered by the second rotation in the $\phi=\pi/2$ case, and in the $\phi=\pi$ case, although the operation is far from unitary, the phase changes according to the theory. We therefore conclude that for demonstration purposes the ensemble should also work.

XII. CONCLUSIONS

We have shown how the analytically solvable sech pulses for a two-level system (Rosen-Zener pulses) may be used in a Λ type system when the two transitions share a common polarization and are close in frequency. The analyticity of the RZ pulses enables us to derive an analytical expression for the angle of rotation. Use of short pulses improves the fidelity of our scheme. Numerical simulation shows a fidelity of at least 96% for a realistic choice of parameters. Our scheme can be used to rotate about the growth direction the spin of electrons trapped in quantum dots via Raman transitions

involving the heavy hole trion. Thus, it does not supplant the full rotations in Ref. 8. However, it suggests the possibility for an experimental demonstration without need of addressing a single dot.

*Present address: Naval Research Laboratory, Washington, DC 20375, USA.

[1] M. V. G. Dutt *et al.*, Phys. Rev. Lett. **94**, 227403 (2005).

[2] M. Atatüre, J. Dreiser, A. Badolato, A. Högele, K. Karrai, and A. Imamoglu, Science **312**, 551 (2006).

[3] A. Greilich *et al.*, Phys. Rev. Lett. **96**, 227401 (2006).

[4] J. G. Tischler, A. S. Bracker, D. Gammon, and D. Park, Phys. Rev. B **66**, 081310(R) (2002).

[5] M. Bayer, A. Kuther, A. Forchel, A. Gorbunov, V. B. Timofeev, F. Schäfer, J. P. Reithmaier, T. L. Reinecke, and S. N. Walck, Phys. Rev. Lett. **82**, 1748 (1999).

[6] M. Kroutvar, Y. Ducommun, D. Heiss, M. Bichler, D. Schuh, G. Abstreiter, and J. J. Finley, Nature (London) **432**, 81 (2004).

[7] Z. Kis and F. Renzoni, Phys. Rev. A **65**, 032318 (2002).

[8] P. Chen, C. Piermarocchi, L. J. Sham, D. Gammon, and D. G. Steel, Phys. Rev. B **69**, 075320 (2003).

[9] T. Calarco, A. Datta, P. Fedichev, E. Pazy, and P. Zoller, Phys. Rev. A **68**, 012310 (2003).

[10] S. E. Economou, L. J. Sham, Y. Wu, and D. G. Steel (unpublished).

[11] N. Rosen and C. Zener, Phys. Rev. **40**, 502 (1932).

[12] A. Bambini and P. R. Berman, Phys. Rev. A **23**, 2496 (1981).

[13] R. I. Dzhioev, V. L. Korenev, B. P. Zakharchenya, D. Gammon, A. S. Bracker, J. G. Tischler, and D. S. Katzer, Phys. Rev. B **66**, 153409 (2002).

[14] S. E. Economou, R.-B. Liu, L. J. Sham, and D. G. Steel, Phys. Rev. B **71**, 195327 (2005).

[15] M. E. Ware, E. A. Stinaff, D. Gammon, M. F. Doty, A. S. Bracker, D. Gershoni, V. L. Korenev, S. C. Bădescu, Y. Lyanda-Geller, and T. L. Reinecke, Phys. Rev. Lett. **95**, 177403 (2005).

[16] C. Piermarocchi, P. Chen, Y. S. Dale, and L. J. Sham, Phys. Rev. B **65**, 075307 (2002).

[17] J. F. Poyatos, J. I. Cirac, and P. Zoller, Phys. Rev. Lett. **78**, 390 (1997).

[18] T. H. Stievater, X. Li, D. G. Steel, D. Gammon, D. S. Katzer, D. Park, C. Piermarocchi, and L. J. Sham, Phys. Rev. Lett. **87**, 133603 (2001).

[19] Q. Q. Wang, A. Muller, P. Bianucci, E. Rossi, Q. K. Xue, T. Takagahara, C. Piermarocchi, A. H. MacDonald, and C. K. Shih, Phys. Rev. B **72**, 035306 (2005).

[20] A. Zrenner, E. Beham, S. Stufler, F. Findeis, M. Bichler, and G. Abstreiter, Nature (London) **418**, 612 (2002).

[21] J. M. Villas-Bôas, S. E. Ulloa, and A. O. Govorov, Phys. Rev. Lett. **94**, 057404 (2005).

[22] N. H. Bonadeo, J. Erland, D. Gammon, D. Park, D. S. Katzer, and D. G. Steel, Science **282**, 1473 (1998).

[23] J. Cheng, M. V. Gurudev Dutt, D. G. Steel, A. S. Bracker, D. Gammon, and L. J. Sham (unpublished).

PHYSICAL REVIEW LETTERS

Density Matrix Tomography through Sequential Coherent Optical Rotations of an Exciton Qubit in a Single Quantum Dot

Yanwen Wu,[1] Xiaoqin Li,[1,*] L. M. Duan,[1] D. G. Steel,[1,†] and D. Gammon[2]

[1]*The H. M. Randall Laboratory of Physics, The University of Michigan, Ann Arbor 48109, Michigan, USA*
[2]*The Naval Research Laboratory, Washington D.C. 20375, USA*

We demonstrate single qubit density matrix tomography in a single semiconductor quantum dot system through consecutive phase sensitive rotations of the qubit via ultrafast coherent optical excitations. The result is important for quantifying gate operations in quantum information processing in the quantum dot systems as well as demonstrating consecutive arbitrary qubit rotations.

PACS numbers: 78.67.Hc, 03.67.Lx, 42.50.Hz, 42.50.Md

Many critical milestones toward practical quantum computation have now been achieved in exciton based qubit systems including single qubit rotation [1], a two-qubit controlled-NOT gate [2], and a two-qubit population swap [3]. The demonstration of density matrix tomography of the exciton based qubit is another critical step enabling valuable quantification on the performance (fidelity) of the operations mentioned above [4]. In addition, achieving multiple consecutive rotations of a qubit within its coherence lifetime is required in quantum computation processes. Maintaining the relative phase information between consecutive operations on the qubit is essential for the accuracy of the end results. For example, logic operations in error correction codes [4] and in the Deutsch-Josa (DJ) problem [5] require a pair of phase-locked Hadamard gates to prepare and collapse the qubit in order to achieve correct outputs.

In this Letter, we combine techniques of signal calibration and optical phase control on an exciton based qubit in a single quantum dot (QD) to demonstrate rotation of the measurement basis of the qubit as done in nuclear magnetic resonance (NMR) [6] and atomic [7] systems. This enables us to realize the first tomographic reconstruction of the density matrix of a qubit in a single QD, laying the ground work for measuring the fidelity of quantum operations in a QD system. Furthermore, it shows the suppression of scattering effects characteristic of higher dimensional semiconductor systems, validating the atomic approximation of the exciton states in QDs.

The sample under investigation consists of interface fluctuation $GaAs/Al_{0.3}Ga_{0.7}As$ QDs [8–10]. Single dots are detected through submicron apertures on a thin aluminum mask deposited on the sample [9]. The excitons in each single dot have an average lifetime of 60 ps with negligible pure dephasing effects inferred from nonlinear spectroscopy studies [11,12].

To achieve multiple operations within the apparent coherence time of the exciton ($\sim$ 100 ps), picosecond laser pulses are used for the ultrafast control of the qubit. A 3 ps pulse is chosen as a compromise between operational speed and spectral selectivity. A modulated time domain

pump-probe technique is used to obtain and process the homodyne-detected nonlinear optical signals from differential transmission (DT).

The physical structure of the interface fluctuation dots allows for the confinement of two linear orthogonally polarized excitons inside a single dot [8]. For the experiments described in this Letter, we approximate the electronic structure of the two Coulomb coupled excitons by a four-level system as shown in Figs. 1(a) and 1(b) [2]. The lower state is the crystal ground state, the intermediate states are two nearly degenerate linear orthogonally polarized excitons, and the upper state is the biexciton. Since the laser bandwidth ($\sim$0.4 meV) is much smaller than the binding energy of the biexciton ($\sim$3.5 meV) [2], we can safely neglect transitions to the biexciton and concentrate on the reduced three level **V** system in the dashed boxes illustrated in Figs. 1(a) and 1(b).

In Ref. [2], both exciton transitions constitute qubits. Here, we define one polarized transition of the exciton (Π_x, horizontal) as the qubit and the orthogonally polarized transition (Π_y, vertical) as the readout for the purpose of this measurement. The qubit states are $|0\rangle$ and $|1\rangle$ and the state $|R\rangle$ is the readout exciton as labeled in Figs. 1(a) and 1(b).

Single qubit rotations for logic operations can be achieved through coherent excitation. The optical pulse area, θ, is defined by $\theta(t) = \int_{-\infty}^{t} dt \boldsymbol{\mu}_{eg} \cdot \boldsymbol{E}(t)/\hbar$, where $\boldsymbol{\mu}_{eg}$ is the optical dipole moment of the ground to exciton state transition and $\boldsymbol{E}(t)$ is the electric field amplitude of the laser pulse. We can apply pulses with corresponding pulse areas from 0 to π to create an arbitrary superposition state of $|0\rangle$ and $|1\rangle$ from the state $|0\rangle$, as demonstrated in the optically driven single exciton Rabi oscillations [1,13–15].

To derive a direct correspondence between the populations of the qubit states, $|0\rangle$ and $|1\rangle$, and the measured DT signal, a calibration scheme is implemented with the readout state $|R\rangle$. The QD system under no optical excitation is initialized in the $|0\rangle$ state ($\rho_{00} = 1$, $\rho_{11} = \rho_{RR} = 0$ where ρ is the density matrix). For calibration, we can resonantly excite transitions between the qubit states with a pump pulse of known pulse area. The weak probe then measures
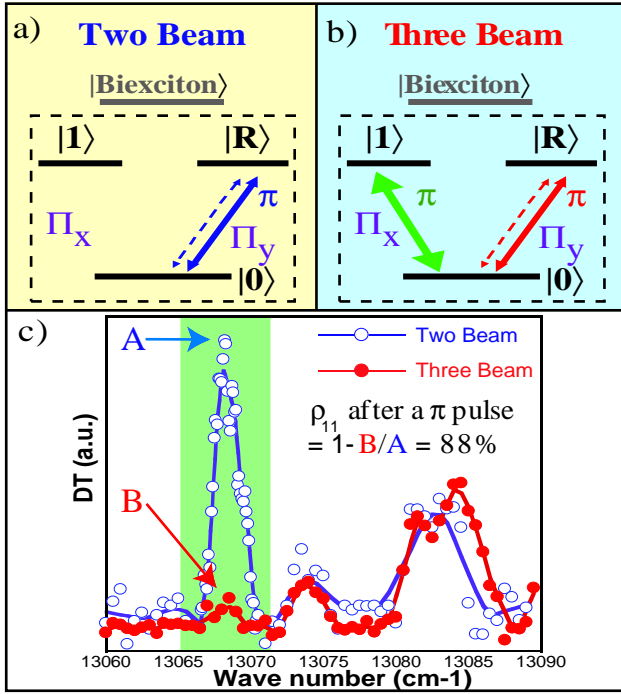
FIG. 1 (color online).   (a) and (b) Four-level representation.
(a) Two-beam setup. (b) Three-beam setup. $|0\rangle$ and $|1\rangle$ are the
crystal ground state and the qubit exciton, respectively, while $|R\rangle$
is the readout exciton. The arrows in (a) and (b) denote the laser
pulses, where the dashed lines are the probes, the normal solid
lines are the pumps and the thick solid line is the prepump.
(c) DT signal obtained by using the two-beam (blue, open circle)
and three-beam (red, solid circle) setups. The state where the
prepump is fixed is highlighted in green (gray). We indicate that
a π pulse inverts 88% of the population to state $|1\rangle$, leaving 12%
in state $|0\rangle$.

the population of the $|0\rangle$ state. The DT signal, which is the
signal with the pump off minus the signal with the pump
on, is proportional to $1 - \rho_{00}$. Since the two-level qubit
system in a single dot is shown to be a closed system
($\rho_{11} + \rho_{00} = 1$) [12], ρ_{11} is linearly proportional to the
signal. Without decay, this is sufficient to completely
calibrate the DT signal. However, in a physical system,
due to the finite pulse width of 3 ps and the short relaxation
time of the exciton at 65 ps, a π pulse does not invoke a
complete population inversion from state $|0\rangle$ to $|1\rangle$. Hence,
we must take decay into consideration.

A pair of experiments is conducted to measure the
amount of population transferred to state $|1\rangle$ for a π pulse.
First, a two-beam setup is used to drive transitions between
states $|0\rangle$ and $|R\rangle$ [thin blue solid and dashed arrows in
Fig. 1(a)], where the solid (dashed) arrow represents the
pump (probe). The pump and probe with the same optical
frequency are scanned in frequency, where the pump is set
at a pulse area of π and the probe is kept weak below a
pulse area of $\pi/2$. The pump and probe are temporally
separated by 10 ps to avoid any contribution from coherent
artifacts. The DT signal is recorded as the blue open circle

plot in Fig. 1(c), where the exciton transition of interest is
highlighted in green. We denote the signal strength of this
measurement as **A**. High spectral resolution spectroscopies
using continuous wave lasers [12] are also made on the
state to ensure single exciton excitation (data not shown).
Next, a three-beam setup measures the population remain-
ing in the $|0\rangle$ state after a π pulse excitation. A prepump
with pulse area π is fixed in frequency at the $|0\rangle$ to $|1\rangle$
transition [thick green solid arrow in Fig. 1(b)], and trans-
fers the maximum population to state $|1\rangle$. A pump and
probe pair similar to the two-beam experiment [thin red
solid and dashed arrows in Fig. 1(b)], is delayed 10 ps from
the prepump and scanned in frequency to read the popula-
tion in state $|0\rangle$ by driving transitions to state $|R\rangle$. The
result is recorded as the red solid circle plot in Fig. 1(c).
The signal strength of the highlighted state in this experi-
ment is denoted as **B**. From the values of **A** and **B** and the
linear correspondence between population difference and
DT signal, we conclude that the maximum population
transferred by a 3 ps wide π pulse is $1 - \mathbf{B}/\mathbf{A} = 88 \pm$
1%. A simulation using the experimental parameters gives
the result of a 85% population transfer, which is in excel-
lent agreement with the data.

The ability of the quantum system to sustain and propa-
gate information in time is enabled by the optical phase-
locking capability of the experimental setup. A Michelson
interferometer is inserted in the path of the pump beam to
create two pump pulses with tunable temporal delay (τ on
scale of ps) and an actively stabilized phase delay (ϕ on
scale of fs) via a translation stage and a piezoelectric
mount, respectively, as shown in Fig. 2. We fixed two
pump pulses each with a pulse area of $\theta = \pi/2$. The
pump pulses are separated by $\tau = 10$ ps to ensure that
the final qubit state is due to two distinct optical operations,
and not the product of optical interference. By varying ϕ,
we are changing the effective pulse area of the pulse
sequence. The changes in ϕ are reflected in the sinusoidal
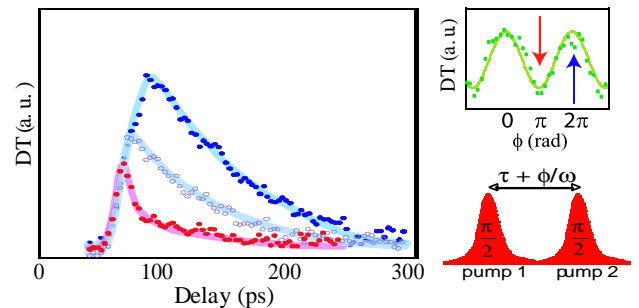oscillations of the $|1\rangle$ state population as illustrated by the

FIG. 2 (color online).   Phase dependent rotations of a qubit in
the exciton system. The red (blue) plot corresponds to a relative
phase of $\phi = \pi(2\pi)$ between the two pump pulses, as indicated
by the red (blue) arrow in the inset. The open circle plot is a
single $\pi/2$ decay, which serves as a comparison. The inset is an
interferogram. Here $\tau = 10$ ps and ω is the laser frequency.

quantum interferograms in the insets of Fig. 2. The maxima of the interferogram correspond to constructive interference ($\phi = 2\pi$, effective $\theta = \pi$) while the minima correspond to destructive interference ($\phi = \pi$, effective $\theta = 0$).

To understand the physical pictures behind the time evolutions of consecutive optical operations, we examine the dynamics of motion in the Bloch sphere representation. The optical Bloch vector, **U** with elements $\{u, v, w\} = \{2\,\mathrm{Re}[\rho_{01}], -2\,\mathrm{Im}[\rho_{01}], \rho_{11} - \rho_{00}\}$, precesses around the field vector $\mathbf{R} = \{\mathrm{Re}[E(t)], -\mathrm{Im}[E(t)], \delta\}$, where δ is the laser detuning for the two-level system ($\delta = 0$ for this work, and **R** lies in the **u**-**v** plane). The equation of motion is thus given by $\dot{\mathbf{U}} = \mathbf{R} \times \mathbf{U}$. The component of the Bloch vector projected onto the **u**-**v** plane represents the coherence, and the projection onto the **w** axis represents the population difference of the quantum system. The $|0\rangle$ ($|1\rangle$) state is represented by the Bloch vector pointing down (up).

Ideally, for two pump pulses each at $\theta = \pi/2$, the qubit state is initially driven from the $|0\rangle$ state to the $(|0\rangle + |1\rangle)/\sqrt{2}$ state described by the Bloch vector rotating around the field vector from a down position to the **u**-**v** plane. By setting $\phi = \pi$, the out-of-phase second pulse drives the quantum state back down to $|0\rangle$. In contrast, for $\phi = 2\pi$, the now in-phase second pulse drives the quantum state up to $|1\rangle$. Hence, phase control between consecutive quantum operations is critical since two consecutive rotations with the same magnitudes but different phases can lead to profoundly different outcomes, a result well known in atomic type systems. The ability to control this phase then ensures control for consecutive and arbitrary qubit rotations as well as accuracy of the operation output, all of which are necessary for practical quantum information processing.

Because of decays, the experimental results deviate from the ideal, as shown in Fig. 2. These data are taken by fixing the pumps and scanning the probe delay to observe the decay dynamics of the system. Clearly, in Fig. 2, the red plot shows that the population is not completely driven back down to state $|0\rangle$ following the second pump pulse due to the short lifetime of the exciton. The fast population decay leads to the loss of coherence between the two-qubit states and limits the accuracy of coherent control by laser pulses.

The phase locking of an optical pulse to the coherence of a quantum system now enables us to perform quantum tomography of the density matrix for a single qubit. We demonstrate the ability to measure the off-diagonal matrix elements (ρ_{01}, ρ_{10}) as well as the diagonal density matrix elements (ρ_{00}, ρ_{11}) of a closed two-level system, which leads to a complete mapping of the density matrix of a qubit in a single QD. To obtain the coherence terms, we rotate the component in the **u**-**v** plane onto the measurement axis **w** through an optical excitation of $\theta = \pi/2$. By

choosing the right phase of this optical rotation field, we can easily extract both the real and imaginary parts of the coherence terms.

From the equation of motion, the time evolution of the Bloch vector **U** is a precession around the field vector **R** by an angle of the pulse area of the field. We utilize this precession in a controlled manner to extract the real and imaginary parts of the coherence terms. Since the real (imaginary) components of the field and coherence lie on the **u** (**v**) axis, a purely real field ($\phi = 0$) at $\theta = \pi/2$ rotates only the imaginary part of the coherence to the **w** axis for measurement. Similarly, a purely imaginary field ($\phi = \pi/2$) only measures the real part of the coherence.

Mathematically, we can see the relation between ϕ and the components of the coherence being measured in the new population term ρ_{11}^{rot}, after the $\pi/2$ rotation,

$$\rho_{11}^{\mathrm{rot}} = \frac{1}{2}[1 - i(e^{-i\phi}\rho_{01} - e^{i\phi}\rho_{10})], \qquad (1)$$

where $\rho_{11}^{\mathrm{rot}} = 1/2 + \mathrm{Im}[\rho_{01}]$ for $\phi = 0$ and $\rho_{11}^{\mathrm{rot}} = 1/2 - \mathrm{Re}[\rho_{01}]$ for $\phi = \pi/2$ for a closed system.

We demonstrate the application of single qubit density matrix tomography on the maximum coherent state of a two-level system created by a $\pi/2$ pulse. The population terms, ρ_{00} and ρ_{11}, are measured through a two-beam experiment where the creation pulse of $\pi/2$ prepares the state and the probe directly reads the value of $\rho_{11} = 0.36$ through the calibrated DT signal as shown in Fig. 3. To measure the coherence terms (ρ_{01} and ρ_{10}), a $\pi/2$ rotation pulse is inserted after the creation pulse to rotate the coherence components to the measurement axis **w**. The values of $\rho_{11}^{\mathrm{rot}} = 0.73$ at $\phi = 0$ and $\rho_{11}^{\mathrm{rot}} = 0.42$ at $\phi = \pi/2$ can be obtained through the calibrated interferogram shown in Fig. 3. In both cases, the creation pulse is temporally separated from the other pulses by 10 ps to avoid interfering with the preparation of the original state.

Using Eq. (1) and values from Fig. 3, we obtain the measured density matrix as seen in Fig. 4(d). The values are notably different from the ideal matrix in Fig. 4(a) and also the expected values of the matrix given the decay parameters of the sample shown in Fig. 4(b).
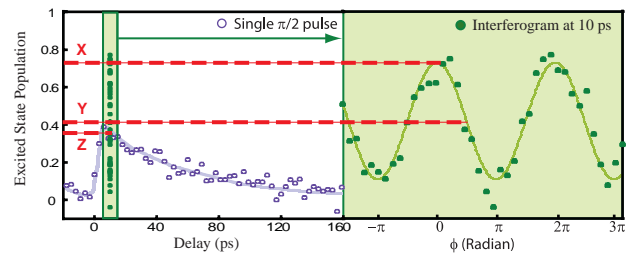

FIG. 3 (color online). Decay plots of single $\pi/2$ pulse and interferogram taken at 10 ps delay from the creation pulse. The horizontal dashed lines mark the values of each population readout. **X** gives $\rho_{11}^{\mathrm{rot}} = 0.73$, **Y** gives $\rho_{11}^{\mathrm{rot}} = 0.42$, and **Z** gives $\rho_{11} = 0.36$.
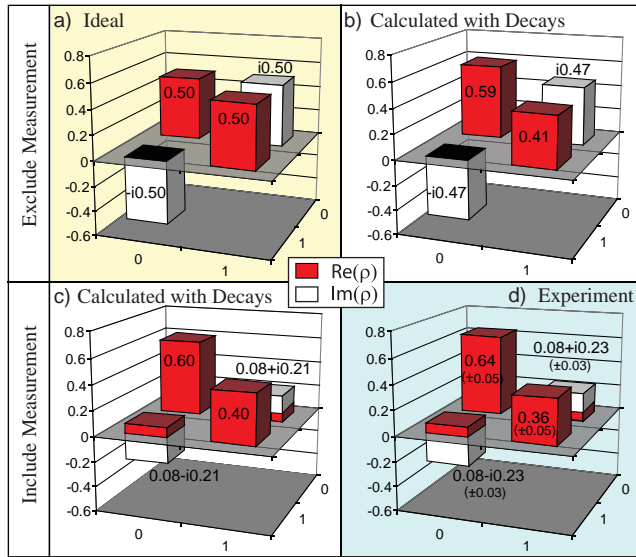
FIG. 4 (color online). Density matrices of a single qubit created by a $\pi/2$ pulse. (a) Ideal matrix. (b)[(c)] Calculated density matrices with decays excluding (including) rotation and probe pulses. (d) Measured density matrix from experiment.

The large discrepancies between the coherence (off-diagonal) terms in these density matrices can be attributed to the measurement process represented by the rotation pulse. In numerical simulations including the measurement process [Fig. 4(c)], the density matrix elements are comparable to the measured values. The excellent agreement between Figs. 4(c) and 4(d) signifies that we have a complete knowledge of the quantum system used and that its behavior under excitation is completely theoretically predictable.

We note that the population terms of all three nonideal density matrices are essentially the same. However, the coherence terms of the density matrices with the inclusion of the rotation pulse stray from their ideal values. Specifically, in the presence of the rotation pulse, the coherence terms have nonzero real components, while in the absence of a rotation pulse, they are purely imaginary regardless of the qubit lifetime. This apparent discrepancy arises from the short decoherence of the system and the temporal overlap of the first and the second pump pulses. Although the two 3 ps wide pump pulses are separated by 10 ps, the pulse tail of the first pulse and the pulse front of the second pulse overlap. The amount of overlap, though small, can still affect the accuracy of the measurement of the coherence terms.

In the Bloch sphere representation, we can attribute the error to population decay and the simultaneous rotation of the Bloch vector by the creation and rotation pulses, both of which lead to a nonzero real component in the measured coherence terms. We can avoid simultaneous rotation of the Bloch vector by separating the two pulses further to eliminate overlaps, but the short decoherence between the qubit states $|0\rangle$ and $|1\rangle$ will begin to introduce greater error as the measurement is made at a larger delay. It may be that the discrepancies can be minimized by using a combination of pulse-shaping techniques on shorter pulses to avoid exciting nearby states [16–18]. Quantum systems with longer decay times, such as the spin qubit system in charged QDs, would also minimize this error.

In summary, we have demonstrated the tomographic reconstruction of the density matrix of a single qubit as well as consecutive arbitrary qubit rotations. These measurements can be easily extended to map the complete physical density matrix of multiqubit systems as in Ref. [2]. Even though the measurement accuracy is limited by the intrinsic decay parameters of the quantum system, the technique itself is proven to be suitable and practical for the purpose of density matrix tomography. Improved performance in optically driven spin based systems [19] is anticipated because spin lifetimes are expected to be 4 orders of magnitude longer than the exciton system [20–23].

*Present address: JILA, University of Colorado, Boulder, CO 80309, USA.
†Electronic address: dst@umich.edu
[1] T. H. Stievater *et al.*, Phys. Rev. Lett. **87**, 133603 (2001).
[2] X. Li *et al.*, Science **301**, 809 (2003).
[3] Q. Q. Wang *et al.*, Phys. Rev. Lett. **95**, 187404 (2005).
[4] M. A. Nielsen and I. L. Chuang, *Quantum Computation and Quantum Information* (Cambridge University Press, Cambridge, United Kingdom, 2000), 1st ed., p. 425.
[5] D. Deutsch and R. Jozsa, Proc. R. Soc. A **439**, 553 (1992).
[6] A. M. Childs, I. L. Chuang, and D. W. Leung, Phys. Rev. A **64**, 012314 (2001).
[7] P. C. Haljan *et al.*, Phys. Rev. A **72**, 062316 (2005).
[8] D. Gammon *et al.*, Phys. Rev. Lett. **76**, 3005 (1996).
[9] D. Gammon *et al.*, Science **273**, 87 (1996).
[10] J. G. Tischler *et al.*, Phys. Rev. B **66**, 081310(R) (2002).
[11] N. H. Bonadeo *et al.*, Science **282**, 1473 (1998).
[12] N. H. Bonadeo *et al.*, Phys. Rev. Lett. **81**, 2759 (1998).
[13] H. Kamada *et al.*, Phys. Rev. Lett. **87**, 246401 (2001).
[14] H. Htoon *et al.*, Phys. Rev. Lett. **88**, 087401 (2002).
[15] A. Zrenner *et al.*, Nature (London) **418**, 612 (2002).
[16] P. Chen, C. Piermarocchi, and L. J. Sham, Phys. Rev. Lett. **87**, 067401 (2001).
[17] T. Calarco *et al.*, Phys. Rev. A **68**, 012310 (2003).
[18] C. Piermarocchi *et al.*, Phys. Rev. B **65**, 075307 (2002).
[19] C. Piermarocchi *et al.*, Phys. Rev. Lett. **89**, 167402 (2002).
[20] M. Kroutvar *et al.*, Nature (London) **432**, 81 (2004).
[21] J. M. Elzerman *et al.*, Nature (London) **430**, 431 (2004).
[22] R. Hanson *et al.*, Phys. Rev. Lett. **94**, 196802 (2005).
[23] J. R. Petta *et al.*, Science **309**, 2180 (2005).